SISSA
Scuola
Internazionale
Superiore di
Studi Avanzati

Physics Area - PhD course in
Theory and Numerical Simulation of Condensed Matter

Many-Body physics of cavity embedded quantum matter

Thesis submitted for the degree of
Doctor Philosophiae

Candidate:
Zeno Bacciconi

Advisors:
Marcello Dalmonte
Massimo Capone

Academic Year 2024-2025



Abstract

Controlling the properties of quantum matter is a central goal of condensed matter physics. In recent years, cavity embedding—that is, shaping the electromagnetic environment surrounding a material by placing it inside a cavity—has emerged as a new potential tuning knob. While such concepts were first successfully explored with ultracold atomic clouds, more recent experiments have demonstrated their feasibility in solid-state systems. Despite the differences between these platforms, they share a key feature: the coexistence of degrees of freedom with distinct levels of locality. On one hand, electrons or atoms exhibit local dynamics (hopping, interactions), while on the other, cavity modes are typically delocalized across the entire system. The study of this unconventional quantum many-body framework—investigated through aspects such as phase transitions, topology, and dynamical properties—constitutes the main focus of this thesis.

Publication list

[1] **Zeno Bacciconi**, Gian Marcello Andolina, Titas Chanda, Giuliano Chiriacò, Marco Schirò and Marcello Dalmonte, *First-order photon condensation in magnetic cavities: A two-leg ladder model*, SciPost **15**, 113 (2023)

[2] **Zeno Bacciconi**, Hernan B. Xavier, Massimo Capone and Marcello Dalmonte, *Cavity-modified quasi-long range order in one dimensional quantum systems*, in preparation

[3] **Zeno Bacciconi**, Hernan B. Xavier, Matteo Marinelli, Devendra Singh Bhakuni and Marcello Dalmonte, *Local vs Nonlocal Dynamics in Cavity-Coupled Rydberg Atom Arrays*, Phys. Rev. Lett. **134**, 213604 (2025)

[4] **Zeno Bacciconi**, Gian Marcello Andolina and Christophe Mora, *Topological protection of Majorana polaritons in a cavity*, Phys. Rev. B **109**, 165434 (2024)

[5] **Zeno Bacciconi**, Hernan B. Xavier, Iacopo Carusotto, Titas Chanda and Marcello Dalmonte, *Theory of Fractional Quantum Hall Liquids Coupled to Quantum Light and Emergent Graviton-Polariton*, Phys. Rev. X **15**, 021027 (2025)

[6] Hernan B. Xavier, **Zeno Bacciconi**, Titas Chanda, Dam Thanh Son and Marcello Dalmonte, *Chiral Gravitons on the Lattice*, arXiv:2505.02905 (2025) (accepted in Phys. Rev. Lett.)

[7] **Zeno Bacciconi**, Giulia Piccitto, Alessandro Maria Verga, Giuseppe Falci, Elisabetta Paladino and Giuliano Chiriacò, *Dissipation and non-thermal states in cryogenic cavities*, arXiv:2504.00591 (2025) (accepted in Quantum)

Other Publications not in the thesis

[8] Gian Marcello Andolina, **Zeno Bacciconi**, Alberto Nardin, Peter Rabl, Marco Schirò and Daniele De Bernardis, *Electrostatics-induced breakdown of the integer quantum Hall effect in cavity QED*, in preparation

Contents

Introduction **3**

1. First-order photon condensation in magnetic cavities: A two-leg ladder model **9**
1.1. Introduction . . . 9
1.2. Hamiltonian . . . 11
1.3. Square ladder . . . 15
1.3.1. Methods . . . 15
1.3.2. Results: Photon mean-field vs. DMRG . . . 18
1.3.3. Results: Gaussian fluctuations . . . 22
1.4. Triangular ladder . . . 26
1.5. Conclusion . . . 27

2. Cavity-modified quasi-long range order in one dimensional quantum systems **29**
2.1. Introduction . . . 29
2.2. Hamiltonian . . . 30
2.3. Magnetic coupling . . . 32
2.4. Electric coupling . . . 35
2.5. Conclusions and outlook . . . 38

3. Local vs non-local dynamics in cavity-coupled Rydberg atom-arrays **41**
3.1. Introduction . . . 41
3.2. Model Hamiltonian . . . 43
3.3. Domain-wall propagation . . . 44
3.4. Meson-polaritons . . . 45
3.5. String dynamics . . . 47
3.6. Experimental blueprint . . . 48
3.7. Conclusions . . . 49

4. Topological protection of majorana-polaritons in a cavity **51**
4.1. Introduction . . . 51
4.2. The model . . . 53
4.3. Signatures of topology . . . 55
4.4. Quasi-adiabatic continuation . . . 56

4.5. Majorana polaritons . . . 59
4.6. Conclusions . . . 60

5. Theory of Fractional Quantum Hall liquids coupled to quantum light and emergent graviton-polaritons 63
5.1. Introduction . . . 63
5.2. The model . . . 67
5.2.1. Landau levels . . . 67
5.2.2. Cavity set-up . . . 69
5.2.3. Quantum light-matter coupling . . . 70
5.2.4. LLL truncation . . . 72
5.2.5. Role of gradients . . . 75
5.2.6. Hamiltonian . . . 76
5.2.7. Numerical methods . . . 79
5.3. Topological order in cavity . . . 80
5.3.1. Hall resistivity via flux insertion . . . 81
5.3.2. Entanglement spectrum . . . 84
5.4. Spectral properties . . . 88
5.4.1. Magnetoroton spectrum . . . 88
5.4.2. Numerical results . . . 90
5.4.3. Effective model . . . 92
5.5. Ultra-strong coupling effects . . . 95
5.5.1. Cavity control of FQH geometry . . . 96
5.5.2. Stripe instability . . . 97
5.5.3. Vacuum-induced Stark shift of quasi-particle energy . . . 101
5.6. Experimental discussion . . . 103
5.7. Conclusions and outlook . . . 107
5.7.1. On recent experiment . . . 109

6. Chiral gravitons on the lattice 111
6.1. Introduction . . . 111
6.2. Lattice model . . . 113
6.3. The continuum limit . . . 113
6.4. Lattice stress tensor . . . 114
6.5. Graviton weights . . . 116
6.6. Open edges . . . 118
6.7. Quench dynamics . . . 118
6.8. Conclusions . . . 119

7. Dissipation and non-thermal states in cryogenic cavities 121
7.1. Introduction . . . 121
7.2. The model . . . 123

7.3. Derivation of the dissipation rates . . . 126
7.3.1. Mirror-cavity interaction . . . 127
7.3.2. Environment dissipation rate . . . 128
7.3.3. Discussion and examples . . . 131
7.4. Non-thermal cavity population . . . 133
7.5. Non-linear mode mixing . . . 138
7.6. Conclusions . . . 140

8. Concluding remarks **143**

Appendices **145**

A. First-order photon condensation in magnetic cavities **147**
A.1. Gaussian states and Wigner function . . . 147
A.2. Photon mean-field in periodic boundary conditions . . . 148
A.3. Perturbation theory . . . 149
A.4. Details about DMRG simulations . . . 150

B. Local vs non-local dynamics in cavity-coupled Rydberg atom arrays **153**
B.1. Derivation of the rydberg-cavity Hamiltonian . . . 153
B.2. Cavity losses . . . 155
B.3. Atom decay and post-selection . . . 156

C. Topological protection of Majorana-polaritons in a cavity **159**
C.1. Details on the light-matter coupling . . . 159
C.2. Topology in absence of cavity . . . 160
C.3. Theory of quasi-adiabatic continuation . . . 161
C.3.1. General formalism . . . 161
C.3.2. Perturbation theory . . . 162
C.4. Details about the DMRG numerics . . . 164

D. Theory of Fractional Quantum Hall liquids coupled to quantum light and emergent graviton-polaritons **167**
D.1. Test of the LLL truncation . . . 167
D.2. Cavity losses . . . 169
D.3. Photon mean-field argument . . . 170
D.4. Stripe energy estimation . . . 173
D.5. Stripes as an array of Tomonaga-Luttinger liquids . . . 174
D.6. Excited state targeting . . . 175
D.7. Large cavity frequency limit . . . 176

Introduction

Controlling the properties of quantum matter is a central goal in modern condensed-matter physics. Historically, this control has come through adjusting electronic interactions, lattice geometries, chemical substitutions, or external fields. In recent years, however, a complementary paradigm has gained traction: *engineering the electromagnetic environment* via embedding systems inside optical or microwave cavities [9–12]. This paradigm, often referred to as *cavity embedding*, provides new knobs to steer correlated quantum systems, enabling routes toward emergent phases, novel excitations, and enhanced quantum control.

Cavity Quantum Electrodynamics - Such ideas build upon the great success of cavity Quantum Electrodynamics (QED) [13, 14] in shaping optical properties of independent emitters. One of the first and paradigmatic example of this is the Purcell effect [15], which demonstrates that controlling the electromagnetic density of states surrounding an atom strongly influence its decay rate. Such physics belong to the so-called weak-coupling regime, where dissipations are stronger than coherent light-matter interaction strengths.

Much interest and efforts have been devoted in pushing the light-matter interaction strength to strong and ultra-strong coupling regimes [16] where light-matter interaction energy scales are greater than losses and become comparable even to bare energies of the individual constituencies. A fundamental and ubiquitous property of such regimes is the formation of *polaritons* [17], hybrid light-matter quasi-particles, which are often used as direct evidence of the composite nature of the systems and of the strong-coupling regime. In the ultra-strong coupling regimes electromagnetic vacuum fluctuations directly have an impact on the ground state of the hybrid system which cannot be thought of as two separate entities anymore.

Reaching ultra-strong coupling regimes however is a more challenging task. This has to face the perturbative nature of QED, which controls the smallness of free-space vacuum corrections, like the Lamb-shift [18]. Cavity QED often relies on *sub-wavelength* compression of electromagnetic modes, i.e. compression below the natural wavelength, in order to reduce the quantization volume and enhance vacuum fluctuations of the field. Different setups can reach such regimes each with their specificity (split-ring resonators [19], surface-plasmons [20], hyperbolic phonon-polaritons [21] etc), making the space of possible configurations for ultra-strong coupling quite broad.

Another route, followed in cold atom setups with Fabry-Perot cavities, is to use external lasers to devise effective models where bare cavity and atomic energies ($\sim 100\,\mathrm{THz}$)

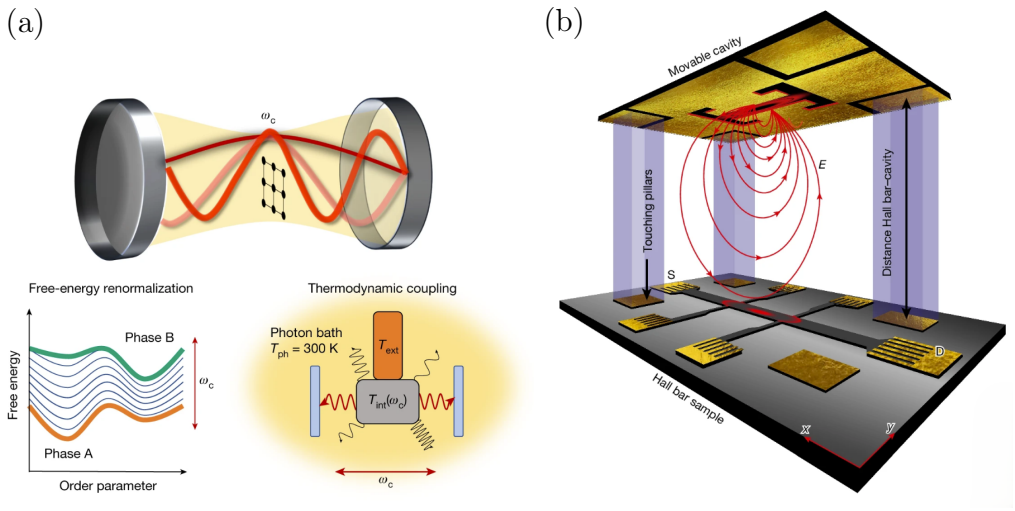


Figure 1.: Example of passive cavity-control of quantum materials, a solid state sample is immersed in a modified electromagnetic enviroment by (a) a Fabri-Perot cavity and (b) a movable split-ring resonator. Figures taken from (a) Ref. [40] and (b) Ref. [46] representing the experimental state-of-the-art.

are effectively reduced to laser detunings ($\sim$ MHz). This allows for a great tunability of atom-light effective couplings, even in non-perturbative regimes, with the drawback of the system being intrinsically out-of equilibrium.

Cavity control of matter - Early theoretical proposals and experimental demonstrations of how strong coupling regimes can modify matter properties were realized exactly in this context of cold atomic gases with high finesse Fabry-Perot cavities [12, 22]. This includes the first realizations of Dicke-like superradiant instabilities as a self-ordering transitions [23], as well as the realization of non-trivial many-body phases such as supersolidity [24].

More recently a lot of efforts have been dedicated to solid-state platforms, with the ultimate goal of using the electromagnetic environment as a tuning knob for quantum materials (Fig. 1). Many of the theoretical proposals focus on the role of enhanced quantum fluctuations in cavity QED to control a variety of phenomena/phases (transport [25, 26], superconductivity [27, 28], topological phases [29–32], quantum magnetism [33, 34], criticality [35, 36], ferroelectricity [37, 38], Fermi liquids [39]). Experimental demonstrations of these ideas are now starting to appear. Among these, leading works showed control, with different extents, of metal-insulator transition [40], magneto-transport [41], mobility in organic semiconductors [42], integer [43, 44] and fractional quantum hall systems[45], stripe phases [46] and superconductivity [47]. Even though further efforts are often needed to provide clear theoretical understanding of such experiments, the results obtained so far are promising.

A new many-body scenario - From a quantum many-body perspective, one of the defining aspect cavity-embedded quantum matter is the coexistence of (i) *local*

degrees of freedom, such as electrons, spins, or atoms which have an intrinsically local dynamics, and (ii) *delocalized* cavity modes that extend coherently across the system. The delocalization of cavity photons over the natural scale of the matter defies locality principles underlying *standard* quantum many-body physics. The broad theoretical challenge is to understand how such familiar notions developed for locally interacting matter (phase transitions, topological protection, excitation structure, universality etc ..) evolve in the presence of such global couplings.

Much of the current understanding of this hybrid systems rely on mean-field approximations and/or on adiabatic eliminations of the cavity modes. The application of different numerically methods have also been quite fruitful. These include exact diagonalization methods [48, 49], dynamical mean-field theory [38], quantum monte carlo [35] and tensor networks [50, 51]; each with different strengths and weaknesses in accessing different quantities (ground state, excitations, entanglement properties etc ..) or many-body systems (different dimensionalities, fermions or spins etc..).

This thesis - The goal of the thesis is to deepen the many-body understanding of cavity-embedded systems, exploring a range of different phenomena concerning phase transitions, dynamics, excitation structure and topology. From a methodological point of view, we have successfully applied hybrid matrix product state (MPS) ansatze to different novel scenarios in the context of cavity-embedded matter, including dynamical properties and 2d quantum matter. The thesis is organized in different chapters (from 1 to 7) which report results from different publications and ends with a brief conclusions chapter (Chapter 8) which summarize the contributions of the thesis and lay out some general open challenges. The chapters 1 to 7 are organized as follows.

In chapter 1 (Ref. [1]) we discuss a toy model for photon condensation, also refereed to as superradiant transition, in a quasi-1D itinerant electron system coupled to the magnetic field degree of freedom of a cavity. We show how such transition can quite generally be of first order when non-linearities are present in the matter magnetic response. This chapter offers also a in depth comparison between photon-mean-field methods and density matrix renormalization group (DMRG) results, showing how gaussian fluctuations beyond mean-field are able to recover many of the missed features and allow to easily construct excitations on top of the ground state.

In chapter 2 (Ref. [2]) we study the effect of non-local cavity modes on strongly correlated 1D systems showing $U(1)$ quasi-long range order. We focus on a light-matter coupling which lowers the symmetry of the system in two different scenarios for the coupling structure. In particular these are distinguished by a cavity-mediated interaction vertex which either do or do not vanish in the mean-field limit.

In the first case where the coupling is Dicke-like, we observe a zero-coupling phase transition which is strongly affectected by the underlying quasi-$U(1)$ matter fluctuations and go beyond the zero-dimensional Dicke phase transition showing Luttinger-Liquid dictated critical exponents. In the second case no phase transition appears, as the coupling comes from a minimal substitution principle and obeys no-go theorems.

However the cavity fluctuations give rise to a strongly anisotropic Luttinger Liquid which loses the $U(1)$ symmetry in its macroscopic response function and at the same time retains the critical behaviors of the no-cavity limit.

In chapter 3 (Ref. [3]) we shift the focus on dynamical properties of low-energy excitations in cavity-embedded system. In particular we consider a Rydberg atom array coupled to an optical cavity mode where the competition between the local Ising interactions and the non-local cavity mediated interaction has a strong impact on the nature of excitations of the system. Elementary domain-walls retain a notion of locality while composite meson-like excitation hybridize with the photons and acquire a non-local dynamics. Such phenomenology is contrasted with the one of a purely local transverse field Ising model, highlighting the marked differences in dynamical properties of the cavity-embedded scenario. A concrete experimental proposal for the observation of such physics is also proposed.

In chapter 4 (Ref. [4]) we investigate the stability of a one-dimensional topological superconducting system to the presence of a global cavity mode. Locality is an important property for topological systems which, in the usual scenario, leads to the so-called topological protection. In cavity embedded systems this has been recently put into question. In the case of Majorana-fermions, we show here how even non-local correlations mediated by the cavity photons do not disrupt the topological protection of the Majorana modes. Using quasi-adiabatic continuation arguments supported by DMRG numerics we show how having a symmetry-conserving coupling between photon and matter is a sufficient condition for the stability. In this study case the important symmetry is fermionic parity, but the arguments are generalizable to other symmetry protected topological (SPT) phases.

In chapter 5 (Ref. [5]) we develop and study a model for cavity-embedded Fractional Quantum Hall (FQH) liquids, a system of direct experimental relevance. We rely mostly on DMRG numerical results, here applied to a 2D system coupled to global cavity modes for the first time. Similarly for the case of SPT phases, we find that the topological order of the system is unaffected by the cavity as witnessed from the bulk conductivity and entanglement spectrum properties. The latter however carry direct fingerprints of the hybrid nature of the system.

An important prediction we make is the formation of new hybrid polaritons modes with elusive collective excitations of the FQH liquid called graviton-modes (hence graviton-polaritons). Furthermore we discuss possible scenarios for the ultra-strong coupling regime, finding possible stripe phase instabilities. Overall, our results lay a solid ground for further and more system-specific analysis on the nature of cavity-induced phenomena in FQH systems.

In chapter 6 (Ref. [6]) we explore the nature of graviton-mode excitations on lattice Fractional Quantum Hall states in Harper-Hofstadter models. In particular we present a framework in which we explicitly derive a field theory incorporating lattice chiral

graviton operators. Extensive numerical evidence suggests that chiral graviton modes persist away from the continuum, and are well captured by the proposed lattice operators. We identify geometric quenches as a viable experimental probe, paving the way for the exploration of chiral gravitons in near-term quantum simulation experiments.

In chapter 7 (Ref. [7]) we study the non-equilibrium state of a multi-mode cavity coupled to different thermal reservoir. Even in absence of matter within the cavity, we show how different cavity modes reach thermal steady-states at different temperatures, making the overall state of the cavity non-thermal. We further highlight how such non-thermal state can be tuned by engineering dissipation of the mirrors composing the cavity and connect our results with the idea of passive thermal control of quantum materials.

Chapter 1.

First-order photon condensation in magnetic cavities: A two-leg ladder model

In this chapter we investigate equilibrium photon-condensation in a toy model of spinless electrons living in a quasi-1D ladder geometry. The main set of methodological tools used in the thesis (hybrid MPS ansatz, photon-mean-field and fluctuations beyond mean-field) is here introduced.

1.1. Introduction

One of the aims of the paradigm of cavity control is to modify the properties of quantum materials using cavity embedding [9, 11, 12]. In strong coupling regimes, vacuum effects [10] can modify the properties of the material even without external illumination, e.g., by affecting magneto-transport of a two dimensional (2D) material [41] or suppressing topological protection of the integer quantum Hall effect [43]. Recently, coupling to a cavity mode has been demonstrated to affect the critical temperature and the phase transition in charge-density wave systems [40]. Theoretical proposals have focused on the possibility of controlling electronic instabilities and ordered phases by quantum fluctuations of the cavity field, including superconductivity [27, 28, 52] and ferro-electricity [37, 53], or even inducing phase transitions in both light and matter degrees of freedom by onset of the so called *superradiant* phase where the ground state has a macroscopic number of coherent photons, hence photon condensed phase. The equilibrium superradiant phase transition, originally introduced in the context of the Dicke model [54–56] describing an ensemble of two-level atoms collectively coupled to a common cavity mode, has been recently discussed for electronic systems coupled to single-mode cavity [57–63].

A proper description of photon condensation requires a gauge invariant framework

for the light-matter interaction, an issue which poses key theoretical challenges for truncated models which only retain a subset of degrees of freedom. In the ultrastrong coupling regime [64], where the light-matter coupling is comparable to the transition energies of the atoms, this truncation could lead to violations of gauge-invariance [65–67], thus questioning the validity of such a description. Indeed, the theoretical predictions of photon condensation have been hindered by the use of truncated models lacking gauge invariance, leading to inaccurate results.

To tackle this issue, Refs. [68, 69] considered an underlying microscopic model without relying on any truncation and proved that photon condensation is prohibited as long as a single-mode spatially *uniform* vector potential is considered. In order to reproduce this result within a truncated model, it is crucial to use a gauge-invariant descriptions of the light-matter interaction such as the Peierls phase and its extensions [70–72].

More recent works[73–78] have relaxed the strong assumption of the spatially uniform vector potential and show that photon condensation is analogous to the Condon magnetostatic instability [79]. According to these studies, photon condensation can occur only in presence of a magnetic field, while a purely electric field cannot condense as a result of no-go theorems[68, 69]. As a corollary, photon condensation is prohibited in a strictly one dimensional (1D) geometry [68, 80] where the orbital motion of electrons cannot be affected by a magnetic field. Therefore, one needs to consider at least two dimension or the spin degree of freedom [77].

Here we investigate the occurrence of photon condensation in a minimal setting beyond 1D – i.e., a two-leg ladder [81–85] – where the orbital motion of spinless fermions is coupled through Peierls substitution to a non-uniform cavity mode which generates a fluctuating uniform magnetic field. Similar cavity set-ups have been proposed in Refs. [86, 87]. Moreover, recent developments have demonstrated ultra-strong coupling between magnons and the magnetic field of a superconducting resonator [88]. In contrast to 1D chains, two-leg ladders allow us to analyze transverse response to non-uniform vector potentials, while still being amenable to a thorough numerical investigation beyond typical mean-field approximations by means of the density-matrix renormalization group (DMRG) techniques [89–92] (recently being also employed in cavity quantum electrodynamics (QED) systems [30, 36, 51, 93–95]).

Our results show that ladder geometries can indeed host an equilibrium superradiant transition (or photon condensation [68]), not to be confused with the non-equilibrium phase transition observed in dye filled microcavities [96]), via a first-order transition from a normal metallic phase. The first order nature of this transition arises from the strongly non-linear orbital paramagnetic response of the ladder system and provides therefore a different scenario for condensation with respect to those discussed so far in the literature [74, 75, 77]. While a photon mean-field (PMF) decoupling of the photon and matter degrees of freedom captures qualitatively the phase transition, we find that for finite sizes the correct treatment of quantum fluctuations is essential to

estimate physically relevant quantities, such as current and photon properties. This demonstrates how, in these settings, the light-matter entanglement and photon squeezing cannot, in general, be neglected. In the thermodynamic limit, we show that the photon condensation allows to modify the properties of an extensive system with a single cavity mode in the collective strong coupling regime. Remarkably, even in this thermodynamic limit, where the photon state is Gaussian, it is necessary to consider both the light-matter entanglement and photon squeezing to determine the photon properties.

The structure of the chapter is the following. In Sec. 1.2 we describe the Hamiltonian of the light-matter coupled system and introduce the main physical gauge-invariant quantities. In Sec. 1.3 we first introduce the PMF approximation and the DMRG numerics. Then we discuss the result comparing the two approaches and recover a qualitative agreement between the two by adding quantum fluctuations on top of the PMF solution. In Sec. 1.4 we move to the triangular ladder geometry highlighting the similarities with the square ladder case. In Sec. 1.5, we draw the conclusions and discuss possible future directions.

1.2. Hamiltonian

We consider a hybrid light-matter system where the light component is represented by a single cavity mode and the matter component is described by a tight-binding model of charged ($q = -1$) spinless free fermions on a ladder geometry. The ladder sits on the $x - y$ plane, extends in the x direction with a lattice spacing d and the spacing between the two legs is also d. Depending on the alignment of the sites on the two legs of the ladder and on the nature of inter-leg hoppings, we consider either a square or triangular geometry, see Fig. 1.1. The Hamiltonian describing the fermion dynamics reads:

$$\hat{H}_0 = \left(\sum_{\sigma=\pm} \hat{H}_\sigma \right) + \hat{H}_\perp, \tag{1.1}$$

$$\hat{H}_\sigma = -t_0 \sum_{j=1}^{L-1} \hat{c}^\dagger_{\sigma,j} \hat{c}_{\sigma,j+1} \ , \tag{1.2}$$

$$\hat{H}_\perp = \left(-t_1 \sum_{j=1}^{L} \hat{c}^\dagger_{+,j} \hat{c}_{-,j} - t_2 \sum_{j=1}^{L-1} \hat{c}^\dagger_{+,j} \hat{c}_{-,j+1} + \text{h.c.} \right) \ , \tag{1.3}$$

where $\sigma = +(-)$ indicates the top (bottom) leg of the ladder, $j = 1, \dots, L$ is the site/rung index on each leg, and $\hat{c}^\dagger_{\sigma,j}$ ($\hat{c}_{\sigma,j}$) creates (destroys) a fermion on the site j and on the leg σ. We consider open boundary conditions and one fermion per rung so that $N = L$, unless specified otherwise. Moreover, we set equal hopping amplitudes $t_0 = t_1$, while $t_2 = 0$ or $t_2 = t_0$ for the square and the triangular geometry, respectively.

The cavity setup we consider is that of a single mode where the cavity Hamiltonian

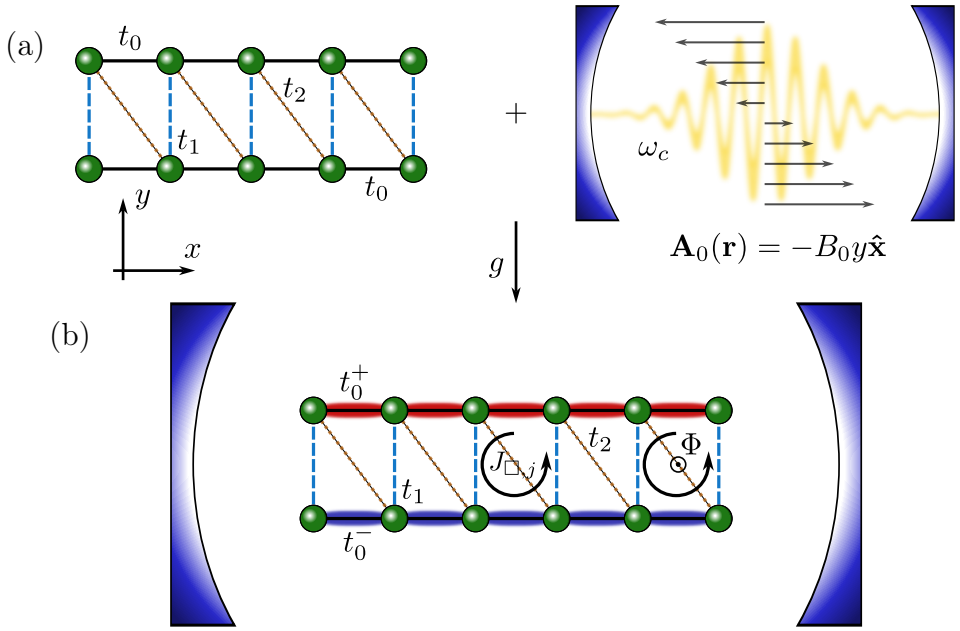


Figure 1.1.: Sketch of the ladder plus cavity system under consideration. (a) Without any coupling to the cavity, the two legs of the ladder have the same intra-leg hopping t_0 (solid lines), an inter-leg hopping between corresponding site t_1 (dashed lines), and (for the triangular ladder) a diagonal inter-leg hopping t_2 (dotted lines). The cavity mode has frequency ω_c and a space profile given by the vector potential $\mathbf{A}_0(\mathbf{r}) = -B_0 y\hat{\mathbf{x}}$. (b) Upon coupling to the cavity, the intra-leg hopping terms are modified by the photon in a different way for the top (t_0^+) and bottom (t_0^-) leg.

is represented by a single quadratic bosonic mode with frequency ω_c:

$$\hat{H}_c = \omega_c \hat{a}^\dagger \hat{a} \ . \tag{1.4}$$

Correspondingly, the cavity vector potential is $\hat{\mathbf{A}}(\mathbf{r}) = \mathbf{A}_0(\mathbf{r})(\hat{a} + \hat{a}^\dagger)$ where $\mathbf{A}_0(\mathbf{r})$ retains the spatial structure of the cavity mode and $\hat{a}$ is the annihilation operator for a photon in this cavity mode. We consider a spatially varying mode function that in the vicinity of the ladder can be written as $\mathbf{A}_0(\mathbf{r}) = -B_0 y\hat{\mathbf{x}}$. The cavity is, therefore, magnetic since the cavity mode has a non-zero curl which in classical electrodynamics gives rise to a magnetic field. In our quantum light model, this means that cavity photons generate a fluctuating magnetic flux through the ladder plaquettes. We remark here that the single-mode approximation is not always valid and it in general depends on the specifics of the system [9, 12, 29, 57–63, 80]. In order to have a gauge-invariant coupling between matter and light, we implement the light-matter coupling by means of the Peierls substitution:

$$\hat{c}^\dagger_{i,\sigma}\hat{c}_{j,\sigma'} \to \exp\left[iq\int_{R_{i,\sigma}}^{R_{j,\sigma'}} d\mathbf{r}\cdot\hat{\mathbf{A}}(\mathbf{r})\right]\hat{c}^\dagger_{i,\sigma}\hat{c}_{j,\sigma'} \ , \tag{1.5}$$

where $R_{i,\sigma}$ denotes the position of the electronic site i,σ. In our case, the Peierls phase is non-zero only for intra-leg hoppings which are along the x direction. The

Peierls phase as discussed by Luttinger [97] is only an approximation of the coupling to electromagnetic fields when the value of the magnetic flux over an area, comparable to the typical size of the fermionic orbitals, is comparable to π [70]. However the corrections strongly depend on the nature of the localized orbitals, and since neglecting these corrections does not spoil the gauge-invariant properties of the coupling, we keep only the Peierls phase.

The full light-matter coupled Hamiltonian then reads:

$$\hat{H} = \omega_c \hat{a}^\dagger \hat{a} - \Big(t_1 \sum_{j=1}^{L} \hat{c}^\dagger_{+,j} \hat{c}_{-,j} + t_2 \sum_{j=1}^{L-1} \hat{c}^\dagger_{+,j} \hat{c}_{-,j+1} + t_0 \sum_{j=1}^{L-1} \sum_{\sigma=\pm} e^{i\sigma g(\hat{a}+\hat{a}^\dagger)/\sqrt{L}} \hat{c}^\dagger_{\sigma,j} \hat{c}_{\sigma,j+1} + \text{h.c.} \Big) \,, \tag{1.6}$$

where we have introduced the dimensionless coupling constant $g = |q| d^2 B_0 \sqrt{L}/2$ which is the parameter that drives the transition. Note that g does not grow explicitly with L given the scaling of the field intensity $B_0 \propto 1/\sqrt{L}$ provided that the density $N/V = L/V$ is fixed. In optical cavities, the frequency of the mode ω_c and the field intensity B_0 are, in general, not independent parameters ($\omega_c \propto B_0^2$). Still we can, in principle, tune the light-matter interaction strength g independently of ω_c, for example, by varying the fermionic charge q. In the following we will in any case stick with $q = -1$ and use g as an independent parameter[1]. The Hamiltonian (1.6) is invariant under the combined application of (1) the parity transformation of the photon $P_{\text{ph}} : \hat{a} \to -\hat{a}$ and (2) the leg inversion $P_\sigma : \sigma \to -\sigma$, so that (c.f. [85])[2]:

$$\mathcal{P} \equiv P_{\text{ph}} P_\sigma, \quad \mathcal{P} \hat{H} \mathcal{P}^{-1} = \hat{H}. \tag{1.7}$$

We now define two important quantities that are physically related in this light-matter system. The first one is the magnetic flux per plaquette $\hat{\Phi}$ pointing in the z direction:

$$\hat{\Phi} = \int_{\square} dxdy \; \nabla \times \hat{\boldsymbol{A}}(\boldsymbol{r}) = \frac{2g}{\sqrt{L}} (\hat{a} + \hat{a}^\dagger) \,, \tag{1.8}$$

where the $\square$ indicates the integral on a plaquette. The light-matter coupling in the Hamiltonian (1.6) only depends on the magnetic flux $\hat{\Phi}$ which is a well-defined physical (and thus gauge-invariant) quantity. The second quantity is the chiral charge current:

$$\hat{J}_\chi = \sum_{j=1}^{L-1} \hat{J}_{\square,j} \,. \tag{1.9}$$

[1] One could think of changing the lattice spacing d, but this would in turn change the hopping integrals. This is one of the main issue of the Peierls phase, it inevitably links the light-matter interaction and hopping integrals as discussed in [72].

[2] However, it is to be noted that independent applications of P_{ph} or P_σ do not leave the Hamiltonian invariant.

The chiral current is defined as the sum of the plaquette currents $\hat{J}_{\square,j} = -\hat{J}_{+,j} - \hat{J}_{\perp,j+1} + \hat{J}_{-,j} + \hat{J}_{\perp,j}$ flowing in a anticlockwise direction, where $\hat{J}_{\perp,j}$ is the inter-leg current flowing from the top $\sigma = +$ to the bottom leg $\sigma = -$ at sites j and $\hat{J}_{\pm,j}$ is the intra-leg longitudinal current flowing from site j to site $j+1$. The gauge-invariant currents can be derived starting from the charge density $\hat{n}_{\sigma,j} \equiv q\hat{c}^\dagger_{\sigma,j}\hat{c}_{\sigma,j}$ with $q = -1$, which fulfills a discrete continuity equation $\partial_t \hat{n}_{\sigma,j} = -\hat{J}_{\sigma,j} + \hat{J}_{\sigma,j-1} - \sigma \hat{J}_{\perp,j}$. By comparing this expression with the Heisenberg equation for the density $\partial_t \hat{n}_{\sigma,j} = i[\hat{H}, \hat{n}_{\sigma,j}]$ and carrying out the explicit calculation, we find for the currents:

$$\hat{J}_{\sigma,j} = -it_0 \left(e^{i\sigma g(\hat{a}+\hat{a}^\dagger)/\sqrt{L}} \hat{c}^\dagger_{\sigma,j}\hat{c}_{\sigma,j+1} - \text{h.c.} \right) \qquad \hat{J}_{\perp,j} = -it_1(\hat{c}^\dagger_{+,j}\hat{c}_{-,j} - \text{h.c.}) \, .$$

Performing the sum, the contributions from the inter-leg current cancel out except for the boundary contributions and we are left with

$$\hat{J}_\chi = it_0 \sum_{j,\sigma} \left(\sigma e^{i\sigma \frac{g}{\sqrt{L}}(a+a^\dagger)} \hat{c}^\dagger_{\sigma,j}\hat{c}_{\sigma,j+1} - \text{h.c.} \right) - it_1(\hat{c}^\dagger_{+,1}\hat{c}_{-,1} - \hat{c}^\dagger_{+,L}\hat{c}_{-,L} - \text{h.c.}) \, . \quad (1.10)$$

The chiral current and the magnetic flux operators defined above correspond to physical, gauge invariant, observables, and as such their expectation values do not depend on the choice of the gauge [98–100]. Different gauge choices are indeed implemented through unitary transformations which act on both operators and states, and leave invariant physical observables. In the following, we will use the expectation values of the chiral current and the magnetic flux as the order parameters for the photon condensation, making it a gauge-invariant phenomenon.

The presented Hamiltonian, although a minimal toy model, serves as a powerful tool in understanding the physics of magnetic photon condensation and the collective strong coupling regime of itinerant electrons coupled to a single quantized cavity mode. Despite its simplicity, realizing such a model in solid state materials embedded in optical cavities could be challenging. Nonetheless, recent advancements have demonstrated ultra-strong magnetic coupling with a superconducting resonator [88], suggesting a potential practical feasibility of our model. Another potential platform lies in cold-atom setups. However, atoms are neutral and our Hamiltonian cannot be straightforwardly realizes if not with dynamical synthetic gauge fields[3]. Here, our primary objective is to have a clearer interpretation of the results and a better understanding of the underlying physics. Therefore, we leave the question of experimental realizations open for future studies and focus on the theoretical aspects of the model in the present chapter.

[3]Note that “dynamical" semi-classical gauge fields for cold atomic set-ups have been studied (see e.g. Ref. [101, 102]) but the dynamics is linked to their driven-dissipative nature and hence differs from the model object of this chapter.

1.3. Square ladder

We start by looking at the half-filled ($N/L = 1$) square ladder geometry ($t_2 = 0$). We solve for the ground state of the model with two approaches: *(i)* using an approximate photon mean-field decoupling where the fermionic problem is non-interacting and the light-matter entanglement is neglected; *(ii)* performing numerical simulations with DMRG where the light-matter entanglement is taken into account and the problem is fully many-body.

1.3.1. Methods

Photon mean-field

In the photon mean-field approximation (PMF) the quantum correlations between photon and matter are neglected by assuming a product ground state $\left|\Psi^{\mathrm{PMF}}\right\rangle = |\psi_{\mathrm{m}}\rangle\,|\psi_{\mathrm{ph}}\rangle$ [29, 74, 75]. This gives rise to two mean-field Hamiltonians for photon $\hat{H}^{\mathrm{PMF}}_{\mathrm{ph}} \equiv \langle\psi_{\mathrm{m}}|\,\hat{H}\,|\psi_{\mathrm{m}}\rangle$ and matter $\hat{H}^{\mathrm{PMF}}_{\mathrm{m}} \equiv \langle\psi_{\mathrm{ph}}|\,\hat{H}\,|\psi_{\mathrm{ph}}\rangle$ that must be solved self-consistently. Up to irrelevant constants they read:

$$\hat{H}^{\mathrm{PMF}}_{\mathrm{m}} = -t_0 R \sum_{j,\sigma} e^{i\sigma\phi/2}\hat{c}^{\dagger}_{\sigma,j}\hat{c}_{\sigma,j+1} - t_1 \sum_{j} \hat{c}^{\dagger}_{+,j}\hat{c}_{-,j} + \mathrm{h.c.}\ , \tag{1.11}$$

$$\hat{H}^{\mathrm{PMF}}_{\mathrm{ph}} = \omega_{\mathrm{c}}\hat{a}^{\dagger}\hat{a} + J_1 \cos\left[\tfrac{g(\hat{a}+\hat{a}^{\dagger})}{\sqrt{L}}\right] + J_2 \sin\left[\tfrac{g(\hat{a}+\hat{a}^{\dagger})}{\sqrt{L}}\right]\ , \tag{1.12}$$

where we introduced the mean-field parameters R, ϕ, J_1 and J_2. The first two depend on the photon state and are defined as

$$R \equiv \left|\langle\psi_{\mathrm{ph}}|\, e^{i\frac{g(\hat{a}+\hat{a}^{\dagger})}{\sqrt{L}}}\,|\psi_{\mathrm{ph}}\rangle\right|\ , \qquad \phi \equiv 2\arg\left[\,\langle\psi_{\mathrm{ph}}|\, e^{i\frac{g(\hat{a}+\hat{a}^{\dagger})}{\sqrt{L}}}\,|\psi_{\mathrm{ph}}\rangle\right]\ , \tag{1.13}$$

such that $R\, e^{i\phi/2} = \langle\psi_{\mathrm{ph}}|\, e^{i\frac{g(\hat{a}+\hat{a}^{\dagger})}{\sqrt{L}}}\,|\psi_{\mathrm{ph}}\rangle$. The matter mean-field parameters J_1 and J_2 are defined as

$$J_1 \equiv -t_0 \sum_{j=1}^{L-1}\sum_{\sigma} \langle\psi_{\mathrm{m}}|\left(\hat{c}^{\dagger}_{\sigma,j}\hat{c}_{\sigma,j+1} + \mathrm{h.c.}\right)|\psi_{\mathrm{m}}\rangle\ , \tag{1.14}$$

$$J_2 \equiv -it_0 \sum_{j=1}^{L-1}\sum_{\sigma} \langle\psi_{\mathrm{m}}|\left(\sigma\hat{c}^{\dagger}_{\sigma,j}\hat{c}_{\sigma,j+1} - \mathrm{h.c.}\right)|\psi_{\mathrm{m}}\rangle\ . \tag{1.15}$$

The photon parameters ϕ and R have respectively the interpretation of a magnetic flux per plaquette and of the cavity renormalization of the hopping process. Whenever the photon quantum state is Gaussian, the expectation values of an exponential can be expressed in terms of expectation values of the two quadratures $\hat{X} \equiv (\hat{a}+\hat{a}^{\dagger})/\sqrt{2}$, $\hat{P} \equiv i(\hat{a}-\hat{a}^{\dagger})/\sqrt{2}$, and their fluctuations. In particular for Gaussian states $|\psi^{G}_{\mathrm{ph}}\rangle$, our

mean-field parameters R and ϕ become:

$$R_G = \exp\Big[-\frac{2g^2}{L}\Big(\langle\psi_{\rm ph}^G|\hat{X}^2|\psi_{\rm ph}^G\rangle - \langle\psi_{\rm ph}^G|\hat{X}|\psi_{\rm ph}^G\rangle^2\Big)\Big] \ , \tag{1.16}$$

$$\phi_G = \frac{g\sqrt{2}}{\sqrt{L}}\langle\psi_{\rm ph}^G|\hat{X}|\psi_{\rm ph}^G\rangle = \big\langle\psi_{\rm ph}^G\big|\,\hat{\Phi}\,\big|\psi_{\rm ph}^G\big\rangle \ . \tag{1.17}$$

Note that if the photonic state is not Gaussian, in principle, we can have $\phi \neq \langle\psi_{\rm ph}|\,\hat{\Phi}\,|\psi_{\rm ph}\rangle$. The physical interpretation of the matter parameters J_1 and J_2 in terms of the chiral current $\hat{J}_\chi$ depends on the values of ϕ and R as

$$\big\langle\Psi^{\rm PMF}\big|\,\hat{J}_\chi\,\big|\Psi^{\rm PMF}\big\rangle = R\Big[J_2\cos(\phi/2) - J_1\sin(\phi/2)\Big] + \big\langle\Psi^{\rm PMF}\big|\,\hat{J}_{\perp,N} - \hat{J}_{\perp,1}\,\big|\Psi^{\rm PMF}\big\rangle \ . \tag{1.18}$$

The solution of the PMF Hamiltonians is obtained by a standard self-consistent procedure:

1. Start from a guess R and ϕ;
2. Solve the single-particle problem given by the matter mean-field Hamiltonian in Eq. (1.11) and compute J_1 and J_2 as Eqs. (1.14) and (1.15);
3. Solve the photonic mean-field Hamiltonian in Eq. (1.12) via exact diagonalization and compute a new R' and ϕ' from Eq. (1.13);
4. Repeat from 2, using R' and ϕ' as a new mean-field parameters until the desired convergence is reached.

Note that in presence of first-order transitions one needs to be careful and try different initial guesses as the self-consistency can get stuck in local minima of the energy.

Density-matrix renormalization group

This ladder geometry, being a quasi-1D system, is well-suited to be approached via the density-matrix renormalization (DMRG) techniques [89–92]. The matrix-product state (MPS) representation that we use for this purpose is similar to those employed in previous works on light-matter systems [36, 51, 93, 94], where the single photon site is placed at one end of the MPS chain, while rest of the MPS is made up of fermionic sites, as depicted in Fig. 1.2. Additionally, to preserve the global $\mathbb{U}(1)$ symmetry associated with the conservation of total fermionic charge $\sum_{\sigma,j} n_{\sigma,j}$, we employ $\mathbb{U}(1)$ symmetric tensors [103, 104] for the fermionic sites, while a standard dense tensor is used for the photon site. Moreover, the use of the matrix-product operator (MPO) representation for the Hamiltonian, as illustrated in Fig. 1.2, is efficient as the long-range light-matter interaction term can be expressed exactly in the MPO form [105, 106]. The ground state obtained through DMRG is a variationally computed state, with an error that can be precisely controlled through the bond dimension χ of the MPS ansatz. By adjusting

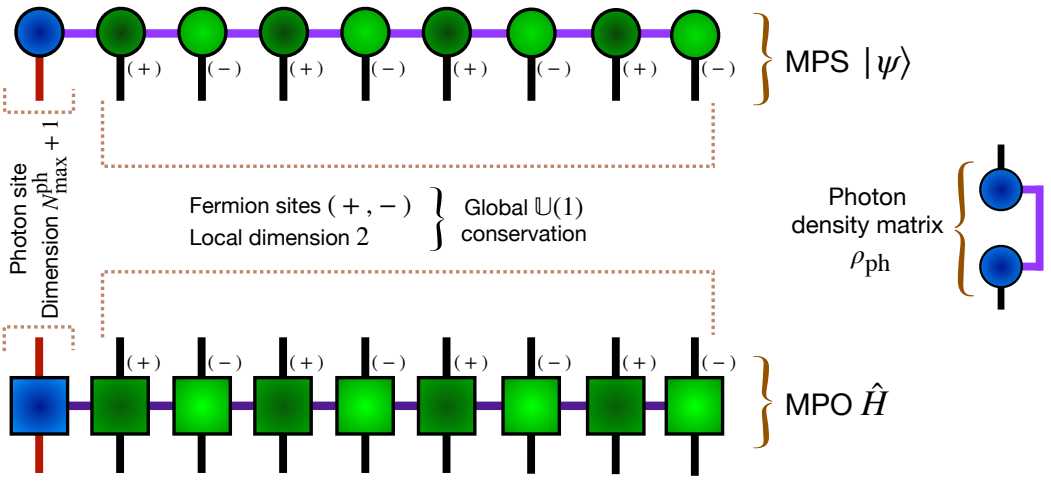


Figure 1.2.: The matrix-product state (MPS) and the matrix-product operator (MPO) representations used in our study. The photonic Hilbert space is truncated to accommodate maximum number of photons $N_{\max}^{\mathrm{ph}} = 63$, while the fermionic local Hilbert space dimension is 2. Note that the photon mean-field (PMF) approximation is implicitly setting $\chi = 1$ for the first link that connects the photon and fermionic degrees of freedom. In this MPS representation, the photon density matrix can be computed efficiently by tracing out the fermionic degrees of freedom.

the bond dimension, one can verify the convergence and attain the desired level of accuracy. See App. A.4 for further details on the convergence of DMRG simulations. For the numerical implementation of the DMRG algorithm we use the ITensor library [107] and the respective codes can be found at GitHub[4].

It is important to note that, in a symmetry-broken phase, while strictly speaking, exact symmetry breaking does not occur in the ground state at finite sizes, it is a well-established characteristic of DMRG to converge to one of the symmetry-broken states, as these states have significantly less entanglement compared to the macroscopic superposition of two (or more) symmetry-broken states. In the following discussion, while considering the symmetry-broken phase, we will focus solely on these symmetry-broken ground states, which can be reached either automatically through the DMRG algorithm or with the aid of a small symmetry breaking term[5].

The DMRG solution allows us then to easily access the photon density matrix by tracing out the matter degree of freedom as (see Fig. 1.2):

$$\rho_{\mathrm{ph}} = \mathrm{Tr}_{\mathrm{m}}\Big[\,|\Psi\rangle\,\langle\Psi|\,\Big]\,. \tag{1.19}$$

From this we can, for example, calculate the entanglement entropy of the cavity with

[4] https://github.com/zenobacciconi/cavity_ladder.git

[5] For large enough system-size L, DMRG may randomly converge to one of the symmetry-broken ground states, which can also be influenced by the choice of initial input state. To eliminate such arbitrariness, we add a very small symmetry breaking term in our simulations and select only a specific symmetry-broken state.

respect to matter $S(\rho_{\rm ph}) = -{\rm Tr}\Big[\rho_{\rm ph}\ln\rho_{\rm ph}\Big]$ that in the PMF decoupling is exactly zero.

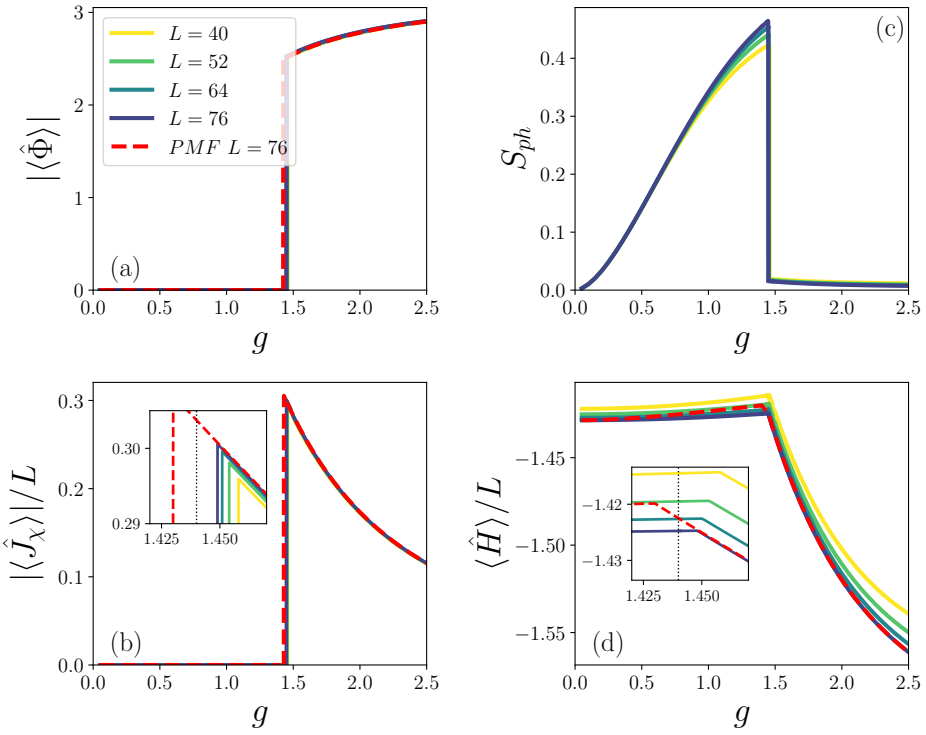


Figure 1.3.: DMRG results for different system sizes and their comparison with the photon mean-field (red dashed line). (a-b) The magnetic flux per plaquette and chiral current as the cavity and the matter order parameters respectively. They both show a discontinuity at the first-order transition point $g_c \simeq 1.44$ that slightly shifts at finite sizes. The relation $|\langle\hat{J}_\chi\rangle| = \frac{L}{2}(\pi - |\langle\hat{\Phi}\rangle|)$ is satisfied in the thermodynamic limit. Note that here we plot the absolute values of the order parameters since they can take on both negative and positive values in the photon condensed phase depending on the degenerate symmetry-broken state, but always have the same sign as each other. (Inset) Zoom near the thermodynamic limit transition point $g_c = 1.44$ marked with a vertical black line. Note that finite size corrections to the transition point and value of the current are different between DMRG and PMF. (c) Photon entanglement entropy with respect to the matter. It is finite in the thermodynamic limit for both phases, although much smaller in the photon condensed phase. (d) Total energy density showing a kink at the transition point as expected for a first-order transition both in DMRG and the photon mean-field. Note that finite size corrections are different.

1.3.2. Results: Photon mean-field vs. DMRG

Phase diagram. A sample of the results obtained with DMRG and PMF are depicted in Fig. 1.3. Overall, we observe that the two approaches match in determining the structure of the phase diagram – both show a first-order phase transition from a normal metallic phase for $g < g_c$ to a photon condensed phase for $g > g_c$ characterized by a $\mathbb{Z}_2$ symmetry breaking where the symmetry $\mathcal{P}$ (see Eq. (1.7)) gets spontaneously broken. The energy kink shown in Fig. 1.3(d) support the first-order nature of the

transition for both DMRG[6] and PMF. The normal phase is connected to the state at $g = 0$ and display metallic properties. The photon condensed phase is a Condon phase where a finite current $\langle \hat{J}_\chi \rangle \neq 0$ (Fig. 1.3(b)) is linked to a finite magnetic flux $\langle \hat{\Phi} \rangle \neq 0$ (Fig. 1.3(a))[7]. In particular, we have $|\langle \hat{J}_\chi \rangle| = \frac{L}{2}(\pi - |\langle \hat{\Phi} \rangle|)$ from both DMRG and PMF with small finite-size corrections, where $|\langle \hat{\Phi} \rangle| \leq \pi$ and $\langle \hat{J}_\chi \rangle$ and $\langle \hat{\Phi} \rangle$ have the same sign. The matter state is a diamagnetic band insulator, also called the Hofstader flux state in the context of fermionic ladder with static magnetic fields [82]. The notion of diamagnetism, however, in the present context is an unusual one. While usually one defines diamagnetism when the magnetization of a material is opposite with respect to an applied magnetic field, here the magnetization is in the same direction but proportional to the difference $\pi - |\langle \hat{\Phi} \rangle|$. Diamagnetism must be interpreted as a response of the system trying to bring the magnetic flux not to 0 but to π.

Finite size effects. The chiral current shown in Fig. 1.3(b) has finite size corrections which compare well between PMF and DMRG, but the exact transition point is shifted towards lower (PMF) and higher (DMRG) values of the coupling strength. The reason is that while the photon condensed phase has low photon entanglement (Fig. 1.3) and is well captured by the PMF, the normal phase has high photon entanglement and then finite-size corrections are different between PMF and DMRG. In particular the finite size effect of the PMF comes mainly from the mean-field hopping renormalization R that tends to 1 in the thermodynamic limit as the squeezing of the cavity remain finite (Eq. (1.16)). The same happens for the total energy and the magnetic susceptibility (not shown).

Magnetostatic instability. We refer to the instability to a ground-state displaying a finite magnetic flux $\langle \hat{\Phi} \rangle \neq 0$ as a "magnetostatic instability"[73, 74, 78, 108]. In Fig. 1.4 we show the mean-field picture of the magnetostatic instability characterizing the first-order transition. Differently to a second-order transition [74] the instability is not controlled by the linear orbital magnetic susceptibility (which is a property of the Fermi-surface[75]) of the normal state $\phi = 0$. Conversely, the first-order nature

[6] To mitigate the negative impacts of metastability near the first-order phase transition, we employ a two-fold approach for each value of g within a range close to g_c. We simultaneously run two separate DMRG simulations, each initialized with a state deep within a distinct phase. From these two simulations, we select the outcome that results in the lowest energy.

[7] It is straightforward to check that under the symmetry operation $\mathcal{P}$, $\langle \hat{J}\chi \rangle$ and $\langle \hat{\Phi} \rangle$ change their sign. Therefore, all the symmetry-preserving eigenstates must have vanishing chiral current and magnetic flux. In the photon condensed phase, the $\mathbb{Z}_2$ symmetry associated with $\mathcal{P}$ gets spontaneously broken, and the ground state exhibits a two-fold degeneracy. This degeneracy arises from the presence of two symmetry-broken states, denoted by $|\Psi_+\rangle$ and $|\Psi_-\rangle$, which have positive and negative values of the order parameters $\langle \hat{J}\chi \rangle$ and $\langle \hat{\Phi} \rangle$ respectively. Under the symmetry operation, we have $\mathcal{P}|\Psi_\pm\rangle = |\Psi_\mp\rangle$, so that the symmetric and anti-symmetric combinations $\frac{1}{\sqrt{2}}(|\Psi_+\rangle \pm |\Psi_-\rangle)$ belong to the even and odd symmetry sectors respectively, each having zero magnetic flux and chiral current.

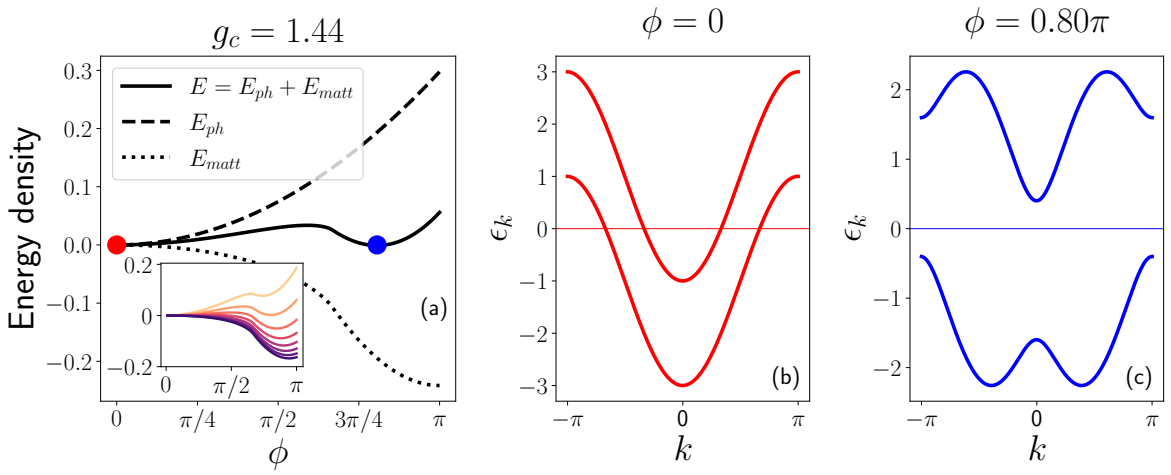


Figure 1.4.: The mean-field picture of the transition. (a) Mean-field energy per particle as a function of a cavity generated 'classical' magnetic flux ϕ at $g = g_c = 1.44$. The photon energy is $E_{\rm ph} = \omega_c(\phi/4g)^2$ and the matter energy $E_{\rm matt} = \langle\psi_{\rm m}|\, \hat{H}_{\rm m}^{PMF}\, |\psi_{\rm m}\rangle / L$ is obtained from the single-particle problem of Eq. (1.11) fixing $R = 1$. (Inset) $E(\phi)$ shown from $g = 1.2$ (light color) to $g = 2.8$ (dark color) across the transition. After the transition the solution at $\phi = 0$ does not immediately become unstable, signaling metastability – a typical feature of first-order phase transitions. (b) Metallic and (c) insulating band structure at two fluxes corresponding to the two minima of the total energy at $g = g_c$ in periodic boundary conditions. Horizontal lines mark the chemical potential.

is given by a strong non-linear response of the system at strong magnetic fluxes. In particular, the non-linear behavior comes together with an indirect gap opening in the band structure at $\phi = 2\pi/3$. Once fixed the fermionic bare energies, the transition point only depends on the energy of the cavity per unit of flux, which is controlled by the combination ω_c/g^2 as the cavity PMF energy density in the thermodynamic limit is $E_{\rm ph} = \omega_c(\phi/4g)^2$.

The numerical results from DMRG simulations confirm the photon mean-field picture for the instability. Our findings show that the only way for a single cavity mode in the collective strong coupling regime to change the macroscopic properties of a thermodynamically large system is via a macroscopic classical state. Quantum fluctuations and light-matter entanglement give $O(1)$ contributions [29, 109, 110], which can be important near quantum criticality, as discussed in Ref. [35] and in Chapter 2.

Cavity quantum state. As shown in Fig. 1.5, the density matrix $\rho_{\rm ph}$ obtained via DMRG shows that the cavity can be can be accurately approximated by a Gaussian state (see App. A.1). In order to quantify the non-Gaussianity of the state, we compute the Quantum relative entropy [111]:

$$\Delta_G = S(\rho_{\rm ph}^{\rm G}) - S(\rho_{\rm ph}) \ , \tag{1.20}$$

where $\rho_{\rm ph}^{\rm G}$ is the Gaussian density matrix that has the same expectation values $\langle\hat{X}^2\rangle$, $\langle\hat{P}^2\rangle$, $\langle\hat{X}\rangle$, $\langle\hat{P}\rangle$ of $\rho_{\rm ph}$. The non-Gaussian nature of the state is a finite size correction (see Fig. 1.5(a)) and it arises from the non-linear nature of the Peierls phase. The non-Gaussianity revealed to be sensitive to numerical details at sizes higher than $L = 76$ for which a more careful analysis is needed (App. A.4). Then in order to have more information on the nature of the corrections we also show, in Figs. 1.5(b)-(d), the Wigner function [112] of the cavity at the smallest investigated system size. The corrections do not spoil the positivity of the Wigner function nor the qualitative shape. Also in the PMF (not shown) the non-Gaussianity goes to zero in the $L \to \infty$ and the squeezing remain constant so that $R \to 1$. The dashed lines in Figs. 1.5(b)-(d) mark the width of the respective Gaussian states and they encode the nature of the Gaussian state. A finite light-matter entanglement is represented by a lager area enclosed in the dashed lines as it increase the variance of both quadratures (see App. A.1), while squeezing reduce the fluctuations in one quadrature while increasing the other one to keep the product constant. The gaussianity of the cavity state can be an important starting point for semiclassical treatments of light-matter problems [113]

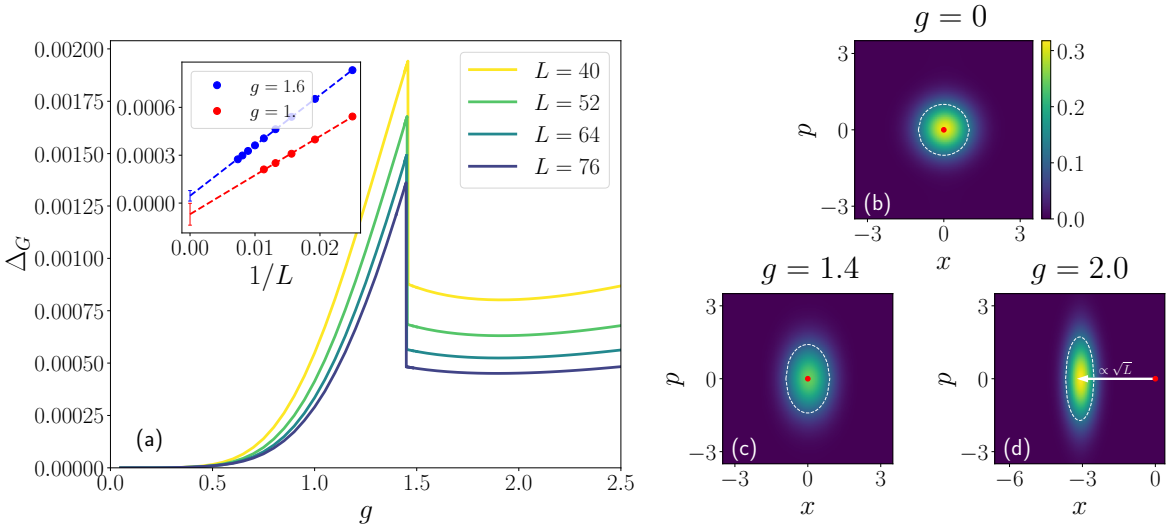


Figure 1.5.: Cavity quantum state obtained with DMRG. (a) Quantum relative entropy Δ_G as a measure of cavity non-Gaussianity for different system sizes. The state is Gaussian in the thermodynamic limit in both phases. (Inset) The numerical extrapolation of the non-Gaussianity to the thermodynamic limit by using a linear fit $f(1/L) = a + b/L$. Errors of 10^{-5} on the DMRG points have been considered to account for slight dependency on numerical parameters (see App. A.4). (b-d) Wigner functions of the photon at finite system-size $L = 40$ for the uncoupled system $g = 0$ (b), in normal phase $g = 1.4$ (c), and in the photon condensed phase $g = 2$ (d). Even at the smallest presented size when the non-Gaussianity is larger, the Wigner function is positive everywhere. White contours display the width of the corresponding Gaussian state $\rho_{\rm ph}^{G}$ having same $\langle\hat{X}^2\rangle - \langle\hat{X}\rangle^2$ and $\langle\hat{P}^2\rangle - \langle\hat{P}\rangle^2$ as the actual photon state $\rho_{\rm ph}$, and the white arrow shows the displaced nature of the photon condensed state. Red dots mark the origin $(x, p) = (0, 0)$.

1.3.3. Results: Gaussian fluctuations

In order to gain further insights into the entangled light-matter ground state one can try to calculate pertubative contribution to the ground state $|\Psi_0\rangle$ in powers of g. Leaving a more detailed discussion in App. A.3 at first order (with periodic boundary conditions) we obtain:

$$\left|\Psi_{(1)}\right\rangle = |\Psi_0\rangle - \frac{g}{\sqrt{L}} \sum_k \frac{2f_k}{\omega_k + \omega_c} |\mathrm{ph}_k, 1_c\rangle \,, \tag{1.21}$$

where $|\mathrm{ph}_k, 1_c\rangle = \hat{\tilde{c}}^\dagger_{k,2}\hat{\tilde{c}}_{k,1}\hat{a}^\dagger |\Psi_0\rangle$ is a polaritonic state with one photon in the cavity and with one direct particle-hole excitation over the Fermi see at momentum k, $\hat{\tilde{c}}_{k,a}$ with $a = 1, 2$ are the fermionic operators that diagonalize $H_{\mathrm{m}}^{\mathrm{PMF}}$, ω_k is the direct band gap, and f_k are the matrix elements for the magnetic transition. This matches the DMRG solution at small values of g (not shown), but it becomes useless at higher values of g, in particular after the photon condensation transition.

As an alternative method to gain analytical insight on the system dynamics, we examine the Gaussian fluctuations above the mean-field solution which, in the normal phase, at first order in g actually recover the above perturbative result. This treatment is motivated by the observation that, for all values of g considered, the photon state is always Gaussian in the thermodynamic limit. We then expand the photon operator as:

$$\hat{a} = \alpha_0 + \delta\hat{a} \,, \tag{1.22}$$

where $\alpha_0 = \phi\sqrt{L}/4g$ is the solution of the photon mean-field decoupling restricted to coherent states and $\delta\hat{a}$ the bosonic quantum fluctuations around it fulfilling the bosonic commutation relations $[\delta\hat{a}, \delta\hat{a}^\dagger] = 1$. Note that the coherent state around which we are expanding does not, in general, correspond to the full solution of the PMF as that is a generic pure quantum state of the cavity Hilbert space.

To simplify the treatment, we work in periodic boundary conditions (details in App. A.2) and introduce the creation operator in momentum space $\hat{c}_{\sigma,k} = \frac{1}{\sqrt{L}} \sum_j e^{-ikj} \hat{c}_{\sigma,j}$. and the pseudospin representation $\hat{\sigma}^\alpha_k = (\hat{c}^\dagger_{+,k} \quad \hat{c}^\dagger_{-,k})\sigma^\alpha(\hat{c}_{+,k} \quad \hat{c}_{-,k})^T$ with σ^α being the Pauli matrices ($\alpha = 0, 1, 2, 3$). Now in order to obtain a quadratic Hamiltonian, we expand the Peierls phase up to second order in $\delta\hat{a}/\sqrt{L}$ obtaining up to constants:

$$\hat{H} \simeq \omega_c \delta\hat{a}^\dagger\delta\hat{a} + \sum_{k,\alpha} \hat{\sigma}^\alpha_k h^\alpha_k + \frac{g}{\sqrt{L}}(\delta\hat{a} + \delta\hat{a}^\dagger) \sum_{k,\alpha} \hat{\sigma}^\alpha_k d^\alpha_{p,k} - \frac{g}{2L}(\delta\hat{a} + \delta\hat{a}^\dagger)^2 \sum_{k,\alpha} \hat{\sigma}^\alpha_k d^\alpha_{d,k} \,, \tag{1.23}$$

where

$$\begin{aligned} \boldsymbol{h}_k &= -(2t_0 \cos(k)\cos(\phi/2), t_1, 0, 2t_0 \sin(k)\sin(\phi/2)) \,, \\ \boldsymbol{d}_{p,k} &= -(-2t_0 \cos(k)\sin(\phi/2), 0, 0, 2t_0 \sin(k)\cos(\phi/2)) \,, \\ \boldsymbol{d}_{d,k} &= -(2t_0 \cos(k)\cos(\phi/2), 0, 0, 2t_0 \sin(k)\sin(\phi/2)) \,. \end{aligned} \tag{1.24}$$

Since the light-matter coupling remains diagonal in the momentum space, the occupation will be conserved at each momentum, and it will be $N_k = \langle \hat{\sigma}_k^0 \rangle = 0, 1, 2$ depending on the mean-field solution encoded in ϕ. The only non-trivial momentum sectors are those singly occupied where a direct particle-hole excitation is allowed, for the others $\langle \hat{\sigma}_k^{1,2,3} \rangle = 0$. For every momentum sector with occupation $N_k = 1$, we can rotate the pseudospin degree of freedom to a new basis $\hat{\tilde{\sigma}}_k$, so that every term in the Hamiltonian, except for the ones containing cavity fluctuations $\delta\hat{a}$, becomes diagonal. Then we use a Holstein-Primakoff transformation of the particle-hole pseudospin for which $\hat{\tilde{\sigma}}_k^3 = -(1 - 2\hat{b}_k^\dagger \hat{b}_k)$ and $\hat{\tilde{\sigma}}_k^1 = (\hat{b}_k + \hat{b}_k^\dagger)$ which is exact if one consider $\hat{b}_k$ as hard core bosons. Since the occupation of a single particle-hole is not expected to be more than $O(1/L)$ we lift the hard core boson constraint. As a last step, we discard non-quadratic terms to obtain a quadratic Hamiltonian:

$$\hat{H}^{(2)} = \omega_c \delta\hat{a}^\dagger \delta\hat{a} + \sum_k \omega_k \hat{b}_k^\dagger \hat{b}_k - D\frac{g^2}{2}(\delta\hat{a} + \delta\hat{a}^\dagger)^2 + g(\delta\hat{a} + \delta\hat{a}^\dagger) \sum_k P_k (\hat{b}_k + \hat{b}_k^\dagger) \ , \quad (1.25)$$

with

$$\omega_k = 2\sqrt{\sum_{\alpha=1}^{3} (h_k^\alpha)^2} \ , \qquad P_k = \delta_{N_k,1} \frac{2}{\sqrt{L}} \frac{d_{p,k}^3 d_{\alpha,k}^1}{\omega_k} \ ,$$
$$D = \frac{1}{L} \sum_k N_k d_{d,k}^0 - \frac{2}{L} \sum_k \delta_{N_k,1} \frac{d_{d,k}^3 d_{d,k}^3}{\omega_k} \ . \quad (1.26)$$

The quadratic Hamiltonian in Eq. (1.25) can be diagonalized with a Hopfield-Bogoliubov transformation [114] obtaining:

$$\hat{H}^{(2)} = E_0 + \sum_{\mu=1}^{M+1} \epsilon_\mu \hat{d}_\mu^\dagger \hat{d}_\mu \ , \quad (1.27)$$

where $\hat{d}_\mu$ is the polariton annihilation operator and

$$M = \sum_k \delta_{N_k,1} \quad (1.28)$$

is the number of available particle-hole transition which depends on the mean-field phase. The latter is $M = L/3$ in the normal phase and $M = L$ in photon condensed phase. The vacuum of polaritons, defined by $\hat{d}_\mu |0_{\rm pol}\rangle = 0$ for all μ, corresponds to a multi-mode Gaussian state of cavity photon and particle-hole excitations, and is different from the mean-field ground state $|\Psi^{PMF}\rangle \neq |0_{\rm pol}\rangle$. In the limit of small g, the ground state wavefunction $|0_{\rm pol}\rangle$ coincides with the first-order perturbative result of Eq. (1.21), and then corrects it with $O(g^2)$ terms that give rise to the squeezing of the cavity mode. In order to check the validity of this treatment, we can directly compare the photon observables in the thermodynamic limit (Fig. 1.6). Note that finite system comparisons should be done carefully as finite size corrections arise both from different

boundary conditions and from higher order terms discarded in Eq. (1.25). Minor discrepancies appear to emerge in the thermodynamic limit, but these are likely due to insufficiently large sizes in our numerical results. Since the system is non-additive due to the cavity's presence, we cannot rule out non-trivial corrections that may not be captured by straightforward $1/L$ extrapolations, particularly for non-linear observables such as entanglement entropy. However, this does not contradict the result presented in Fig. 1.5, as it is, in general, unable to spoil the Gaussianity of the cavity density matrix. Nonetheless, up to this minimal errors, the treatment of Gaussian fluctuations is able to faithfully capture the nature of the light-matter correlated ground state (see the comparisons in Fig. 1.6).

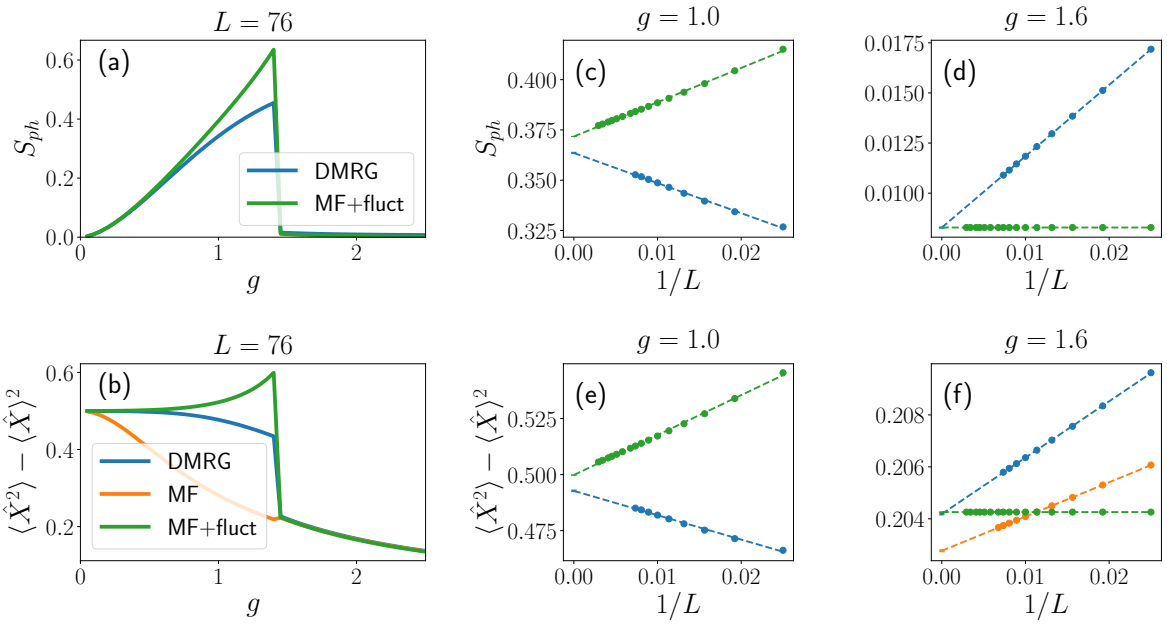


Figure 1.6.: (a-b) The photon entropy S_{ph} and the variance of the quadrature X for the three different methods: DMRG (red), mean-field (blue), and mean-field plus Gaussian fluctuations (green). S_{ph} is zero by definition for the PMF, and hence is not shown. Note that while the system-size is fixed at $L = 76$ for all three methods, the boundary condition for the treatment with Gaussian fluctuations have been set to periodic instead of open. (c-f) The scaling analysis at two representative points inside each phase: $g = 1$ (c,e) and $g = 1.6$ (d,f). Dashed lines are linear fits to a function $f(1/L) = a + b/L$, and have been extrapolated to $L \to \infty$. For $g = 1$, the extrapolation of $\langle \hat{X}^2 \rangle - \langle \hat{X} \rangle^2$ for the PMF is not plotted and its extrapolated value is $a = 0.279$. The difference with the bare mean-field is most evident in the normal phase, where the photon entanglement is higher. Discrepancies between MF+gaussian fluctuations are on the order of 10^-3, hence we cannot exclude some non-trivial corrections beyond $1/L$ in particular for non-linear observables as S_{ph}.

Now given the quadratic Hamiltonian in Eq. (1.27) we can also get information on the excited states of the light-matter system. In particular, we show, in Fig. 1.7, the zero temperature spectral function of the photon, calculated in the Lehmann representation

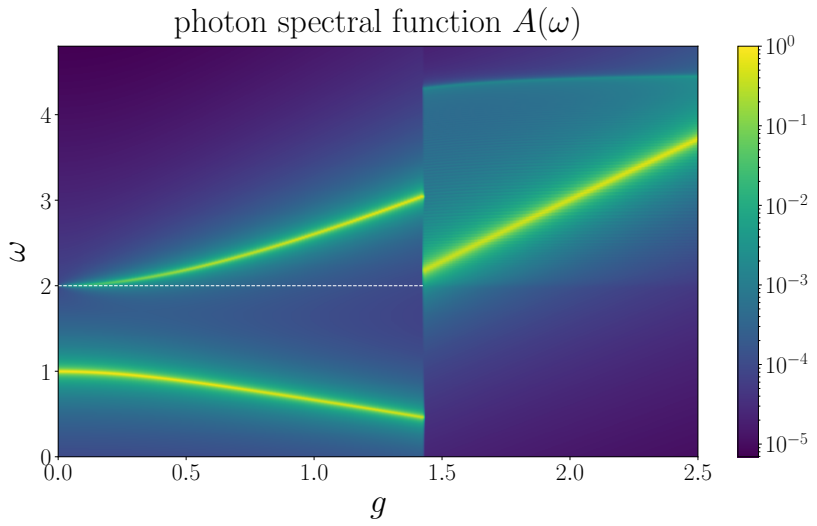


Figure 1.7.: The photon spectral function $A(\omega)$ obtained from the treatment with Gaussian fluctuations, for the square lattice case. Each polariton energy is smeared with a Lorentzian of width $\eta = 10^{-2}$. In the normal phase, there are two bright polariton modes starting at frequencies $\omega_c = 1$ and $\omega = \omega_k = 2$, and $M - 1$ dark modes at $\omega = \omega_k = 2$ signaled by a white dashed line (see Eq. (1.28) for the definition of M). In the photon condensed phase only the one polariton mode is clearly visible while the the other one is shared between all the particle-hole excitations that now have a non-uniform energy structure. The polariton gap does not close at the first-order transition. System size here is $L = 400$.

as:

$$A(\omega) = \sum_{\mu=0}^{M+1} |\langle\mu|\hat{a}^\dagger|0_{\rm pol}\rangle|^2 \delta(\omega - \epsilon_\mu) - |\langle\mu|\hat{a}|0_{\rm pol}\rangle|^2 \delta(\omega + \epsilon_\mu) \ , \tag{1.29}$$

where $|\mu\rangle = \hat{d}^\dagger_\mu |0_{\rm pol}\rangle$ for $\mu > 0$ and $\mu = 0$ corresponds to the vacuum $|0_{\rm pol}\rangle$. In the normal phase $g < g_c$ we clearly see two polariton lines. The lower polariton starts at the cavity frequency $\omega_c = 1$ and the upper polariton at the energy $\omega = \omega_k = 2$ that corresponds to the excitation energy of all direct particle-hole excitations, as clear from the band structure of Fig. 1.4(b). The hybridized degree of freedom is then a superposition of all M available particle-hole excitations leaving $M - 1$ dark polariton dark states, akin to what happens for intersubband exciton-polaritons [115] where intersubband particle-hole excitations provide a macroscopic electric dipole moment. In the photon condensed phase $g > g_c$ instead one polariton mode brings almost all the photon spectral weight and crosses the rest of the polariton modes made up by the particle-hole continuum. Indeed, whether or not a clear polariton doublet can form depend on the band structure presented in figure 1.4(b,c). The energy of the brightest polariton in the photon condesed phase is increasing with g as the cavity fluctuations are more and more squeezed due to the term proportional to D in Eq. (1.27). Consistently with the first order nature of the transition the polariton gap does not close.

1.4. Triangular ladder

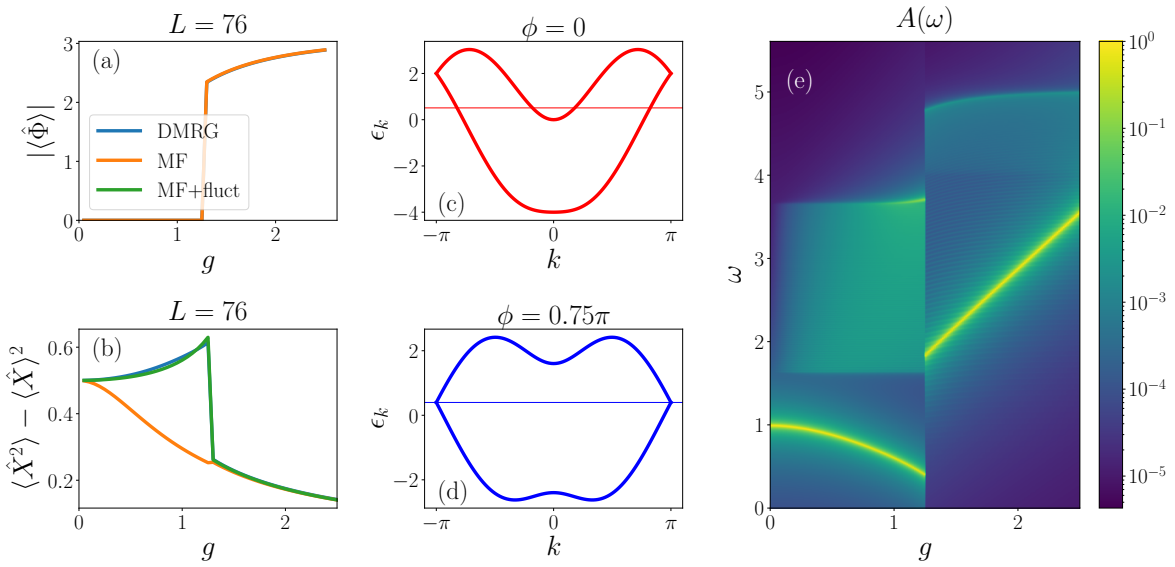


Figure 1.8.: Results for the triangular ladder geometry. (a) The photonic order parameter showing the first-order photon condensation at $g = 1.26$ for both DMRG and PMF. (b) Variance of the cavity quadrature $\hat{X}$ with the three different methods. We show only one system size and the PMF+fluctuations is done with periodic boundary conditions while DMRG and PMF are in open boundary conditions. (c-d) Band structures of the PMF problem for fixed $R = 1$ and two values of ϕ corresponding to the two minima at the transition. Horizontal lines mark the chemical potential. (e) Photon spectral function obtained via the Gaussian fluctuations. Again the gap does not close at the transition due to its first order nature. Each polariton energy has been smeared with a Lorentzian of width $\eta = 10^{-2}$

We now discuss the similar case of a triangular ladder geometry with $t_0 = t_1 = t_2 = \omega_c = 1$. We do not present explicitly all the calculations for the PMF and for the Gaussian fluctuations, as these can be done in close analogy with the square ladder case. We only mention here that the inclusion of the t_2 hopping changes $\boldsymbol{h}_k$, and the parameters ω_k, D, and P_k appearing in Eq. (1.25). As shown in Fig. 1.8, we find again a first order transition to a photon condensed state with $\langle\hat{\Phi}\rangle \neq 0$. The main qualitative difference is in the state of the matter which now goes from a metallic state with 4 Fermi points to a metallic state with 2 Fermi points as evident from the band structure in Fig. 1.8. Again the normal phase has more photon entanglement with respect to the photon condensed phase, and indeed the PMF does not correctly capture the fluctuations of the cavity quadrature $\hat{X}$ below the transition but Gaussian fluctuations are in good agreement. We remind the reader here that the treatment with Gaussian fluctuations is done with periodic boundary conditions while PMF and DMRG are with open boundary conditions. However, in the thermodynamic limit (not shown) results are compatible with the interpretation given for the square ladder case.

Now by looking at the photon spectral function it is now clear that high photon entanglement in the normal phase is not directly linked to a strong coupling to a single

collective excitation. While for the square only one collective excitation was mixing with the cavity, here it is evident that the whole continuum of particle-hole excitations is contributing as there is no polariton doublet in the spectrum at $g < g_c$. In the photon condesed phase, the ground state of the cavity is strongly squeezed and hence its excitation energy is pushed to higher frequencies as we increase g.

1.5. Conclusion

In this chapter, we have proposed a class of minimal toy models for charged fermions coupled through a Peierls phase to a non-uniform cavity mode. The cavity hosts a fluctuating magnetic flux which above a critical light-matter coupling develops a non-zero expectation value, leading to a first-order transition. The crucial element to overcome no-go theorems, as also noted in [75–77, 116], is the presence of a magnetic coupling. To the best of our knowledge, this is the first example of an equilibrium first-order photon condensation for an electronic system. Alternative examples of first-order photon condensation have been proposed [117, 118]. However, these examples do not involve itinerant electronic systems and, more importantly, have been demonstrated to be artifacts resulting from Hilbert space truncation of the model.[69]. We have shown how the key element for such transition is a strong non-linear magnetic response of the ladder band structure, coming with a sudden change of the number of Fermi points as a function of the photonic order parameter, 4 to 0 (2) for the square (triangular) ladder case. Thanks to the quasi-1D nature of the ladder geometry, we have been able to study the ground state via DMRG, hence fully taking into account light-matter entanglement and all kinds of quantum fluctuations. Our numerical results confirms that quantum fluctuations of a single cavity mode alone in the so-called collective strong coupling regime ($g = \text{const}$ for $L \to \infty$) do not alter the phase diagram of a thermodynamically large system [29, 109] and mean-field solutions are accurate up to finite size corrections [110].

Indeed the transition we discussed is agnostic to the PMF decoupling. Still, we find that light-matter entanglement is essential to properly describe the quantum state of a strongly coupled cavity mode as discussed in Fig. 1.6. As already found in other systems with linear dipole-like light-matter couplings[30] the cavity state is Gaussian. Here we have shown how the non-linear nature of the Peierls phase gives a small non-Gaussian correction at finite sizes without any qualitative changes in the Wigner function that remains positive in all the explored phases.

Supported by the Gaussian nature of the cavity ground state in the thermodynamic limit, we analytically derived the quadratic fluctuations on top of the mean-field solution. This highlights the role of polariton states whose ground state gives a qualitatively correct result for the photon entropy and gives access to the cavity spectral function. The latter reflects the first-order nature of the transition.

The presented model is a valid starting point to study photon condensations for large enough system sizes in a numerically exact way. Although not shown in the main text the magnetic instability of the ladder geometry exists for a wide range of geometries and Hamiltonian parameters, including both metal-metal and insulator-insulator first and second order transitions. Interacting electrons coupled to static magnetic fields have also been investigated in higher-dimensional systems [119], showing similar first-order behaviour. This finding supports the notion that first-order photon condensation could be prevalent in various settings, and solely examining instabilities of the normal phase might be restrictive. Moreover, local fermion-fermion interactions can be included without any added cost to the DMRG simulations, as done in [50] for a single XXZ chain. Another element that would be interesting to add to the model is the electronic spin which should favor the paramagnetic response of the system and could have a non-trivial interplay with the orbital magnetism subject of this chapter.

Chapter 2.

Cavity-modified quasi-long range order in one dimensional quantum systems

In this chapter we study the impact of a single cavity mode on quasi-long range order in 1D systems. The presence of strong correlations and the direct coupling between the cavity and the low energy degrees of freedom leads to a stronger impact of the cavity with respect to what discussed in the previous Chapter. In particular we find zero-coupling photon condensation transition (when allowed) and sizable renormalization of macroscopic matter response functions.

2.1. Introduction

The interplay between light and strongly correlated quantum matter has emerged as a fertile ground for exploring new phases of matter and nonequilibrium phenomena [120]. Embedding quantum matter within electromagnetic cavities [10, 22, 121, 122] provides a versatile route to tune interactions and correlations. Over the past decade, this paradigm has been realized across diverse platforms, from atoms in optical cavities [24, 123, 124] to electron gases in terahertz resonators [43, 44, 46]. A common property of these set-ups is that the quantized electromagnetic field acts as a global, non-local degree of freedom, mediating interactions among distant constituents (atoms, electrons, spins) and thus reshaping the collective behavior of many-body systems [1, 3–5, 7, 25, 29, 30, 33, 34, 38, 53, 110, 125–132].

In low-dimensional systems, such effects can acquire a particularly rich character due to the enhanced role of quantum fluctuations. A paradigmatic example of the consequence of large fluctuations is the lack of spontaneous symmetry breaking (SSB) of continuous symmetries in 2D systems at $T > 0$ and 1D quantum systems at $T = 0$, which goes under the name of Mermin-Wagner-Hohenberg-Colemann theorem [133–

135]. Instead these systems display quasi-long range order (QLRO), commonly identified with algebraically decaying correlations. The collective excitations of such critical systems in 1D for the case of $U(1)$ symmetry are described by Luttinger liquids [136], where the the power-law exponents of correlation functions and divergences of various physical quantities are controlled by few parameters.

How these quantum correlations respond to coupling with a global photonic mode remains largely unexplored. Unlike local perturbations, a cavity mode couples coherently to the entire system, acting as a collective, symmetry-breaking field whose fluctuations are both global and quantum in nature.

Here we investigate the effect of a single cavity mode on quasi-long range order in the paradigmatic 1D XXZ model at $T = 0$ by means of density matrix renormalization group (DMRG) simulations [1, 51, 89–91], supported by simple analytical arguments based on a mean-field treatment of the photons [1] and on a Luttinger liquid analysis [136]. We explore two physically distinct coupling mechanisms corresponding to magnetic (Zeeman-like) and electric (described by minimal-substitution) light–matter interactions.

We will show that in the magnetic case, the cavity field acts as an effective transverse Zeeman field, leading to a zero-threshold transition to a spontaneously symmetry-broken phase with a nontrivial critical behavior beyond mean-field expectations. In contrast, when the coupling is electric (i.e. it includes the self-polarization term required by gauge invariance [29, 70]), long-range order remains absent: the system retains its Luttinger-liquid character but develops a pronounced anisotropy in its correlations and response functions. These results demonstrate that global cavity modes can qualitatively reshape the nature of quasi-long-range order in one dimension, offering a new route to control collective quantum phases through light–matter coupling.

2.2. Hamiltonian

We consider a one-dimensional *matter* system described by L localized moments treated as spin-1/2 degrees of freedom σ_j^α (with $\alpha = x, y, z$ and $j = 1, .., L$) coupled to global *cavity* mode. The two types of degrees of freedom are described by the following hamiltonian:

$$\hat{H}_{mat} = -2J \sum_{j=1}^{L-1} \left(\hat{\sigma}_j^+ \hat{\sigma}_{j+1}^- + \text{h.c.} \right) + J\Delta \sum_{j=1}^{L-1} \hat{\sigma}_j^z \hat{\sigma}_{j+1}^z \ , \tag{2.1}$$

$$\hat{H}_c = \omega_c \hat{a}^\dagger \hat{a} \tag{2.2}$$

with J the ferromagnetic in-plane coupling, $J\Delta$ the antiferromagnetic out-of plane coupling and ω_c the frequency of the cavity mode. From now on we take for simplicity $J = \omega_c = 1$. The matter counter-part is an XXZ model with a $U(1)$ symmetry

related to the magnetization in the z-direction. We will focus on the case $\Delta \in [0, 1]$ where the system displays quasi-long range order and is described by a Luttinger liquid [136]. Here the important low energy degrees of freedom are encoded in the pair of conjugate bosonic fields $\hat{\phi}(x)$ and $\partial_x \hat{\theta}(x)$ which encode fluctuations of the magnetization $\hat{\sigma}^z_j \sim \hat{\phi}(x)$ and $\hat{\sigma}^{\pm}_j \sim e^{i\hat{\theta}(x)}$. The gapless nature of these fields is then reflected in spin-spin power-law correlations:

$$\langle \hat{\sigma}^z_0 \hat{\sigma}^z_r \rangle \sim r^{-2K} \quad ; \quad \langle \hat{\sigma}^a_0 \hat{\sigma}^a_r \rangle \sim r^{-1/2K} \text{ for } a = x, y \tag{2.3}$$

with K the Luttinger parameter [136].

We then consider two possible microscopic couplings between the cavity mode and the localized moments described by a parameter A which can be either 0 or 1. These reads:

$$\hat{H}_{mat-c} = \frac{g}{\sqrt{L}}(\hat{a} + \hat{a}^\dagger)\hat{M}_x + A\frac{g^2}{\omega_c L}(\hat{M}_x)^2 \tag{2.4}$$

with g the coupling strength and $\hat{M}_x$ the magnetization:

$$\hat{M}_x = \sum_j \hat{\sigma}^x_j \tag{2.5}$$

Both cases $A = 0$ and $A = 1$ have the important consequence of reducing the in-plane $U(1)$ symmetry (total z magnetization) to a combined Z_2 of cavity and matter (parity of the z magnetization plus number of photon). The main difference, as we will soon show in the next sections, is that the $A = 0$ case allows for a condensation of the photonic field, while the $A = 1$ does not. Before discussing the physics that these coupling structure realize, we also want to motivate their study on the basis that they can describe different physical systems.

The case $A = 0$, to which we will refer as *magnetic*, naturally describes a Zeeman coupling between locally interacting magnetic spins and the magnetic field of a cavity mode polarized in the x-direction. This can be relevant for microwave resonators where magnon-photon ultra-strong coupling has been realized [88]. Cold-atom in optical lattices coupled to Fabry-Perot cavities, as well as other quantum simulation platforms such as Rydberg atoms, circuit QED and trapped ions, may offer another natural way to engineer such Hamiltonian [12]. Instead the case $A = 1$ is more relevant for *electric* dipoles, for example those carried by excitons, coupled to the vacuum electric field of a cavity, i.e. in absence of driving. Here a minimal substitution prescription for the coupling [70, 72] give rise to the self-polarization term $\sim \hat{M}^2_x$ in our case. In particular, the $\Delta = 1$ case can be derived as a strong-coupling limit of a two-band fermionic model describing inter-band excitons used in [71].

2.3. Magnetic coupling

We start by analyzing the $A = 0$ case for the coupling where the cavity can mediate photon condensation transitions because of the absence of a self-polarization term [70, 72].

Numerical results In order to perform DMRG simulations we use an hybrid MPS ansatz [1, 30, 50, 51] where the cavity site (with a maximum number of photons $N_{\max} = 200$) is located at the beginning of the 1D chain (see also Ch. 1). Bond dimensions of 500 are enough to have truncation errors below 10^{-9}. As our DMRG simulations implement the Z_2 symmetry $\hat{a} \to -\hat{a}$ and $\hat{\sigma}^x \to -\hat{\sigma}^x$ exactly using the total parity of excitations (photons plus spin-up), we need to rely on symmetry-conserving operators to detect the possible long-range order. In particular, the long-range order is signaled by:

$$\lim_{|i-j|\to\infty} \langle \hat{\sigma}_i^x \hat{\sigma}_j^x \rangle = \text{const} \ , \tag{2.6}$$

then we can use the following quantity to detect it:

$$\mathcal{M}_x = \frac{1}{L}\sqrt{\langle \hat{M}_x^2 \rangle} = \frac{1}{L}\sqrt{\sum_{i,j=1}^{L} \langle \hat{\sigma}_i^x \hat{\sigma}_j^x \rangle} \ . \tag{2.7}$$

Note that for quasi long range order, i.e. $\langle \hat{\sigma}_i^x \hat{\sigma}_j^x \rangle \propto |i-j|^{-s}$ with $s > 0$, this order parameter vanished algebraically as $L^{-s/2}$. Another observable we can use to pinpoint the photon condensation is the photon number:

$$n_{ph} = \langle \hat{a}^\dagger \hat{a} \rangle \tag{2.8}$$

which is invariant under the Z_2 symmetry $\hat{a} \to -\hat{a}$ but is expected to develop an $O(L)$ value in a SSB phase where $\hat{a} \sim \sqrt{L}$. A more refined analysis on the cavity state $\hat{\rho}_c$ can be done by looking at its Wigner function [112]:

$$W(x,p) = \frac{1}{\pi}\int dy e^{2ipy} \langle x+y| \, \hat{\rho}_c \, |\delta(x-y)\rangle \ , \tag{2.9}$$

where $|\delta(x)\rangle$ are eigenstates of the position operator. We will only focus on its projection on the real quadrature $P(x) = \int dp \, W(x,p)$, as this is expected to show a bimodal structure for a ground state which is superposition of two symmetry broken states with $\hat{a} \sim \pm\alpha$.

We show DMRG results for these quantities in Fig. 2.1 panels (a,b,c) for $\mathcal{M}_x$, (e,f,g) for $\sqrt{n_{ph}/L}$ and (h) for $P(x)$. For all different anisotropies $\Delta = 0, 0.5$ and 1 the order parameters seems to be finite as soon as the cavity coupling is switched on $g > 0$, thus implying immediate developing of the Z_2 long-range oreder. Focusing

on the Wigner function of the cavity in panel (h), we see how this exactly shows the expected bimodal shape, with photon fluctuations breaking this picture only at small size. Following this intuition, we analyze better the limit of small g within a photon-mean field approximation.

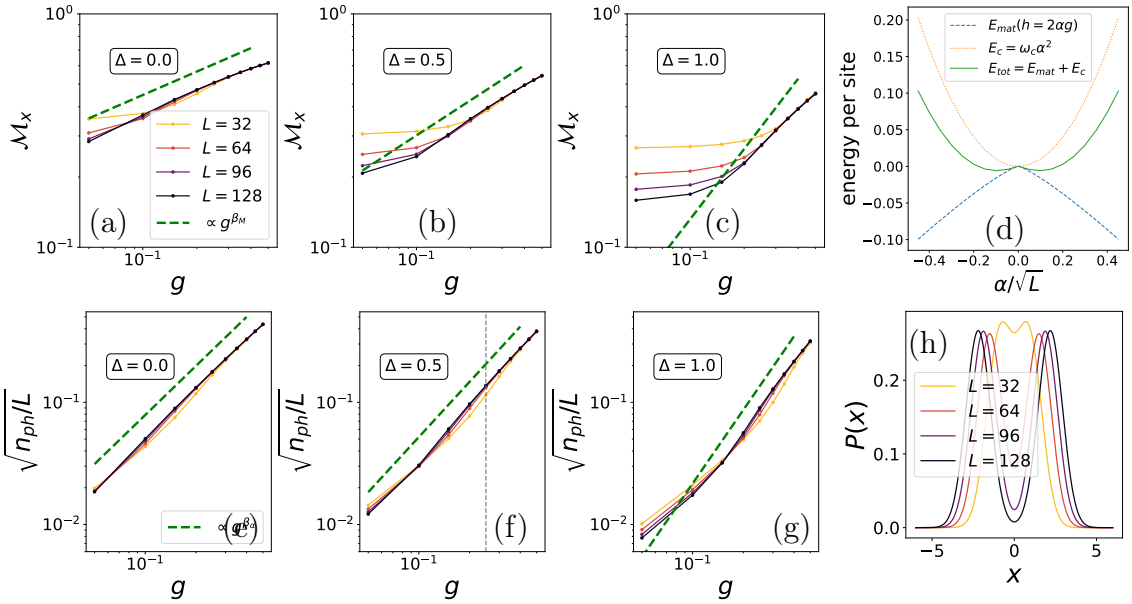


Figure 2.1.: (a,b,c) Order parameter for long-range order on x direction and number of photons (e,f,g) in the $A = 0$ case different values of Δ and system sizes L. Dashed green lines are the critical behaviour predicted by the photon-mean-field with a fitted proportionality constant. (d) Mean-field energy (green line) for $\Delta = 0.5$ and $g = 0.$ as a function of the intensive $\alpha/\sqrt{L}$ expressed in the different contributions: matter E_{mat} (dashed blu) obtained with DMRG at $L = 128$ and cavity (dotted orange). (h) Wigner function of the cavity for the real coordinate α for $\Delta = 0.5$ and $g = 0.25$ (dashed gray line in panel (f)) for different system sizes.

Photon mean field We use as a working ansatz for the photon mean-field (PMF) [1] a decoupled wavefunction:

$$|\Psi_{\mathrm{PMF}}\rangle = |\psi\rangle\,|\phi_c\rangle \tag{2.10}$$

which assumes absence of light-matter entanglement but importantly allows for a non-trivial matter state. This is crucial as the matter part at $g = 0$ features in-plane quasi-long range order, with ferromagnetic power law correlations on the xy-plane. We remark that this classical approximation for the cavity field is realized in the *adiabatic* limit $\omega_c \to 0$ with g^2/ω_c fixed. The solution of the PMF for the photon part is a coherent state determined by a matter expectation value:

$$|\phi_c\rangle = |\alpha\rangle \qquad \alpha = -\frac{g}{\omega_c\sqrt{L}}\langle \hat{M}_x\rangle \tag{2.11}$$

where $\langle..\rangle$ is an expectation value over $|\psi\rangle$. We remark that non-trivial solutions $|\alpha| > 0$ will inevitably break the $U(1)$ symmetry, in particularly lowering it to a Z_2 as α has to

be real. In general finding the solution of such mean-field can be cast in a minimization of the coherent state α and the matter state $|\psi\rangle$:

$$E_{tot}(\alpha, |\psi\rangle) = \langle \hat{H}_{mat} + h(\alpha)\, \hat{M}_x \rangle_\psi + \omega_c |\alpha|^2 \tag{2.12}$$

where $h(\alpha) = 2g\alpha/\omega_c\sqrt{L}$ and $\langle \dots \rangle_\psi$ an expectation value over the matter state $|\psi\rangle$. A possible solution of the problem is to evaluate the ground state $|\psi\rangle$ of the only matter Hamiltonian $\hat{H}_{\text{mat}} + h(\alpha)\hat{M}_x$ at fixed α and then minimize the overall energy as a function of α. This is shown for a specific value of Δ and g (and L) in Fig. 2.1(d), where different contribution to the total energy are highlighted (note that the energy is given relative to the $\alpha = 0$ case). This indeed shows two minima at $\alpha \neq 0$ and support the SSB of the Z_2 symmetry.

Instead of numerically evaluating the energy and ground state of the matter part, we can actually make some analytical predictions. Even though the XXZ model in an external in-plane field is not exactly solvable, its behavior at small in-plane field h is known [136]. In particular the energy (and thus magnetization) is non-analitic with h:

$$E_{mat}(h) - E_{mat}(0) \propto -L\,|h|^b \tag{2.13}$$

$$\langle \hat{M}_x \rangle_{|h|>0} = -\frac{\partial}{\partial h} E_{mat}(h) \propto |h|^{b-1} \tag{2.14}$$

where:

$$b = \frac{8K}{8K-1} \qquad K = \frac{\pi}{2(\pi - \arccos\Delta)} \tag{2.15}$$

Now we can minimize $E_{tot}(\alpha)$ (shown numerically in Fig. 2.1(d)) by taking derivatives with respect to α we then get two equal minima at:

$$\frac{\alpha}{\sqrt{L}} \sim \pm g^{\beta_\alpha} \qquad \beta_\alpha = \frac{b}{2-b} = \frac{4K}{4K-1} \tag{2.16}$$

where the prefactor depends on the unknown matter energy scale C. With this one can also infer the behavior of the magnetization order parameter:

$$\mathcal{M}_x = 2g\frac{\alpha}{\sqrt{L}} \sim \pm g^{\beta_M} \qquad \beta_M = \frac{2}{2-b} = \frac{8K-1}{4K-1} \tag{2.17}$$

These predictions for the small g behavior of the order parameters are show as dashed green lines in Fig.2.1(a,b,c,e,f,g) and well match the numerical data (for α we actually show $\sqrt{n_{ph}}$), except for the case of $\Delta = 1$. In this case further corrections might arise, possibly coming from quantum fluctuations of the cavity or from missed logarithmic behaviour. For all green dashed lines in panels (a,b,c) we fix the prefactor in order to match the value of the largest system size at $g = 0.25$.

We now also wish to remark the non-trivial behavior of the Z_2 order parameters α and $\mathcal{M}_x$. For mean-field transition of the Dicke model one typically has $\alpha, \mathcal{M}_x \sim (g - g_c)^{1/2}$ which correspond to a mean-field Ising order parameter exponent $\beta = 1/2$. Here the presence of critical $U(1)$ fluctuations at the $g_c = 0$ point strongly renormalize the Z_2 SSB and the critical exponents of the matter and photon order parameter.

2.4. Electric coupling

We now pass to the $A = 1$ scenario describing the coupling with electric dipoles. Here a self-polarization term is present and cavity-induced long-range order inhibited.

Absence of long-range order In Fig. 2.2(a,b) we show DMRG results which exclude the presence of long-range order on the x direction. In particular scaling the order parameter $\mathcal{M}_x$ with system size we see a clear dependence towards 0, with the same dependence of the $g = 0$ case. We remark that a finite value of such expectation value is expected as power-law correlation on x contribute to $\mathcal{M}_x$ non-trivially.

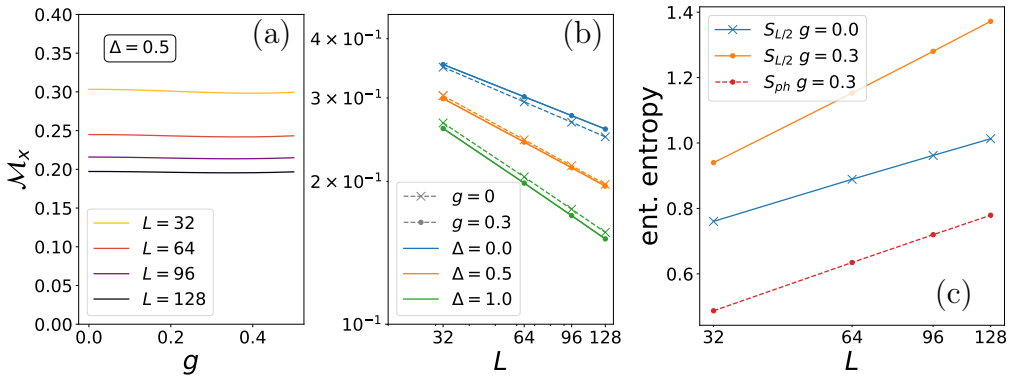


Figure 2.2.: (a,b) Order parameter for x-magnetization and entanglement entropy in case $A = 1$. (a) Different system sizes as a funciton of g for $\Delta = 0.5$. (b) power-law scaling of the order parameter $\mathcal{M}_x \sim L^{-1/4K}$ which does not change between $g = 0$. (dashed cross) and $g = 0.3$ (full dots) for different values of $\Delta = 0, 0.5, 1.$. (c) Von Neuman entanglement entropy of the cavity (red dashed $g = 0.3$) and of half of the spins (blu $g = 0$ and orange $g = 0.3$) as a function of the system size in log scale for $\Delta = 0.5$. The log-scale highlights the $\log(L)$ dependence.

In order to understand why no long-range order is appearing we re-use the photon mean-field arguments of the previous section, including the self polarization term $\sim \hat{M}_x^2$. We rewrite the energy functional $E_{tot}(\alpha)$ using $\alpha = \frac{g}{\omega_c\sqrt{L}}\langle \hat{M}_x \rangle_\psi$ and we get:

$$E_{tot} = \langle\, \hat{H}_{mat} + \frac{g^2}{\omega_c L}\left(\hat{M}_x - \langle \hat{M}_x \rangle_\psi\right)^2 \rangle_\psi \;; \tag{2.18}$$

where the expectation value is taken on a self-consistent matter many-body state $|\psi\rangle$. Even without finding $|\psi\rangle$, we can note that the cavity-induced term is essentially the variance of the x magnetization and as such it is a positive definite term. As a consequence of this, there is no energy gain in developing a macroscopic order parameter $\mathcal{M}_x$ and one should not expect *photon condensation* transitions to occur. Nonetheless, already at this mean-field level, one might expect a non-trivial renormalization of the fluctuations of $\hat{M}_x$ as these now have an higher energy cost.

However in this respect, the photon-mean-field should be taken with care since, as shown by DMRG results in Fig. 2.2, the photon entanglement entropy S_{ph} grows as $\log(L)$. In the same panel we also show that the mid-chain entanglement entropy $S_{L/2}$ is increasing as $\log(L)$ but with a different prefector with respect to the known $g = 0$ case. Here it follows the known scaling $S_{L/2} = \frac{c}{6}\log(L) + \text{const}$ with $c = 1$ the central charge of the free boson CFT describing the Luttinger liquid [137]. The prefactor of the scaling at finite g however varies continuously with g and Δ and does not seem to be universal. We also remark that the mid-chain entanglement entropy is not a matter-only quantity as we are not only tracing on the other half of the matter but also on the cavity degree of freedom[1].

Anisotropic Luttinger Liquid We explore the nature of the phase at $g > 0$ by analyzing more in details the ground-state and low-energy properties of the system with DMRG. We start by looking at in-plane correlation functions:

$$C_r^{aa} = \langle \hat{\sigma}^a_{L/3}\hat{\sigma}^a_{L/3+r}\rangle + \langle \hat{\sigma}^a_{L/3+1}\hat{\sigma}^a_{L/3+1+r}\rangle \tag{2.19}$$

where $a = x, y, z$ and we are summing over two sites to reduce oscillations. We also restrict sites to be in the bulk $L/3 < j < 2L/3$ in order to avoid edge contributions.

Results are then shown in Fig. 2.3. We show two values of $\Delta = 0$ (left panels) and $\Delta = 1$ (right panels), and focus on in-plane correlation functions $\alpha = x, y$. These are exactly symmetric at $g = 0$ because of the in-plane $U(1)$ symmetry of the matter Hamiltonian, which at $\Delta = 1$ actually becomes $SU(2)$. As we can see from the top panels (a,b) the long-range part of the in-plane correlation function is modified in an anisotropic way (i.e. $x \neq y$) by the presence of the cavity $g = 0.4$. This anisotropy more clearly represented in the bottom panels (c,d) where we explicitly show the difference betweeen the correlations as a function of distance. This reveals that the cavity-mediated anisotropy is also *scale* dependent, i.e. it is not just a constant. Furthermore the spatial dependence of such corrections (and also the sign) differs for different values of Δ, highlighting the non-trivial interplay between quasi-long range order of the matter system and the global fluctuations of the cavity photons.

As the amplitude of such corrections depends on the system size, one may wonder whether the overall effect vanishes in the thermodynamic limit $L \to \infty$. We then further explore macroscopic observables, in particular the long-wavelength static structure factors and the zero-frequency susceptibility:

$$S_{aa} = \frac{1}{L}\sum_{ij}\langle \hat{\sigma}^a_i\hat{\sigma}^a_j\rangle \qquad \chi_{aa} = \lim_{h_\alpha\to 0}\frac{1}{h_a}\langle \hat{M}_a\rangle_{h_a} \tag{2.20}$$

where h_a represent an external field and $\langle..\rangle_{h_a}$ the expectation value on the ground state of $\hat{H} + h_\alpha\hat{M}_a$. These are divergent quantities in a Luttinger liquid which follow

[1] Similar non-universal scaling have also witnessed in only-matter models with infinite range interactions [138].

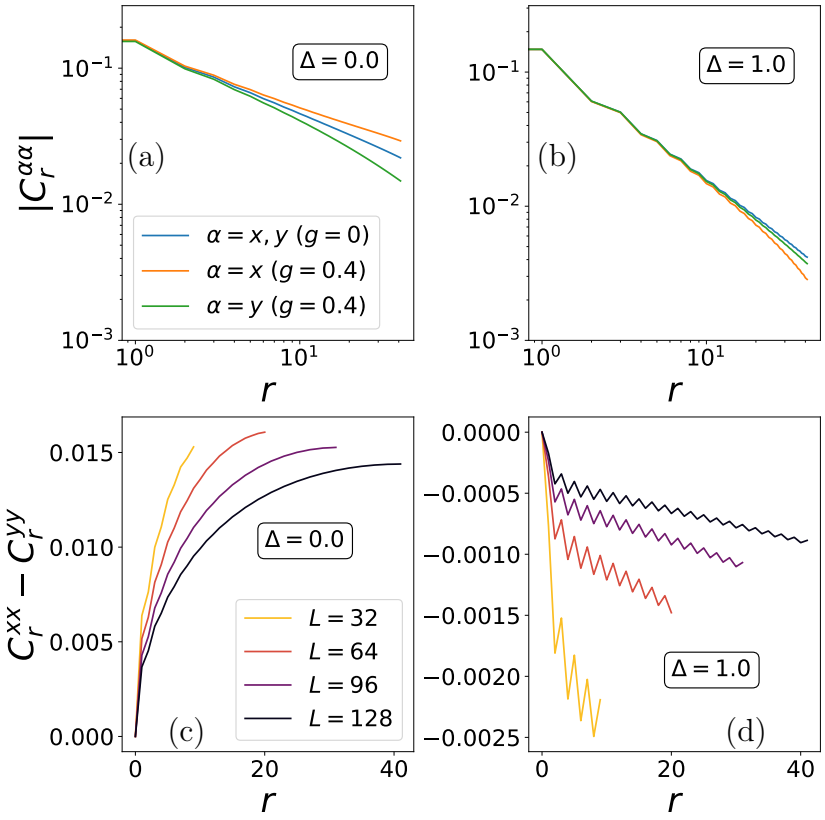


Figure 2.3.: Correlation functions for case $A = 1$, showing the broken $U(1)$ symmetry only at large distances but without long-range order, i.e. no finite value for $r \gg 1$.

the scaling behaviour:

$$S_{aa} = C_S \, L^{1-\frac{1}{2K}} \qquad \chi_{aa} = C_\chi \, L^{2-\frac{1}{2K}} \qquad a = x, y \tag{2.21}$$

with C_χ and C_S two proportionality constants which are independent of a because of the underlying $U(1)$ symmetry.

In Fig. 2.4 we show DMRG results for such response functions in presence of the cavity. In the left panels (a,c) we normalize to their value at $g = 0$, S^0_{aa} and χ^0_{aa}, and show results for a fixed system size $L = 128$ and different values of Δ. These reveal the strong in-plane anisotropy as $a = x$ (full) and $a = y$ (dashed) are clearly different. The cavity has a much stronger effect on the susceptibility with respect to the the static structure factor. We trace this back to the fact that the susceptibility non-trivially averages finite-frequency properties of the systems and the cavity-mediated interaction vertex has finite contributions only at finite frequencies [72, 110]. Nonetheless also zero-frequency properties are renormalized by the presence of fluctuations, as indicated by the static structure factor.

Despite this strong cavity-induced in-plane anisotropy of the response functions showcasing the broken $U(1)$ symmetry, the power-law divergences of these quantities remain unaffected (Fig. 2.4(b,d). Here we show that the absolute value of response functions at $g = 0$ (cross) and $g = 0.3$ (dot) diverges in the same manner with system

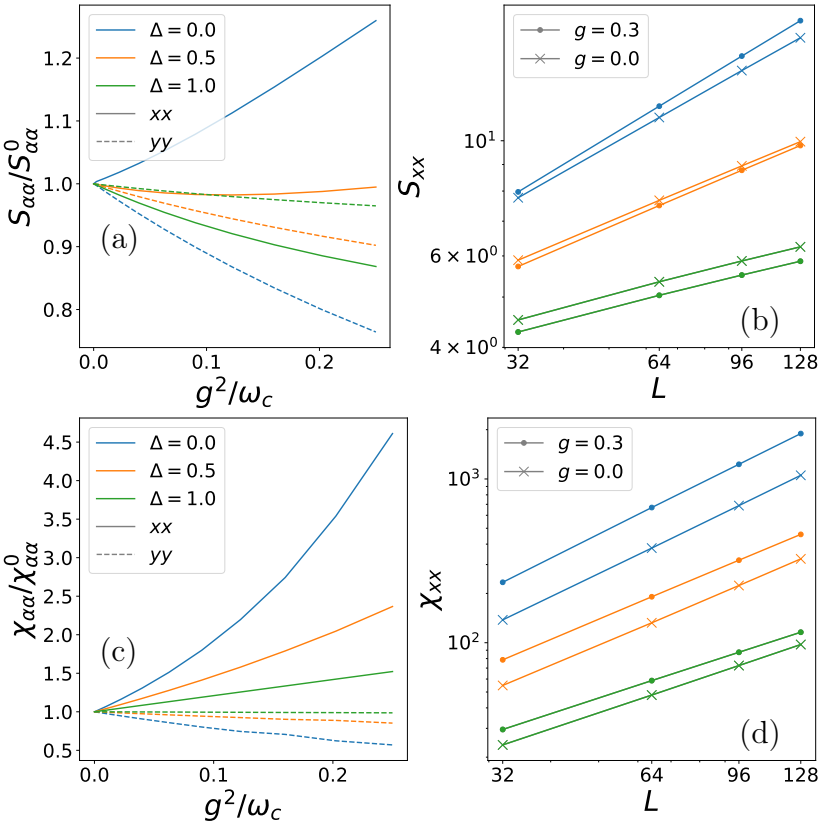


Figure 2.4.: In plane long-wavelength static structure factor (a,b) and susceptibility (c,d) in the $A = 1$ case. (a,c) Behaviour at fixed $L = 128$ as a function of g^2/ω_c for $\omega_c = 1$ at different values of Δ and normalized to their value at $g = 0$. Full (dashed) lines represent observables with x (y) polarization, which are equal at $g = 0$ but different otherwise. (b,d) Divergence of these quantities as a function of system size for $g = 0$ (dots) and $g = 0.3$ (cross).

size. Note that the $\Delta = 1$ case would actually give $S_{aa} \sim const$ and the observed increase actually comes from logarithmic corrections.

2.5. Conclusions and outlook

In this chapter we have explored the fate of 1D quasi-long range order in an XXZ model under the action of a single global cavity-field for two different forms of the coupling, which reflect two fundamentally different physical situations. When the mean-field contribution of the cavity is finite (magnetic coupling), we observe a zero coupling instability $g_c = 0^+$ towards long-range Z_2 ferromagnetic order with unusual critical exponents for the order parameters. These are predicted already by a photon-mean-field ansatz and agree with large scale DMRG numerics. In the other explored scenario (electric coupling) where the mean-field contribution vanish, the system retains a form of quasi-long-range-order, albeit strongly modified with respect to common knowledge from locally interacting systems. Correlation functions are not simple power-laws but

acquire cavity-mediated corrections which increase with distance in a non-trivial manner. An evident consequence of this is found in macroscopic long-wavelength response functions which are not anymore $U(1)$ symmetrics but present a strong anisotropy even for small values of the light-matter coupling strength.

A field theoretical description of the physics discussed in this chapter is object of current work. The basic idea is to couple a Luttinger Liquid action to the cavity and deriving perturbative corrections to critical behaviour similarly to what done in Ref. [35] but with a frequency dependent interaction vertex of the cavity [72, 110]. This should allow us to further explore finite temperature behaviors and more realistic scenarios where a continuum of cavity modes is considered [38, 39, 139, 140], as well as generalization to quasi-long-range-order in 2D.

Chapter 3.

Local vs non-local dynamics in cavity-coupled Rydberg atom-arrays

In this chapter we focus on dynamical properties of cavity-embedded matter, in particular on how the coexistence of local and non-local degrees of freedom can impact its low-energy excitations. We do so in the context of Rydberg atom arrays coupled to optical Fabry-Perot cavities, devising simple protocols that can be realized in the yet-to-come first generation of such experiments.

3.1. Introduction

There is presently considerable interest in exploring the real time dynamics of strongly interacting quantum matter in quantum simulators and computers [141, 142]. A major goal of this endeavor is to shed light on the role of low-lying excitations, in particular, in the context of gauge theories and spin models, where basic constituents such as mesons and strings play a prominent role [143–149]. Remarkable recent experiments have begun to investigate this within the realm of Abelian gauge theories as well as Ising-like models, exploring string [150–155] as well as meson-driven dynamics [156, 157] and false-vacuum decay [158, 159]. The dynamics considered so far has been driven by local couplings, which severely constrain the effective interactions between quasiparticles. That is not generally the case for cavity embedded quantum matter [9, 10, 12, 22, 160], an emerging class of quantum many body systems characterized by the interplay between local degrees of freedom (atoms [24, 36, 161–166], spin [33, 131, 138, 167–173], electrons [4, 5, 25, 31, 40, 43–45]) and non-local cavity modes — leading to a plethora of phenomena not accessible in traditional spin models. It is thus an open question whether such couplings to global modes can give rise to qualitatively new meson and string dynamics, and whether that can be experimentally probed.

In this chapter, we consider a setup consisting of an array of neutral atoms, whose ground state is coupled to a Rydberg state via a two-photon transition involving a

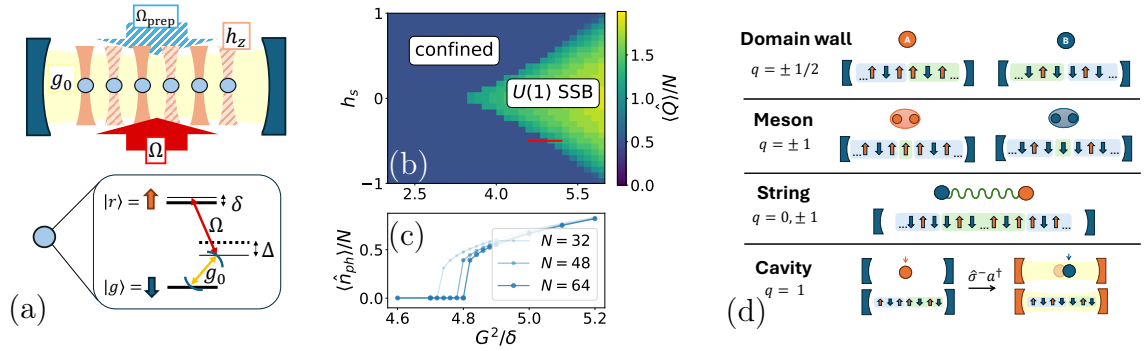


Figure 3.1.: (a) Sketch of the set-up under consideration, an array of individually controlled rydberg atoms coupled to a cavity mode via a two-photon transition assisted by an external laser Ω, giving a tunable coupling $g = \Omega g_0/\Delta$. (b-c) Phase diagram of the TC-Ising model as a function of h_z and $G = g\sqrt{N}$ via (b) the ground state charge sector Q (ED and $N = 10$) and (c) photon number (DMRG); the latter at a fixed $h_z = -0.5$ and varying G (red line of (b)). In both (b) and (c) $V = \delta = 1.$ and $\lambda = 0$. (d) Sketch of the relevant low-energy degrees of freedom and their $U(1)$ charge in the confined antiferromagnetic phase.

cavity field, see Fig 3.1(a). Our proposal builds upon and combines outstanding achievements in the field of cavity QED [24, 123, 174] and Rydberg atom experiments [151, 175, 176], with the promise of achieving unexplored regimes where both local and non-local interactions are dominating over cavity losses and realize coherent light-matter many body dynamics.

Within this setting, locally interacting spins couple to a global mode in a controllable manner, realizing a perfect setting where to investigate hybrid meson and string dynamics. After deriving the phase diagram of the model, we show that the cavity field has a drastic impact on its low-energy dynamics: different types of solitons emerge, featuring very distinct energetics due to cavity-assisted processes. Some of the solitons can propagate freely thanks to the cavity, while others are dynamically blocked, and effectively stay confined due to energetics.

The effect of light onto composite objects is drastic. Meson quasiparticles hybridize with light, generating a meson-polariton excitation that immediately de-localizes single mesons. In deconfined regimes instead, mesons melt during the real-time dynamics via a multi-stage local process involving a combination of spin and cavity excitations. String dynamics is instead informative about the fate of confinement in the presence of light. Remarkably we observe that strings, independently of their length, always acquire a finite kinetic energy, contrasting with local spin models where this is typically exponentially suppressed. This is due to cavity-mediated long-range interactions solitons, allowing for an exchange between string tension and kinetic energy. We illustrate this new class of dynamical behavior using exact (ED) and matrix product states (MPS)[1, 89, 91, 93, 177] simulations, and conclude the chapter detailing a realistic experimental proposal.

3.2. Model Hamiltonian

We consider a collection of N Rydberg atoms coupled to single cavity mode via a two photon transition through a far detuned intermediate state (see Fig. 3.1). This can be mapped onto a Tavis-Cumming model with an antiferromagnetic Ising interaction, in abbreviation Tavis-Cumming-Ising or TC-Ising. The Hamiltonian is (see App. B.1 for derivation):

$$\begin{aligned}\hat{H} &= \delta\hat{a}^\dagger\hat{a} + h_z\sum_j(-1)^j\hat{\sigma}_j^z + V\sum_j\hat{\sigma}_j^z\hat{\sigma}_{j+1}^z \\ &+ g\sum_j\left(\hat{a}\hat{\sigma}_j^+ + \hat{a}^\dagger\hat{\sigma}_j^-\right) + \lambda\,\hat{a}^\dagger\hat{a}\sum_j\hat{\sigma}_j^z,\end{aligned} \tag{3.1}$$

where δ is the cavity detuning, h_z a staggered longitudinal field achieved by AC Stark shifts coming from the optical tweezers, V the Rydberg-Rydberg interaction truncated to the nearest neighbor for simplicity [1], $g = g_0\Omega/\Delta$ the effective cavity-atom coupling strength and $\lambda = g_0^2/\Delta$ a cavity dependent Stark shift. A further laser Ω_{prep} is needed for state preparation purposes. We set $\lambda = 0$ for simplicity and $V = 1$.

Importantly the model has a $U(1)$ symmetry associated to the number of photons and Rydberg excitations:

$$\hat{Q} = \hat{a}^\dagger\hat{a} + \sum_j\hat{\sigma}_j^+\hat{\sigma}_j^-. \tag{3.2}$$

In Fig. 3.1(b,c) we show the phase diagram obtained with exact diagonalization (ED) and matrix product state (MPS) simulations as a function of the *collective* light-matter interaction $G = g\sqrt{N}$ and the longitudinal staggered field h_z with fixed interaction $V = 1$. Two phases are present (see Fig. 3.1(c)), distinguished by the charge sector Q in which the ground state lives. The ground state is antiferromagnetic when $Q = N/2$, corresponding to the confined phase[2]. When the charge Q instead changes we find an in-plane ferromagnet with spontaneous symmetry breaking (SSB) of the continuous $U(1)$ symmetry related to the charge Q [138, 178–180]. In Fig. 3.1(c) we show the photon occupation for large systems obtained with DMRG, highlighting the first order nature of the transition (see SM of Ref. [3] for more details). The phase diagram is similar to that of the longitudinal field Ising model, whose AFM phase can also be understood as a confined phase of a Z_2 lattice gauge theory. The strong coupling phase however is here enriched by the $U(1)$ SSB instead of being a simple disordered paramagnet. Note that also Dicke-Ising models [132, 172] show the same feature with the SSB being of a discrete Z_2 instead of a continuous $U(1)$ symmetry.

In the following we will focus only on the AFM, or confined, phases dynamical properties by studying the low energy excitations depicted in Fig 3.1(d). Note also

[1] Minor effects coming from longer-range interactions are discussed in the SM of Ref. [3].

[2] While Q does not stricly reveal confinement, this can be detected by expectation values of string operators, in this case $W(i,j) = \prod_{i\le l\le j}\hat{\sigma}_l^x$ which we indeed checked to be vanishing in the confined phase.

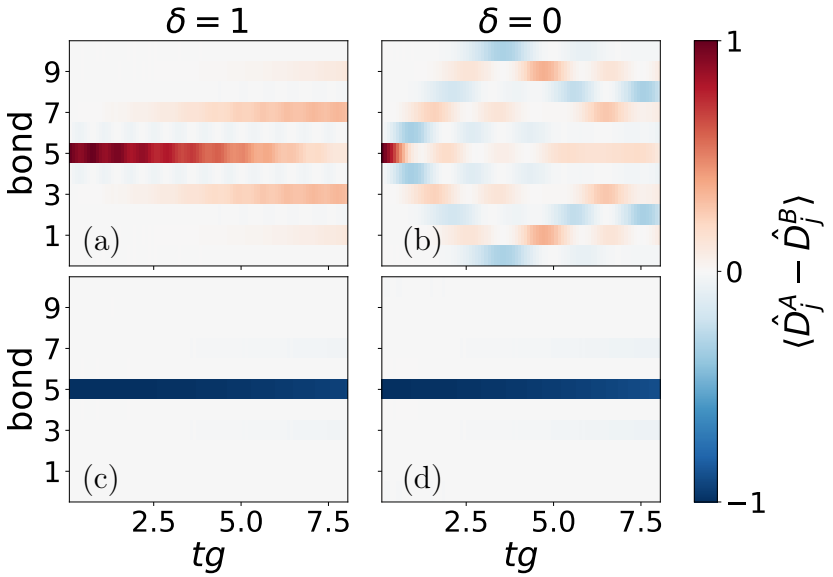


Figure 3.2.: Single domain wall cavity-mediated dynamics via domain wall density $\langle \hat{D}_j^A - \hat{D}_j^B \rangle$ obtained with ED. The system is initialized in a classical state with a single domain wall either of (a,b) type A or type B (c,d). The cavity photon energy is $\delta = 1$ on the left (a,c) while $\delta = 0$ on the right (b,d). $N = 12$, $V = 1$, $g = 0.12$ and $h_z = 0$.

that as long as the cost of creating a pair of domain walls $4V$ is larger than the light-matter collective coupling $g\sqrt{N}$, their number is going to be approximately conserved.

3.3. Domain-wall propagation

The presence of a global $U(1)$ symmetry induces strong differences between domain walls formed by up-up or down-down spins, unlike the standard phenomenology of Z_2 symmetric Ising models. We thus introduce two domain wall densities:

$$\hat{D}_j^A = |\uparrow_j\uparrow_{j+1}\rangle\langle\uparrow_j\uparrow_{j+1}| \quad \hat{D}_j^B = |\downarrow_j\downarrow_{j+1}\rangle\langle\downarrow_j\downarrow_{j+1}| \tag{3.3}$$

which measure the presence of domain walls of type A or B at the bond between atom j and $j+1$ ($j = 0, \ldots, N-1$). We study quenches of the light-matter interaction g, starting from initial classical domain wall states (Fig. 3.1(d)) with zero cavity photons. We remark that the system has no quantum dynamics in absence of g.

In Fig. 3.2 we show ED results for the propagation of type A (top row) and type B (bottom row) domain walls in two different regimes for the cavity detuning ($\delta = 1$ and $\delta = 0$). The timescale of the cavity-induced dynamics is different in all four resulting cases but can be understood by simple perturbation theory. Starting from the cavity detuned regime, $\delta = 1$, for domain walls of type A we have a second-order process:

$$|\uparrow\downarrow\uparrow\uparrow\downarrow\uparrow\rangle\,|0\rangle \;\rightarrow\; |\uparrow\downarrow\uparrow\overline{\downarrow\downarrow}\uparrow\rangle\,|1\rangle \;\rightarrow\; |\uparrow\downarrow\uparrow\overline{\downarrow\uparrow}\uparrow\rangle\,|0\rangle\,, \tag{3.4}$$

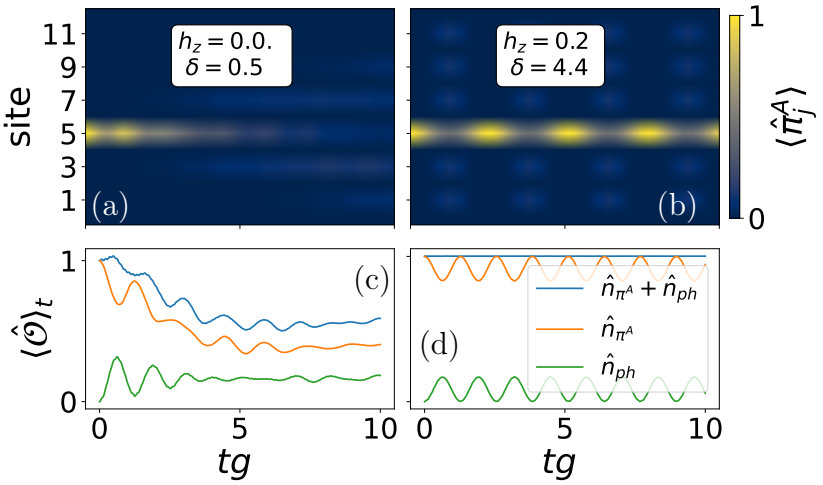


Figure 3.3.: Meson-polariton dynamics (a,c) in a de-confined case ($h_z = 0$, $\delta = 0.5$) and (b,d) in a confined case ($h_z = 0.2$, $\delta = 4.4$) obtained with ED. Top panels (a,b) show the dynamics in real space via the meson density, while bottom panels (c,d) show the evolution in time of key observables (total meson number, photon number and their sum). $V = 1$, $g = 0.1$ and $N = 13$.

with a rate $J_A = g^2/\delta$. The peculiarity of this process is that the domain wall can only jump by two sites and will remain type A, as indeed clear in Fig. 3.2(a). Type B domain walls instead can only move through creation and destruction of other domain walls, thus costing much more energy. At lowest order:

$$|{\downarrow}{\uparrow}{\downarrow}{\downarrow}{\uparrow}{\downarrow}\rangle\,|0\rangle \;\rightarrow\; \left|{\downarrow}{\uparrow}{\downarrow}{\downarrow}\bar{\uparrow}\bar{\downarrow}{\downarrow}\right\rangle|1\rangle \;\rightarrow\; \left|{\downarrow}{\uparrow}{\downarrow}\bar{\uparrow}\bar{\downarrow}{\downarrow}{\downarrow}\right\rangle|0\rangle\,, \tag{3.5}$$

with a rate $J_B = g^2/(\delta + 4V)$ which effectively result in an apparent freezing of the domain wall.

Moving to small photon frequencies $\delta < g$ the propagation mechanism changes. The main difference is that, instead of being virtually populated by second-order processes, now the cavity can be resonantly populated. For example starting from a domain wall of type A we have:

$$|{\uparrow}{\downarrow}{\uparrow}{\uparrow}{\downarrow}{\uparrow}\rangle\,|0\rangle \;\rightarrow\; \left|{\uparrow}{\downarrow}{\uparrow}\bar{\downarrow}\bar{\uparrow}{\downarrow}{\uparrow}\right\rangle|1\rangle \tag{3.6}$$

happening with a rate g. Here the domain wall type can oscillate between A and B during the propagation as a photon is coherently exchanged back and forth. The other case of an initial condition with a domain wall of type B (and no initial photons) does not allow these resonant processes but only the second order processes thus still giving a frozen dynamics.

3.4. Meson-polaritons

Another important low-energy excitation which can be built on top of an AFM ground state is a single spin-flip, i.e., a magnon or, in connection with the LGT inter-

pretation, a meson. As for domain walls, we can identify two different type of mesons A and B corresponding respectively to a spin flipped up ($\downarrow$ to $\uparrow$) and vice versa. In particular at $g = 0$ the simplest meson states are classical configurations:

$$|\pi_j^{A/B}\rangle\,|0\rangle = \hat{\sigma}_j^{\pm}|AFM\rangle\,|0\rangle \qquad \text{(for } j \text{ odd/even)} \tag{3.7}$$

where $|AFM\rangle$ is the Néel state with up (down) spins on even (odd) sublattices and $|0\rangle$ the cavity vacuum, as sketched in Fig.3.1(d). In order to track the dynamics of these excitations we use the classical, type resolved, meson density:

$$\begin{aligned}\hat{\pi}_j^A &= |\uparrow_{j-1}\uparrow_j\uparrow_{j+1}\rangle\langle\uparrow_{j-1}\uparrow_j\uparrow_{j+1}|\,,\\ \hat{\pi}_j^B &= |\downarrow_{j-1}\downarrow_j\downarrow_{j+1}\rangle\langle\downarrow_{j-1}\downarrow_j\downarrow_{j+1}|\,.\end{aligned} \tag{3.8}$$

In Fig. 3.3 we study the meson dynamics [3] starting from a classical meson state (Eq. 3.7) in different regimes for h_z and δ, keeping $g = 0.1$. The leftmost panels (a,c) show the dynamics in absence of confinement $h_z = 0$. Here the two domain walls forming the meson split-up and propagate independently, as highlighted by a quickly decaying meson number $\hat{n}_{\pi^A} = \sum_j \hat{\pi}_j^A$. In the right panels (b,d), we show the emergence of confinement with a finite $h_z = 0.2$ for a cavity detuning $\delta = 4V+2h_z = 4.4$ which makes cavity photons (δ) and mesons ($4V + 2h_z$) resonant. Note that, despite confinement, only the combined sum (blue) of number of photons (green) and meson (orange) is conserved. This hybridization can be traced back to the formation of collective meson-polariton states which imprint a non-local dynamics on the initially local meson excitation, i.e., a de-localization of the meson on the whole spin-chain. In order to better understand the physics at play, we explicitly construct the collective states responsible for the meson-polariton formation:

$$|C_1\rangle = |AFM\rangle|1\rangle, \quad |C_2\rangle = \frac{1}{\sqrt{N_{odd}}}\sum_{j\ odd}|\pi_j^A\rangle|0\rangle. \tag{3.9}$$

The dynamics within this subspace then reduces to a simple two-level system dynamics:

$$\langle C_i|\hat{H}|C_j\rangle = \begin{pmatrix}\delta & g\sqrt{N_{odd}}\\ g\sqrt{N_{odd}} & 4V+2h_z\end{pmatrix} + const. \tag{3.10}$$

Kinetic terms for the mesons are order g^4 and thus neglected in this simple picture. Still from the two state model dynamics we can readily understand three important properties. (i) The non-local meson-polariton oscillations are collective, controlled by $G = g\sqrt{N}$, while the local dynamics is controlled by g. (ii) At resonance, $\delta = 4V + 2h_z$ there is a stronger hybridization giving rise to coherent Rabi oscillations. (iii) A local meson has a vanishing overlap $1/\sqrt{N_{odd}}$ with the collective states, thus limiting the amplitude of the Rabi oscillations.

[3] Note that the classical meson density is a good indication of the presence of a meson only when this is close to its classical configuration, i.e. when $\delta \gg g$

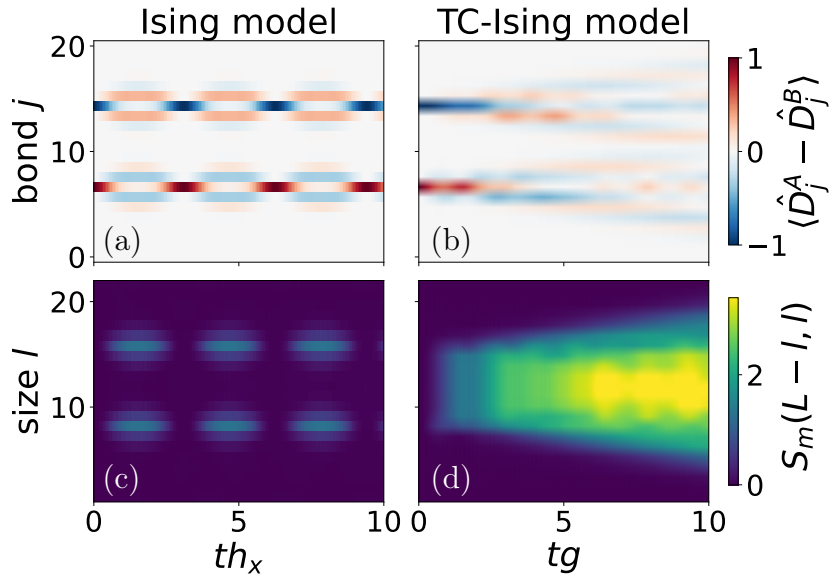


Figure 3.4.: String dynamics comparison between Ising model (a,c) and TC-ising model (b,d) obtained with TDVP. Top panels (a,b) show the domain wall density while the bottom panel (c,d) present the bipartite mutual information $S_m(L-l,l)$. In order to have comparable dynamics, we set $h_x = 0.1$ in the Ising case and $g = 0.1$ in the TC-Ising one with $\delta = 0.$; both cases have $V = 1$, $h_z = 0.2$ and $N = 23$.

3.5. String dynamics

In the context of confining LGT theories, an important role is played by *string* excitations, namely bound states of two distant elementary excitations. In the simple case of the Ising model, two distant domain walls feel a confining potential proportional to their separation r_0 and the longitudinal field h_z. This induces an exponentially slow dynamics $(h_x/h_z)^{r_0}$ due to the underlying locality of the LGT dynamics (represented by a local transverse field h_x). This phenomenology is lost in the TC-Ising model where, independently of r_0, distant domain walls can interact via the exchange of cavity photons. We illustrate this fundamental difference in Fig. 3.4 by direct comparison of the real-time evolution of a string in the two cases of Ising model (a,c) and TC-ising model (b,d), obtained via time-dependent variational principle (TDVP) simulations [177] (see SM of Ref. [3] for details). The domain wall density (top panels) clearly shows that in the local Ising case strings are effectively immobile, while in the TC-Ising case strings can have a finite kinetic energy, comparable to that of single domain walls (Fig. 3.2). In particular the process which allow for the motion of arbitrary length strings r_0 is the following:

$$|..\downarrow\overbrace{\uparrow\downarrow\uparrow\downarrow\uparrow\downarrow}^{r_0}\downarrow\uparrow\downarrow..\rangle\,|0\rangle \rightarrow |..\downarrow\uparrow\downarrow\overbrace{\downarrow\uparrow\downarrow\uparrow\downarrow}^{r_0-1}\downarrow\uparrow\downarrow..\rangle\,|1\rangle \rightarrow |..\downarrow\uparrow\downarrow\overbrace{\downarrow\uparrow\downarrow\uparrow\downarrow\uparrow}^{r_0}\uparrow\downarrow..\rangle\,|0\rangle \tag{3.11}$$

with a rate $J_s = g^2/(\delta \pm 2h_z)$ depending on whether the hopping is towards the direction where the type A domain wall is or not.

In order to confirm that the important emergent dynamical degree of freedom is the string and that single domain walls do not move independently, we calculate the mutual information (Fig 3.4(c,d)) between two subsystem of length l and $L-l$:

$$S_m(L-l,l) = S(\rho_{1..l}) + S(\rho_{l+1..L}) - S(\rho_c), \tag{3.12}$$

where $S(\rho_X)$ is the von Neumann entropy of a subsystem X being either the first l atoms, the last $L-l$ atoms or the cavity c. In the case of the Ising model this just reduces to twice the bipartite entanglement entropy. The important different feature distinguishing the Ising and TC-Ising case is the presence of a *plateau* already at early times ($t \lesssim 50$) when the bipartition length l varies along the string ($8 < l < 14$). This highlights the immediate build-up of long-range correlations between the two domain walls forming the end of the string, which then can move coherently as a single object via the exchange of virtual photons.

3.6. Experimental blueprint

The proposed experimental implementation uses ^{87}Rb atoms trapped in optical tweezers, though the model Hamiltonian and excitation scheme described above are applicable to a range of atomic species, including alkali [181] and alkaline-earth-like atoms [182]. Rydberg control is achieved via a two-photon excitation from the ground state $|g\rangle = \left|5S_{1/2}F = 2, m_F = -2\right\rangle$ to the Rydberg state $|r\rangle = \left|70S_{1/2}, J = 1/2, m_J = -1/2\right\rangle$ via an intermediate state $|e\rangle = \left|6P_{3/2}, F = 3, m_F = -3\right\rangle$ [151]. This transition is driven by circularly polarized lasers at wavelengths of 420 nm and 1013 nm, respectively, with an intermediate state detuning $\Delta \simeq 2\pi\times 0.5$ GHz. The set-up allows for a simple state preparation scheme of specific initial states (see SM of Ref. [3]).

The one-dimensional array of atoms is coupled to a bow-tie cavity that sustains two counter-propagating unidirectional modes, of opposite circular polarization. This configuration balances the requirements of strong cavity coupling, compatibility with Rydberg physics, and scalability to large atom arrays. The cavity design provides substantial optical access, enabling hundreds of optical tweezers for single-atom control while maintaining a large distance between the atoms and the dielectric surfaces of the mirrors, thereby mitigating stray charge effects on Rydberg atoms [183]. Importantly, this design also achieves small mode volumes, ensuring the strong cavity coupling essential for the proposed implementation [184].

Assuming a cavity waist (w_0) of 3 µm, a cavity length of 6.9 cm, a finesse of 50000 along with the measured decay rates and branching ratios of the $6P_{3/2}$ states [185], the cavity parameters are $\{g_0, \kappa, \Gamma\} = 2\pi \times \{800 \text{ kHz}, 20 \text{ kHz}, 1.35 \text{ MHz}\}$. Here, g_0 represents the on-resonance atom-cavity coupling, κ denotes the half-linewidth of the cavity, and Γ the full linewidth of the intermediate state. Notably, planar ring cavities with similar w_0/λ_c ratios have already been demonstrated for the same finesse [184].

In order to minimize off-resonant scattering from the intermediate state ($\Gamma\Omega^2/\Delta^2$) and maximize the two-photon transition strength ($g_0\Omega/\Delta$), we propose to operate the 1013 nm laser at a Rabi frequency $\Omega \simeq \Delta/10 \simeq 2\pi \times 50$ MHz. The total effective atom decay, which includes direct Rydberg decay $\Gamma_r = 2\pi \times 1.5$kHz, is estimated as $\gamma_{at}/g = [\Gamma_r + \Gamma(\Omega/\Delta)^2]/g = 0.18$. Togheter with a cavity photon loss rate $2\kappa/g = 0.5$, this justify the choice of studying the coherent dynamics up to $tg \lesssim 10$. As we discuss in detail in App. B.3, simple post-selection strategies which mitigate the effect of atom decay are likely needed. The effect of photon loss is not as severe due to small cavity population during the dynamics as investigated in App. B.2.

3.7. Conclusions

We have studied real-time dynamics of low energy excitations in a Tavis-Cumming-Ising model. This highlights the non-trivial interplay between local and non-local degree of freedoms, contrasted with usual locally interacting models. Real time and space resolved dynamics in particular is key to distinguish the degree of "locality" of the emergent composite excitations in the confined phase. We further expect new interesting physics arising also in the deconfined phase, where non-local interactions dominate from the start giving rise to an otherwise forbidden continuous $U(1)$ SSB in one dimension [138]. All these phenomena naturally arise in a simple combination of two well-developed quantum simulation platforms, Rydberg atom arrays [151, 175] and atomic cavity QED [24, 123]. Nonetheless, the physical ideas explored in such simple setting can be translated to other cavity embedded quantum many-body systems [9, 10, 12, 160], where local and non-local emergent quasi-particles coexist.

Chapter 4.

Topological protection of majorana-polaritons in a cavity

The principle of locality, broken by the non-locality of the cavity, is fundamental to the notion of topological protection. In this chapter we show that for symmetry protected topological states, exemplified by a 1D topological superconductor, the symmetry of light-matter coupling is essential for the resilience of topological properties in absence of locality. This adds a solid many-body understanding of topological states of matter in cavity-embedded systems, that will also be partly subject of Chapter 5.

4.1. Introduction

In recent years the possibility of controlling quantum matter by cavity embedding has attracted a lot of attention [9–12]. Strong coupling to cavity vacuum fluctuations has been predicted to affect material properties in many different contexts such as superconductivity [27, 28, 52], ferro-electricity [37, 38, 53] and topology [29, 30, 33, 129, 186]. It has been shown experimentally that cavity embedding can modify the critical temperature of a charge density wave transition [40], magneto-transport properties [41], and induce the breakdown of topological protection in integer quantum hall transport [43]. In this context, a single-particle electron-photon Chern number was introduced in Ref. [31]. Addressing topological properties with a global cavity mode is a subtle issue. As a general rule, the robustness of topological properties is ensured by the locality of perturbations. Coupling to a cavity is inherently non-local, and therefore, there is no guarantee that quantum fluctuations preserve topological protection. A contrasting argument in the context of Majorana fermions is that they bear no charge and therefore couple inefficiently to a cavity electric field [187] (see also Refs. [188–192] in the context of microwave resonators). Naive expectations relying on the weak effect of vacuum fluctuations of single-mode cavities on extensive quantities [68, 109, 110] should also be taken with care since topological edge states are intrinsically not extensive.

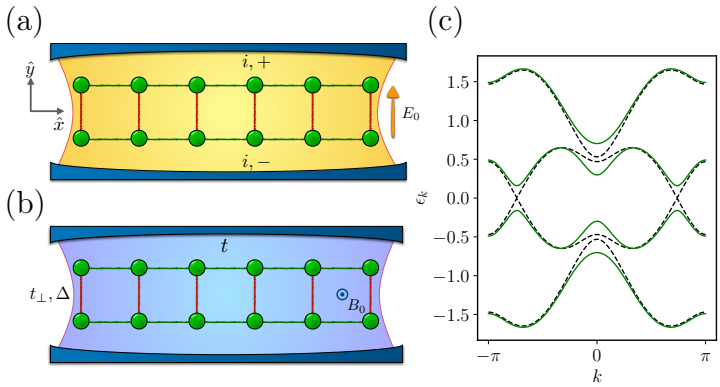


Figure 4.1.: Sketch of the two different cavity embeddings. The ladder couples either (a) to a quantized electric field, (b) a quantized magnetic field. (c) Band structure of the cavity-free Hamiltonian $\hat{H}_0$ with (full green line) and without (dashed black line) superconducting pairing.

In this chapter, we address this issue by studying a one-dimensional toy model of a topological superconductor [193, 194], featuring Majorana end states, strongly coupled to a single-mode cavity, and therefore interacting [195–198] via long-range forces. We discuss two models for the cavity, either with an electric field [41, 43] or a magnetic field coupling [88, 199, 200]. Both models respect the fermionic parity $\mathbb{Z}_2$ symmetry of the superconductor [193]. Our approach to studying these many-body topological properties is twofold. We first employ analytical arguments, based on quasi-adiabatic continuation approach [201, 202], to establish the resilience of the topological phase to the all-to-all interaction mediated by the cavity mode. The edge modes transform into Majorana polaritons [188] with a light component and are no longer purely fermionic objects. We also perform controlled Density Matrix Renormalization Group (DMRG) numerical simulations [89–91] with a mixed cavity-matter Matrix Product State (MPS) ansatz [1, 30, 50, 51] implementing the $\mathbb{Z}_2$ fermionic parity. We identify four markers for topological order [202–204]: (i) ground state degeneracy, (ii) entanglement spectrum degeneracy, (iii) non-local edge-edge correlations, and (iv) robustness to local symmetry-preserving perturbations (e.g. disorder), and demonstrate that they all survive strong cavity quantum fluctuations. We moreover confirm the hybrid nature of the dressed Majorana end operators. Our main finding is that the topological superconducting state is robust to the coupling to the cavity, by adapting its Majorana edge modes, as long as fermionic parity is preserved and no gap closing occurs upon gradually increasing the strength of cavity coupling. Additionally, Majorana in the absence of a cavity are strong edge modes [205] which commute with the Hamiltonian, imposing an exponential degeneracy in the full spectrum. In contrast, we find that they change into weak edge modes [201, 206, 207] and lose commutation with the Hamiltonian as they combine with light into composite polaritons. This restricts the exponential degeneracy to the ground state manifold.

The chapter is structured as follows: in Section 4.2, we introduce the toy model illus-

trating a topological superconductor and its coupling to the non-local cavity degree of freedom. Section 4.3 presents a comprehensive numerical analysis covering all relevant topological properties (i)-(iv). Following this, Section 4.4 applies the quasi-adiabatic continuation approach, crucial for understanding the resilience of Majorana fermions to non-local cavity fluctuations. In section 4.5, perturbative analytical expressions are derived highlighting the composite character of the Majorana polaritons. They are shown to be weak edge modes, localized for their fermionic part on the edges of the chain. Finally, in section 4.6 we draw general conclusions about the stability of Majorana Fermions to non-local cavity fluctuations and discuss possible extensions of our arguments to other topological states of matter.

4.2. The model

The starting point of our discussion is a tight-binding model for a one-dimensional topological superconductor. We employ a toy model of spinless electrons hopping on a square ladder geometry [1] in the presence of an external magnetic field and a superconducting pairing along the rung of the ladder. The Hamiltonian reads:

$$\begin{aligned}\hat{H}_0 = &- t\sum_{j=1}^{L-1} e^{i\sigma\phi_{ext}/2}\hat{c}^\dagger_{\sigma,j}\hat{c}_{\sigma,j+1} - t_\perp\sum_{j=1}^{L}\hat{c}^\dagger_{+,j}\hat{c}_{-,j} + \\ &+ \Delta\sum_{j=1}^{L}\hat{c}^\dagger_{+,j}\hat{c}^\dagger_{-,j} + \mu\sum_{\sigma,j=1}^{L}\hat{c}^\dagger_{j,\sigma}\hat{c}_{j,\sigma} + \text{h.c.}\ ,\end{aligned} \tag{4.1}$$

where Δ is the pairing strength, μ the chemical potential, t the intraleg hopping, $t_\perp$ the interleg hopping, ϕ_{ext} the external magnetic flux per plaquette and $\hat{c}_{j,\sigma}$ annihilates an electron on the leg $\sigma = \pm$ and rung $j = 1,..,L$ with $+$ is the top leg and L the number of rungs. While unconventional, this model can be straightforwardly mapped to the nanowire model [208, 209] with strong Rashba spin-orbit coupling and proximity-induced superconductivity, a system that has undergone extensive experimental investigation [210]. In the ten-fold non-interacting classification [211], the model Eq. (4.1) falls into class D, protected only by particle-hole symmetry. It has a $\mathbb{Z}_2$ topological invariant and allows for a topological phase with Majorana end states. However, within a many-body context, the true symmetry protecting the topological phase is fermionic parity.

We now add a single-mode cavity with the bare Hamiltonian $\hat{H}_c = \hbar\omega_c\hat{a}^\dagger\hat{a}$. In order to draw general conclusions, we examine two distinct physical realizations concerning the vector potential in the cavity: a constant magnetic (B) component along z or a constant electric (E) component along y (Fig 4.1). The light-matter coupling is achieved through a Peierls substitution [70, 72, 97, 212], where the hoppings are dressed

as (see App. C.1):

$$\text{B}: \quad \hat{c}^\dagger_{\sigma,j}\hat{c}_{\sigma,j+1} \to e^{ig_B(\hat{a}+\hat{a}^\dagger)}\hat{c}^\dagger_{\sigma,j}\hat{c}_{\sigma,j+1}\ , \tag{4.2}$$

$$\text{E}: \quad \hat{c}^\dagger_{+,j}\hat{c}_{-,j} \to e^{ig_E(\hat{a}+\hat{a}^\dagger)}\hat{c}^\dagger_{+,j}\hat{c}_{-,j}\ , \tag{4.3}$$

depending on the scenario. In the following discussion, when referring to both couplings, we will use g as a combined notation for g_E and g_B. The full Hamiltonian is $\hat{H} = \hat{H}_0 + \hat{H}_c$ with either the dressing of Eq. (4.2) or Eq. (4.3). We are interested in a mesoscopic regime and do not scale g with the system size. Our choice is motivated by the nature of strongly confined cavity modes in nanophotonics, such as split-ring resonators, where there are usually a few, energetically well-separated modes with a significant coupling to the electrons [43].

No-go theorems [68, 69] prevent photon condensation, *i.e.* a coherent non-zero $\langle\hat{a}\rangle$, for the electric field coupling, whereas $\langle\hat{a}\rangle \neq 0$ can emerge in the magnetic case [73–75]. In the latter case, the coherent part of the field simply renormalizes ϕ_{ext} and can potentially drive the system out of a topological state or vice-versa. Although very interesting, this effect does not come from quantum fluctuations and can described semiclassically [1]. We henceforth fix $\omega_c = t = t_\perp = -\mu = 1$, $\Delta = 0.4$ and $\phi_{ext} = 0.6889\pi$ such that $\langle\hat{a}\rangle$ remains close to zero and the fermionic chain is in a topological phase.

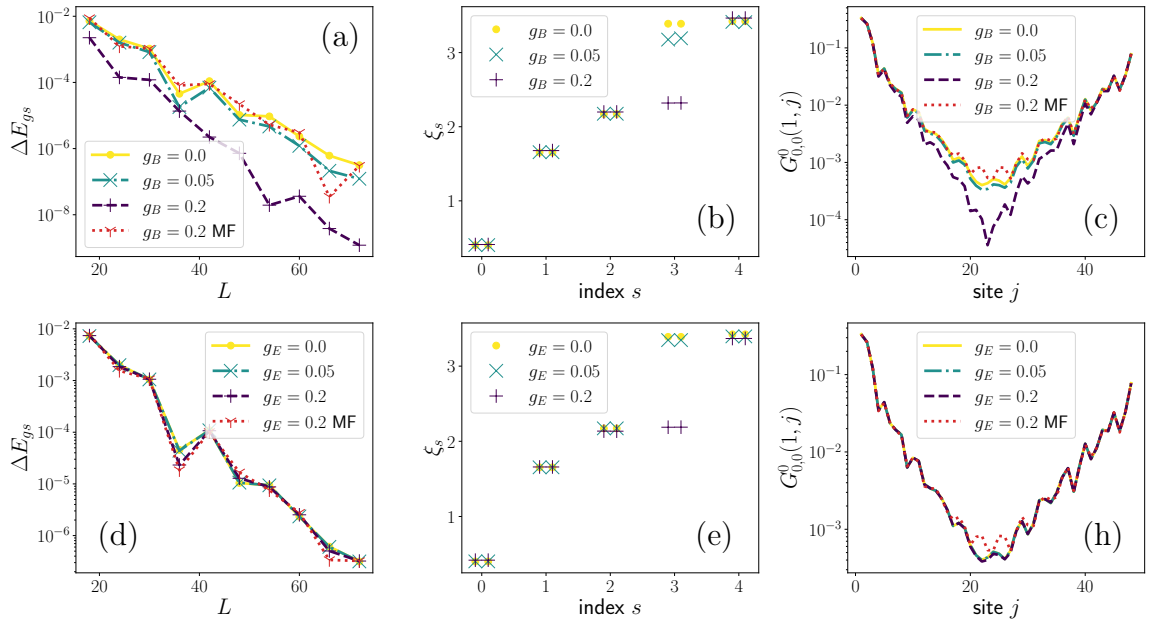


Figure 4.2.: The top (bottom) row shows DMRG results for the magnetic (electric) coupling. (a,d) Ground state energy splitting $\Delta E_{gs} = |E_0^{gs} - E_1^{gs}|$ for different coupling strength. The mean-field (MF) result is also shown for comparison. (b,e) Entanglement spectra $\xi_s = -\log\lambda_s$ for an half-chain bipartition of the ground state in the even parity sector. The twofold degeneracies come from $(even, even)$ and (odd, odd) parity resolved partitions. (c,f) Correlation function for the top leg of the ladder geometry. $L = 48$ except for (a,e)

4.3. Signatures of topology

We first present a detailed DMRG numerical investigation of the topological properties of the ground state of the Hamiltonian $\hat{H}$. We use a hybrid light-matter MPS in which the $\mathbb{Z}_2$ fermionic parity symmetry is implemented, separating the exponentially degenerate even and odd parity sectors. We specifically investigate the four markers, labeled (i)-(iv) in the introduction, as signatures of the topological phase.

The ground state degeneracy $\Delta E_{gs} = |E_0^{gs} - E_1^{gs}|$ is exponential with the system size up to relatively strong light-matter couplings g, confirming point (i). This is reported in Figs. 4.2(a,d) where the ground state energy difference between the two parity sectors is computed. For small g, this energy difference can also be evaluated using perturbation theory (see SM of Ref. [4]), confirming its exponential scaling. Interestingly we also report of few ground state parity switches [193, 213] as a function of g (not shown). The second signature (ii) is the twofold degeneracy in the entanglement spectrum of the half-chain bipartition. Differing from typical fermionic Hamiltonians, the coupling to the cavity introduces non-locality and a choice for where to park the cavity in a bipartition of the system. We use an alternative way of partitioning by tracing out the cavity field,

$$\hat{\rho}_{j>L/2} = Tr_{j<L/2}\left[\hat{\rho}_{matt}\right] = Tr_{j<L/2}\left[Tr_{ph}\left[|gs\rangle\langle gs|\right]\right] \tag{4.4}$$

where $|gs\rangle$ is the full many-body ground state, $\hat{\rho}_{matt}$ the reduced density matrix after tracing out the photons. $\hat{\rho}_{j>L/2}$ is obtained by further tracing out half of the chain. As shown in Fig. 4.2(b,f) the $g = 0$ twofold degeneracy is not broken at finite g. It can be checked to correspond to the two choices of parity for each half. The entanglement spectra are nonetheless changing with g, signaling the presence of finite light-matter entanglement.

Edge-edge correlations (iii) are shown in Fig. 4.2(c,g) where the correlator $G^p_{\sigma,\sigma'}(i,j) = \langle p|\, \hat{c}^\dagger_{\sigma,i}\hat{c}_{\sigma',j}\, |p\rangle$ is calculated on the ground state $|p\rangle$ with parity $p = \{0,1\}$. The revival on the opposite edge of the green's function reveals the presence of the two ends Majorana fermions that both permute the ground states and is essential to verify the non-local nature of the zero-energy mode.

We now verify (iv) by adding local disorder to the model. Without loss of generality, we consider a Gaussian distributed chemical potential, centered around μ, and with the standard deviation $\overline{\delta\mu_{\sigma,i}\delta\mu_{\sigma',j}} = W^2\delta_{i,j}\delta_{\sigma,\sigma'}$, where $\overline{\mathcal{A}}$ denotes the disorder average of $\mathcal{A}$. As an indicator for edge-edge correlations, we introduce the quantity

$$Q = \sum_{\sigma,\sigma'} |G^0_{\sigma,\sigma'}(1,L) - G^1_{\sigma,\sigma'}(1,L)|\ . \tag{4.5}$$

For $g = 0$, we have exactly $G^0_{\sigma,\sigma'}(1,L) = -G^1_{\sigma,\sigma'}(1,L)$ as a result of the anticommutation of the two Majorana fermions. In Fig. 4.3, we show the indicator Q and the ground state energy splitting ΔE_{gs} for one disorder realization at each disorder strength (Fig. 4.3(a,c)) and their disorder average (Fig. 4.3(b,d)). The results hardly depend on

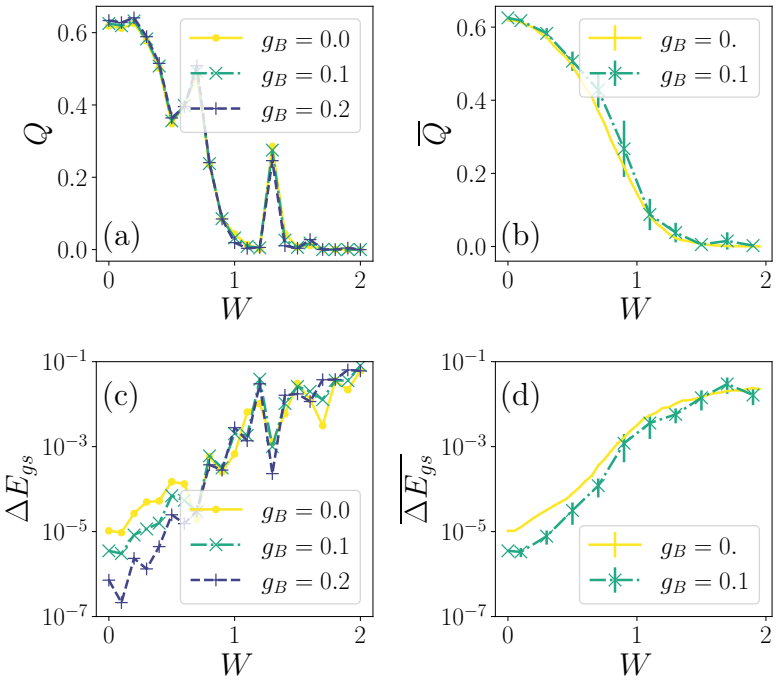


Figure 4.3.: Magnetic cavity: DMRG results ($g_B > 0$) and exact results ($g_B = 0$) for topological markers as a function of disorder strength W. (a) Edge-edge correlator Q from Eq. (4.5) and (c) ground state degeneracy ΔE_{gs} for a single disorder realization at each strength W. The corresponding disorder averaged quantities are shown in (b,d) with $N_{\text{dis}} = 20\,(1000)$ realizations for $g_B = 0.1\,(0.)$. Error bars indicate two standard deviations and $L = 48$.

the strength of cavity coupling, reflecting the robust topological phase. Interestingly, Kohn's theorem yields a different behavior in the quantum Hall effect, where disorder and cavity collaborate to diminish topological protection [128, 129, 186]. Here, disorder plays no role in enhancing the cavity effect on Majorana fermions.

4.4. Quasi-adiabatic continuation

In this section we present analytical arguments that elucidate the resilience of topological order to non-local cavity quantum fluctuations. In the absence of a cavity, the model exhibits Majorana edge modes in its topological phase. The Majorana fermionic operators $\hat{\gamma}_L^0$ and $\hat{\gamma}_R^0$ permute the even and odd parity sectors and protect the ground state (exponential) degeneracy. We employ the theory of quasi-adiabatic continuation [201, 202] to show that the Majorana operators

$$\hat{\gamma}_L = \mathcal{V}\hat{\gamma}_L^0\mathcal{V}^\dagger \qquad \hat{\gamma}_R = \mathcal{V}\hat{\gamma}_R^0\mathcal{V}^\dagger\,, \tag{4.6}$$

undergo a continuous transformation as the coupling to the cavity is gradually enhanced. The unitary operator $\mathcal{V}$ maps the ground state manifold in the absence of a

cavity to the one with the cavity. Importantly, under the assumption that the gradual increase of the cavity coupling maintains both the $\mathbb{Z}_2$ symmetry and a finite spectral gap, it can be shown (see App. C.3) that $\mathcal{V}$ preserves fermionic locality such that the two deformed Majorana modes remain localized on the two ends of the chain. In addition, $\hat{\gamma}_L$ and $\hat{\gamma}_R$ acquire a finite entanglement with the cavity mode $\hat{a}$ from Eq. (4.6) and a polaritonic character associated with photonic excitations. They also keep satisfying the Clifford algebra, as $\mathcal{V}$ is unitary, and they permute the even- and odd-parity ground states.

Aside from the deformed edge Majorana modes, we also need to prove the persistence of the ground state degeneracy. Denoting P_0 ($P = \mathcal{V}P_0\mathcal{V}^\dagger$) the projector onto the ground state manifold without (with) cavity, it is known that [193, 201]

$$P_0 \mathcal{O} P_0 = \lambda P_0, \tag{4.7}$$

up to exponential corrections with the system size. Here, $\mathcal{O}$ is a local $\mathbb{Z}_2$-symmetric operator and λ its eigenvalue in the ground state. Physically, Eq. (4.7) simply states that a local perturbation cannot distinguish the two ground states because of topological order. Applying Eq. (4.7) for $\mathcal{O} = \hat{H}_0$ recovers the ground state twofold degeneracy. $\mathcal{V}^\dagger \hat{H} \mathcal{V}$ is also local for fermions as $\mathcal{V}$ maintains locality. Therefore, we obtain that the even and odd parity states are still exponentially degenerate in the presence of the cavity, or

$$P\hat{H}P = \mathcal{V}P_0\mathcal{V}^\dagger \hat{H} \mathcal{V}P_0\mathcal{V}^\dagger = E_{gs}\mathcal{V}P_0\mathcal{V}^\dagger = E_{gs}P \tag{4.8}$$

where E_{gs} is the energy of the two ground states. Furthermore, with no cavity, $[\hat{\gamma}_\alpha^0, \hat{H}_0] = 0$ (up to exponential corrections), which implies that the twofold degeneracy extends to the whole spectrum and the Majorana operators are called strong edge modes [202, 205, 206]. Such a vanishing commutator is no longer guaranteed in the presence of the cavity, that is $[\hat{\gamma}_\alpha, \hat{H}] \neq 0$. The deformed $\hat{\gamma}_\alpha$ are then weak edge modes as they do not enforce a twofold degeneracy for excited states, only in the ground state manifold. We further elaborate on this point in the next Section.

In Fig. 4.4 we numerically test the absence of gap closing and the evidence of transition from strong to weak edge modes as the coupling to the cavity is increased. Note that the degeneracy is lifted for a state whose energy ($\epsilon_k \simeq 0.33$) is much detuned from the cavity frequency ($\omega_c = 1$). The fact that different type of couplings produce different splittings is expected on the basis of the difference in interaction matrix elements. The weakening of the edge modes could be related to the predicted [192] sensitivity of the cavity damping to the parity of excited electronic states. Moreover, the comparison with a mean-field approach (red lines) highlights the need for light-matter entanglement to quantitatively address strong coupling and the many-body nature of the spectrum (see the supplemetary material of Ref. [4] for details on the mean-field).

Remarkably, the above arguments based on the quasi-adiabatic continuation are very general. They show that any topological superconductor with Majorana end modes is

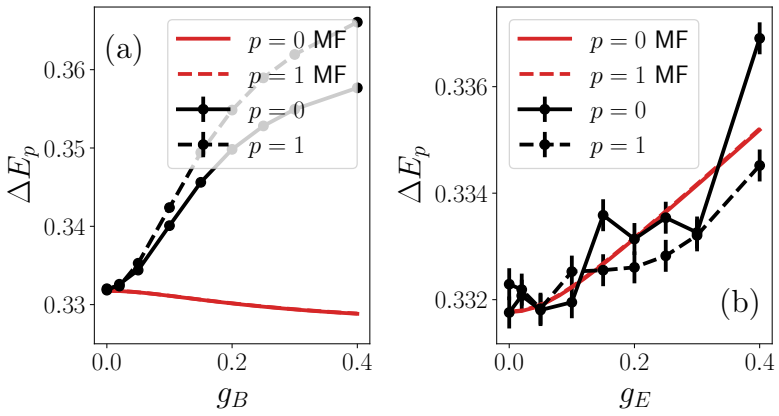


Figure 4.4.: Energy gap to the first excited state in the two parity sectors $p = 0$ (full lines) and $p = 1$ (dashed lines) calculated via DMRG. The red lines represent the mean-field predicted values of gaps. Panel (a) and (b) show respectively the result for the magnetic coupling and electric coupling. $L = 48$.

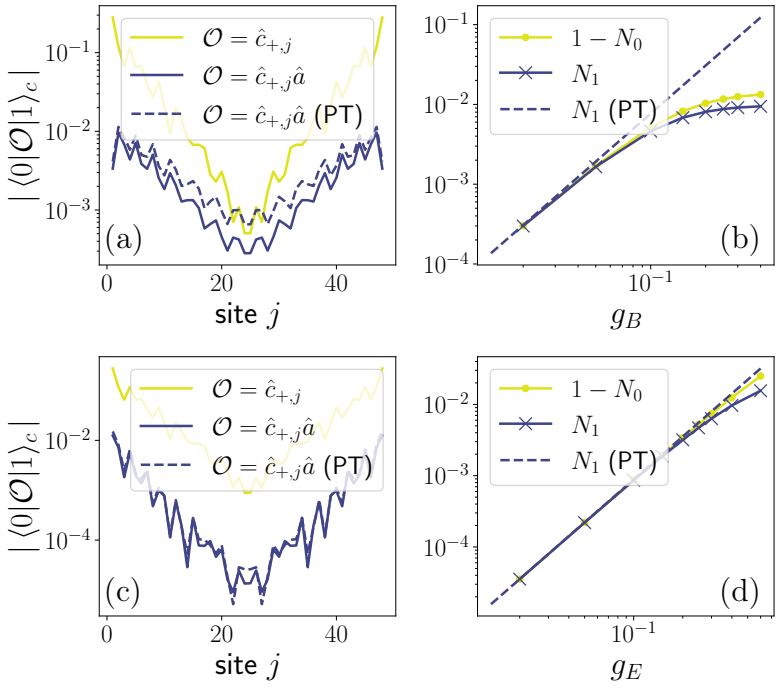


Figure 4.5.: (a,c) Connected matrix elements revealing the hybrid nature of Majorana polaritons for (a) magnetic coupling $g_B = 0.1$ and (c) electric coupling $g_E = 0.4$, with zero ($\mathcal{O} = \hat{c}_{+,j}$) and one photon ($\mathcal{O} = \hat{c}_{+,j}\hat{a}$). (b,d) Evolution of the total zero- and one-photon weights N_0 and N_1, Eq. (4.12), with light-matter coupling for the magnetic (b) and electric (d) cavities. Here $L = 48$.

robust to the presence of a non-local cavity, as long the coupling conserves parity ($\mathbb{Z}_2$) and there is an adiabatic path without gap closing to a cavity-free limit.

4.5. Majorana polaritons

In this section we discuss in more detail the composite light-matter nature of the edge modes. An explicit polaritonic form can be given to the Majorana fermions from Eq. (4.6) in perturbation theory

$$\hat{\gamma}_\alpha \simeq \hat{\gamma}^0_\alpha + \sum_{n=(\sigma,j)} \left(\Psi^{1+}_\alpha(n)\hat{c}^\dagger_n\hat{a}^\dagger + \Psi^{1-}_\alpha(n)\hat{c}_n\hat{a}^\dagger + \text{h.c.}\right) , \tag{4.9}$$

assuming weak coupling to the cavity. The wavefunction

$$\Psi^{1+}_\alpha = \psi^{1+}_\alpha + \phi^{1+}_\alpha = 2\sum_{\mu\neq 1} \frac{\lambda^\alpha_\mu u_{n,\mu}}{\epsilon_\mu + \omega_c} + 2\sum_{\mu\neq 1} \frac{\lambda^\alpha_\mu v^*_{n,\mu}}{\epsilon_\mu - \omega_c} \tag{4.10}$$

is obtained together with a similar expression for $\Psi^{1-}_\alpha(n)$ given in App. C.3. The coefficients λ^α_μ denote the projections of the perturbative cavity coupling onto the Bogoliubov modes diagonalizing Eq. (4.1) with energies ϵ_μ. $u_{n,\mu}$ and $v_{n,\mu}$ are the corresponding electron and hole components. The first term ψ^{1+}_α in Eq. (4.10) combines a photon creation with a Bogoliubov excitation whereas the second term (ϕ^{1+}_α) annihilates a Bogoliubov mode while still adding a photon. The second term ϕ^{1+}_α in Eq. (4.10) exhibits a divergence whenever the photon energy $\hbar\omega_c$ lies within the Bogoliubov spectrum and $\epsilon_{\mu_0} = \hbar\omega_c$ for a certain μ_0. As detailed in App. C.3, this divergence can be cured by excluding the mode μ_0 (along with modes with nearby energies) from the sum in Eq. (4.10) all the while preserving the properties of the quasi-adiabatic continuation detailed in Sec. 4.4. However, the Majorana polaritons then fail to commute with the Hamiltonian, $[\hat{\gamma}\alpha, \hat{H}] \neq 0$, and consequently transition into weak edge modes. Since ϕ^{1+}_α annihilates Bogoliubov modes, the commutation with the Hamiltonian persists within the ground state, explaining its robust twofold degeneracy. A perturbation analysis to higher orders reveals additional divergences occurring when $n\hbar\omega_c = \epsilon_{\mu_0}$, where n is the order of perturbation. These unavoidable divergences indicate that the Majorana composite polaritons consistently manifest as weak edge modes.

In order to test the locality of the Majorana polaritons, we evaluate the connected matrix element $\langle 0|\,\hat{c}_n\hat{a}\,|1\rangle_c = \langle 0|\,\hat{c}_n\hat{a}\,|1\rangle - \langle 0|\,\hat{a}\,|0\rangle\,\langle 0|\,\hat{c}_n\,|1\rangle$, given in perturbation theory by (see App. C.3) ($n = (\sigma, j)$)

$$\langle 0|\,\hat{c}_n\hat{a}\,|1\rangle_c \simeq \psi^{1+}_L(n) + i\psi^{1+}_R(n) . \tag{4.11}$$

Other combinations of $\psi^{1\pm}_\alpha(n)$ ($\alpha = L/R$) are obtained from the connected matrix elements of $\hat{c}_n\hat{a}^\dagger$,$\hat{c}^\dagger_n\hat{a}$ and $\hat{c}^\dagger_n\hat{a}^\dagger$ between $|0\rangle$ and $|1\rangle$. They are calculated using the MPS wavefunctions and are illustrated in Fig. 4.5(a,c).

Interestingly, these matrix elements all decay far from the edges and thus demonstrate both the resilient locality of the Majorana polaritons and their composite nature. We further quantify the photon mixing by introducing the weights of each component

of the Majorana polaritons:

$$N_0^\alpha = \sum_n |\psi_\alpha^0|^2 \qquad N_1^\alpha = \sum_n |\psi_\alpha^{1+}|^2 + |\psi_\alpha^{1-}|^2 \,, \tag{4.12}$$

where $N_0^R = N_0^L$ and $N_1^R = N_1^L$ by symmetry. $\psi_\alpha^0(n)$ denotes the purely electronic components of the Majorana operators. These weights can also be calculated in perturbation theory. Numerically, we use Eq. (4.11) to define the weights, the results are shown in Fig. 4.5(b,d). In order to quantify higher order corrections, we compare the weight missing from the purely electronic component N_0, with the weight in the single photon component N_1. As expected at low enough values of g they perfectly match the perturbation theory prediction, while at higher couplings one would need to take into account higher order corrections beyond Eq. (4.9). These are expected to involve multi-photon and multi-fermion operators which makes the Majorana-polariton expression more complicated; without breaking the quasi-adiabatic arguments given in section 4.4.

4.6. Conclusions

We have shown that a one-dimensional topological superconductor with Majorana end modes is protected against the vacuum quantum fluctuations of an embedding cavity mode, despite its long-range nature. The quasi-adiabatic approach explains this protection and reveals that Majorana evolves into Majorana-polaritons to maintain topological order. We confirm this with DMRG simulations where topological markers are shown to persist through the cavity coupling, and the photonic component of Majorana-polaritons is demonstrated up to strong cavity coupling. The main difference is that the Majorana-polaritons are no longer assured to be strong edge modes. Instead, they can transition into weak edge modes where only the ground state is doubly degenerate. In the strong cavity coupling regime, mean-field techniques prove to be insufficient, making it crucial to account for light-matter entanglement. Our argumentation is highly general and is applicable to any 1D phase featuring end Majorana states, regardless of the nature of the cavity coupling, electric or magnetic. Even though not explicitly discussed, the results can be straightforwardly generalized to multi-mode cavities. The crucial prerequisite however is the absence of fermionic parity breaking induced by the cavity coupling.

Our results suggest that a qubit using Majorana polaritons also requires control over the cavity due to their hybrid nature [31]. We also anticipate that the topological insensitivity to vacuum cavity fluctuations will extend to other topological phases [214], in higher dimensions. For instance, in 2D class A models, such as the quantum Hall effect, the topology is robustly protected by a many-body Chern number [215]. This does not contradict recent works where finite-size effect and disorder [26, 129] or coupling to external degrees of freedom [128] have been advocated to predict the loss

of conductance quantization observed experimentally [43]. It would be interesting to build a comprehensive classification of cavity-embedded fermionic models in the spirit of recent classifications of interacting models [196, 197].

Chapter 5.

Theory of Fractional Quantum Hall liquids coupled to quantum light and emergent graviton-polaritons

In this chapter we deepen the understanding on topological states coupled to global cavity-modes, focusing on the more challenging case of Fractional Quantum Hall liquids. These are fundamentally different from the symmetry-protected states discussed in the previous Chapter 4, as they display genuine topological order. Furthermore, as this is a system of high experimental relevance, we also focus on developing a detailed microscopic model for the light-matter coupling. This captures the importance of electric field gradients for the coupling between Lowest Landau Level electrons and the cavity degree of freedom. After discussing in details the physics of this scenario we comment on the recent experimental results [45] on enhanced Fractional Quantum Hall gaps in a split-ring resonator (Sec. 5.7.1).

5.1. Introduction

The possibility of controlling quantum matter properties via cavity embedding has sparked a lot of interest in recent years [9, 10, 12, 160]. Vacuum fluctuations of strongly confined electromagnetic modes have been proposed as handles on various phenomena [25, 26, 29, 33, 37, 38, 75, 86, 130, 216–222], and pioneering experiments have demonstrated the non-trivial role of cavity quantum electrodynamics (QED) set-ups in shaping matter properties [40–43, 45]. A particularly intriguing framework is that of topological phases, whose traditional many-body understanding faces fundamentally new questions due to the non-local nature of the cavity degree of freedom.

On this point, a recent breakthrough experiment [43] has shown that transport properties in the integer quantum Hall (IQH) regime can be affected by a split-ring cavity in the ultra-strong coupling regime, even in the absence of any driving. This effect has

been proposed to arise from cavity mediated hoppings [129] involving cyclotron transitions to higher Landau levels (LLs) assisted by vacuum photons or, more recently, as a consequence of cavity losses [128]. While significant progress has been made in the understanding of IQH states coupled to quantum light [26, 128, 129, 219], its effect on the much richer physics of fractional quantum Hall (FQH) matter [223, 224] remains largely unexplored.

Fundamentally different from its integer counterpart, the FQH effect [223] can only arise from genuine many-body correlations, responsible to lift the degeneracy in the partially filled Landau level and open a bulk gap. In FQH phases, new collective degrees of freedom emerge, such as the paradigmatic fractionally-charged anyonic quasiparticles [225], one of the smoking guns of topological order, and neutral magnetoroton modes [226, 227], also dubbed as gravitons [228] at long wavelengths given the link to a more recent geometric description of FQH correlations [229–237]. Another hallmark of topologically ordered phases is their peculiar many-body entanglement structure [238, 239], which naturally connects to their spectral properties and has proven to be a valuable tool for the classification of quantum phases of matter. In the face of this, it is tempting to ask what is the fate of such rich and profound phenomena under the action of quantum light?

In this chapter we address this question by putting forward a theory describing FQH liquids coupled to a cavity QED environment. The starting point of our analysis is a careful modeling of lowest Landau Level (LLL) electrons coupled to quantum light. In particular, we introduce a projected lowest Landau level (LLL) model written in the Dipole gauge and justified in terms of energy scale separation. This recovers the projected minimal coupling procedure of Ref. [72] with the addition of a novel vacuum-induced Stark shift effect, proportional to the local value of the cavity field fluctuations. This highlights the role of cavity field gradients which, in agreement with Kohn's theorem [240], are essential to non-trivially couple to electronic correlations within the LLL[241, 242].

As a proof of principle, we investigate a simplified scenario given by the $\nu = 1/3$ Laughlin state coupled to a cavity with a smoothly varying gradient (constant or linearly varying), and no losses. The setting is schematically depicted in Fig. 5.1(a). The full quantum dynamics of the system (light and matter) is studied numerically with a novel hybrid tensor network ansatz shown in Fig. 5.1(b) that combines the success in representing FQH states [243, 244] using matrix product states (MPS) [91, 92, 245], with cavity-matter correlations in 1D [1, 4, 36, 50]. This allows us to investigate in an unbiased way properties of both ground and low-energy excited states, using algorithms based on the density-matrix-renormalization group (DMRG) [89, 90] and on the time-dependent variational principle (TDVP) [246, 247]. Exact diagonalization (ED) is also used in order to test our findings.

We show that the topological properties of the Laughlin state remain stable against

the introduction of the non-local mode, as signaled by the quantized Hall resistivity, which we calculate by adapting the original flux insertion argument [248]. However, entanglement properties are drastically affected: the entanglement spectrum features different series of eigenvalues featuring typical $U(1)$ counting of FQH states [238], with each series corresponding to an approximately quantized value of the cavity photon, and with an inter-series separation that we denote as *polariton entanglement gap*. This reveals a collective coupling with matter excitations at zero transferred momenta which we also detect in spectral properties. These matter excitations are revealed to be gravitons, i.e., the long-wavelength part of the magnetoroton dispersion, and, once they hybridize with cavity photons, become graviton-polaritons. They give rise to a typical polariton doublet, which can be used in spectroscopy experiments as a smoking gun for the strong-coupling regime. Through a simple effective model that almost matches quantitatively with the finite-size numerical simulations, see Fig. 5.1(c), we also provide analytical predictions for the collective Rabi frequency in terms of the graviton quadrupole moment.

Another major consequence of the cavity mode on the ground state is the squeezing of the FQH metric [229], that is revealed by a striking change in the long-wavelength correlations and by the spatially anisotropic profile of electron correlation holes. Only in regimes where the cavity field gradients are strong at the single-particle level cavity-mediated interactions can drive an instability of the FQH liquid to a stripe phase, reminiscent of other transitions mediated by different anisotropy sources [249], accompanied by the softening of the full magnetoroton dispersion. However, before such transition occurs, spatially dependent cavity-induced vacuum Stark shifts become important and potentially generate phase separation. Their role in the FQH phase is to renormalize the energy cost of charged quasi-particles.

Summary of results.— Before describing the structure of the chapter, we summarize here our main findings:

- A microscopic QED theory describing the coupling of quantum light to electrons in the LLL, pointing out that the relevant light-matter coupling is expressed in terms of field gradients;
- Resilience of the quantized Hall resistivity upon the introduction of the non-local cavity-mode degree of freedom, with the latter imprinting an anisotropic FQH geometry in the ground state;
- A new entanglement structure in hybrid quantum Hall states, where the role of quantum light is to introduce a “band" of chiral Luttinger liquids multiplets, each with an approximately quantized photon number;
- The prediction of graviton-polariton modes, describing the hybridization of the typical magnetoroton mode with quantum light in the setup we consider;

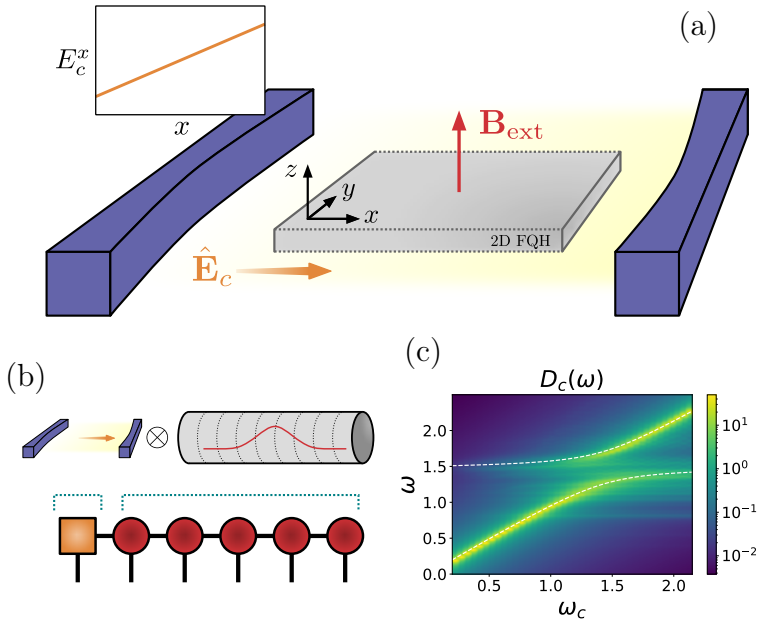


Figure 5.1.: (a) Illustration of the FQH bar placed inside the cavity. The electrons are confined to move in the 2D plane under the action of a perpendicular magnetic field $\boldsymbol{B}_{\text{ext}}$. The in-plane component of the cavity electric field pierces the principal edges of the strip perpendicularly. Periodic boundary conditions on y are depicted as dotted edges, while open boundary conditions on x are depicted as a sharp cut. The inset shows the mode profile with a uniform gradient used in most of the discussion. (b) MPS ansatz used to describe the hybrid light-matter system. Orange square represent the cavity degree of freedom while the red circles represent LLL electronic orbitals on a cylinder geometry. (c) Cavity density of states $D_c(\omega)$ as a function of cavity frequency ω_c revealing graviton-polaritons. Dashed lines represent an analytical effective model for the polariton frequencies with no fitting parameters.

- Cavity vacuum-induced Stark shifts for charged quasi-particle excitations, controlled by the same collective energy scale which controls the splitting of graviton-polaritons.

The chapter is organized as follows.

In Sec. 5.2 we describe the system under study, starting from a brief recap on LLs and the microscopic derivation of the LLL light-matter model based on energy scale separation between LL, ensuring a proper treatment of the ultra-strong coupling regime. We discuss the role of cavity field gradients, and detail the numerical methods we use to solve the full cavity-matter problem.

In Sec. 5.3 we present a detailed study of the nature of the FQH topological order in the presence of a strongly coupled non-local cavity degree of freedom. We do so by looking at two key markers, viz., the entanglement spectrum structure and the transverse Hall resistivity.

In Sec. 5.4 we investigate bulk spectral properties of the hybrid light-matter FQH

state. We start by reviewing the magnetoroton spectrum, i.e., the low-energy gapped neutral excitations on top of FQH states. Then we present numerical evidence for the effect of the cavity degree of freedom on the full magnetoroton dispersion, from the formation of the hybrid graviton-polariton to the lowering of the magnetoroton minimum. We then construct an effective model which builds on top of the Girvin-MacDonald-Platzman (GMP) treatment of magnetorotons, and is able to capture analytically the salient features of the graviton-polaritons that we observe numerically.

In Sec. 5.5, we extend our study of other ground state properties in the ultra-strong coupling regime. We first find that in the FQH phase strong cavity fluctuations can squeeze the emergent FQH geometry. Only at the single-particle strong coupling regime we find an instability towards a stripe phase, which however can be realized only if single-particle cavity-induced terms are compensated or neglected. By reintroducing them we show how vacuum-induced Stark shift are governed by a collective energy scale and, in the FQH phase, can renormalize the energy cost of charged quasi-particles.

In Sec. 5.6, we discuss the connection of our findings to realistic experimental scenarios taking as a reference a split-ring resonator [43]. While energy scales match, we highlight how carefully designed resonators with strong field gradients are needed to reach strong coupling to FQH physics. We also comment on the possible role of cavity screening of Coulomb interactions neglected in our treatment.

To conclude in Sec. 5.7, we summarize our results and draw a more general picture on how confined electromagnetic modes can be used to both probe and control correlations in the LLL.

5.2. The model

In this section we start by reviewing the LL physics (Sec. 5.2.1) and the split-ring cavity set-up (Sec. 5.2.2). In Sec. 5.2.3 we discuss the light-matter coupling in a full model without LL truncation. Then in Sec. 5.2.4 we present the first original result of this chapter, namely the derivation of a QED Hamiltonian for LLL electrons coupled to a cavity. After discussing some of the physical implications of the obtained model (Sec. 5.2.5), we spell out the full Hamiltonian used in the rest of the chapter (Sec. 5.2.6) and describe the MPS ansatz used to solve it (Sec. 5.2.7).

5.2.1. Landau levels

We consider a collection of N_e spinless electrons with mass m_e and elementary charge $q = |e|$ living on the (x, y) plane under a strong magnetic field $\boldsymbol{B}_{\text{ext}} = (0, 0, B)$ in the z-direction, Fig. 5.1(a), represented in the so called Landau gauge by an external vector potential $\boldsymbol{A}_{\text{ext}} = (0, xB, 0)$. We choose to work with periodic boundary conditions

along y, implying a cylinder geometry with a finite circumference L_y. The single-particle eigenstates can be written as [250]:

$$\psi_{k,n}(x,y) = \frac{1}{\sqrt{L_y}} e^{iky} \phi_n(x - X_k), \qquad k = \frac{2\pi}{L_y} j_k, \tag{5.1}$$

with $n = 0, 1, 2, ...$, being the LL index and $j_k \in \mathbb{Z}$ labeling the momentum along y. Here ϕ_n are eigenfunctions of the harmonic oscillator with characteristic length equal to the magnetic length $l_B = \sqrt{\frac{\hbar}{eB}}$, frequency equal to the cyclotron frequency $\omega_B = \frac{eB}{m_e}$, and centered around $X_k = k l_B^2$. In presence of an external potential W, which can account for both disorder and confining potential, the single-particle Hamiltonian in the LL basis takes the following general form:

$$\hat{\mathcal{H}}_0 = \sum_{n,k} \left(n + \frac{1}{2} \right) \omega_B \, \hat{n}_{k,n} + \sum_{k,k',n,n'} W_{k,k'}^{n,n'} \hat{c}_{k,n}^\dagger \hat{c}_{k',n'} \tag{5.2}$$

where $\hat{c}_{k,n}$ is the annihilation operator for the orbital (k,n), $\hat{n}_{k,n} = \hat{c}_{k,n}^\dagger \hat{c}_{k,n}$, and $W_{k,k'}^{n,n'}$ are the matrix elements of the external potential. Importantly, we focus on the LLL ($n = 0$) where the single-particle Hamiltonian then reads:

$$\hat{H}_0 = \hat{\Pi} \hat{\mathcal{H}}_0 \hat{\Pi} = \sum_{k,k'} W_{k,k'}^{0,0} \hat{c}_k^\dagger \hat{c}_{k'}, \tag{5.3}$$

where $\hat{\Pi}$ is a projector onto the LLL, and we dropped the LL index on the fermionic operator. In the following we are going to focus on $W = 0$, except when explicitly stated.

The other important ingredient are two-body interactions represented by a central potential $V(|\boldsymbol{r}_1 - \boldsymbol{r}_2|)$. In the continuum this read:

$$\begin{aligned} \hat{\mathcal{H}}_{int} = \int \mathrm{d}^2 \boldsymbol{r}_1 d^2 \boldsymbol{r}_2 \hat{\psi}^\dagger(\boldsymbol{r}_1) \hat{\psi}^\dagger(\boldsymbol{r}_2) \cdot \\ \cdot V(|\boldsymbol{r}_1 - \boldsymbol{r}_2|) \hat{\psi}(\boldsymbol{r}_2) \hat{\psi}(\boldsymbol{r}_1) \end{aligned} \tag{5.4}$$

with $\hat{\psi}(\boldsymbol{r}) = \sum_{k,n} \psi_{k,n}(\boldsymbol{r}) \hat{c}_{k,n}$. Neglecting LL mixing and projecting onto the LLL, the interaction term can be written as:

$$\hat{H}_{\text{int}} = \sum_{k_1,k_2,k_3,k_4} V_{k_1,k_2,k_3,k_4} \hat{c}_{k_1}^\dagger \hat{c}_{k_2}^\dagger \hat{c}_{k_3} \hat{c}_{k_4}, \tag{5.5}$$

where V_{k_1,k_2,k_3,k_4} are the matrix elements of $V(r)$ in the LLL. In order to keep the analysis simple, we adopt the first Haldane pseudopotential [251], i.e., the shortest range fermionic interaction, for which the Laughlin wavefunction is an exact zero-energy ground-state. Its matrix element on the cylinder are [251]:

$$\begin{aligned} V_{k_1,k_2,k_3,k_4} = V_0 \delta_{k_1+k_2}^{k_3+k_4} \frac{\sqrt{2\pi}}{L_y} \left[(k_1 - k_3)^2 - (k_2 - k_3)^2 \right] \\ \times e^{-\frac{1}{2}(k_1 - k_3)^2} e^{-\frac{1}{2}(k_2 - k_3)^2}, \end{aligned} \tag{5.6}$$

where the energy scale of the interaction is set to $V_0 = 1$, and the $1/L_y$ factor guarantees the interaction term to be extensive. In absence of disorder, both total number of particles $\hat{N} = \sum_k \hat{n}_k$ and total momentum along the y direction $\hat{K}_y = \sum_k k\,\hat{n}_k$ are conserved and can be fixed to N_e and K_y. We will consider a finite cylinder in the x direction by truncating in the orbital space, e.g., $j_k = -(M-1)/2, \ldots, (M-1)/2$. This give rise to a cylinder of circumference L_y and length in the OBC direction of $L_x = 2\pi M/L_y$. To fix the correct filling, we fix M with the condition $M = 3N_e - 2$. Such choice also guarantees a unique ground state at $K_y = 0$, which is the $\nu = 1/3$ Laughlin state.

5.2.2. Cavity set-up

We consider a single-mode cavity model, inspired by the split-ring resonator used in Ref. [43]. Other cavity resonances are expected to appear higher in energy and are thus going to be neglected. The split-ring mode can be understood in terms of an LC resonance [252, 253] at frequency $\omega_c = 1/\sqrt{LC}$, where L and C are the effective inductance and capacitance, respectively. By shrinking the capacitor region, one can reach impressive enhancement of the vacuum electric field fluctuations, and in some cases, enter the strong-coupling regimes, even at the single-electron level [254]. The free quantized Hamiltonian for the LC resonator can be written in terms of the electric and magnetic field energy density as:

$$\hat{H}_c = \int \mathrm{d}^3 r \left[\frac{\epsilon_0}{2} \hat{\boldsymbol{E}}_c^2 + \frac{1}{2\mu_0} (\boldsymbol{\nabla} \times \hat{\boldsymbol{A}}_c)^2 \right] = \omega_c \hat{a}^\dagger \hat{a}, \tag{5.7}$$

where $\hat{\boldsymbol{E}}_c$ is the electric field and $\hat{\boldsymbol{A}}_c$ is the vector potential.

In the region of interest, i.e., where the Hall bar is placed, these are expanded on a single quantized bosonic mode as:

$$\hat{\boldsymbol{A}}_c = A_c \boldsymbol{f}_c (\hat{a} + \hat{a}^\dagger), \tag{5.8}$$

$$\hat{\boldsymbol{E}}_c = i E_c \boldsymbol{f}_c (\hat{a} - \hat{a}^\dagger), \tag{5.9}$$

with $\boldsymbol{f}_c$ the dimensionless mode function. Here, we assume in fact to have a negligible cavity magnetic field component $\hat{\boldsymbol{B}}_c = \boldsymbol{\nabla} \times \hat{\boldsymbol{A}}_c \simeq 0$ implying $\boldsymbol{\nabla} \times \boldsymbol{f}_c \simeq 0$. The intensity of cavity vacuum fluctuations is:

$$E_c = \omega_c A_c = \sqrt{\hbar \omega_c / (2\epsilon_0 V_{\mathrm{mode}})} \tag{5.10}$$

and is expressed as a function of the effective mode volume V_{mode}. With this choice, we have $\int \mathrm{d}^3 r\, \boldsymbol{f}_c \cdot \boldsymbol{f}_c = V_{\mathrm{mode}}$.

We focus on the specific case of vanishing electric field component in the y direction and generic field along x. The in-plane part of the mode function can be written as:

$$\boldsymbol{f}_c^{\parallel}(\boldsymbol{r}) = f_c(x) \boldsymbol{u}_x, \tag{5.11}$$

with $f_c(x)$ being a generic function and $\boldsymbol{u}_x$ being the unit vector in the x direction. In the following we will also use a shorthand notation for the cavity field $E_c(x) = E_c f_c(x)$.

In the ideal case of infinite parallel mirror plates [252] living in the yz-plane, we have $f_c(x) = f_c$ independent of x. However, relevant field gradients are expected [43], and can be controlled to some extent. Note that the gradient of the cavity mode function in 3D is constrained by Gauss's law such that, in the case of an uniform dielectric within the capacitor plates, we have $\boldsymbol{\nabla} \cdot \boldsymbol{f}_c = 0$. This does not constrain the in-plane gradients which can indeed be finite. The split-ring set-up naturally implements an electric field perpendicular to the edges of the Hall bar [43], modeled here as the open edges of the cylinder in our configuration, Fig. 5.1(a). We remark that this particular choice of cavity configuration differs from that considered in Ref. [186] where the electric field is exactly parallel to edge of the system.

5.2.3. Quantum light-matter coupling

In the continuum model one can implement minimal substitution, $\hat{\boldsymbol{p}} \to \hat{\boldsymbol{p}} - e\hat{\boldsymbol{A}}_c$, as an unitary transformation $\hat{\mathcal{U}}$ [72]. In the case of purely electric field ($\nabla \times \hat{\boldsymbol{A}}_c \simeq 0$), the unitary operator $\hat{\mathcal{U}}$ depends on the cavity mode function via the cavity electric pseudopotential $\chi(\boldsymbol{r})$:

$$\chi(\boldsymbol{r}) = e \int_{\boldsymbol{r}_0}^{\boldsymbol{r}} \mathrm{d}\boldsymbol{r}' \cdot A_c \boldsymbol{f}_c(\boldsymbol{r}') \, . \tag{5.12}$$

which satisfies $\nabla\chi(\boldsymbol{r}) = eA_c\boldsymbol{f}_c(\boldsymbol{r})$. This allows us to define an unitary operator $\hat{\mathcal{U}}$ which implements the light-matter coupling:

$$\hat{\mathcal{U}} = \exp\left[i(\hat{a} + \hat{a}^\dagger)\hat{\mathcal{P}}\right] \, , \tag{5.13}$$

where $\hat{\mathcal{P}}$ is the polarization-like dimensionless electronic operator summarizing the coupling to the mode function (from now on, in short, polarization):

$$\hat{\mathcal{P}} = \int \mathrm{d}^2\boldsymbol{r} \, \chi(\boldsymbol{r}) \hat{\psi}^\dagger(\boldsymbol{r}) \hat{\psi}(\boldsymbol{r}) \, . \tag{5.14}$$

The so-called Coulomb gauge Hamiltonian can then obtained by applying the unitary $\hat{\mathcal{U}}$, which shifts the electronic momenta $\hat{\boldsymbol{p}} \to \hat{\boldsymbol{p}} - e\hat{\boldsymbol{A}}_c$, on the bare electron part:

$$\begin{aligned} \hat{\mathcal{H}}^{coul} &= \hat{\mathcal{U}}^\dagger \left(\hat{\mathcal{H}}_0 + \hat{\mathcal{H}}_{int}\right) \hat{\mathcal{U}} + \hat{H}_c = \\ &= \hat{\mathcal{H}}_0 + \hat{\mathcal{H}}_{int} + \hat{H}_c + \hat{\mathcal{H}}_{para} + \hat{\mathcal{H}}_{dia} \end{aligned} \tag{5.15}$$

with the light-matter coupling now expressed in terms of a paramagnetic and diamagnetic terms:

$$\hat{\mathcal{H}}_{para} = \int \mathrm{d}^2\boldsymbol{r} \hat{\psi}^\dagger(\boldsymbol{r}) \frac{e}{2m} \left(-i\nabla \cdot \hat{\boldsymbol{A}}_c - i\hat{\boldsymbol{A}}_c \cdot \nabla\right) \hat{\psi}(\boldsymbol{r}) \tag{5.16}$$

$$\hat{\mathcal{H}}_{dia} = \int \mathrm{d}^2\boldsymbol{r} \hat{\psi}^\dagger(\boldsymbol{r}) \frac{e^2}{2m} \left(\hat{\boldsymbol{A}}_c \cdot \hat{\boldsymbol{A}}_c\right) \hat{\psi}(\boldsymbol{r}) \tag{5.17}$$

Here the light-matter coupling is expressed via currents, hence momentum of electrons.

The Dipole gauge Hamiltonian can then be obtained by applying the inverse unitary transformation $\hat{\mathcal{T}} = \hat{\mathcal{U}}^\dagger$ [72], also known as Power-Zienau-Wolley (PZW), to the full Coulomb gauge Hamiltonian $\hat{\mathcal{H}}^{coul}$ (and not just to the bare electron part as done above):

$$\hat{\mathcal{H}}^{dip} = \hat{\mathcal{U}}\hat{\mathcal{H}}^{coul}\hat{\mathcal{U}}^\dagger = \hat{\mathcal{H}}_0 + \hat{\mathcal{H}}_{int} + \hat{\mathcal{U}}\hat{H}_c\hat{\mathcal{U}}^\dagger \tag{5.18}$$

$$= \hat{\mathcal{H}}_0 + \hat{\mathcal{H}}_{int} + \hat{H}_c + \hat{\mathcal{H}}_{DP} + \hat{\mathcal{H}}_{PP} \; ; \tag{5.19}$$

where the light-matter coupling is encoded in two new terms:

$$\hat{\mathcal{H}}_{DP} = i\omega_c(\hat{a} - \hat{a}^\dagger)\hat{\mathcal{P}} \tag{5.20}$$

$$\hat{\mathcal{H}}_{PP} = \omega_c\hat{\mathcal{P}}^2 \tag{5.21}$$

with the latter often referred to as self-polarization term. Here the light-matter coupling is expressed through the polarization (position) rather than through currents (momentum) of electrons as in the Coulomb Hamiltonian. We also remark that, despite the nomenclature, no dipole approximation ($\hat{\boldsymbol{E}}_c$ uniform) has to be performed. Indeed we can verify that the polarization operator carry information about all multipoles of the charge distribution. Expanding the cavity field up to first order around $\boldsymbol{r} = 0$ and substituting it into $\chi(r)$, we get:

$$\hat{\mathcal{P}} \simeq e\frac{E_c}{\omega_c}\boldsymbol{f}_c^{\parallel}(0) \cdot \int \mathrm{d}^2r \; \boldsymbol{r}\, \hat{\psi}^\dagger(\boldsymbol{r})\hat{\psi}(\boldsymbol{r}) + \tag{5.22}$$

$$+ e\frac{E_c}{\omega_c}\sum_{a,b}\left[\partial_a(\boldsymbol{f}_c^{\parallel}(0)\cdot\boldsymbol{u}_b)\right]\int \mathrm{d}^2r \; \frac{r_a r_b}{2}\, \hat{\psi}^\dagger(\boldsymbol{r})\hat{\psi}(\boldsymbol{r}) \; ,$$

where a and b run over $\{x, y\}$. This clearly includes both dipole (first line) and quadrupole (second line) contributions. In particular for a cavity mode as that of Eq. 5.11 only the $(a, b) = (x, x)$ contribution of the quadruople will contribute to the in-plane dynamics. Note that the the z direction is absent from the discussion as the well thickness is assumed to be infinitesimal.

In order to specialize to the case of Landau Levels we just need to expand the polarization operator on the single particle basis introduced in Sec. 5.2.1 as:

$$\hat{\mathcal{P}} = \sum_{k,k'}\sum_{n,n'} \chi_{k,k'}^{n,n'}\hat{c}_{k,n}^\dagger\hat{c}_{k',n'} \tag{5.23}$$

where the electric pseudopotential (or, equivalently, polarization) matrix elements are defined as:

$$\chi_{k,k'}^{n,n'} = \int \mathrm{d}^2r \; \psi_{k,n}^*(\boldsymbol{r})\, \chi(\boldsymbol{r})\, \psi_{k',n'}(\boldsymbol{r}) \; . \tag{5.24}$$

For our specific choice of cavity mode ($\boldsymbol{f}_c^{\parallel}(\boldsymbol{r}) = f_c(x)\boldsymbol{u}_x$) and neglecting second order

derivatives of the cavity field, we can write a more explicit expression:

$$\begin{aligned}\chi^{n,n'}_{k,k'} = &\frac{l_B}{\sqrt{2}}\chi'(X_k)\left[\sqrt{n}\delta_{n,n'+1} + (n \leftrightarrow n')\right]\delta_{k,k'} + \\ &+ \frac{l_B^2}{4}\chi''(X_k)\left[\sqrt{n(n-1)}\delta_{n,n'+2} + (n \leftrightarrow n')\right]\delta_{k,k'} + \\ &+ \left[\chi(X_k) + \frac{l_B^2}{4}\chi''(X_k)(2n+1)\right]\delta_{n,n'}\delta_{k,k'}. \end{aligned} \tag{5.25}$$

Here l_B is the magnetic length, X_k is the center of the orbital with momentum k, and χ' and χ'' represent the first and second order derivatives of the cavity electric pseudopotential, giving respectively dipole $\chi' \sim E_c$ and quadrupole $\chi'' \sim E_c'$ contributions. Higher order derivatives of the cavity field just give further cyclotron transition. There are in general two rather different kind of terms: *i)* those contained in the first two lines which drive inter-LL cyclotron transition; *ii)* those contained in the last one affect the intra-LL dynamics. In the rest of the discussion we are often going to shorten the notation of the LLL matrix elements of interest as $\chi^{0,0}_{k,k'} = \chi_k\delta_{k,k'}$.

We now want to remark that gauge transformations change the physical meaning of both cavity and matter operators. One should instead focus on physical observables, which are gauge invariant. For example, the cavity electric field is expressed differently in the two gauges:

$$\text{Coulomb}: \quad \hat{\boldsymbol{E}}_c = iE_c(\hat{a} - \hat{a}^\dagger)\boldsymbol{f}_c, \tag{5.26}$$

$$\text{Dipole}: \quad \hat{\boldsymbol{E}}_c = E_c\left[i(\hat{a} - \hat{a}^\dagger) - 2\hat{\mathcal{P}}\right]\boldsymbol{f}_c. \tag{5.27}$$

In this sense the no-go theorems [68, 69], which forbid a macroscopic coherent occupation of the cavity in the Coulomb gauge, constrain the groundstate coherent occupation in the Dipole gauge to be:

$$\langle\hat{a}\rangle_C = 0 \implies \langle\hat{a}\rangle_D = i\langle\hat{\mathcal{P}}\rangle_D, \tag{5.28}$$

where $\langle\dots\rangle_{C(D)}$ denotes the expectation value in the Coulomb (Dipole) gauge. We also note that there is an extra freedom in the choice of an overall constant in $\hat{\mathcal{P}}$, the origin of our system, which guarantees us that we can always find a basis where $\langle\hat{a}\rangle_D = 0$ also in the Dipole gauge.

5.2.4. LLL truncation

Simple LLL models have been incredibly succesful in describing FQH systems. This relies on the fact that at high magnetic fields B the cyclotron frequency $\omega_B \sim B$ dominates the interaction energy scale $V \sim e^2/\epsilon l_B \sim \sqrt{B}$ (Coulomb energy). Corrections in V/ω_B have also been extensively studied [255–257] and are often required for more quantitative comparison with experiments.

Performing a LLL truncation in the cavity QED set-up under consideration should however done with care. Truncations of light-matter interactions in ultra-strong coupling regimes have been shown to be problematic [66, 252]. In this regard, many efforts have been devoted to devising controlled, effective low-energy models for truncated electronic systems that are strongly coupled to quantized electromagnetic modes [70, 72].

Here we start from the single mode cavity QED model coupled to the full continuum of Landau Level electrons and perform a Lowest Landau Level truncation of the light-matter interaction terms based on controlled energy scale separation. As we will see, this procedure recovers results that can be obtained by a truncated minimal substitution prescription described in Ref. [72], up to a re-normalization of single particle terms. Numerical insights on the effect of the LLL truncation performed here can be found in App. D.1.

We first require a cavity frequency $\omega_c \ll \omega_B$, which is usually verified in the experimental situations under consideration [43]. Then also the light-matter interaction energy scale should be controlled. This however depends on the desciption we adopt, either Dipole or Coulomb, where the interaction is wrtitten in terms of different operators. In the Dipole gauge we have that cavity-mediated inter-LL transitions (see Eq. (5.25)) are controlled by the energy scale:

$$\epsilon_{lm}^{dip} \sim e l_B E_c \, . \tag{5.29}$$

Contrary, in the Coulomb gauge the light-matter coupling is expressed via the momentum of electrons (Eq. (5.16)) which carry a factor $1/m$ and hence a cyclotron frequency $\omega_B = eB/m$, leading to an energy scale for the light-matter interaction term of:

$$\epsilon_{lm}^{coul} \sim e l_B E_c \frac{\omega_B}{\omega_c} \, . \tag{5.30}$$

Even though the two energy scales are different we remind that the total Hamiltonians, before truncation, are equivalent up to global unitary transformations. It is clear however that performing a LLL truncation is more suitable in the Dipole gauge, where inter-LL matrix elements do not scale with ω_B. We also remark that at the theoretical level the LLL limit ($\omega_B = eB/m \to \infty$) should be taken with the mass of the electrons $m \to 0$ rather than with the magnetic field $B \to \infty$. This allows us to have a non-zero length scale for the system l_B which also controls other intra-LL matrix elements (see Eq. (5.25)).

Dipole gauge.— Given that ω_B dominates on all other terms in the Dipole gauge, we can directly truncate $\hat{\mathcal{H}}^{dip}$:

$$\hat{H}^{dip} = \hat{\Pi}_{LLL} \hat{\mathcal{H}}^{dip} \hat{\Pi}_{LLL} = \hat{H}_{int} + \hat{H}_c + \hat{H}_{DP} + \hat{H}_{PP} \, , \tag{5.31}$$

where in general we use $\hat{O}_\alpha = \hat{\Pi} \hat{\mathcal{O}}_\alpha \hat{\Pi}$ as a short notation for the LLL projected version of an operator. Equation (5.31) can be understood as the zeroth order expansion in

$1/\omega_B$ of the full model in Eq. (5.19), with neglected second order corrections akin to what usually happens for standard FQH systems [255, 257]. Expanding the two projected light-matter interaction terms we get the following form:

$$\hat{H}_{DP} = i\omega_c(\hat{a} + \hat{a}^\dagger)\hat{P} \tag{5.32}$$

$$\hat{H}_{PP} = \omega_c \hat{P}^2 + \sum_k \mu_k \hat{c}^\dagger_{k,0}\hat{c}_{k,0} \tag{5.33}$$

where $\hat{P} = \hat{\Pi}\hat{\mathcal{P}}\hat{\Pi}$ is the truncated polarization operator:

$$\hat{P} = \sum_k \chi^{0,0}_{k,k}\hat{c}^\dagger_{k,0}\hat{c}_{k,0} \ , \tag{5.34}$$

and μ_k a cavity mediated single particle potential:

$$\begin{aligned}\mu_k &= \omega_c \left(\chi^{0,1}_{k,k}\chi^{1,0}_{k,k} + \chi^{0,2}_{k,k}\chi^{2,0}_{k,k}\right) = \\ &= \frac{\left(el_B E_c(X_k)\right)^2}{2\omega_c} + \frac{\left(el_B^2 \partial_x E_c(X_k)\right)^2}{8\omega_c} \ .\end{aligned} \tag{5.35}$$

The structure of the light-matter interaction is then very similar to the one of the one of the full model (Eq. (5.20) and (5.21)) except for the single particle contribution μ_k in the self-polarization term which arises from the fact that:

$$\hat{\Pi}\,\hat{\mathcal{P}}^2\,\hat{\Pi} \neq \left(\hat{\Pi}\,\hat{\mathcal{P}}\,\hat{\Pi}\right)^2 \ . \tag{5.36}$$

As a general comment we note that this term is important only for inhomogenues cavity electric fields, reducing to a global energy shift in the homogeneous case. In the above equation we can clearly distinguish dipole and quadrupole contributions, with higher order missing because of the assumption of negligible higher order derivatives of the electric field.

From a physical perspective it is possible to understand this term as a renormalization of the LLL vacuum energy ($\frac{1}{2}\omega_B$) via a spatially dependent *depolarization shift* [258] of the cyclotron frequency. Another equivalent interpretation is via a spatial dependent renormalization of the electronic mass, which enters in $\omega_B = eB/m$. Given the dependence of this single particle term on local vacuum fluctuations of the cavity electric field and the dipole/quadrupole moment of the cyclotron transition, we dub it vacuum-induced Stark shift, in analogy with other well known Stark shifts effects in quantum optics.

Coulomb gauge.— As we discussed above, truncating in the Coulomb gauge is problematic because of the energy scale governing inter-LL transitions. However one can still define a *Coulomb gauge* Hamiltonian using a truncated unitary transformation [72]:

$$\hat{U} = \hat{\Pi}\,\hat{\mathcal{U}}\,\hat{\Pi} = \exp\left[i(\hat{a} + \hat{a}^\dagger)\sum_{k,k'} \chi^{0,0}_{k,k'}\hat{c}^\dagger_{k,0}\hat{c}_{k',0}\right] \tag{5.37}$$

to get:

$$\hat{\tilde{H}}^{coul} = \hat{U}\hat{H}^{dip}\hat{U}^\dagger = \tag{5.38}$$

$$= \hat{U}\left(\hat{H}_0 + \hat{H}_{int}\right)\hat{U}^\dagger + \hat{H}_c + \sum_k \mu_k \hat{c}_k^\dagger \hat{c}_k \tag{5.39}$$

Note that we have used a tilde on the coulomb gauge Hamiltonian to stress that it differs from a bare truncation of the full one $\hat{\tilde{H}}^{coul} \neq \hat{\Pi}\hat{\mathcal{H}}^{coul}\hat{\Pi}$. Interestingly the effect of the truncated unitary transformation $\hat{U}$ on LLL electron operators correspond to a simple Peierls phase dressing:

$$\hat{c}_k \to \hat{U}\hat{c}_k\hat{U}^\dagger = e^{i(\hat{a}+\hat{a}^\dagger)\chi_k}\hat{c}_k \,, \tag{5.40}$$

also found for tight-binding models [72].

5.2.5. Role of gradients

In a clean system, gradients are fundamental to couple the cavity field to electrons within the LLL. This is a consequence of the celebrated Kohn's theorem [240], whose corollary is that a uniform field can only couple to the cyclotron mode [128], generating transitions among different Landau levels. In view of that we now consider a further simplified cavity mode by considering a linear expansion $f_c(x) = C_0 + C_1 x$ and leave the discussion of more complicated modes for Sec. 5.6. For this particular shape of the mode function, the LLL matrix elements are:

$$\chi_k = \frac{eE_c}{\omega_c}\left(\frac{l_B^2}{4}C_1 + C_0(kl_B^2 - x_0) + \frac{1}{2}C_1(kl_B^2 - x_0)^2\right), \tag{5.41}$$

with x_0 the origin for the integration in Eq. (5.12). In the Coulomb gauge $\hat{\tilde{H}}^{coul}$, the matrix elements of the coupling can be readily understood by the dressing of $\hat{H}_{\text{int}}$ and $\hat{H}_0$. For the interaction term $\hat{H}_{\text{int}}$, we have that the four-body terms $\hat{c}_{k_1}^\dagger \hat{c}_{k_2}^\dagger \hat{c}_{k_3}\hat{c}_{k_4}$ get dressed with the following phase factor:

$$\exp\left[i(\hat{a}+\hat{a}^\dagger)(\chi_{k_1} + \chi_{k_2} - \chi_{k_3} - \chi_{k_4})\right]. \tag{5.42}$$

However, from momentum conservation along y, we have that $k_1 + k_2 = k_3 + k_4$, and for the explicit expression of χ_k the dressing phase can be written as:

$$\exp\left[i\frac{eE_cC_1l_B^4}{\omega_c}(\hat{a}+\hat{a}^\dagger)(k_1 - k_4)(k_4 - k_2)\right]. \tag{5.43}$$

The other important cavity-induced effect is the presence of a vacuum-induced Stark shift μ_k which, in the case of a simple gradient and up to overall constants, reads:

$$\mu_k = \frac{1}{\omega_c}\left[el_BE_c(C_0 + C_1kl_B^2)\right]^2 \tag{5.44}$$

At this point, we highlight two important properties:

- First, as anticipated from the Kohn's theorem [240], the constant part of the electric field (C_0) is decoupled;
- Second, an uniform gradient of the electric field generates a uniform light-matter coupling plus a non-uniform single particle potential.

The latter follows by the fact that in Eq. (5.43) only differences in momenta, hence relative distance on x, appear. Alternatively, when sticking to the dipole gauge formulation, one can see that, single-particle potentials aside, the constant part of the field (C_0) only couples to conserved quantities, such as the number of electrons and momentum along y. In contrast, the gradient (C_1) couples to the xx-component of the quadrupole moment operator, $\hat{Q}^{xx} \propto \sum_{kk'} \int \mathrm{d}^2 r\, x^2 \psi_k^*(\boldsymbol{r})\psi_{k'}(\boldsymbol{r})\hat{c}_k^\dagger \hat{c}_{k'}$, associated to electrons in the LLL [242].

Another way to avoid Kohn's restriction and actually couple the LLL to a constant electric field is via the presence of an external potential for the electrons. Either a confining potential [259] or disorder will do the job, realizing however quite different scenarios. A confining potential on x will have a dominant effect at the edges where its variation are stronger while disorder will contribute to bulk properties [260]. These effects can be important in actual experimental realization but go beyond the scope of this thesis.

5.2.6. Hamiltonian

In order to better understand the many-body physics at play we will first study the effect of cavity mediated interactions (χ_k) and only later reintroduce cavity induced single particle potentials (μ_k). We will thus label the model Hamiltonians according to the terms present in it, $\hat{H}_\chi$ and $\hat{H}_{\chi,\mu}$ for generic cavity modes $f_c(x)$.

In particular we first focus on the effect of uniform electric field gradients by choosing $f_c(x) = C_0 + C_1 x$ and setting both cavity vacuum-induced Stark shifts (μ_k) and other external potentials (W), or equivalently their sum, to zero. We choose to work in the Dipole gauge where the toy model Hamiltonian reads:

$$\begin{aligned}\hat{H}_\chi = \hat{H}_{\mathrm{int}} + \omega_c \hat{a}^\dagger \hat{a} + i\omega_c g(\hat{a} - \hat{a}^\dagger) \sum_k \Big(\frac{k^2}{2} - \kappa_0\Big)\hat{n}_k \\ + \omega_c g^2 \Big[\sum_k \Big(\frac{k^2}{2} - \kappa_0\Big)\hat{n}_k\Big]^2,\end{aligned} \tag{5.45}$$

with $\hat{H}_{\mathrm{int}}$ the interaction Hamiltonian for the first Haldane pseudopotentials, Eq. (5.5), κ_0 the overall constant in the definition of χ_k related to the choice of origin, and

$$g = \frac{eC_1 E_c l_B^2}{\omega_c} \tag{5.46}$$

a dimensionless coupling constant proportional to the electric field gradient $\partial_x E_c(x) = E_c C_1$. The energy scale of the interaction and the magnetic length are all set to unity, $V_0 = l_B = 1$, and $\omega_c = 1$, unless specified otherwise. The latter choice is motivated by the fact that we need to focus on a limited parameter space, and is not related to any fine tuning.

For a more direct comparison of different cavity frequencies ω_c, we will sometimes rescale the coupling g and use $g\sqrt{\omega_c}$ as a tuning parameter for the light-matter coupling. This choice indeed guarantees that, following Eq. (5.10) and Eq. (5.46), the coupling $(g\sqrt{\omega_c})$ does not carry hidden dependencies on ω_c, but only depends on the magnetic length l_B and the cavity mode via its overall effective volume and its spatial variations. In Sec. 5.4.3 it will also become clear that this choice guarantees a fixed physical Rabi coupling between gravitons and cavity photons (see Eq. (5.75)).

We are now going to reintroduce the cavity induced potential μ_k, although for a slightly different profile of the cavity electric field which keeps inversion symmetry $x \to -x$. Inspired by the cavity field reported in Ref. [43], we choose a parabolic profile $f_c(x) = C_0 + \frac{1}{2}C_2 x^2$. In this case, to allow for a direct comparison with the uniform gradient case, we will require $|\partial_x E_c(x)| \in [0, 2g]$ between $x \in [-\frac{L_x}{2}, \frac{L_x}{2}]$ and $E_c(\pm L_x/2) = E_c(0)$, obtained by fixing $C_2 = g/(L_x/2)$ and $C_0 = \frac{1}{2}C_2(L_x/2)^2$. Within this choice, the Hamiltonian can be written as:

$$\hat{H}_{\chi,\mu} = \hat{H}_\chi + \frac{\omega_c g^2 L_x^2}{16} \sum_k \hat{n}_k \left[1 + \left(\frac{k}{L_x/2}\right)^2\right]^2 + const \tag{5.47}$$

where now χ_k is changed accordingly to the new mode function.

The single-particle term above is in fact exactly the same found in cold atom gases trapped by optimal means: there, the microscopic reason for such spatially dependent Stark shifts stems from a finite waist of the lattice laser beam. As in the latter physical setting, getting rid of this term seems challenging: however, owing to its simple functional form, it is relatively easier to understand their physical effects. We can then borrow a considerable understanding on how these terms affect the system dynamics from the abundant cold atom literature on the topic.

In particular, the above mentioned terms have long been investigate in the context of the local density approximation (LDA), which describes a given physical system as a collection of subsystems, each one at its own value of the effective local potential μ. Such approximation works particularly well in the presence of incompressible phases: those occupy finite region of each sample, and are by definition stable to local potentials (even more so if their nature is topological). A paradigmatic example of the relevance and validity of such approximation is the observation of Mott insulator phases with cold atoms in optical lattices [261], characterized by typical wedding-cake like structures [262]. A comprehensive review of such phenomenology for the specific case of fractional quantum Hall states is presented in Ref. [263], and additional methods to exploit space dependent structures are described in Ref. [264]. Based on the

arguments reported above and extensively review in literature [263, 265], below, we will focus most of our ground state analysis on $\hat{H}_\chi$, and present a further discussion on the effects of μ in Sec. 5.5.3 and App. D.1.

Observables. - We also introduce some relevant observables that we use throughout the chapter. The expressions we provide below are valid for the Dipole gauge, where cavity operators are dressed rather than matter ones. First, we have the real-space charge density:

$$\hat{n}(x) = \frac{1}{L_y}\sum_k \hat{n}_k |\phi_0(x - X_k)|^2, \tag{5.48}$$

which is independent on the position y because of the translational invariance. In order to get information about correlations in the y direction we use the density-density correlations from the two-particle correlator $G^{(2)}$ defined as:

$$G^{(2)}(\boldsymbol{r}_1, \boldsymbol{r}_2) = \langle \hat{\psi}^\dagger(\boldsymbol{r}_1)\hat{\psi}^\dagger(\boldsymbol{r}_2)\hat{\psi}(\boldsymbol{r}_2)\hat{\psi}(\boldsymbol{r}_1)\rangle. \tag{5.49}$$

Another important quantity is the guiding center density operator [226, 266], which in second quantization reads:

$$\hat{\bar{\rho}}(\boldsymbol{q}) = \frac{1}{M} e^{-iq_x q_y/2} \sum_k e^{-iq_x k} \hat{c}_k^\dagger \hat{c}_{k+q_y}. \tag{5.50}$$

From this we define the connected guiding center static structure factor:

$$S(\boldsymbol{q}) = \langle \mathrm{GS}| \, \delta\hat{\bar{\rho}}(-\boldsymbol{q})\delta\hat{\bar{\rho}}(\boldsymbol{q}) \, |\mathrm{GS}\rangle \,, \tag{5.51}$$

with $\delta\hat{\bar{\rho}} = \hat{\bar{\rho}} - \langle \mathrm{GS}| \, \hat{\bar{\rho}} \, |\mathrm{GS}\rangle$, and its dynamical counterpart:

$$\begin{aligned} S(\omega, \boldsymbol{q}) = &\frac{1}{M}\sum_n |\, \langle n| \, \delta\hat{\bar{\rho}}(\boldsymbol{q}) \, |\mathrm{GS}\rangle \, |^2 \delta_\eta(\omega - E_n + E_{\mathrm{GS}}) \\ &- \{\omega \to -\omega\}, \end{aligned} \tag{5.52}$$

with $|n\rangle$ being a many-body eigenstate with energy E_n, and η being a broadening parameter that should be sent to zero. Regarding the cavity, we use its density of states as a way to probe polaritons at finite frequency:

$$\begin{aligned} D_c(\omega) = &\sum_n |\, \langle n| \, \hat{a}^\dagger \, |\mathrm{GS}\rangle \, |^2 \delta_\eta(\omega - E_n + E_{\mathrm{GS}}) \\ &- \sum_n |\, \langle n| \, \hat{a} \, |\mathrm{GS}\rangle \, |^2 \delta_\eta(\omega + E_n - E_{\mathrm{GS}}), \end{aligned} \tag{5.53}$$

which can be obtained from the retarded cavity Green's function as $D_c(\omega) = -\frac{1}{\pi}\mathrm{Im}\, G_c^R(\omega)$, with $G_c^R(t) = i\theta(t)\langle[\hat{a}(t), \hat{a}^\dagger(0)]\rangle$. We remark that in the ultra-strong coupling regime a precise calculation for the outcome of transmission/reflection experiments should also take into account anomalous correlations [267, 268] and use the gauge invariant electric field, rather than the gauge dependent cavity operator $\hat{a}$ [269]. We leave these refinements for a future work.

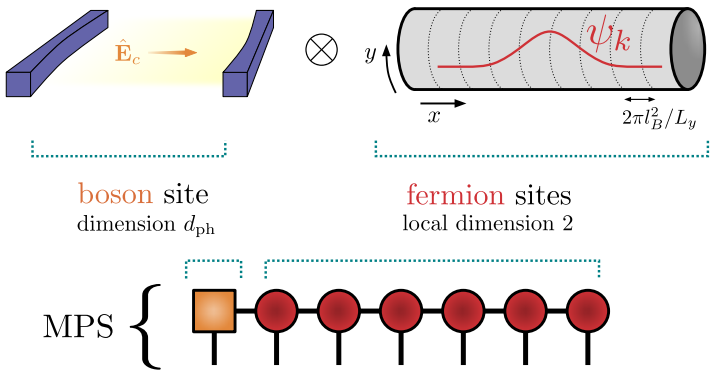


Figure 5.2.: Cartoon for the hybrid MPS ansatz. The cavity photon is placed at the first site of the MPS, while the rest of the MPS sites represent the LLL wavefunctions ψ_k. Each electronic site (red circles) represent an orbital k of the LLL with $k = 2\pi j_k/L_y$ and $j_k = -(M-1)/2, \ldots, (M-1)/2$.

5.2.7. Numerical methods

In order to study the strongly-coupled light-matter system, we perform DMRG simulations for the ground state, and a combination of TDVP and ED for spectral functions. DMRG methods have been extensively used in the context of FQH systems to find the ground state of microscopic Hamiltonians in an unbiased way [243, 270, 271]. The cylinder geometry, in particular, allows for a very direct mapping of the LLL orbitals spanned by a single quantum number k to a quasi-1D chain with long range interactions. Each electronic orbital k is mapped onto a different MPS site, keeping track of both momentum and charge quantum numbers. In the case of the first Haldane pseudopotential the range is finite and depends on the circumference of the cylinder $O(L_y)$. The price to pay in order to use a 1D MPS ansatz is twofold: (i) The MPO representation of the interaction Hamiltonian requires a large bond dimension; and (ii) the MPS bond dimension needs to grow exponentially with L_y.

Hybrid MPS ansatz

Here we introduce a hybrid cavity-matter finite MPS ansatz where the photon is placed at the beginning of the MPS, Fig. 5.2, also used in Refs. [1, 4, 36, 50]. Empirically we observed that this MPS ansatz is still efficient enough in representing the non-local correlations of the cavity mode, provided that the bond dimension m is large enough. On a more speculative ground, we also argue that a single collective state, crucial in carrying light-matter correlations, can be represented as a finite bond dimension MPS. Thus adding a few of these collective states only results in a finite computational cost. The light-matter interactions are also easy to represent as an MPO due to their infinite range nature [105]. Here the choice of the Dipole gauge is actually important to avoid the dressing of the 4-body operators in the only matter part, which can become quite expensive, differently from the dressing of 2-body operators [1]. Moreover

we make use of the freedom in the choice for the overall constant in the light-matter matrix elements κ_0, Eq. (5.45), such that the constraint given in Eq. (5.28) gives zero coherent occupation of the photon $\langle \hat{a} \rangle_D = 0$. This guarantees a good convergence with the truncation of the cavity Hilbert space at $d_{\text{ph}} = 64$. Note that the total number of electrons and total momentum along y are still good quantum numbers that we conserve in our simulations. We limit the bond dimension of the MPS up to $m = 1600$ which allows us to keep the truncation error always below 10^{-6}.

Apart from ground state properties via DMRG, we also investigate excited states and dynamical properties using different methods. Regarding the excited states, it is possible to directly get good results from the local effective Hamiltonians constructed during DMRG runs, as discussed in Ref. [272]. In particular, local targeting of the excited states has been found to be quite accurate for critical systems in 1D [272], whose success owes to the delocalized nature of the low-lying spectrum. As discussed in more depth in Sec. 5.4.2, we find that this method gives good qualitative results and is even able to capture mixed light-matter polariton states (see Appendix D.6 for more details on convergence). We further study dynamical properties via time evolution with TDVP (two-site updates), or directly using Lanczos methods in ED [273]. For these TDVP runs we limit the bond dimension of the MPS to $m = 200$ which still guarantees good convergence for small circumferences at a reduced computational cost.

Interestingly, the TDVP algorithm can also be used to implement change of gauges via the unitary $\hat{U}$. In particular we divide $\hat{U}$ in many steps and apply them sequentially as commonly done in TDVP evolutions. The "Hamiltonian" of this gauge change is:

$$\hat{h}_{\text{gauge}} = (\hat{a} + \hat{a}^\dagger) \sum_k \chi_k \hat{n}_k, \tag{5.54}$$

so that:

$$\hat{U} = \exp\left(-i\hat{h}_{\text{gauge}}\right), \tag{5.55}$$

and, in this units, the evolution time is $\tau = 1$. The fact that the MPS representation of the many-body ground state in a different gauge remains efficiently compressible (i.e., with a small enough bond dimension) is not guaranteed a priori and has to be checked. We find this to be the case in the FQH phase. During the change of gauge we keep the bond dimension of the MPS constant.

5.3. Topological order in cavity

The presence of a genuine non-local degree of freedom makes the present setting not immediately classifiable within the framework of topological phases of matter. In the context of cavity mediated topology, a lot of attention has been dedicated to regimes where the cavity degree of freedom can be integrated out, both in the quantum materials context [29, 33, 129, 274] and in cold atom set-ups [162, 275–277]. Integrating out

the non-local mode generally produces effective long-range interactions which simplify the picture of a mixed cavity-matter system and require the inspection of a matter-only model. This neglects by construction light-matter entanglement and gives a direct interpretation of cavity mediated topology in terms of "standard" topology.

Here, we are interested in the opposite situation, where light-matter entanglement cannot be neglected – and, as we show below, does carry key signatures of topological order.

Few works [4, 31, 32, 214] have recently investigated the questions above in the context of symmetry protected topological (SPT) phases. In particular, Ref. [4] pointed out that, in the case of Majorana fermions, respecting the symmetry that protects the topology is fundamental. The FQH effect instead belongs to a fundamentally different set of topological states which display topological order – that is, where order is intrinsically related to emergent gauge theories and entanglement. Addressing the interplay of topological order and quantum light is thus a completely distinct challenge with respect to the above mentioned SPTs.

As a paradigm of FQH, we are going to study the effect of the non-local cavity degree of freedom on the topological properties of a $\nu = 1/3$ Laughlin state. In particular we focus on two markers, first on the Hall resistivity (Sec. 5.3.1) and second on the entanglement properties (Sec. 5.3.2). They represent two key aspects of topological order: quantization of transport properties, and fingerprints in the entanglement structure of the state. A final discussion on the resilience of topological properties is given at the end of the section. Throughout this section we are going to neglect single particle terms and use the toy model hamiltonian $\hat{H}_\chi$ (Eq. (5.45)).

5.3.1. Hall resistivity via flux insertion

A key feature of the FQH effect is the fractionally quantized transverse resistivity ρ_{xy}. An easy way to probe this quantity numerically on the cylinder geometry is via the so-called adiabatic flux insertion [248, 278], sketched in Fig. 5.3(a). In the following we derive independently an expression that links the the transverse bulk resistivity to the density at a certain position.

Let us now consider the adiabatic insertion of a single magnetic flux quanta $\Phi_0 = 2\pi\hbar/e$ in the cylinder over a time τ. This process can be described by a uniform time-dependent vector potential $\boldsymbol{A}_p(t) = \frac{\Phi_0}{L_y}\frac{t}{\tau}\boldsymbol{u}_y$, so that $\Phi(t) = \Phi_0 t/\tau$. The vector potential $\boldsymbol{A}_p(t)$, in turn, generates an electric field $\boldsymbol{E}_p = -\partial_t \boldsymbol{A}_p = -\frac{\Phi_0}{\tau L_y}\boldsymbol{u}_y$, which is constant in time, and directed towards the y direction. Hence, we can find the Hall resistivity by calculating the current $\hat{J}_x = \hat{\boldsymbol{J}} \cdot \boldsymbol{u}_x$ flowing transversely to the electric field $\boldsymbol{E}_p$. Since our system is homogeneous in the y-direction, but not along the x-direction, the result

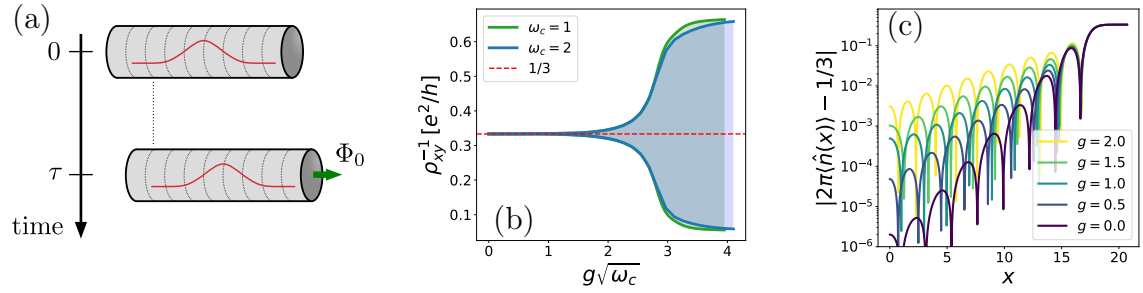


Figure 5.3.: (a) Sketch of the adiabatic flux insertion; as a unit of time τ passes a unit of flux Φ_0 is inserted resulting in relative shift in position of the cylinder along x. (b) Inverse resistivity in the bulk as measured by the density (Eq. (5.62)) with a shaded area representing the values it takes for $x_0 \in [-2, 2]$ and quantized value $\rho_{xy}^{-1} = 1/3$ as a dashed red line. At strong cavity field gradients g the quantization is lost because of strong bulk density oscillations (see Sec. 5.5.2). (c) Exponential decay from the edge of density modulations $\hat{n}(x)$ around the bulk quantized value. $x = 0$ is the center of the cylinder while $x = 20$ is already outside of it. Obtained via DMRG at system size $(L_y, N_e) = (14, 25)$ in (b) and $(16, 30)$ in (c) with $\omega_c = 1$ for the Hamiltonian without single particle terms $\hat{H}_\chi$ (Eq. (5.45))

.

is a spatially dependent resistivity:

$$\rho_{xy}(x) = \frac{E_y}{e\langle \hat{J}_x(x)\rangle}. \tag{5.56}$$

For the FQHE the bulk value is expected to be quantized as $\rho_{xy} = \frac{1}{\nu}\frac{h}{e^2}$, with $\nu = 1/3$ in this chapter.

In the adiabatic limit $\tau \to \infty$, and assuming the existence of a many-body gap, we can focus on the ground state of the instantaneous total Hamiltonian $\hat{H}(\Phi)$ which in principle depends on Φ. Now we know that a constant vector potential $\boldsymbol{A}_p$ does not couple to the LLL. Indeed, the effect of a flux Φ is to change the y-momentum quantization of the single particle orbitals $\psi_{n,k}$ (Sec. 5.2.1) and consequently their position:

$$k_\Phi = \frac{2\pi}{L_y} m_k + \frac{2\pi}{L_y}\frac{\Phi}{\Phi_0}, \qquad X_{k_\Phi} = k_\Phi\, l_B^2, \tag{5.57}$$

with $m_k \in \mathbb{Z}$. This means that the projection $\mathcal{P}_\Phi$ to the LLL depends on Φ. This is not an issue as long as we focus on adiabatic processes. Given Eq. (5.57), we can now inspect how the many-body light-matter Hamiltonian $\hat{H}(\Phi)$ looks like. The electron-electron interaction clearly remains unchanged as it only depends on difference of momenta. The light-matter coupling, for this purpose, is more conveniently formulated within the Coulomb gauge formulation (Sec. 5.2.3). Here the interaction is only controlled by difference in momenta $k_\Phi - k'_\Phi$ and hence the full Hamiltonian $\hat{H}(\Phi)$ remains unchanged. As a key consequence, we have that the ground state wavefunction in second quantization $|\mathrm{GS}_\Phi\rangle$, hence fixing an orbital basis, will be the same:

$$\hat{H}(\Phi) \equiv \hat{H}(\Phi = 0) \quad \Rightarrow \quad |\mathrm{GS}_\Phi\rangle \equiv |\mathrm{GS}_{\Phi=0}\rangle\,. \tag{5.58}$$

It is important to stress that in Eq. (5.58), we have not used the equality sign. The reasons is that the Hilbert spaces in which the two sides of the equations are defined are not, strictly speaking, the same: they refer to different LLL projection $\hat{\Pi}_\Phi$. In order to perform a meaningful comparison, we can consider relevant physical observables such as the charge density $\hat{n}(x)$, which is expressed as:

$$\hat{n}(x) = \frac{1}{L_y} \sum_{k_\Phi} \hat{n}_{k_\Phi} |\phi_0(x - X_{k_\Phi})|^2, \tag{5.59}$$

and can be evaluated at different Φ by just using the $\Phi = 0$ solution with a change in the single particle orbitals $\phi_0(x - X_{k_\Phi})$.

In order to calculate the current $\langle \hat{J}_x \rangle$ we use the continuity equation:

$$\boldsymbol{\nabla} \cdot \langle \hat{\boldsymbol{J}} \rangle = -\partial_t \langle \hat{n} \rangle, \tag{5.60}$$

where $\hat{\boldsymbol{J}}$ is the current operator. Given our finite cylinder geometry we can integrate both sides of the equation above in a region $\mathcal{V} = \{(x, y) \text{ s.t. } x < x_0\}$ to get:

$$\langle \hat{J}_x(x_0) \rangle = -\partial_t \int_{-\infty}^{x_0} \mathrm{d}x \langle \hat{n}(x) \rangle_{\Phi(t)}, \tag{5.61}$$

with $\hat{J}_x(x_0)$ the current density along x at position x_0. Because of translational invariance on y the current and the density do not depend on y making the integration over y trivial. Using Eq. (5.59) and the ramp protocol $\Phi(t) \propto t$, we can express the local transverse resistivity in terms of the static density:

$$\rho_{xy}(x_0) = \frac{1}{2\pi \langle \hat{n}(x_0) \rangle} \frac{h}{e^2}, \tag{5.62}$$

where h/e^2 is the von Klitzing constant, and the factor 2π is the area occupied by a single-particle state (in units of l_B^2). The above equation directly links the bulk density to the fractional Hall response of the system. In particular, for a topologically ordered state in the class of the Laughlin $\nu = 1/3$, one expects the bulk density to be constant $2\pi \langle \hat{n}(x_0) \rangle = 1/3$.

In Fig. 5.3(b) we show the bulk resistivity (shaded area represent all positions $x_0 \in [-2, 2]$) as a function of cavity field gradients g in the Hamiltonian $\hat{H}_\chi$ (Eq. (5.45)) where cavity induced inhomogeneous single particle potentials are neglected. In order to compare two different cavity frequencies, we show the results as a function of $g\sqrt{\omega_c}$, as discussed in Sec. 5.2.6. The resistivity is quantized up to exponential corrections even at relatively large values of the cavity field gradient $g\sqrt{\omega_c} \simeq 2$. At stronger gradients the bulk density features strong oscillations (see Sec. 5.5.2) hence a non-quantized Hall response. Here the FQH liquid becomes unstable towards the formation of stripes that, as we will show in Sec. 5.4.2, is linked to the softening of finite momentum magnetorotons. The fact that changing the cavity frequency by a factor 2 leaves the instability region unchanged indicates that this is not a resonant

effect. We remark however that the actual fate of the system in this regime strongly depend on the inclusion of single particle potentials and will be better characterized in Sec 5.5. In Fig. 5.3(c) we depict the deviations of the density from its bulk value when approaching an edge of the cylinder ($x = 0$ is the center of the system while $x = 20$ is outside of it). For all depicted couplings in the FQH phase, the corrections decay exponentially in the bulk with a correlation length l_{edge} which increase with g.

It has been recently argued [128] that the finite lifetime of the cavity mode can give a correction to the quantized transverse conductivity at temperature $T = 0$ in the IQH regime. We note that at the many-body level the flux insertion argument can be adapted to the case of weak cavity losses (see Appendix D.2). The key physical insight is that the steady state of the whole system (cavity plus matter) is at thermal equilibrium with the bath [279], hence the ground state results, regarding the Hall resistivity, are expected to hold provided that the photonic bath is at a small enough temperature. It would be interesting to check, in the spirit of Ref. [128], what finite temperature corrections are. We leave this to future work.

5.3.2. Entanglement spectrum

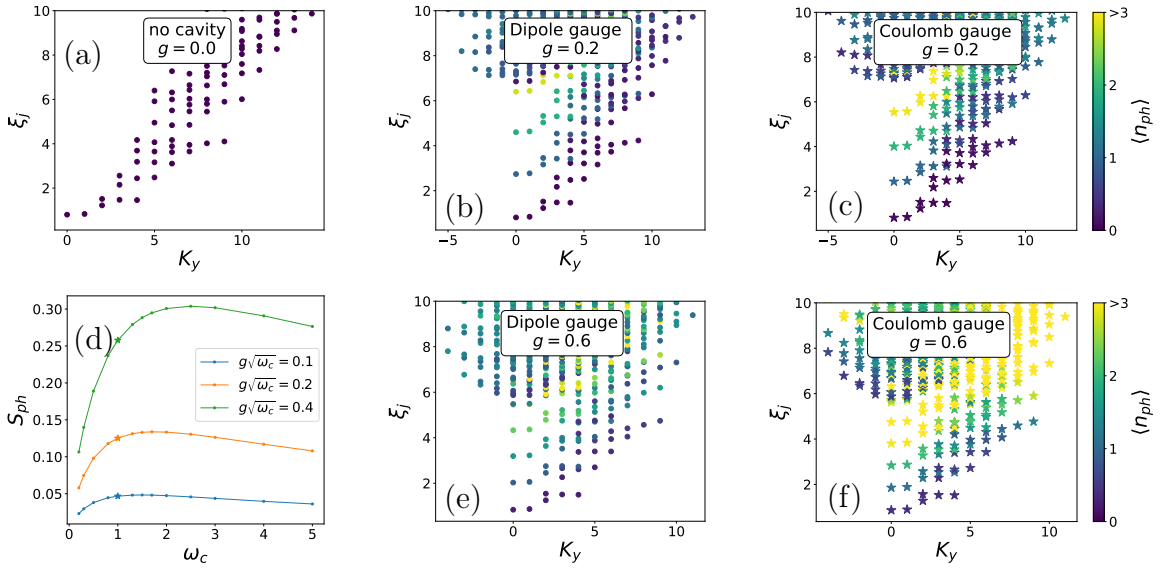


Figure 5.4.: (a,b,c,e,f) Entanglement spectra obtained via DMRG for the asymmetric bipartition of Eq. (5.65) on system size $L_y = 20$ and $N_e = 34$ and (d) Entanglement entropy of the cavity in the Dipole gauge as a function of ω_c and fixed $g\sqrt{\omega_c}$. All results obtained from the Hamiltonian $\hat{H}_\chi$ in Eq. (5.45). The charge sector of the shown spectra is $N_e/2 = 17$ while the momentum along y gives the x-axis. In panel (a) the state is pure Laughlin ($g = 0$) while in panels (b,c) and (e,f) we have a finite light-matter coupling $g = 0.2$ and $g = 0.6$ in Dipole and Coulomb gauge respectively. The color represent the number of photons in each Schmidt state and the colorbar is the same for all (a,b,c,e,f) panels

The entanglement spectrum at a bipartition of a topologically ordered state exhibits

distinct signatures, which can be used to detect topological order [238, 243, 280, 281]. In particular, one expects to find information about the edge theory of the topological state under consideration. This procedure, dubbed entanglement spectroscopy, is not only widely used as a theoretical tool, but has also been also proposed as an experimental protocol to detect topology in cold atom systems [281]. The deep roots of this topology-entanglement connection lie in a very general results in relativistic quantum field theory, the Bisognano-Wichmann theorem [282, 283], which dictates closed functional form expressions for the entanglement (or modular) Hamiltonian, and explain the Li-Haldane result [284]. A natural question to ask is, what is left about this topology footprint on entanglement in the presence of quantum light.

Before discussing our hybrid cavity-matter setting, we review some general concepts. Let us define the pure state $|\Psi\rangle$ of the full system and the density matrix $\hat{\rho}_A$ of a subsystem A as $\hat{\rho}_A = \mathrm{Tr}_B\left[|\Psi\rangle\langle\Psi|\right]$ with B being the rest of the system. In general, we can write:

$$\hat{\rho}_A = \exp\left(-\hat{H}_{ee}\right) = \exp\left(-\sum_{q,i} \xi_{\{q\},i} \left|\phi_{\{q\},i}\right\rangle\left\langle\phi_{\{q\},i}\right|\right), \tag{5.63}$$

where $\hat{H}_{ee}$ is the entanglement Hamiltonian, $\xi_{\{q\},i}$ the entanglement energies, $\left|\phi_{\{q\},i}\right\rangle$ the Schmidt vectors corresponding to the bipartition, and $(\{q\}, i)$ an index tuple labeling the quantum numbers $\{q\}$ and the Schmidt state i. Following the Li-Haldane conjecture [238, 239], the entanglement spectrum for a bipartition in the bulk must follow, at low energies, the Hamiltonian of the edge. For Laughlin states, the edge theory is a chiral Luttinger liquid (χLL) [285, 286] which, once the $U(1)$ charge sector is fixed, gives a specific fingerprint in terms of degeneracies at each total momentum:

$$(d_0, d_1, d_2, d_3, d_4, d_5, \dots) = (1, 1, 2, 3, 5, 7, \dots), \tag{5.64}$$

with d_k being the degeneracy at momentum quantum number k. At finite sizes, the degeneracies are usually broken but a gap still separate a universal low energy part from a non-universal part of the entanglement spectrum [239]. This remark that this also happens for energy spectra at physical edges [259] and not only for entanglement spectra in bulk bipartitions.

In the case of a cavity embedded systems there is no clear notion of pure state bipartition as the non-local bosonic mode cannot be "divided" in two. As already done in [4, 36], one needs to define asymmetric bipartitions where the cavity mode resides on one side. A possible choice is the following:

$$\hat{\rho}_{X_k>0} = \mathrm{Tr}_{x<0;c}\left[|\Psi\rangle\langle\Psi|\right], \tag{5.65}$$

where $|\Psi\rangle$ is the many-body ground state, $\hat{\rho}_{X_k>0}$ is the reduced density matrix for electrons in orbitals k with $X_k > 0$, and $\mathrm{Tr}_{X_k<0;c}$ is the trace over electrons at $X_k < 0$ and the cavity mode c. One can, however, always recover the notion of an only matter bipartition by considering the electronic density matrix $\hat{\rho}_{el} = \mathrm{Tr}_c[|\Psi\rangle\langle\Psi|]$. Taking its

bipartition will give as a result the same density matrix of the asymmetric bipartition with the cavity in Eq. (5.65).

In light of the discussion about different possible representations of the cavity-matter system (Sec. 5.2.3), we want to stress that (not unexpectedly) the entanglement spectrum is not a gauge invariant quantity. Indeed, it can change under global unitary transformations $\hat{U}$, which implement the change of gauge in the truncated LLL model, since a global change of basis can change the reduced density matrix of subsystems. However, as discussed in Sec. 5.2.7, we can easily change the gauge in which a state $|\Psi\rangle$ is represented by applying the unitary $\hat{U}$ and just check whether the entanglement spectrum displays features that are stable against the change of gauge. We remark that the change of gauge here implemented (after LLL truncation) leads to results which are in general different from a truncation in the Coulomb gauge.

Entanglement spectrum bands and polariton entanglement gap

In Fig. 5.4 we show the DMRG results for the entanglement spectrum of the asymmetric bipartition in Eq. (5.65) at $g = 0$ (a) and at finite $g = 0.2$ in the Dipole (b) and Coulomb (c) gauges of the Hamiltonian $\hat{H}_\chi$, described in Eq. (5.45) in the Dipole gauge. In particular, we fix the number of particles of the bipartition to be $N_e/2$ and look at momentum quantum number K_y. It is worth noting that we are interested here solely in regimes where electrons and cavity modes are hybridized, so that their mutual entanglement - portrayed in Fig. 5.4(d) is finite. The limit $\omega_c \to \infty$ cannot be immediately extrapolated from here, as the LLL truncation made in the model building part is not generically applicable when $\omega_c \sim \omega_B$.

At finite light-matter coupling g the entanglement spectrum still show the χLL counting, but the higher energy part clearly changes. In order to understand the difference between entanglement eigenvectors, we color the markers based on the number of photons in the respective Schmidt state:

$$n^{ph}_{\{q\},i} = \left\langle \phi_{\{q\},i} \right| \hat{a}^\dagger \hat{a} \left| \phi_{\{q\},i} \right\rangle , \tag{5.66}$$

where the Schmidt states are readily available from the total MPS. This highlights a very informative pattern. The χLL counting is repeated for number of photons roughly equals to integers. We empirically find for each of these branches:

$$n^{ph}_{k,j} \simeq j, \qquad \xi_{k,j} \simeq \epsilon_k + j\Delta_{pol}, \tag{5.67}$$

with ϵ_k a size dependent non-universal dispersion, and $j = 0, 1, 2, \ldots$ an integer.

We remark that this phenomenology does not indicate multiple edge modes, but rather the presence of a mixed cavity-matter bulk excitation at zero momentum, akin to what happens for finite momentum magnetorotons in the case of Coulomb FQH ground states [239] that also give rise to high entanglement-energy features. In the present case,

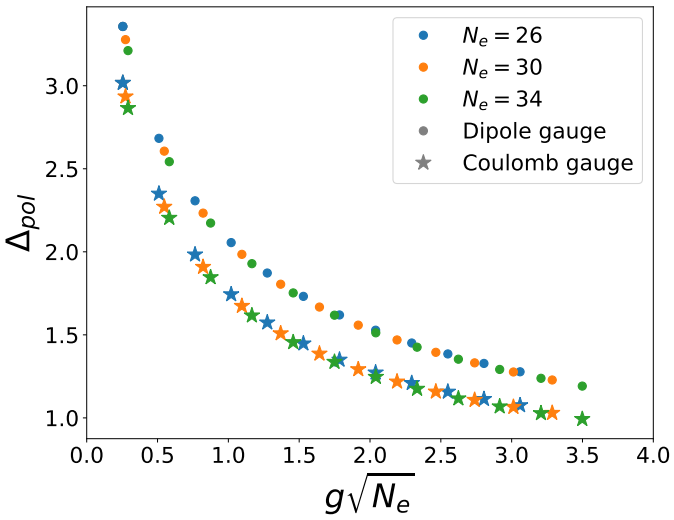


Figure 5.5.: Polariton entanglement gap. Data extracted from DMRG entanglement spectra in the middle of the cylinder for different number of particles N_e, and fixed $L_y = 20$, in the Dipole gauge (circles) and Coulomb gauge (stars) as a function of the collective coupling $g\sqrt{N_e}$.

the repeated χLL counting of entanglement spectrum without any momentum-shift is a clear signature of the graviton mode getting hybridized with the cavity photons (see Sec. 5.4.3 for the corresponding spectroscopic analysis).

The quantity Δ_{pol}, which we call *polariton entanglement gap*, controls the separation between different sectors of the χLL with different number of photons and needs to be finite to preserve the χLL structure. Importantly, qualitative features of the entanglement spectrum are observed to persist in different gauges at least up until $g = 1$ for the volumes considered here (see. Fig. 5.4b-c and e-f for two direct comparisons).

In Fig. 5.5 we study the polariton entanglement gap dependence with system size. We show its dependence as a function of a re-scaled collective coupling $g\sqrt{N_e}$ for different number of particles N_e. The perfect collapse highlights the collective nature of polariton excitations, i.e., they are controlled by the collective coupling $g\sqrt{N_e}$. By showing the entanglement gap for both gauges it is evident that this is a gauge dependent quantity, nonetheless both gauges reveal the same collective behavior. Moreover, we find that the value of Δ_{pol} does not depend on L_y (not shown).

The nature of this gapped polaritonic excitation will be clarified in Sec. 5.4, where we show that a strong hybridization between a collective emergent electronic mode, the momentum $q \simeq 0$ part of the magnetoroton spectrum, and the cavity is taking place. An important consequence of the collective coupling is that taking thermodynamic limit $N_e \to \infty$ at fixed g breaks the χLL counting and the topological order of the state. The stability of the FQH phase at finite g then needs to be understood in a mesoscopic sense – another important scale $g\sqrt{N_e}$ is controlling the many-body gap of

the FQH phase and hence its topological order.

Overall, our prediction of a stable FQH topology upon the inclusion of the non-local cavity mode should be thought as parallel to recent precise experimental measurements in the IQH regime [44]. The non-local element introduced by the cavity mode can make this prediction a priopri not trivial. We can rationalize this result in two key factors which are still satisfied: (i) there must be a finite bulk excitation gap (see Sec. 5.4) and (ii) the non-local cavity mode couples to local charge conserving operators. Breaking (ii) would for example immediately generate a cavity-mediated inter-edge scattering thus breaking the topological protection, even in presence of (i). It is indeed a cavity-mediated inter-edge scattering due to small sample size [129], that likely leads to a loss of good transport properties [43].

5.4. Spectral properties

In this section we discuss the effect of the cavity mode on the neutral bulk spectral properties of the FQH liquid. We first give an introduction to the neutral excitations in absence of the cavity mode (Sec. 5.4.1), e.g., the magnetoroton spectrum, using the so-called single-mode approximation [226] for the magnetorotons due to Girvin, MacDonald and Platzman. In Sec. 5.4.2 we present numerical results which map out the phenomenology of the low-lying excited state spectrum in presence of the cavity mode. Finally, we provide a simple effective polariton model that captures the essential physics of hybridized cavity-matter excitations, the graviton-polaritons, and test its predictions against numerics (Sec. 5.4.3).

5.4.1. Magnetoroton spectrum

Magnetorotons are the lowest-energy excitations above the gapped FQH ground state. They manifest as charge density modulations within the LLL that arise from the bound state of a quasi-electron and a quasi-hole [287, 288]. Crucial to the stability of the FQH state, the magnetoroton spectrum has been subject of intense study [226, 235, 236, 249, 266, 288]. Their dispersion relation exhibits a pronounced minimum at finite wavevector $q \sim 1/l_B$, which descends below the two-particle continuum, see Fig. 5.6(a). The minimum is known as the magnetoroton gap, and is the precursor of ordered phases such as the Wigner crystal and stripes [249].

More recently the $q \to 0$ magnetorotons have been associated to the fluctuations of the quantum Hall geometry tensor [229, 242]. These emergent spin-2 gravitons (gapped and non-relativistic) have a strong quadrupolar moment with a vanishing dipole moment and have a preferred chirality, exact for model wavefunctions. We remark that

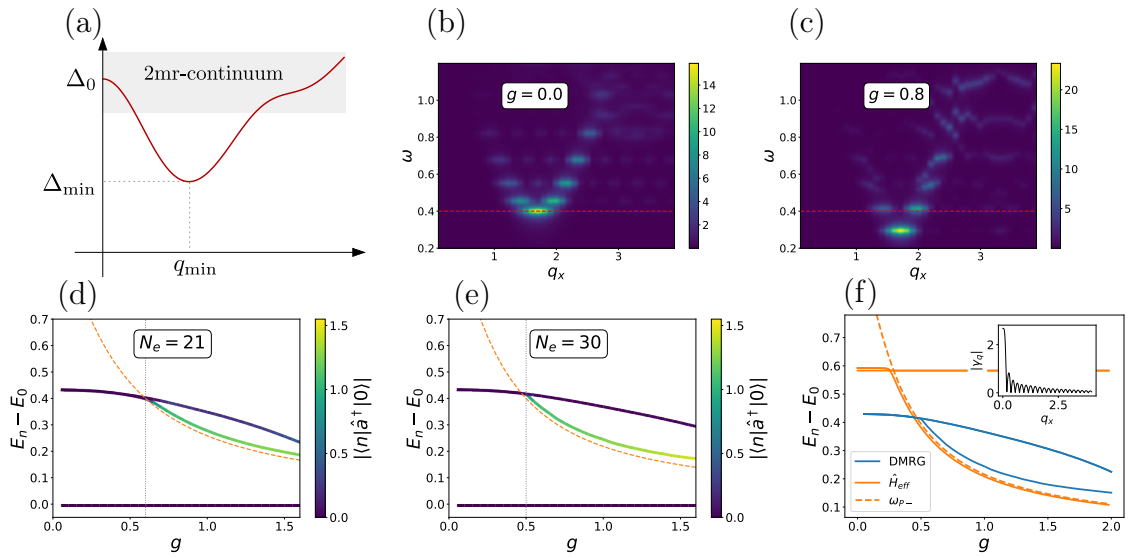


Figure 5.6.: (a) Magnetoroton dispersion as calculated from the SMA (red) with a sketch of the two-magnetoroton continuum. The SMA magnetoroton gap $\Delta_{\min} \simeq 0.6$ occurs at a finite wavevector $q_{\min} \simeq 1.7$ and a gap is also present at small wavevectors $\Delta_0 \simeq 1.5$. (b,c) Dynamical structure factor as a function of momentum along x at $g = 0$ (b) and $g = 0.8$ (c). The red dashed line is a guide to the eye that signals the energy of the first excited state at $g = 0$. $L_y = 10$ and $N_e = 10$ in (b) and (c). (d),(e) Low energy spectrum in the $K_y = 0$ sector as a function of g calculated via DMRG for different number of particles $N_e = 21$ (d) and $N_e = 30$ (e) at the same $L_y = 16$. The colorbar represent the photon creation matrix element from the ground state to each state and the vertical grey dashed line a guide to the eye for the value at which a polariton becomes the first excited state. The orange dashed line represent the lower polariton frequency obtained from the bare graviton-polariton model Eq. (5.73). (f) Comparison between DMRG results and the eigenfrequencies of the effective model in Eq. (5.70) for the first two excited states. These are always either magnetoroton states or polaritons. The effective model uses the coupling parameters γ_q shown in the inset. The orange dashed line represent again the lower polariton frequency from the bare graviton polariton model Eq. (5.73). $L_y = 16$ in (d),(e),(f). The cavity frequency is always $\omega_c = 1$, and cavity vacuum-induced Stark shifts are absent.

chiral FQH gravitons have also been recently detected in inelastic scattering experiments with circularly polarized light [228].

We now briefly review a simple physical picture of the magnetoroton mode, provided by Girvin, MacDonald and Platzman (GMP) with the single-mode approximation (SMA) [226]. Note that here the “single mode" term does not refer to our cavity model. The SMA is a variational ansatz that describes the magnetoroton excitations as long wavelength charge modulations on top of the liquid ground state of uniform density. With this picture in mind, GMP built a set of excited states as:

$$|\boldsymbol{q}\rangle = \hat{\bar{\rho}}_{\boldsymbol{q}} |\Psi_L\rangle \,, \tag{5.68}$$

where $\hat{\bar{\rho}}_{\boldsymbol{q}}$ is the guiding center density operator in the LLL defined in Eq. (5.50). Using the static structure factor $S(\boldsymbol{q})$ to normalize the variational state, the excitation energy

then becomes fixed by the ratio:

$$\Delta_{\mathrm{SMA}}(\boldsymbol{q}) = \frac{F(\boldsymbol{q})}{S(\boldsymbol{q})}, \qquad F(\boldsymbol{q}) = \langle \boldsymbol{q} | \, \hat{H}_{\mathrm{int}} - E_0 \, | \boldsymbol{q} \rangle \,, \tag{5.69}$$

where $F(\boldsymbol{q})$ is the oscillator strength and $S(\boldsymbol{q})$ the guiding center structure factor. The LLL density operator $\hat{\rho}_{\boldsymbol{q}}$ obeys the Lie algebra: $\left[\hat{\rho}_{\boldsymbol{q}}, \hat{\rho}'_{\boldsymbol{q}}\right] = 2i \sin\left(\frac{1}{2}\boldsymbol{q} \times \boldsymbol{q}'\right) \hat{\rho}_{\boldsymbol{q}+\boldsymbol{q}'}$, named after GMP [226, 266], which allows to express the oscillator strength $F(\boldsymbol{q})$ as a sole function of $S(\boldsymbol{q})$ and the interaction potential [226].

As shown in Fig. 5.6(a), the GMP ansatz captures the essential features of the magnetoroton mode, reproducing a fully gapped mode with a mininum at finite momenta. It is worth noting that the SMA overestimates the magnetoroton mode energy gap as the wave vector is increased. This is a well-known shortcoming of the ansatz [226], given that the density operator also couples to high-energy states containing a greater number of quasi-electron and quasi-hole pairs [266].

In our notations, the SMA predicts a gap minimum of $\Delta_{\mathrm{min}} \simeq 0.6$ close to the momenta $q_{\mathrm{min}} \simeq 1.4$. This is to be contrasted with the ED calculation of the dynamical structure factor shown in Fig. 5.6(b). We observe the actual gap is smaller, around $\Delta_{\mathrm{min}} \simeq 0.4$ with a corresponding wave vector $q_{\mathrm{min}} \simeq 1.7$. Long-wavelength magnetorotons hide inside the two-quasi-particle continuum as the SMA predicts $\Delta_0 \simeq 1.5$. While the SMA fails to predict a quantitatively correct magnetoroton gap, it is believed to capture the graviton energy Δ_0. It is less clear however up to what extent the two particle continuum damps the pristine magnetoroton dispersion found in the SMA. In what follows, we will see that for suitable values of the light-matter coupling, the energy of the lower graviton-polariton gets shifted below the two excitation continuum, making it protected against such an absorption channel.

5.4.2. Numerical results

We now investigate numerically the effect of the cavity mode on the low-lying FQH bulk spectrum. Again, in order to mantain homogeneity in the system, we will work with $\hat{H}_\chi$ (Eq. (5.45)) in absence of cavity mediated single particle potentials ($\mu_k = 0$). Note also that because of the choice of "hard" boundaries, the edge states are gapped out, and only bulk excitations remain. In order to track the magnetoroton dispersion we look at the dynamical structure factor $S(\boldsymbol{q}, \omega)$, Eq. (5.52). The dynamical structure factor probes the response of the system to density excitation at a certain frequency ω. In the following we will focus on the response to modulation only along x (uniform on y) so on $S(q_x, \omega)$. In Fig. 5.6 we show this quantity for $g = 0$ (b) and for $g = 0.8$ (c) at a small system size ($L_y = 10$ and $N_e = 10$) accessible via ED. Note that due to the open boundary conditions on x the momenta is not a good quantum number and excitations are expected to spread over a finite region of q_x. Cavity mediated interactions (proportional to χ_k) are clearly lowering the magnetoroton gap with no

particular modification of the wavevector at which the minimum is found $q_{\min} \simeq 1.75$. As we will see later in Sec. 5.5.2, this is the precursor of a cavity-mediated instability of the FQH liquid towards a stripe state.

In order to access larger system sizes we look directly at the excited state spectrum by targeting excited states via local effective Hamiltonians constructed during DMRG calculations [272] as explained in Section 5.2.7. More details about the accuracy of this method can be found in Appendix D.6. Moreover by looking at the excited states we can gain more information also on the cavity degree of freedom. It is important to remark that this method allows us to probe excitations in the $K_y = 0$ sector only, hence exploring only quasi-momenta q_x. In Fig. 5.6(d,e) we show the first two low-lying excited states as a function of g for number of particles: $N_e = 21$ (d) and $N_e = 30$ (e) at $L_y = 16$. The result are obtained from the middle-chain local effective Hamiltonian. The colors of the lines represent the strength of the matrix element $|\langle n|\,\hat{a}^\dagger\,|0\rangle|$, which enters in the cavity density of states $D_c(\omega)$, see Eq. (5.53), helping us to spot the polaritonic character of the states. The orange dashed line is an analytical prediction for the lower polariton that will be discussed in Sec. 5.4.3. We can distinguish two qualitatively different regimes. These are the following:

1. Near $g = 0$, the two low lying states are part of the magnetoroton dispersion around the $q_{\min}$ and they start at around $\Delta_{\min} \simeq 0.4$ which is the bulk neutral gap of the Laughlin state. All these states show a vanishingly small one-photon matrix element with the ground state. The cavity photon mode is located well above, at his bare energy $\omega_c = 1$.

2. For finite g, the cavity mode mixes with matter excitations, in particular with the quadrupole-active graviton mode at Δ_0. This results into a pair of graviton-polaritons, characterized by a sizable one-photon matrix element with the ground state. In particular, the energy of the lower graviton-polariton starts at the bare cavity frequenxy $\omega_c = 1$ and is then shifted down for growing g. At a strong enough value of the coupling g_P marked with a vertical dashed line, the lower graviton-polariton becomes the first excited state and gets immune from absorption processes into other matter excitations. This happens sooner for larger systems, for system sizes shown in Figure 5.6 we find $g_P = 0.65$ vs $g_P = 0.5$ ($N_e = 21$ vs $N_e = 30$). An effective model (orange dashed line, see Sec. 5.4.3) capture this feature. The upper graviton-polariton (not visible in the figure) starts at $\Delta_0 > \omega_c$ and gets blue-shifted for larger g.

Note that having the polariton state lower in energy with respect to the magnetoroton implies that the gap protecting the topological order from finite temperatures will be the polariton gap, as pointed out in Ref. [128] for the IQH case. We then want to remark that there seems to be a difference between the dependence with system size of the polariton state and of the magnetoroton dispersion. While the latter is empirically controlled by g, the polariton state sees the collective enhancement thus it is controlled

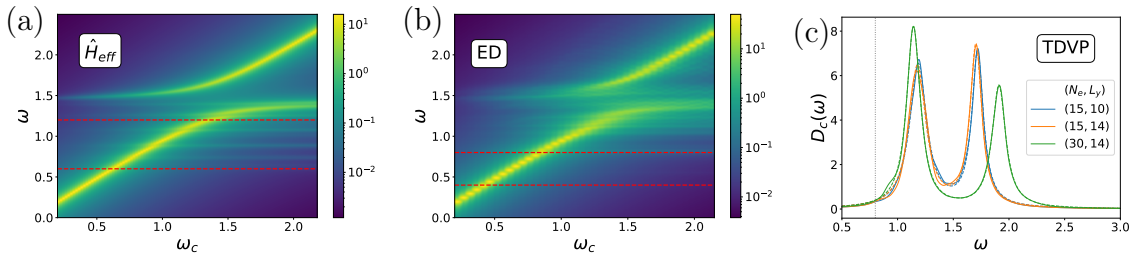


Figure 5.7.: Cavity density of states $D_c(\omega)$ in the Dipole gauge with different methods in absence of cavity induced single particle potentials. The ED results (b) and effective model (a) show the avoided crossing when changing the cavity frequency ω_c, signalling the strong coupling between the graviton mode and the cavity mode. Dashed red lines mark the frequency range between the magnetoroton gap Δ_{min} and $2\Delta_{min}$ where the two-particle continuum begins. In the effective model there is a residual small coupling to the finite q part of the magnetoroton while the ED results only highlight a coupling to the two-particle continuum and not to single magnetorotons states. In panel (c) we show TDVP results with fixed cavity frequency $\omega_c = 1.5$, almost resonant with the graviton, and we change N_e and L_y. By fitting with two Lorentzians (dashed lines) we extract the Rabi splittings between the two polariton resonances (Table 5.1). System size (N_e, L_y) in (a) is $(10, 10)$, in (b) is $(30, 16)$, in (c) are described in the legend. The couplings for (a, b) are respectively $g = 0.1, 0.1/\sqrt{30/10}$ to have the same collective coupling. In (c) $g = 0.1$. Broadening parameters $\eta = 0.02$ in (a,b) and $\eta = 0.05$ in (c).

by $g\sqrt{N_e}$ (we are assuming here the cavity mode volume to be independent of N_e). In the next subsection we propose an effective model to explain this feature and the nature of the polariton state.

5.4.3. Effective model

We introduce an effective model to describe the coupling between magnetorotons and the cavity field, neglecting for the moment cavity mediated single particle terms. Treating the magnetorotons as free bosons, we express the matter Hamiltonian as a collection of independent oscillators: $H_{\mathrm{MR}} \approx \sum_{\boldsymbol{q}} \Delta(\boldsymbol{q}) \hat{b}^\dagger_{\boldsymbol{q}} \hat{b}_{\boldsymbol{q}}$, where $\hat{b}_{\boldsymbol{q}}$ represents the bosonic excitation of the magnetoroton at momentum $\boldsymbol{q}$, and $\Delta(\boldsymbol{q})$ denotes the energy dispersion. For the sake of simplicity we neglect interactions. In the original model the coupling to the cavity is performed via the polarization operator $\hat{P} = \frac{1}{2}\sum_k k^2 \hat{n}_k$. For the effective model we replace it with $\hat{P} \to \sum_q \gamma_q (\hat{b}_q + \hat{b}^\dagger_q)$, where γ_q represents the effective coupling governing the transition, and the momenta $\boldsymbol{q} = (q, 0)$ is restricted to the x direction since the electric field does not depend on y. The effective model

Hamiltonian is then expressed as

$$\hat{H}_{\text{eff}} = \omega_c \hat{a}^\dagger \hat{a} + \sum_q \Delta(q) \hat{b}_q^\dagger \hat{b}_q + \omega_c g^2 \Big[\sum_q \gamma_q (\hat{b}_q + \hat{b}_q^\dagger) \Big]^2 + i\omega_c g (\hat{a} - \hat{a}^\dagger) \sum_q \gamma_q (\hat{b}_q + \hat{b}_q^\dagger), \tag{5.70}$$

where we factor out the g coupling in order to facilitate the power counting. The sum on q should be sensitive to boundary conditions: in the present case of a finite cylinder of length L_x in the direction of OBC we will consider modes with momentum $q = \pm(2j_q - 1)\pi/L_x$ ($j_q = 1, \ldots, M/2$), whose symmetric and antisymmetric combination form even and odd standing waves with proper boundary conditions. Then, being Eq. (5.70) a quadratic bosonic Hamiltonian, it can be easily solved via Bogoliubov-Hopfield transformations. Note that the $q = 0$ mode cannot be constracted from the SMA procedure.

To draw a comparison with the numerical simulations of the actual FQH plus cavity setup, we fix the effective parameters of our model by using the SMA. The energy dispersion follows from the variational ansatz in Eq. (5.69) and is sketched in Fig. 5.6(a). The light-matter interaction parameters γ_q are obtained from the matrix elements of the polarization operator $\hat{P} = \frac{1}{2}\sum_k k^2 \hat{n}_k$ with respect to the Laughlin ground state and the SMA excited states:

$$\gamma_q = \frac{1}{\sqrt{MS(q)}} \sum_{k,k'} \frac{1}{2} k^2 e^{-ik'q} \langle \Psi_L | \, \delta\hat{n}_k \delta\hat{n}_{k'} \, | \Psi_L \rangle \, . \tag{5.71}$$

The matrix element γ_q is shown in the inset of Fig. 5.6(f). We observe it displays a prominent peak as $q \to 0$ and some smaller oscillations for finite wave vectors. These have a period of roughly $2\pi/L_x$ and are caused by the open cylinder geometry. The behaviour at $q \to 0$ can be obtained from the long-wavelength expansion of the structure factor $S(q) \simeq S_4^{xx} q^4$, which in the thermodynamic limit ($L_y, N_e \to \infty$ and $L_y/L_x \propto L_y/\sqrt{N_e} = const$ for a fixed aspect ratio) yields:

$$\tilde{\gamma}_0 \equiv \lim_{q\to 0} \gamma_q = -\sqrt{N_e S_4^{xx}/\nu} \propto \sqrt{N_e}. \tag{5.72}$$

Note that, although the $q = 0$ momentum state is strictly speaking excluded from the SMA ansatz, by taking the limit we can define a well behaved collective mode. At finite but big enough system sizes, the relevant coupling strength is going to be peaked around $q = 0$ and spread over a region of momenta $\delta q \simeq \pi/L_x$ thus allowing a further simplification to single matter mode model that captures this behaviour. The collective enhancement factor $\sqrt{N_e}$ is signalling that the graviton is expected to be a good collective excitation able to couple to the field gradient.

We remark that in Eq. (5.72) there is no explicit dependence on L_y nor N_e, just on the parameter S_4^{xx} which controls the long-wavelength correlations of the FQH liquid.

The behaviour at finite q is a boundary effect and is also the regime where the SMA should be taken with an extra grain of salt. The collective enhancement of the $q \to 0$ mode only suggests that the effective model can be further simplified to a bare graviton-polariton model, with a single collective matter mode $\hat{\tilde{b}}_0$ coupled to the cavity mode $\hat{a}$:

$$\begin{aligned}\hat{H}_{\text{eff},0} = \omega_c \hat{a}^\dagger \hat{a} + \Delta_0 \hat{\tilde{b}}_0^\dagger \hat{\tilde{b}}_0 + i\omega_c g \tilde{\gamma}_0 (\hat{a} - \hat{a}^\dagger)(\hat{\tilde{b}}_0 + \hat{\tilde{b}}_0^\dagger) \\ + \omega_c g^2 \tilde{\gamma}_0^2 (\hat{\tilde{b}}_0 + \hat{\tilde{b}}_0^\dagger)^2,\end{aligned} \tag{5.73}$$

where Δ_0 denotes the graviton energy, and $\tilde{\gamma}_0$ is taken from Eq. (5.72). By means of a Bogoliubov-Hopfield transformation we can directly get the two polariton energies resulting from Eq. (5.73):

$$\omega_{P\pm}^2 = \frac{1}{2}\left(\omega_c^2 + \Delta_0^2 + \Omega^2 \pm \sqrt{(\omega_c^2 + \Delta_0^2 + \Omega^2)^2 - 4\omega_c^2 \Delta_0^2}\right), \tag{5.74}$$

where we have introduced the Rabi frequency:

$$\Omega = 2g\tilde{\gamma}_0 \sqrt{\omega_c \Delta_0}. \tag{5.75}$$

In Fig. 5.6(f) we compare the predictions of the effective models (orange lines) with the low-lying energy spectrum obtained from DMRG simulations (blue lines). We observe that the effective model $\hat{H}_{\text{eff}}$ successfully captures the emergence of the polariton mode that comes down in energy as a function of g. This energy closely follows the lower polariton energy ω_{P_-} where only an effective $q = 0$ mode is taken into account. Small deviations are compatible with the accuracy of the DMRG variational estimate for the polaritonic state (see App. D.6). In stark contrast, the effective model misses the gap softening of other magnetoroton states which live at finite q. The red-shift of the magnetoroton mode under the effect of light-matter interactions seems indeed very important at strong coupling, signaling the emergence of an instability towards a density modulated stripe phase as we describe next section.

In this respect, we wish to repeat that even at $g = 0$ the effective model, being based on the SMA, does not accurately capture the exact value of the gap. Interactions, both matter-matter and cavity-mediated, play a key role in the renormalization of the gap and capturing them requires the treatment of the full many-body problem beyond the effective model.

Spectroscopy of the graviton-polariton

Thanks to the hybrid nature of the polariton excitations [17], it is possible to have distinct simple spectroscopic signature of both the upper and the lower modes, which gives direct evidence of the strong-coupling regime. To this end we show (Fig. 5.7) the cavity density of states $D_c(\omega)$ as defined in Eq. (5.53). Here we compare the prediction

of the effective model (b) with ED (a) and TDVP (c) results. The ED and effective model result indicates the dominant hybridization at small g occurs at the energy scales of the graviton Δ_0. In the ED result we also spot subdominant couplings to other states inside the two-particle continuum which are not captured in the effective model. The latter instead predicts a weight on the finite q part of the magnetoroton that in ED is not present (region between the red dashed lines), consistent with the failure of the effective model in capturing the softening of the magnetoroton at finite momenta. The predicted collective enhancement of the graviton hybridization is confirmed by the TDVP results. By fitting the spectral function with two Lorentzians, we can extract the Rabi splitting between the two polariton resonances, which are reported in Table 5.1.

(N_e, L_y)	$(15, 10)$	$(15, 14)$	$(30, 14)$	Effective model
Ω	0.53	0.53	0.77	$1.0 \times \omega_c g\sqrt{N_e}$
$\Omega/\omega_c g\sqrt{N_e}$	0.91	0.91	0.94	1.0

Table 5.1.: Rabi splittings between graviton-polaritons resonances obtained by fitting TDVP results, Fig. 5.7(c), compared with the effective model prediction in the thermodynamic limit and assuming $\Delta_0 = \omega_c = 1.5$. Small corrections due to small detunings are expected, as well as finite-size corrections with both N_e and L_y on Δ_0 and Ω.

According to the graviton-polariton model, Eq. (5.74), and assuming a resonance condition $\Delta_0 = \omega_c = 1.5$ the Rabi splitting at small enough $g\sqrt{N_e}$ coincide with the Rabi frequency, and hence should increase with $\sqrt{N_e}$. Indeed we find that Ω increases by a factor $1.45 \simeq \sqrt{2}$ when the number of particles N_e is doubled while keeping the mode volume constant, and it does not change with L_y, confirming $\tilde{\gamma}_0$ to be independent of it. The precise value is also quite close to the graviton-polariton effective model and the discrepancy gets smaller as the circumference L_y is increased.

We now comment on the role of cavity induced single particle potentials. Since the strength of these is of order g^2 (see Eq. (5.47)), they will not disturb the resonant, small g, splitting of the graviton-polariton doublet. However they will be important for a quantitative prediction of the corrections to the magnetoroton gap (Fig. 5.6) which only takes off-resonant contributions of order g^2. Note also that, while our results with $\hat{H}_\chi$ (withouth cavity vacuum-induced Stark shifts μ_k) indicate no collective enhancement in the renormalization of the magnetoroton gap, the single-particle terms (μ_k) which appear in Hamiltonian $\hat{H}_{\mu,\chi}$ (Eq. 5.47) are *collectively* enhanced by a geometric factor $L_x^2 \sim N_e$ when finite variations of the electric field g are present.

5.5. Ultra-strong coupling effects

In this section we analyze other important effects which arise in the so-called ultra-strong coupling regime. Although this term is used with specific tresholds for g in the

literature, we will be more naive and term ultra-strong coupling the generic regime where g is not infinitesimal. We will however carefully distinguish single-particle (g) and collective ($g\sqrt{N_e}$) ultra-strong coupling regimes.

In Sec. 5.5.1 we first discuss the impact of the cavity on FQH long-wavelength fluctuation, related to the FQH emergent metric and the finite frequency graviton mode. In Sec. 5.5.2 we then show how, in absence of inhomogeneus cavity-induced vacuum Stark shifts, the FQH liquid becomes unstable towards the formation of stripes. This however only arise at the single-particle strong coupling regime. A much stronger (collective) effect is instead imprinted by the non-uniform cavity vacuum-induced Stark shift (Sec. 5.5.3) which renormalize the energy cost of charged quasi-particles.

5.5.1. Cavity control of FQH geometry

An important property of FQH states which have received a lot of interest in recent years is their intrinsic geometry or metric [229–231, 233, 234]. This controls many of its ground state correlations and its long-wavelength gapped excitations quanta that, in analogy with gravitational theories, have been dubbed as "gravitons" [230–232]. Here we focus on ground state referring to Sec. 5.4 for the discussion about excitations.

A key ground state footprint of non-trivial geometry can be found in guiding-center correlations [234, 289], in particular via the guiding-center structure factor $S(\boldsymbol{q})$, Eq. (5.51), at small momenta. For a gapped FQH state it is possible to show [234, 289] that:

$$S(\boldsymbol{q}) \simeq S_4^{xx} q_x^4 + 2S_4^{xy} q_x^2 q_y^2 + S_4^{yy} q_y^4. \tag{5.76}$$

In the case of unbroken rotational invariance, we further have $S_4^{xx} = S_4^{xy} = S_4^{yy} = s_4$, with s_4 satisfying the Haldane bound $s_4 \geq (1-\nu)/24\nu$ saturated by the Laughlin state [289, 290]. Anisotropic interactions and/or anisotropic LLs [229] induce an intrinsic anisotropic geometry on the FQH liquid.

In Fig. 5.8 we show the effect of cavity fluctuations on the long-wavelength properties of $S(\boldsymbol{q})$, in the simplified case of $\hat{H}_\chi$ where single particle potentials are absent. The behaviour for momenta along x is still quartic and the proportionality factor S_4^{xx} is plotted against the collective coupling $g\sqrt{N_e}$ in Fig. 5.8(a). To extract it we look at the definition of $S(q_x)$ and expand for small q_x:

$$S_4^{xx} = \lim_{q_x \to 0} \frac{1}{4!} \partial_{q_x}^4 S(q_x) = \frac{1}{4M} \sum_{k,k'} k^2 k'^2 \langle \delta\hat{n}_k \delta\hat{n}_{k'} \rangle, \tag{5.77}$$

with $\delta\hat{n}_k = \hat{n}_k - \langle \hat{n}_k \rangle$. Finite-size effects with both N_e and L_y are expected, and signaled by the discrepancy with the known value $s_4 = (1-\nu)/24\nu$ at $g = 0$ shown as a dashed black line. Nonetheless, the finite g reduction is consistent and likely hold in the thermodynamic limit. The extraction of all three parameters in Eq. (5.76) is hindered by strong finite size effects along y. This is highlighted in the inset of

Fig. 5.8, where we show the full dependence of $S(q_y)$, which cannot capture the q_y^4 dependence. Qualitatively we still see that correlations along y are enhanced at finite g, as opposed to those on x. There is also an evident dependence on the cavity frequecy as highlighted in Fig. 5.8(b). As the cavity frequency increases, keeping $g\sqrt{\omega_c}$ fixed, we find a monotonous descrease on the metric squeezing, i.e. the magnitude of the corrections to S_4^{xx} decreases. This hints at the fact that for larger ω_c the effect of the cavity on the long-wavelength properties of the FQH is reduced, even though in Fig. 5.3 we found a qualitative similar coupling regime for the loss of transport quantization at two quite different cavity frequencies.

Another key signature of a distorted metric is the shape of the correlation hole of the G_2, shown in Fig. 5.9(c) for $g = 1$ (white line) and compared with the circular one of the $g = 0$ Laughlin case (blue line). As already noticed for other anysotropic FQH model wavefunctions [291], we also find that the short distance behaviour of the $G_2(r)$ changes from r^6 to r^2 going from isotropic ($g = 0$) to anisotropic cases ($g > 0$). We also note that the effect at long wavelength shown in Fig. 5.8 is greater in magnitude with respect to the reshaping of the correlation hole. As a rule of thumb, we expect the latter to be more sensible to short wavelength properties (electron-electron interactions) while the former to long-wavelength (cavity-mediated interactions). We suggest this to be related to the cavity-induced modifications of the magnetoroton dispersion (Sec. 5.4), which are collectively enhanced ($g\sqrt{N_e}$) only around the graviton part $q \to 0$, while at finite q seems only to see the single-particle coupling g. This is intuitively related to the fact that a uniform field gradient couples collectively to a uniform quadrupolar excitation, the graviton ($q \to 0$), and not to quadrupolar excitations at finite momenta, the rest of the magnetoroton dispersion (q finite).

We further remark that single-particle potentials, such as the cavity vacuum-induced Stark shift neglected so far, are also expected to shape the emergent geometry of the FQH liquid [229].

5.5.2. Stripe instability

We now explore even stronger values of the coupling g within the toy model $\hat{H}_\chi$ (Eq. (5.45)) with a uniform gradient and no single particle terms.

In Fig. 5.9 we present a sample of the numerical results obtained via DMRG simulations as discussed in Sec. 5.2.7. In order to get immediate insight on the state of the system we can look at the orbital density $\hat{n}_k$ in the left panels (a) and (b). The Laughlin state ($g = 0$ red line) shows a quantized bulk density $\hat{n}_k$ with modulations only close to the edge due to the open boundaries. A strong bulk modulation instead appears around $g \simeq 2-3$ for both system sizes $L_y = 16$ and $L_y = 20$. The modulation in orbital space follows a different pattern for the two system sizes. In particular, we have that the number of electron per peak are $n_S = 3$ and $n_S = 4$ for system sizes

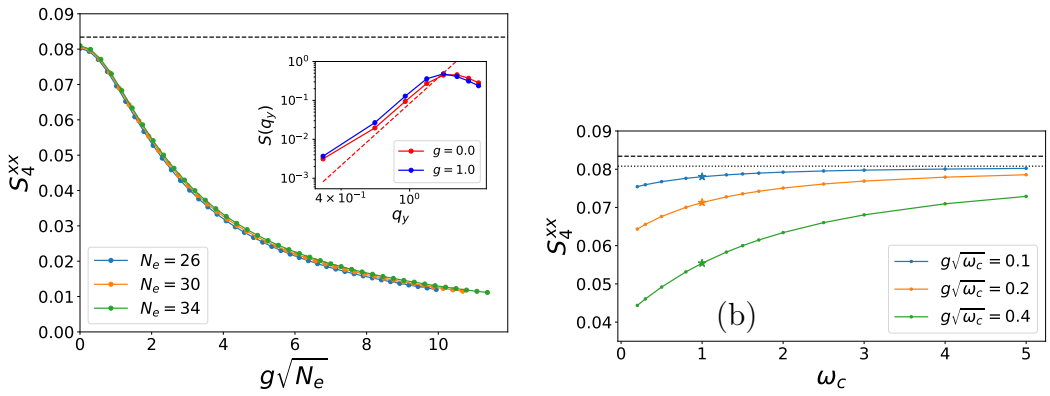


Figure 5.8.: DMRG results for the long wavelength static structure factor parameter S_4^{xx} in the model $\hat{H}_\chi$ as a function of (a) the collective coupling $g\sqrt{N_e}$ ($\omega_c = 1$) for different number of electrons N_e at fixed $L_y = 20$ and (b) as a function of the cavity frequency ω_c for different fixed coupling $g\sqrt{\omega_c}$ at $N_e = 21$ and $L_y = 16$. The black dashed line represent in both (a) and (b) the Haldane bound $s_4 = (1-\nu)/24\nu$ valid for isotropic interactions and saturated by the Laughlin at $g = 0$ in the thermodynamic limit, while the dotted line in (b) represent the Laughlin value ($g = 0$) at the finite system size studied there.. Inset: Static structure factor as a function of momenta along y for $g = 0$ (red) and $g = 1$ (blue) showing enhancement of the small wavevector part. The dashed red line represent the thermodynamic limit behaviour $S(q_y) = s_4\, q_y^4$ of the Laughlin state.

$L_y = 16$ and $L_y = 20$ respectively. In order to understand this we recall that the distance between two neighboring orbitals decreases as $\Delta X_k = 2\pi/L_y$. Hence to keep the distance between the peaks λ_S independent of L_y, the number of particle per peak n_S must increase. This constrains the generic behavior of λ_S to be

$$\lambda_S = \frac{2\pi}{L_y} 3 n_s(L_y), \tag{5.78}$$

with the factor 3 coming from the filling and where we expect $n_s(L_y) \propto L_y$ in the thermodynamic limit.

In order to check the 2D stripe nature of the phase we show the density-density correlator $G^{(2)}(\boldsymbol{r}_1, \boldsymbol{r}_2)$ in the center panels (c) and (d) as defined in Eq. (5.49). In the FQH phase, $g = 1$ panel (c), we find the characteristic correlation hole at short distances and a constant value at long distances as one should expect from a liquid state. Note that, as discussed in Sec. 5.5.1, the anisotropic nature of the cavity mode reflects into an anisotropic correlation hole. To highlight this, two lines are shown which tracks the maximum of the $G^{(2)}$, one for the Laughlin at $g = 0$ (blue line) and one for the $g = 1$ case (white line) whose $G^{(2)}$ is actually plotted. In the strong coupling regime instead, $g = 4$ panel (d), there is clear ordering on x and absence of ordering on y, confirming the interpretation of the phase as a stripe phase. Weak density modulations on y are present within the stripe, likely due to finite size effects and not to a true crystalline order in 2D.

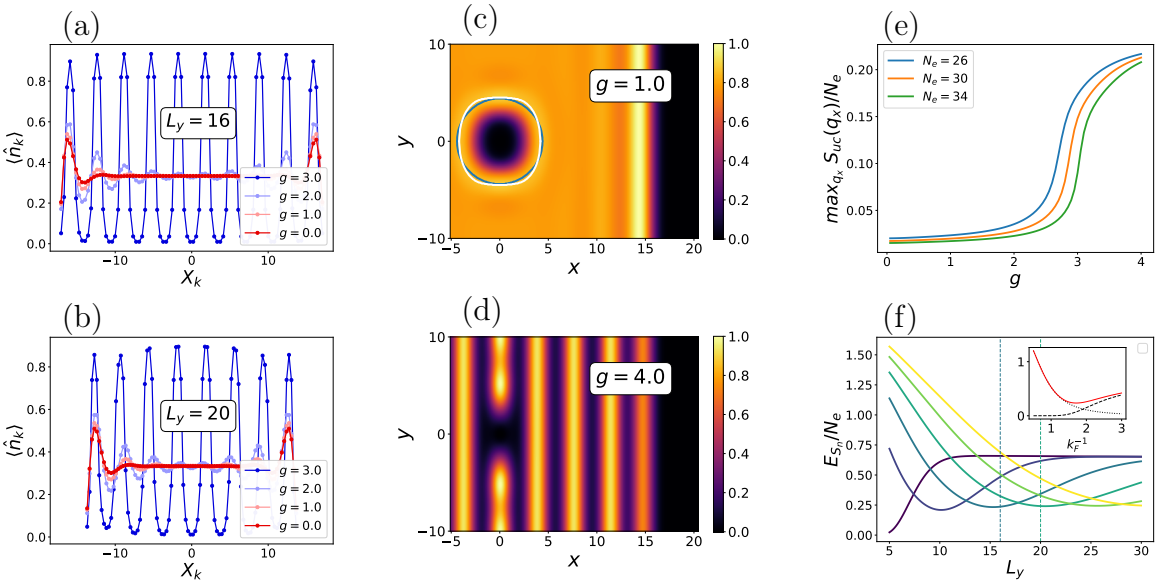


Figure 5.9.: DMRG (a-e) and photon mean-field (f) results in the ultrastrong coupling regimes in absence of vacuum-induced Stark shifts $\hat{H}_\chi$. Left panels (a,b) show the orbital occupancies from Laughlin state at $g = 0$ (red) to stripe phase at $g = 3$ (blue) for two circumferences of the cylinder $L_y = 16$ (a) and $L_y = 20$ (b) at fixed $N_e = 30$. Note that at fixed number of particles the size of the system along x reduces. Center panels (c,d) show the densisty-density correlations $G^{(2)}(0, \boldsymbol{r})$ in the two phases, at $g = 1$ for the FQH phase in panel (c) and at $g = 4$ for the stripe phase in panel (d). In the FQH phase (panel (c)) we also compare the shape of the correlation hole between $g = 1$ (white line) and the Laughlin $g = 0$ (blue line) by tracking the local maximum of the $G^{(2)}$. For both panels (c,d) $L_y = 20$ and $N_e = 34$. Panel (e) show the peak height of the static structure factor as defined in the main text and serve as an order parameter, $L_y = 20$. Panel (f) show the mean-field energy density of a stripe state $|S_n\rangle$ (see main text) for differnt number of electrons n per stripe (from $n = 1$ dark blue to $n = 6$ yellow) as a function L_y. The inset shows the thermodinamic limit ($L_y, n \to \infty$) value of the energy density as a function of $k_F^{-1} = 2\pi n/L_y$. Vertical dashed lines mark the $L_y = 16$ and $L_y = 20$ used in the other panels.

In the right top panel (e) we show an electronic order parameter which tracks the instability. We consider the maximum of the disconnected static structure factor $S_{uc}(\boldsymbol{q})$ at finite momenta, expected to scale with N_e in a charge density wave phase and not in a liquid phase. $S_{uc}(\boldsymbol{q})$ is defined as in $S(\boldsymbol{q})$, Eq. (5.51), but with the full guiding center density operator $\hat{\bar{\rho}}(\boldsymbol{q})$ replacing fluctuations $\delta\hat{\bar{\rho}}(\boldsymbol{q})$ in the definition. Panel (e) shows the normalized finite-momenta peak height of the disconnected static structure factor $\max S_{uc}(\boldsymbol{q})/N_e$ which is found around $\boldsymbol{q} \simeq (1.75, 0)$. At fixed L_y the transition point seems to shift towards higher values of g with increasing N_e. However, a more careful investigation is hindered by commensurability effects on y which likely renormalize the energy cost of the stripes for finite L_y. We note that considering the thermodynamic limit in the x direction with an infinite MPS is not possible with the present cavity-matter structure.

In order to better understand this instability, we propose a photon mean-field argument, detailed in Appendix D.3. While we have also investigated a different cavity elimination scheme based on a large cavity frequency, i.e. a Schrieffer-Wolff transformation, this results in vanishing cavity corrections to the only-matter model up to second order in g (see App. D.7) and hence cannot capture the instability. The photon-mean field instead can be seen as the limit case for $g\omega_c \gg \omega_c$ (or $\omega_c \to 0$ with $g\sqrt{\omega_c} \sim const$ as shown in Fig. 5.4(d)). In this limit, the state of the cavity has to be *classical* to leading order (vanishing light-matter entanglement) as $\hat{H}_c \ll \hat{H}_{DP}$ and only one of the two non-commuting terms for the cavity survives.

Neglecting light-matter correlations we can write the following photon mean-field (PMF) Hamiltonian:

$$\hat{H}_{\text{PMF}} = \hat{H}_{\text{int}} + \omega_c g^2 \left[\sum_k \frac{k^2}{2} \left(\hat{n}_k - \langle \psi | \, \hat{n}_k \, | \psi \rangle \right) \right]^2 , \tag{5.79}$$

where $\hat{H}_{int}$ is the electron-electron interaction (Haldane pseudopotential), $|\psi\rangle$ a generic electronic many-body state to be found self-consistently. The second term encodes the effect of cavity mediated interactions which in this form becomes quite simple to interpret. It exactly correspond to the variance of the quadrupole moment along x in the LLL:

$$\hat{Q}^{xx} = \frac{1}{2} \sum_k X_k^2 \, \hat{n}_k \tag{5.80}$$

whose fluctuations define the S_4^{xx} component of the FQH geometry (Eq. (5.76)). The squeezing of the geometry observed in Sec. 5.5.1, i.e. the reduction of S_4^{xx}, is a consequence of penalizing quadrupole fluctuations in one direction. The energy of the FQH liquid, at the photon mean-field level, is indeed renormalized as:

$$E_{FQH}/N_e \simeq \nu^{-1} S_4^{xx} \omega_c g^2 \tag{5.81}$$

The extreme limit where no fluctuations are present is represented by stripe states of the form:

$$|S_n\rangle = |\underbrace{0 \ldots 0}_{n} \underbrace{1 \ldots 1}_{n} \underbrace{0 \ldots 0}_{n}\rangle \tag{5.82}$$

which exactly minimize the cavity-mediated interaction energy. The energy cost of forming stripes is rather contained in the interaction energy $\hat{H}_{int}$, which in the case of Haldane pseudopotentials is shown in Fig. 5.9(f) as a function of cylinder circumference for different number n of electrons per stripe. In the thermodynamic limit ($L_y, n \to \infty$ with $L_y/n \to const$) the energy per particle is fixed $E_{S_n}/N_e \simeq 0.25$ and should be compared with the cavity mediated energy cost of the FQH state. Using the Laughlin state value for the quadrupole fluctuations S_4^{xx}, we get a crossing between E_{FQH} and E_{S_n} as a function of g around a transition point:

$$g^*_{PMF} \sqrt{\omega_c} \simeq 1 \, . \tag{5.83}$$

This value does not account for the reduction of S_4^{xx} which indeed push the instability towards higher value of g, as observed in numerics, but correctly captures the fact that once we look at rescaled $g\sqrt{\omega_c}$ the instability arises at roughly the same value (~ 2 for the volume studied in Fig. 5.3). Another ingredient which is missing and instead should favor the stripe state is the inclusion of fluctuations on top of the classical state depicted in Eq. (5.82). Already the numerical results on the orbital occupation (Fig. 5.9(a,b)) show that at finite g the state is not exactly $|S_n\rangle$. The nature of the phase at g large but finite should be understood as an array of Tomonaga-Luttinger liquids, one for each stripe, with a sliding symmetry as elaborated in Appendix D.5. We also remark that all this discussion assumes a cancellation of single particle potentials, external potentials W and cavity vacuum-induced Stark shifts μ_k.

Still, within the assumption of cancellation of single-particle potentials, we emphasize our results regarding the stripe transition are not conclusive. In fact, such a conclusive statement about the strong-coupling states is very hard to formulate within computational methods available (see Appendix D.6). The answer to this question likely depends on the inclusion of longer range Coulomb interactions and is left for future works.

5.5.3. Vacuum-induced Stark shift of quasi-particle energy

We now reintroduce the cavity vacuum-induced single particle Stark shift and study the full LLL Hamiltonian $\hat{H}_{\chi,\mu}$ of Eq. (5.47). Moreover, we change the spatial profile of the cavity mode, which is now a parabola with a minimum at the center, thus a gradient varying linearly from $-2g$ to $2g$, as shown in Fig. 5.10(a) and explained in Sec. 5.2.6. This mimics the experimental configurations of Ref. [43] where the cavity field intensity is minimum in the middle and higher towards the edges, producing a potential which tries to confine charge.

In Fig. 5.10 we show DMRG simulations for the ground state and charged quasi-particle states of $\hat{H}_{\chi,\mu}$. Quasi-particle states have been already studied via DMRG on both infinite [243] and finite [270] cylinders. Converging such excited states is relatively convenient as they live in a different total momentum sector K_y. Note that in finite momentum sectors, states are not inversion symmetric with respect to $x = 0$. In order to check the charged quasi-particle nature, we show the density of such states compared to the *vacuum* FQH liquid (Fig. 5.10(b)) and the integrated charge difference (Fig. 5.10(c)) between the vacuum case and FQH state:

$$\int^x \delta n = \int^x \mathrm{d}x' \, \langle \hat{n}(x') \rangle_{FQH+qp} - \langle \hat{n}(x') \rangle_{FQH} \tag{5.84}$$

This quantity shows a jump of $q = +1/3$ near the center of the cylinder where the quasi-particle is created and a corresponding jump of $q = -1/3$ towards the right edge where a quasi-hole is also created in order to ensure charge neutrality. The $g = 0$ and $g = 0.09$ case overlap, giving (inderect) evidence of a stable quasi-particle charge.

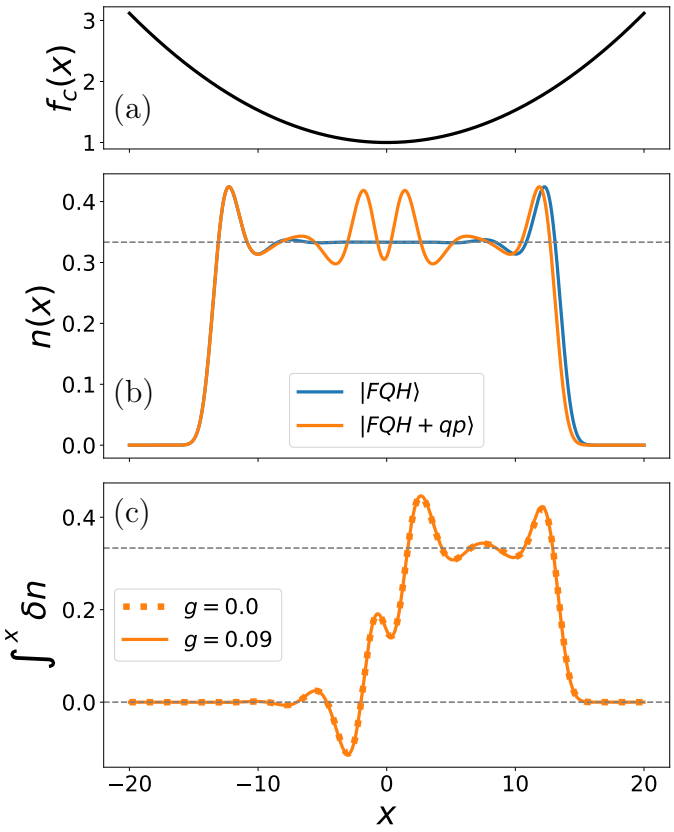


Figure 5.10.: (a) Cavity mode profile under consideration. Note that the spatial dependence of the vacuum-induced Stark shift is governed by $f_c^2(x)$. (b,c) DMRG results for the density profile quasi-particle states in the full Hamiltonian $\hat{H}_{\chi,\mu}$ of Eq. (5.47). (b) Real space density of the FQH ground state (blu) and of the quasi-particle state (orange). (c) Integrated density difference between ground state and quasi-particle state at $g = 0$ (dotted) and $g = 0.09$ (full). Two jumps of $\pm 1/3$ occur at $x \simeq 0$ and $x \simeq L_x/2$ corresponding to a bulk quasi-particle and a quasi-hole pushed to the edge of the system. The cavity does not affect the quasi-particle state density. The system size is $L_y = 16$ and $N_e = 24$. Dashed lines mark the $1/3$

The main effect of the cavity is in the energy of such quasi-particles, as shown in Fig 5.11. Here we measure the energy of the quasi-particle state E_{qp} described above relative to the ground state energy E_0, hence the gap $\Delta E_{qp} = E_{qp} - E_0$. The data collapsed performed with different system sizes shows how the energy scale controlling the quasi-particle energy renormalization is:

$$\Delta E_{qp}(g) - \Delta E_{qp}(0) \simeq -2.4\, r^2 \omega_c g^2 N_e \simeq \\ \simeq -2.4\, \frac{r^2 \Omega^2}{\Delta_0} \tag{5.85}$$

where Ω is the same collective Rabi frequency controlling the graviton-polaritons (Eq. (5.75)) and $r = L_x/L_y$ is the aspect ratio. The prefactor is fitted from the numerical data. The physical origin of the lower cost for creating quasi-particles is the vacuum-induced Stark shift introduced by the spatially dependent cavity mode. Indeed this

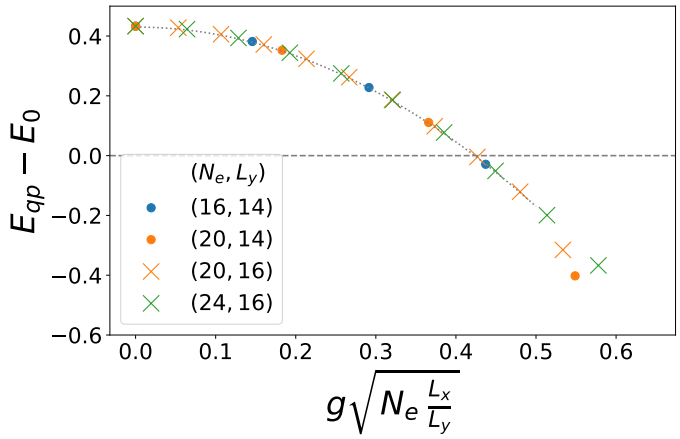


Figure 5.11.: DMRG results for the quasi-particle energy gap over the ground state as a function of a rescaled coupling for various system sizes (N_e, L_y) in presence of the vacuum Stark shift (using $\hat{H}_{\chi,\mu}$). The data collapse indicate that the energy scale governing the renormalization is a collective one $\sim g\sqrt{N_e}$ and is the one of the vacuum Stark shift (see Eq. 5.47). Dashed horizontal line marks zero energy, while the dotted line is a parabolic fit $y = 0.43 - 2.4x^2$.

favors having a charged quasi-particle created in the center where the field fluctuations are lower. At strong enough couplings, the pristine FQH liquid alone is not the total ground state anymore ($\Delta E_{qp} < 0$) and quasi-particles can be created in the bulk. This can also be understood in terms of a renormalized area and hence filling ν of the system, which is now subject to an extra trapping potential. At even stronger couplings this single particle potential likely give rise to phase separation, as we find for small systems in Appendix D.1. This scenario bears a lot of similarities with cold atom set-ups, where the role of trapping on many-body system has been extensively studied. Note that in our case, thanks to the incompressibility of the FQH liquid which is mantained in presence of the non-local cavity mode, creating a quasi-particle always cost a finite amount of energy.

5.6. Experimental discussion

In this section, we discuss in more detail the implications of our theoretical and numerical findings for relevant experimental conditions in solid-state systems.

Non-uniform gradients.— The choice of studying uniform gradients has simplified our analysis so far as it enabled to characterize a simpler uniform effect of the cavity mode. However in realistic scenarios [43] this is not in general the case. In particular the vacuum Stark shift effect discussed in Sec. 5.5.3 will depend on the structure of the cavity mode. On the other hand the formation of graviton-polariton is not hindered by

the inclusion of smoothly varying field gradients (inset of Fig. 5.12(a)), as we explicitly verify in Fig. 5.12 (b). The blue line represent the reference uniform linear gradient (i) while the orange one is a parabolic profile (ii). Note that we choose to compare two cases such that the "average" gradient is the same, namely in the case (ii) the gradient is 0 in the bulk and twice the uniform value of case (i) at the edge. The bigger Rabi splitting observed in the non-uniform case can be rationalized by noting that the effective coupling constant is likely averaged as $g_{\text{eff}} \simeq \sqrt{\int \mathrm{d}x\, g^2(x)}$, thus giving two slightly different Rabi splittings in the two cases. For completeness we also show that the stripe instability appearing in absence of vacuum Stark shifts ($\hat{H}_\chi$) depends on the local value of the electric field gradient (Fig. 5.12(a)), possibly leading to an inhomogeneous phase.

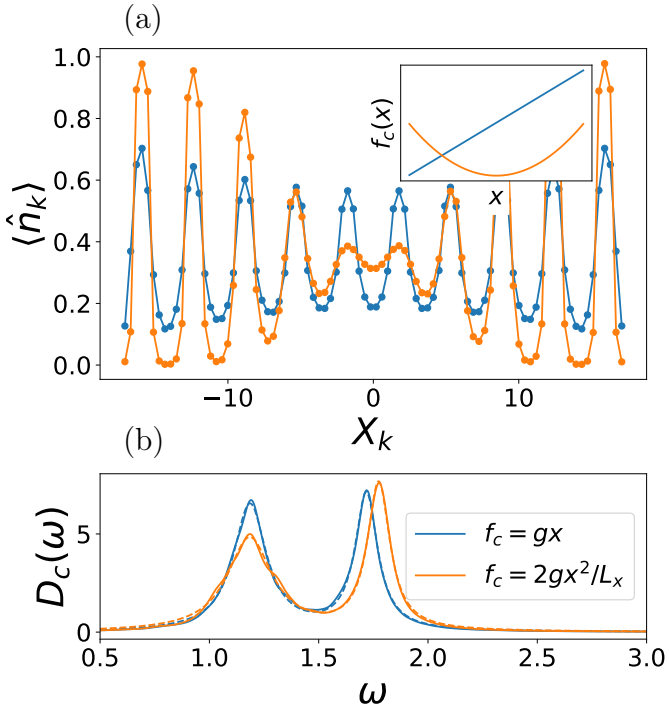


Figure 5.12.: Sample of numerical results comparing uniform and non-uniform cavity electric field gradients, using $\hat{H}_\chi$ without vacuum Stark shifts. In panel (a) we show DMRG results for the orbital occupation in the two cases of a uniform gradient (blue) and of a non-uniform gradient (orange). The corresponding mode profiles $f_c(x)$ are shown in the inset which correspond to a straight line $f_c = gx$ (uniform) and a parabola $f_c = 2gx^2/L_x$ (non-uniform). Note that with this choice the non-uniform case has field gradients going form zero (bulk) to twice the value of the uniform case (edge). In (a) $N_e = 30$,$L_y = 16$ and $g = 2.5$ so that the uniform case is unstable towards a uniform modulation but the non-uniform case clearly show two different behaviours in the bulk and at the edge. In panel (b) we show the cavity density of states in the two cases obtained via TDVP which still show the formation of graviton-polaritons with fitted rabi splittings $\Omega = 0.53$ and $\Omega = 0.59$ for uniform and non-uniform case respecively. In (b) $N_e = 15$, $L_y = 10$ and a smaller $g = 0.1$ so that the ground state is still a FQH liquid.

We further note that the assumption of a fixed mode function f_c is also an approx-

imation, which implicitly derive from the single-mode restriction of QED. Setting a precise limit of validity for this approximations is an open problem for most of cavity QED set-ups which try to achieve non-perturbative regimes, and is beyond the scope of this thesis.

Energy scales.— We now verify that a resonance condition between the typical energy scales of the electronic component (interaction V) and of the cavity (frequency ω_c) can be obtained in realistic systems. The strength of interactions are controlled by the Coulomb energy $E_C = e^2/4\pi\epsilon_0\epsilon_r l_B \simeq 56\,\mathrm{meV}\sqrt{B[\mathrm{T}]}/\epsilon_r$, which for a typical GaAs quantum well (with $n_e = 10^{11}\,\mathrm{cm}^{-2}$ and $\epsilon_r = 13$) at filling $\nu = 1/3$ (with $l_B = \sqrt{\nu/2\pi n_e} \simeq 7\,\mathrm{nm}$ and $B = \hbar c/e l_B^2 \simeq 12\,\mathrm{T}$) give $E_C \simeq 14\,\mathrm{meV}$. The energy of the collective modes is then a fraction of the Coulomb energy. In Ref. [228] the graviton energy has been measured as $\Delta_0 \simeq 0.05 E_C \simeq 0.65\,\mathrm{meV}$ for $\nu = 1/3$ but the precise value of the prefactor likely depends on the experimental details such as the well thickness and the strength of disorder [292]. On the cavity side, split-ring resonator devices with similar frequencies $\omega_c \simeq 2\pi \cdot 0.1 - 1\mathrm{Thz} \simeq 0.4 - 4\,\mathrm{meV}$ have been realized. In order to observe the polariton anticrossing (Fig. 5.7), direct tunability of the cavity frequency [293] or a full series of cavity devices covering a range of frequencies ω_c are likely to be needed.

In standard semiconductor systems there is in fact very little tunability of the frequency of the matter excitations. Changing E_C via a change in the magnetic field B imply also a corresponding change in the filling ν, which is expected to destabilize the targeted FQH state [227, 228]. We suggest that this issue may be resolved using graphene samples which allow for tuning the electron density n_e via a suitable gate [294], so to achieve a tunable interaction energy E_C at a constant filling ν.

Coupling strength.— The other important discussion is on the magnitude of the dimensionless coupling constant g used in this chapter. To do so we remind the definition of the coupling:

$$g = e\frac{E_c l_B^2}{\omega_c}\partial_x f_c(x)\ , \tag{5.86}$$

where f_c is the mode function, and $E_c = \sqrt{\hbar\omega_c/(2\epsilon_0 V_{\mathrm{mode}})}$ is the strength of vacuum fluctuations which account for the mode confinement.

As a first example, we consider the micron-sized split-ring resonator device used in Ref. [43]. We extract an average electric field gradient of roughly $\partial_x E_c^x = E_c \partial_x f_c(x) \simeq (1\mathrm{V/m})/10\mu\mathrm{m} = 10^5\,\mathrm{V/m}^2$ in relevant sample area $S \simeq 40\mu\mathrm{m} \times 200\mu\mathrm{m}$ and a cavity frequency $\omega_c = 2\pi \times 140\,\mathrm{GHz}$.[1] Considering again $n_e = 10^{11}\,\mathrm{cm}^{-2}$ and $\nu = 1/3$ which

[1] Higher field gradients by three orders of magnitude have been recently reported in Ref. [45].

give $l_B = 7\,\mathrm{nm}$, we get:

$$g \simeq \frac{10^5\,\mathrm{eV/m^2}}{2\pi \times 140\,\mathrm{GHz}}(7\,\mathrm{nm})^2 \simeq 10^{-9}. \tag{5.87}$$

The number of particle in the estimated sample area S is $N_e = n_e S \simeq 8 \times 10^6$, giving a rather small collective coupling $g\sqrt{N_e} \simeq 3 \times 10^{-6}$. Using Eq. (5.75) for the Rabi frequency and reminding that the adimensional coefficient $\tilde{\gamma}_0$ is of order unity, we would get:

$$\frac{\Omega}{\omega_c} = 2g\tilde{\gamma}_0\sqrt{N_e} \simeq 6 \times 10^{-6}. \tag{5.88}$$

A much stronger value of the coupling can be obtained using the nano-cavities of Ref. [254]: here, the tighter in-plane confinement of the electric field over distances on the order of a few 100 nm allows for a dramatic enhancement to the quadrupolar coupling to the graviton mode. The distance between capacitor plates L_x^c roughly controls the volume of the mode as $V_{mode} \sim (L_x^c)^3$, assuming a similar size of the resonator on y. While the reduced effective surface of the mode $(L_x^c)^2$ is compensated by an analogous reduction of the maximum number of electrons that can be fit in the cavity region $N_e \sim n_e(L_x^c)^2$, the reduction in the thickness of the cavity mode orthogonally to the plane $L_z \sim L_x$ strongly enhances field gradients. In particular we can expect the collective Rabi frequency of Eq. (5.88), controlled by field gradients, to be proportional to $L_x^{-3/2}$; contrary to the case of Landau polaritons and cyclotron transitions where the collective Rabi frequency is controlled by the electric field intensity [129, 295] hence scaling as $L_x^{-1/2}$. The larger value of the in-plane gradients are then expected to bring the graviton-polariton Rabi frequency up to values around $\Omega/\omega_c \sim 0.005$.

Given the rather small value of the quality factor of state-of-the-art micro- and nano-cavity devices $Q = \omega_c/\Gamma \simeq 10$ [43, 254], these designs still fall in the weak coupling regime $\Omega/\omega_c < Q^{-1}$ but the active on-going progress in the fabrication technology of high-Q cavities [296] make us optimistic about entering the strong-coupling regime with well-resolved graviton-polaritons in a next generation of samples. Considering other type of resonators could be beneficial as well as a more ad-hoc design for the resonators which enhances field gradients. In this respect we remark that a strictly uniform gradient is not necessary and also slowly varying gradients couple to the $q \simeq 0$ collective mode.

Then we also mention that slightly greater couplings can be also be achieved by looking at more dilute FQH liquids where, at a given filling ν, one has a larger ℓ_B. For example reducing the electronic density of the quantum well gives $g\sqrt{N_e} \propto l_B^2\sqrt{n_e} \propto 1/\sqrt{n_e}$ or focusing on higher fractions like $\nu = n + \bar{\nu}$ (with n integer and $\bar{\nu} < 1$) gives $g\sqrt{N_e^{\mathrm{eff}}} \propto \nu\sqrt{N_e\bar{\nu}/\nu}$ with N_e^{eff} the electrons available in the last partially filled LL.

Beyond single cavity mode. — As a last remark we discuss the possible effect of a more complex electromagnetic enviroment, expecially related to physics discussed

in Sec. 5.5. Without entering too much into the details, we point out two different contributions that are neglected in our modelling. The first is the presence of higher frequency LC resonances or other plasmonic modes which and are expected to give contributions similar to what has been discussed so far. These will certainly contribute to vacuum Stark shift effects as well as enter in the determination of the FQH emergent geometry. The second important one is the modification of Coulomb forces, both at the single particle and many-body level [253]. The former will have a similar role as the vacuum Stark shift of the LLL. The latter has actually been automatically neglected by considering an electron-electron interaction, the first Haldane pseudopotential, independent from the cavity setting. Changing the precise form of the only-matter interaction potential could provide a nice handle on the isotropy of the quantum metric in the underlying FQH liquid [229] as well on the magnetoroton dispersion or even drive itself instabilities in higher LL [249].

5.7. Conclusions and outlook

In this chapter we have developed a theoretical framework, readily generalizable to experiments, in which it is possible to understand key effects of confined electromagnetic modes on lowest Landau level physics. Importantly, together with the proposed QED model, we have discussed a tensor network architecture which allows for an in depth study of ground state and spectral properties for large number of particles.

This allowed us to uncover many aspects of the interplay between quantum light and fractional quantum Hall physics. Here we summarize and discuss the main points:

- Constant cavity fields are decoupled from intra-Landau level correlations [240] in absence of an external potential. The coupling strength of the quantum light-matter interaction is directly proportional to field gradients and quadrupole moment of the electron fluid. Ref. [43] reported a higher resilience of FQH physics to cavity vacuum fluctuations with respect to the IQH effect. This can be traced back to the smaller value of the effective Rabi frequency, Eq. (5.88), coming from relatively weak field gradients.

- The quantized Hall response of the FQH liquid is stable against non-local cavity fluctuations. This theoretical results for FQH states is parallel to recent precise measurements of quantized Hall resistivity in the integer quantum Hall regime [44].

- A new entanglement structure in hybrid quantum Hall states is found. The role of quantum light is to introduce a “band" of chiral Luttinger liquids multiplets, each with an approximately quantized photon number and separated by a finite entanglement polariton gap.

- We predict the formation of graviton-polariton modes, describing the hybridization of the long-wavelength magnetorotons with cavity photons. The Rabi frequency is collectively enhanced and is directly proportional to the quadrupole matrix element of the gravitons. We confirm numerically the presence of a polariton doublet in the cavity density of states, smoking gun of the strong coupling regime.
- Cavity vacuum fluctuations can squeeze the FQH geometry [229]. The latter can be thought as a hidden variational parameter for the FQH liquid that is thus able to adapt to the long-range anisotropic interactions induced by the cavity.
- Off-resonant cyclotron transitions induce a vacuum Stark shift of the LLL independent of the cyclotron frequency ω_B. This can be used to locally renormalize the energy cost of quasi-particles, provided that the cavity mode is non-uniform.
- At electric field gradients that are strong at the single-particle level and assuming a cancellation of single-particle potentials, we find the FQH phase to be unstable towards sliding Luttinger liquids with strong density modulations in the cavity field gradient direction. The instability depend on the local value of the electric field gradient, thus strong non-uniform gradients give rise to non-uniform states.

The simple but rich scenario we discussed here gives a proof of principle on how cavity vacuum fields can be used to probe and control intra-Landau level correlations. This hopefully lays the ground for more detailed and complex many-body investigations, as well as serves as a motivation for a more careful analysis on which experimental cavity set-up best adapts to the need of strong field gradients. Below we give few possible interesting future directions.

As a first example, we remark that the peculiar chiral nature of the graviton excitation [228] has not entered our discussion, mainly because of the choice of the cavity mode. However, a set-up with a pair of chiral cavity modes have been recently demonstrated to be in a chiral-selective strong coupling regime with cyclotron transition [199]. We expect this set-up to be sensible to the chirality of the gravitons. This will also likely play a role in the FQH regime of a recently demonstrated optical pumping experiment [297], paving the way for a coherent control of FQH excitations. Tuning the cavity-modes can also be interesting to explore periodic spatial modulation with periodicity on the scale of few magnetic lengths, ranging from approximately 10nm to 100nm, achievable with subwavelength set-ups. This will results in coupling to finite momentum magnetoroton excitations. Another effect, likely important away from perfect fillings, is the interplay between the cavity electric field and disorder which allows for a non-trivial coupling to the constant part of the field.

From a more theoretical perspective, it would be interesting to extend our treatment to more complex FQH phases and the effect of a non-local mode on non-Abelian topological ordered states, such as the Moore-Read state. We can anticipate for exam-

ple that the presence of multiple magnetoroton branches will enrich the entanglement structure on one side and the landscape of polaritons on the other, possibly giving distinct signatures to the nature of the phases. Moving away from gapped liquids; it is also tempting to imagine scenarios where, starting from gapless states such as the $\nu = 1/2$ composite Fermi sea, the cavity can be used as a handle to induce instabilities towards desired states. It would also be intriguing to connect some of our findings – which are inherently related to bulk properties – to recent works focusing on edge dynamics [186].

Finally, from an experimental viewpoint, one immediate follow up is the extension of our treatment to different setups, including atomic systems in cavities and other solid state platforms. In those contexts, it will be interesting to exploit the strong matter-light correlations we report as a mean to probe so far unexplored features of quantum Hall states, such as their entanglement structure, and eventually understand whether such correlations can be utilized to access and control the functioning of topological quantum memories.

5.7.1. On recent experiment

I would like to now use the insights obtained in this thesis to analyze the results reported in Ref. [45], which were not known to us before posting our work [5].

Ref. [45] identifies electric-field gradients as responsible for the increase of transport activation gaps in FQH states in the range $1 < \nu < 2$ in a set-up very similar to what discussed in this chapter. According to the theory analysis in Ref. [45], electric field gradients allow for a long-range cavity-mediated attraction in the LLL which cancels the long-range tail of Coulomb interactions. This can make interactions effectively shorter ranged, thus increasing the magnetoroton gap of the FQH liquid. The situation we analyzed is very similar, i.e. it considers only LLL electrons and a uniform electric field gradient, and it differs mostly by the type of electron-electron interaction considered (Coulomb vs first Haldane pseudopotential) and the cavity frequency (here kept comparable to the interaction energy scales). Keeping this in mind, the following considerations are in order:

- In presence of sizable electric field gradients, the single particle inhomogeneous vacuum-induced Stark shift seems to dominate the ground state physics and the charged quasi-particle energies (Fig. 5.11). These effects (not discussed in Ref. [45]) are likely to be modified in a system with coulomb interactions which suppresses charge separation. However, as vacuum-induced Stark shifts are second-order in the gradients while the cavity-mediated interactions of Ref. [45] are of fourth order, their effect should be thoroughly analyzed.
- In our large scale numerical simulations, the renormalization of the finite momentum magnetoroton gap (Fig. 5.6) seems to be controlled by a single particle

coupling and not collectively enhanced by the number of particles or, equivalently, the size of the sample.

- We have provided strong evidence for the renormalization of the long-wavelength structure factor (Fig. 5.8). This effect should be included in single-magnetoroton-approximation estimate for the gap used in Ref. [45].
- The strength of bulk electric field gradients we have estimated for a similar set-up (Ref. [43]) at $\partial_x E_c^x \sim 10^5\, V/\mathrm{m}^2$ are too small, even at the collective level to produce sizable modifications. Ref. [45] uses an estimate valid for gradients localized at the sample edges, which is more than three order of magnitude larger than what used here. The formation of graviton-polaritons and their experimental detection via spectroscopy would give a direct way to measure the influence of such strong vacuum electric field gradients on the FQH liquid and give an indirect measure of them through the amplitude of the graviton-polariton Rabi splitting.
- FQH states in the regime $1 < \nu < 2$ are not are not spin-polarized [298] and the Zeeman energy is actually much smaller that the coulomb energy. In this regimes it is expected that spin-textures on top of charge excitations can affect the quasi-particle energies and hence transport gaps. A study of the impact of the cavity on this is still missing.

Overall, the strong experimental results of Ref. [45] have opened a new important avenue for the field of cavity quantum materials, showing the non-trivial interplay between strongly correlated quantum matter and cavity QED which still needs to be fully understood.

Chapter 6.

Chiral gravitons on the lattice

The focus of this chapter drifts from the theme of cavity-embedded system. Here we propose and study the properties of graviton-mode excitations in lattice Fractional Quantum Hall system, where continuum translation symmetry is lost. The results highlight how such excitations can be found away from continuum FQH liquids and pose cold-atom quantum simulators as natural settings where the physics of these excitations can be thoroughly analyzed.

6.1. Introduction

There is currently considerable interest in exploring topological phenomena in synthetic quantum platforms [145, 299–301], which offer fundamental and complementary information in terms of probes and modeling, compared to widely successful solid state experiments [302–305]. In particular, cold atoms in optical potentials have shown promising developments in realizing lattice models pierced by synthetic magnetic fields, broadly belonging to the dynamics of the paradigmatic Harper-Hofstadter Hamiltonian [306, 307]. The exploration of the fractional quantum Hall effect (FQHE), and, more broadly, strongly interacting topological matter, remains an overarching goal of such endeavor [308–316]. Building on the theory proposal of utilizing laser fields to modify atomic motions [307], early experiments have observed key properties of Harper-Hofstadter models [317, 318], from measuring the Chern number of its bands [319–321], to demonstrating and visualizing chiral edge currents in both fermionic [322] and bosonic [323] ribbons, as well as the chiral motion of interacting excitations [324]. More recently, a remarkable study [325] demonstrated coherent dynamics of interacting particles, a feat that remained so far elusive due to the intrinsic difficulty of combining interactions with time-dependent fields needed to introduce an effective magnetic field.

These recent developments naturally raise the question: to what extent can future experiments provide insight into genuine features of the FQHE? One particularly intriguing direction is the possibility of probing its rich spectral structure, including the presence of the recently proposed [229, 231, 289, 326, 327] and observed [228] chiral

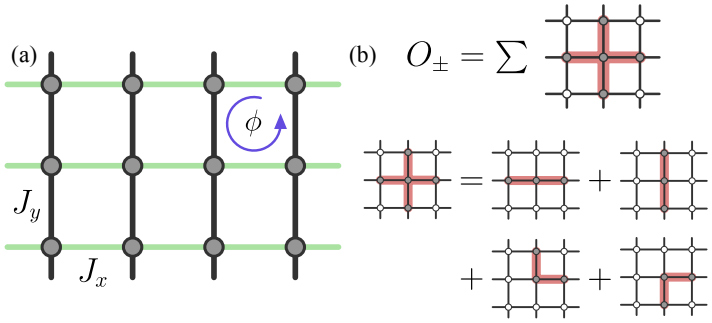


Figure 6.1.: Schematic representations of (a) the Harper-Hofstadter model and (b) the graviton operators we propose. The lattice model has tunneling rates J_x and J_y along perpendicular directions, and magnetic flux ϕ per plaquette. Chiral graviton operators are expressed as the sum of different correlated hopping terms centered at a given site.

graviton mode excitations. Chiral gravitons are spin-2 excitations stemming from the quantum geometric nature of quantum Hall wave functions [224], which, despite being usually embedded into the continuum [226], seems to remain a well defined quasiparticle whose decay into *dipolar* excitations is suppressed [231, 328]. Whether such excitations persist in lattice models of the FQHE – and if so, *how* they can be probed – remains an open question. These modes are particularly striking because their dynamics encode fluctuations of the underlying quantum metric [328], extending the geometric responses already familiar from the Hall viscosity and Wen–Zee shift [289, 329], and thereby providing a direct probe of the emergent geometry in FQHE states [229], with no direct analogue in non-interacting systems. A central challenge lies in identifying a low-energy emergent symmetry on the lattice [330, 331], that could protect gravitons from inevitable decay into the continuum due to the breaking of translational invariance induced by the lattice.

In this thesis, we report the existence of an emergent graviton mode in bosonic $\nu = 1/2$ Harper-Hofstadter models at diverse fluxes. We start by formulating a lattice ansatz for the chiral graviton operators, distilling fundamental ingredients out of its continuum counterpart: the chiral components of the kinetic stress tensor within the lowest Landau level (LLL) [332, 333]. We systematically corroborate our ansatz through an extensive numerical analysis, which combines exact diagonalization (ED) and matrix product state (MPS) [91, 92, 334] methods. We find clear signatures for the graviton mode by computing the spectral densities of the proposed lattice operators in various geometries. Finally, we discuss concrete protocols for the detection of gravitons in cold atom arrays. In particular, we describe a *geometric quench* [233, 234, 335, 336], that activates the graviton mode highlighting the connection of this mode to the quadrupolar charge correlations in the fluid [229, 337]. Additional information and method details are made available in the Supplemental Material (SM) [338].

6.2. Lattice model

We study the bosonic Harper-Hofstadter model, with generic anisotropic tunneling rates $J_x = J$ and $J_y = \eta J$ along x and y. The Hamiltonian is written as

$$H = -J \sum_{\mathbf{r}} \left(b^\dagger_{\mathbf{r}} b_{\mathbf{r}+\mathbf{e}_x} e^{\mathrm{i}2\pi n_\phi y/a} + \eta b^\dagger_{\mathbf{r}} b_{\mathbf{r}+\mathbf{e}_y} + \text{h.c.} \right), \tag{6.1}$$

where $b^\dagger_{\mathbf{r}}$ and $b_{\mathbf{r}}$ are the creation and annihilation operators at site $\mathbf{r}$, n_ϕ is the flux number, and a the unit spacing. We incorporate interactions by implementing the hardcore constraint: $b^2_{\mathbf{r}} = 0$. We consider rational fluxes of the form $n_\phi = 1/q$ (with $q \in \mathbb{N}^+$) and magnetic filling $\nu = 1/2$, achieved by setting the density of particles to $\rho_0 = \nu n_\phi$. This model is readily accessible in cold-atom [318, 339] and superconducting qubits [340, 341] platforms.

6.3. The continuum limit

We establish a link to the continuum theory of the FQHE. The continuum limit correspond to the case where $a/\ell_B = \sqrt{2\pi n_\phi}$ goes to zero. To take into account interactions coming from the hard-core constraint on the lattice, we employ a Holstein-Primakoff transformation [303], and motivated by the dilute limit of the system in the low-flux limit $\rho_0 \to 0$, we expand in powers of the local density $n_{\mathbf{r}} = b^\dagger_{\mathbf{r}} b_{\mathbf{r}}$. With this, we write:

$$\frac{b_{\mathbf{r}}}{a} \approx \psi(\mathbf{r}) - \frac{a^2}{2} \psi^\dagger(\mathbf{r})\psi(\mathbf{r})\psi(\mathbf{r}) + \cdots, \tag{6.2}$$

where $\psi(\mathbf{r})$ is a continuum bosonic field capturing collective (spin wave) excitations on top the reference vacuum state on the lattice. Replacing this expression into the lattice Hamiltonian of Eq. (6.1), we arrive at the continuum model:

$$H = \int \mathrm{d}^2 r \Big(- \frac{g^{ij}}{2m} \psi^\dagger D_i D_j \psi + \frac{\kappa}{2} \psi^\dagger \psi^\dagger \psi \psi \Big) + \cdots, \tag{6.3}$$

where we introduce the covariant derivatives $D_x = \partial_x + \mathrm{i}y/\ell_B^2$ and $D_y = \partial_y$, as well as the unimodular rank-2 tensor g_{ij}, with nonzero components $g_{xx} = 1/g_{yy} = \sqrt{\eta}$. The effective band mass reads $m = 1/2\sqrt{\eta}Ja^2$, while the strength of interactions scales as $\kappa = 4(1+\eta)Ja^2$. As a result, the cyclotron frequency is $\omega_B = 1/m\ell_B^2 = 4\pi\sqrt{\eta}Jn_\phi$, and the effective isotropic pseudopotential interaction within the LLL has strength $V_0 = \kappa/2\pi\ell_B^2 = 4(1+\eta)Jn_\phi$ [342]. The continuum model has two Ward identities we exploit below. They concern charge $\rho = |\psi|^2$ and momentum conservation:

$$\partial_t \rho + \nabla \cdot \boldsymbol{j} = 0, \qquad \partial_t (m\boldsymbol{j}) + \nabla \cdot \overleftrightarrow{\mathfrak{T}} = \boldsymbol{f}_{\text{ext}}, \tag{6.4}$$

where $\boldsymbol{j}$ is the particle current, and $\overleftrightarrow{\mathfrak{T}}$ is the stress tensor, whose divergence bounds the flux of momentum, modulo external forces $\boldsymbol{f}_{\text{ext}}$.

Proceeding to a LLL description, graviton operators are associated with the chiral components of the stress tensor [232, 332]. The LLL limit is equivalent to a zero mass approximation $m \to 0$ [330], where the free kinetic term gets quenched. To simplify matters we consider the isotropic limit ($\eta \to 1$). In this case, the continuum, long-distance field theory is written as follows:

$$\mathscr{L} = \psi^\dagger \mathrm{i}\partial_t \psi + 2\ell_B^2 \chi^\dagger D_z D_{\bar{z}} \psi + 2\ell_B^2 D_{\bar{z}} D_z \psi^\dagger \chi - \frac{\kappa}{2}|\psi|^4. \tag{6.5}$$

The LLL projection is enforced by the introduction of the Lagrange multiplier χ [333], which ensures that ψ is a linear superposition of wavefunctions of the form $e^{\mathrm{i}k_x x - (y + k_x \ell_B^2)/2\ell_B^2}$. The complex variables are defined as $z = x + \mathrm{i}y$ and $\bar{z} = x - \mathrm{i}y$, with the corresponding holomorphic derivatives are given by $D_z = \partial_z - \mathrm{i}A_z$ and $D_{\bar{z}} = \partial_{\bar{z}} - \mathrm{i}A_{\bar{z}}$, where $A_z = A_{\bar{z}} = -y/2\ell_B^2$ in the cylindrical gauge. The traceless part of the stress tensor is obtained from Noether's theorem:

$$\mathcal{T}_{zz} = -\ell_B^2 \chi^\dagger D_z^2 \psi, \qquad \mathcal{T}_{\bar{z}\bar{z}} = -\ell_B^2 D_{\bar{z}}^2 \psi^\dagger \chi, \tag{6.6}$$

where we use the fact that the operator $D_{\bar{z}}$ annihilates ψ to simplify our formulas. To eliminate the Lagrange multiplier we minimize the action with respect to $\psi^\dagger$, which leads us to the Schrödinger-type equation:

$$\mathrm{i}\partial_t \psi + 2\ell_B^2 D_z D_{\bar{z}} \chi - \kappa |\psi|^2 \psi = 0. \tag{6.7}$$

To solve the constraint, one must expand field operators onto different Landau levels [333], e.g., $\psi = \psi_0 + \psi_1 + \cdots$, and as we are interested in the LLL theory, then solve the equation for $\chi_2 = -\kappa|\psi|^2\psi/2$ that enters Eq. (6.6). In this form, we arrive at the chiral components of the stress tensor:

$$\mathcal{T}_{zz} = \frac{\kappa \ell_B^2}{2} \psi^\dagger \psi^\dagger \psi (D_z^2 \psi), \qquad \mathcal{T}_{\bar{z}\bar{z}} = \frac{\kappa \ell_B^2}{2} (D_{\bar{z}}^2 \psi^\dagger) \psi^\dagger \psi \psi. \tag{6.8}$$

The chiral graviton operators derive from the long wavelength mode of these operators, with $\mathcal{O}_- = \mathcal{T}_{zz}(\mathbf{q} \to 0)$ and $\mathcal{O}_+ = \mathcal{T}_{\bar{z}\bar{z}}(\mathbf{q} \to 0)$. In momentum space, these operators assume the form [232]:

$$\mathcal{O}_\pm \propto \sum_{\mathbf{q}} (q_x \pm \mathrm{i}q_y)^2 e^{-q^2\ell_B^2/2} \bar{\rho}_{\mathbf{q}} \bar{\rho}_{-\mathbf{q}}, \tag{6.9}$$

where $\rho_{\mathbf{q}}$ is the LLL guiding-center density operator.

6.4. Lattice stress tensor

We now return to the isotropic lattice model to look for operator representations of $\mathcal{T}_{zz}$ and $\mathcal{T}_{\bar{z}\bar{z}}$. The strategy is to inspect the momentum flux in the lattice, from where we bootstrap the operator that matches the stress tensor in the continuum. Given

charge conservation is also a symmetry of the lattice model, first we match the current operators. Using the discrete continuity equation, we obtain:

$$j_x(\mathbf{r}) = -\frac{\mathrm{i}J}{a}\big(b^\dagger_{\mathbf{r}} b_{\mathbf{r}+\mathbf{e}_x} e^{\mathrm{i}2\pi n_\phi y/a} - \text{h.c.}\big), \qquad j_y(\mathbf{r}) = -\frac{\mathrm{i}J}{a}\big(b^\dagger_{\mathbf{r}} b_{\mathbf{r}+\mathbf{e}_y} - \text{h.c.}\big), \tag{6.10}$$

where we add an $1/a$ factor that reflects its engineering dimension. Performing the low-density expansion, we find the current operators correctly reproduce: $\mathbf{j}(\mathbf{r}) = \boldsymbol{j}(\mathbf{r}) + \cdots$, where $\boldsymbol{j}(\mathbf{r}) = \frac{1}{2m}\big[\psi^\dagger(-\mathrm{i}\overleftrightarrow{\nabla})\psi - 2e\mathbf{A}|\psi|^2\big]$, and $A\overleftrightarrow{\nabla}B = A(\nabla B) - (\nabla A)B$, and all other parameters follow the definitions given around Eq. (6.3).

The second Ward identity, Eq. (6.4), only emerges in the continuum. Two key points are (i) this is not related to a conservation law in the lattice; and (ii) any direct computation of $\partial_t j_i = \mathrm{i}[H, j_i]$ shall produce not only differences of T_{ij} but also an external force contribution. To circumvent these limitations we combine long-distance properties with a lattice trick. First we consider diagonal terms T_{xx} and T_{yy}, which are not affected by an external force of Lorentz type $f_i \propto \epsilon_{ij} j_j$. We isolate this contribution by splitting the Hamiltonian into terms that generate motion along x and y: $H = H_x + H_y$. In this way the T_{ii} component can be directly identified from the evaluation of $\Delta T_{ii} = -\mathrm{i}m[H_i, j_i]$. Note that the expressions depend explicitly on the effective mass m, as we use continuum symmetry considerations to guide our lattice calculations. Taking the xx-component as an example, from this we find:

$$T^{full}_{xx}(\mathbf{r}) = mJ^2\Big[b^\dagger_{\mathbf{r}-\mathbf{e}_x}(2n_{\mathbf{r}} - 1)b_{\mathbf{r}+\mathbf{e}_x} e^{\mathrm{i}4\pi n_\phi y/a} + \text{h.c.} + 2n_{\mathbf{r}}\Big]. \tag{6.11}$$

We call this the full stress tensor as it carries a free contribution, quenched in the LLL projection. We can get rid of it by repeating the calculation with free bosons, and taking the difference. By doing this, we kill all but the correlated hopping terms:

$$T_{xx}(\mathbf{r}) = J\Big(b^\dagger_{\mathbf{r}-\mathbf{e}_x} n_{\mathbf{r}} b_{\mathbf{r}+\mathbf{e}_x} e^{\mathrm{i}4\pi n_\phi y/a} + \text{h.c.}\Big), \tag{6.12}$$

where we substitute $m = 1/2Ja^2$, and set the lattice spacing to unity. An analogous computation for the yy-component leads us to the identification of

$$T_{yy}(\mathbf{r}) = J\Big(b^\dagger_{\mathbf{r}-\mathbf{e}_y} n_{\mathbf{r}} b_{\mathbf{r}+\mathbf{e}_y} + \text{h.c.}\Big). \tag{6.13}$$

In analogy to the diagonal components, the off-diagonal T_{xy} must be generated by processes that divert current from one axis to its perpendicular direction, what motivates L-shaped correlated hopping moves as shown in Fig. 6.1(b). Such composite moves inherit the symmetry properties of the underlying square lattice. Broken parity implies this component should be odd under this symmetry transformation. Putting all together, we propose:

$$T_{xy}(\mathbf{r}) = J\Big(b^\dagger_{\mathbf{r}-\mathbf{e}_y} n_{\mathbf{r}} b_{\mathbf{r}+\mathbf{e}_x} e^{\mathrm{i}2\pi n_\phi y/a} - b^\dagger_{\mathbf{r}+\mathbf{e}_y} n_{\mathbf{r}} b_{\mathbf{r}+\mathbf{e}_x} e^{\mathrm{i}2\pi n_\phi y/a} + \text{h.c.}\Big). \tag{6.14}$$

The overall constant can be checked via the low-density, continuum expansion. For instance, for the zz-component we indeed find: $T_{zz} \sim \mathcal{T}_{zz}$. We then propose lattice

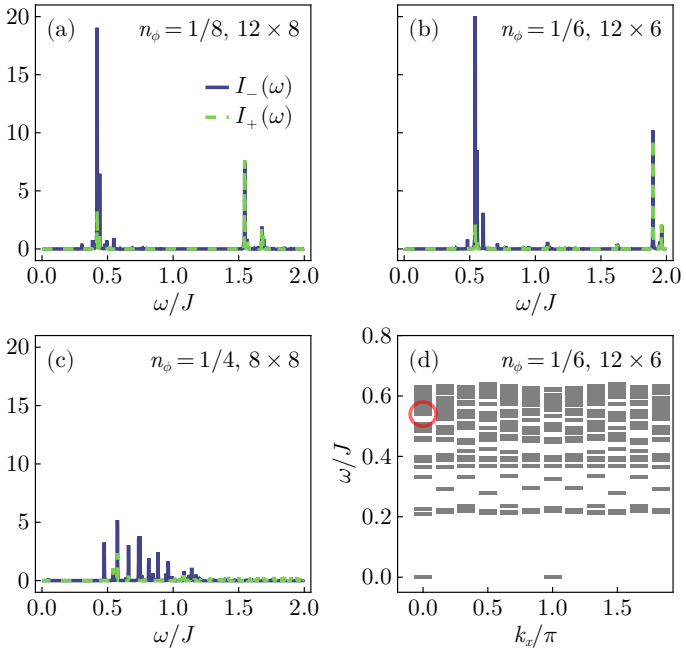


Figure 6.2.: Graviton weights $I_\pm(\omega)$ for: (a) 12×8 torus with $n_\phi = 1/8$ flux; (b) 12×6 torus with $n_\phi = 1/6$ flux; and (c) 8×8 torus with $n_\phi = 1/4$ flux. (d) Low-energy spectrum for a 12×6 torus. The red circle indicates the energy scale of the graviton-mode, $\omega_G \approx 0.54$. All results extracted from ED methods. Spectral densities obtained by taking $n_{\text{Krylov}} = 1000$ Krylov states, and a Lorentzian broadening factor of $\gamma = 0.001$.

forms for the chiral graviton operators O_+ and O_-, constructing them from the long-wavelength components of the stress tensor:

$$O_\pm = \sum_{\mathbf{r}} \Big[T_{xx}(\mathbf{r}) - T_{yy}(\mathbf{r}) \pm 2\mathrm{i} T_{xy}(\mathbf{r}) \Big]. \tag{6.15}$$

6.5. Graviton weights

We now numerically inspect the spectral density of the lattice chiral graviton operators in Eq. (6.15) at the isotropic point ($\eta = 1$). Their weights are defined as:

$$I_\pm(\omega) = \frac{1}{\mathcal{N}} \sum_n |\langle n| O_\pm |0\rangle|^2 \delta(\omega - E_n), \tag{6.16}$$

where E_n represents the excitation energy of the many-body state $|n\rangle$, and the normalization constant ensures $\int_{-\infty}^{+\infty} \mathrm{d}\omega\, I_\pm(\omega) = 1$. In Fig. 6.2 we show ED results on the chiral graviton weights for different fluxes (a) $n_\phi = 1/8$, (b) $n_\phi = 1/6$, and (c) $n_\phi = 1/4$. All results are obtained on the torus geometry at commensurate filling [1].

[1] Commensurate filling is obtained by loading the lattice with $N = \nu \times n_\phi \times A$ particles, with $A = L_x \times L_y$ the number of sites.

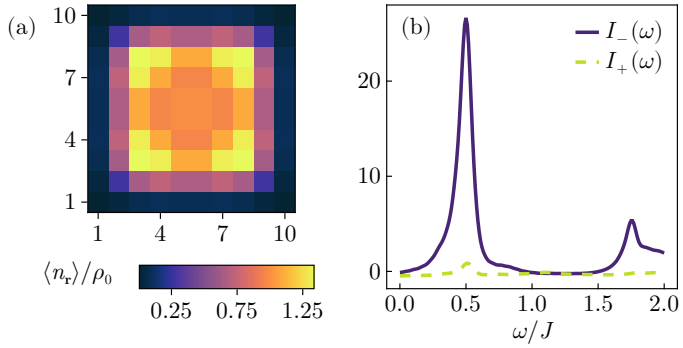


Figure 6.3.: Graviton mode on a FQHE droplet for $n_\phi = 1/6$ with $N = 5$ particles. (a) Expectation value of the density in the ground state, $\langle n_{\mathbf{r}}\rangle$. (b) Graviton response obtained through time evolution with a Lorentzian broadening of $\gamma = 0.05$. Total duration of $T = 100/J$, performed in time steps of $\delta t = 0.1/J$. MPS results obtained with a maximum bond dimension $\chi_{\max} = 300$, attaining truncation errors of the order $\varepsilon_{\text{trunc}} \sim 10^{-6}$.

Coming from low to high fluxes, we first consider the cases with $n_\phi = 1/8$ and $n_\phi = 1/6$. We observe a great resemblance in both scenarios, which feature a strong chiral signal. At low frequencies, most of the $I_-(\omega)$ weights are accumulated by a few peaks around $\omega \approx 0.5J$. We highlight the nontrivial character of such an emergent, spin-2 excitation in a lattice model whose maximum rotational symmetry is reduced to C_2, 180 degree rotations [2]. These states are hidden into the continuum, as shown explicitly in Fig. 6.2(d) where we plot the many-body spectrum for $n_\phi = 1/6$. The graviton-mode energy ω_{G} is slightly more than double the many-body gap, set by magnetoroton excitations ω_{R} [232, 266, 343]. Both ω_{R} and ω_{G} shift up as the flux n_ϕ is increased (see SM for more details), agreeing with the continuum limit effective model prediction, which sets the energy scale of interactions to $V_0 = 8Jn_\phi$. A rough linear fit of these values indicates the energy scale of the graviton-mode is given by $\omega_{\text{G}} \approx 0.42 \times V_0$ [233]. A second, nonchiral response is found at higher energies which roughly match the single-particle gap dictated by the continuum cyclotron frequency $\omega_B = 4\pi Jn_\phi$.

The graviton spectrum seems to drastically change once the flux reaches $n_\phi = 1/4$, as shown in Fig. 6.2(c). Even though the response remains chiral, the weight is now distributed on the whole continuum of states instead of a showing a sharp response as for the lower flux cases. We also find a similar chiral but broad graviton response function at $n_\phi = 1/4$ computed via the time-dependent variational principle (TDVP) [245–247] on long open cylinders [338]. It however remains not clear whether the mixing of the graviton mode with the many-body continuum at $n_\phi = 1/4$ is a fundamental feature of the lattice model, or a finite size effect.

[2] Although the maximum rotational symmetry of the square lattice is C_4, corresponding to 90 degree rotations, the use of a cylindrical gauge reduces it to a C_2 subgroup.

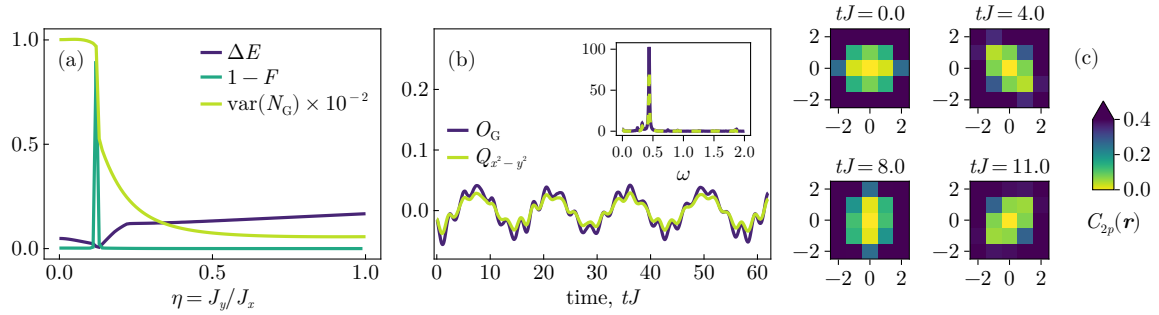


Figure 6.4.: Anisotropy study for $n_\phi = 1/8$ flux. (a) Ground state phase diagram characterization. Plot shows the behavior of energy gap, fidelity, and variance of the graviton number as a function of the anisotropy η in the $k_x = 0$ momentum sector. ED results for a 10×8 torus. (b) Quench dynamics on a 8×8 torus. Real time behavior of the monitored observables. The inset shows the Fourier transform obtained after a time evolution $T = 600/J$, with a damping $\gamma = 5/T$. (c) Snapshots of the two-particle function $C_{2p}(\mathbf{r})$ showing the clockwise precession of the correlation hole during the quench.

6.6. Open edges

Next we address the resilience of the chiral graviton response on a small FQHE droplet, relevant for current quantum simulation platforms [325, 339]. We use MPS methods to investigate a plane of size 10×10, with edges left open. The flux is that of $n_\phi = 1/6$ per plaquette, and we load the lattice with $N = 5$ particles [338]. Figure 6.3(a) shows the (normalized) local density on the ground state obtained with density matrix renormalization group (DMRG) [89, 90] simulations. Density oscillations sensitive to the system's geometry arise close to the hard egdes, but the bulk displays a tendency towards the uniform density $\langle n_{\mathbf{r}} \rangle / \rho_0 \approx 1$. The spectral weights are shown in Fig. 6.3(b), which are obtained via TDVP [338]. Note that in open geometries $O_\pm$ acquire finite expectation values which must be subtracted according to the definition of the graviton weights in Eq. (6.16). We observe a strong graviton signal, comparable to that found in the torus geometry of Fig. 6.2(c), indicating that such excitations remain robust and detectable even in small lattice droplets.

6.7. Quench dynamics

Geometric quenches, i.e., sudden changes in the mass anisotropy g^{ij}, have been proposed in continuum models as a simple way to activate graviton-modes [233, 234, 335]. This can be readily generalized to the lattice case via sudden changes of the tunneling ratios $\eta = J_y/J_x$, which are directly linked to g^{ij} in the continuum limit, see Eq. (6.3). As opposed to solid-state systems, such protocols are very natural for cold-atom experiments and quantum simulators in general. We first test the endurance

of the FQHE phase on the lattice as η is varied. In Fig. 6.4(a) we show ED results obtained for a torus of size 10×8 and flux $n_\phi = 1/8$. They indicate a transition only occurs at small $\eta \approx 0.12$, where the excitation gap ΔE closes and the ground state fidelity $F(\eta) = |\langle\psi(\eta)|\psi(\eta + \delta\eta)\rangle|^2$ drops. In the same plot we further include the variance of the number-like operator $N_{\mathrm{G}} = \frac{1}{2}(O_- O_+ + O_+ O_-)$, which not only captures the transition but its lower variance inside the FQHE phase is suggestive of an approximate symmetry leading to a well-defined graviton mode. We emphasize these results are compatible with larger volume, MPS simulations on finite cylinders [338]. Having set up a window of phase stability, we consider a slingshot dynamics around the isotropic point. We first prepare an anisotropic ground state with $\eta = 0.6$, and then change suddenly $\eta \to 1$. We choose to monitor two observables: the so called graviton displacement $O_{\mathrm{G}} = O_+ + O_-$ [232], and the quadrupolar density-density correlations $Q_{x^2-y^2} = \sum_{\mathbf{r}} (n_{\mathbf{r}} n_{\mathbf{r}+\mathbf{e}_x} - n_{\mathbf{r}} n_{\mathbf{r}+\mathbf{e}_y})$ [337]. Figure 6.4(b) shows the real-time dynamics of these observables for early times. We see both have very similar characteristics. Indicative of a close relationship among the graviton mode and the quadrupole density correlations, as occurs in continuum instances of the FQHE. Collecting data up to the final time $T = 600/J$ ultimately leads to the sharp Fourier responses shown in the inset. The two-particle function $C_{2p}(\mathbf{r} - \mathbf{r}') = \langle b^\dagger_{\mathbf{r}} b^\dagger_{\mathbf{r}'} b_{\mathbf{r}'} b_{\mathbf{r}} \rangle / \rho_0^2$ is another informative quantity during the dynamics. In Fig. 6.4(c) we show four snapshots of $C_{2p}(\mathbf{r})$ taken at different times. The snapshots reveal the clockwise precession of the elliptical correlation hole, with period $T_{\mathrm{G}} = 2\pi/\omega_{\mathrm{G}} \approx 14/J$. This is to be contrasted with the counterclockwise direction of the flux thus highlighting the negative angular momentum of the graviton-mode.

6.8. Conclusions

In this thesis, we assessed the existence of the chiral graviton mode in a Harper-Hofstadter model with hardcore bosons; a system of direct experimental interest [339]. Importantly, we introduced a new lattice operator representation for LLL graviton operators [232, 333], ensuring consistency with the continuum limit – an approach that could potentially be applied to recent findings in the context of fractional Chern insulators [319, 331, 337, 344]. To validate our approach, we performed a series of numerical simulations. For fluxes as high as $n_\phi = 1/5$, we found clear evidence of a sharp chiral graviton mode by computing the weights of the proposed lattice operators. We conducted additional simulations to (i) test the resilience of the graviton mode in small FQHE droplets and (ii) extract its dynamical response from a geometric quench. These results show that a direct experimental study of graviton-mode in quantum simulators is possible. Our study leaves several promising directions open for future research. Future questions regard the fate of the graviton at high fluxes as the overlap to Laughlin states decreases [345–347], and the extension to other non-Abelian FQHE states which are also realized in the Harper-Hofstadter model [312, 348]. Another step

would be to investigate realistic state-preparation and quench protocols, in order to test the stability of graviton excitations against heating and noise in current simulators [317, 321]. In addition to density observables, the recent current-based probes [325] could be even applied to investigate other quantities such as edge modes and the lattice stress tensor ansatz.

Chapter 7.

Dissipation and non-thermal states in cryogenic cavities

In this chapter we move from closed-cavity scenarios and study an open-cavity situation. In particular we focus on generic multi-mode cavities exposed to two thermal reservoirs, mimicking the set-up used in Ref. [40], and study the steady-steady properties of the photonic field. This serves as a starting point to understand the potential role of engineered non-thermal electromagnetic environments.

7.1. Introduction

Interaction between light and matter is at the heart of many fundamental physical phenomena. Recent research in this field has begun exploring more extreme regimes, revealing new effects such as the Floquet-driven dynamics of quantum systems [349–359], transient phases in light-induced phenomena [27, 360–370] and the vacuum effects arising from interaction with cavity fields.

Cavity quantum electrodynamics (cQED) provides a versatile platform for investigating light-matter interactions at the quantum level, with significant implications for quantum technologies and fundamental physics [371, 372]. In particular, the study of cavity systems at cryogenic temperatures has recently gained particular attention, since many promising phenomena occur at low temperatures, where thermal fluctuations are suppressed and quantum effects become more pronounced. Indeed, in the last few years several theoretical proposals have explored the potential of cavities as tools to control and manipulate properties and phases of matter at low temperatures, including superconductivity, topological phases, transport of charge and energy, ferroelectricity and many more [1, 4, 5, 10, 25, 29, 30, 33, 36, 37, 48, 52, 68, 70, 72, 74, 109, 121, 127, 373–383].

Recent experimental studies have also investigated these phenomena, including the effects of cavity on chemical reactions and topological states [42, 43, 46, 384–389].

In particular, Ref. [40] studied the effect of a cavity on 1T-TaS_2, revealing a large renormalization of its metal-insulator transition temperature, indirectly measured from the temperature of a nearby cryostat. The experimental observations can be interpreted in terms of a cavity-induced modification of thermal dissipations [40, 222, 390], rather than microscopic effects arising from the coupling of the material to the cavity.

Indeed, dissipation [279, 391, 392] is an important phenomenon which is often neglected in most theoretical models of strongly coupled light-matter systems. Dissipative processes suppress quantum correlations, and may destroy any collective phenomena that rely on the coherent coupling of matter to photons. This is particularly important, for the cryogenic cavity setups realized so far [40, 393], since the cavity is not completely shielded from the environment at room temperature T_e, while the mirrors of the cavity are cooled to a cryogenic temperature T_m. Thus, the field in the cavity is not in a vacuum state, as the cavity modes are populated with thermal photons leaking into the cavity. Although the effects due to thermal photons are generally expected to be small, they have been shown to produce substantial temperature corrections in certain cases [40, 222, 390, 394].

It is therefore important to characterize the properties of the cavity photons, in order to identify the regimes in which dissipation and thermal effects may be safely neglected. Previous studies have explored related scenarios, such as a single-mode cavity coupled to two baths [395] or the emission statistics of a driven cavity [396]. However, no comprehensive studies on multimode cavities coupled to multiple reservoirs currently exist in the literature.

The goal of this chapter is to bridge this gap, and provide a simple theory to calculate thermal effects in realistic cryogenic cavities. To that end, we investigate the dissipative dynamics and thermal properties of photons in a multi-mode cavity connected to two distinct reservoirs. We find that the photons are not thermally distributed, and that their properties crucially depend on the dissipation rates into the two reservoirs. This makes it possible to control and manipulate the distribution of the photons inside the cavity. We calculate the dissipation rates from a miscroscopic model and express them in terms of measurable macroscopic quantities. We also consider the effect of non-linear interactions between the photons and verify that they do not qualitatively alter the physics of the system. These are the main results of our work.

We model the cryogenic cavity as a multimode harmonic system coupled to two thermal baths at different temperatures: the cryogenically cooled mirrors at temperature T_m and the warmer external environment at temperature T_e. We write a Lindblad master equation to describe the dissipation into the two thermal reservoirs. While our formalism is very general and applies to different cavity setups – e.g. Fabry-Perot cavities, nanoplasmonic cavities, split ring resonators, etc [397, 398] – we focus on Fabry-Perot cavities, that most accurately describe current experimental setups [40, 393].

We initially assume that all cavity modes are independent, with each mode coupled

individually to the two reservoirs through photon creation and annihilation processes. The dissipation rates satisfy a detailed balance relation at the temperature of each respective reservoir. Unlike the typical case of a cavity coupled to a single reservoir, where the photons thermalize to the temperature of the reservoir, we consider a fundamentally different situation, where the two reservoirs maintain the photons in a non-equilibrium state. Indeed, solving the Lindblad equation shows that each photon mode obeys a thermal statistic with an effective temperature that depends on the frequency of the mode, so that the cavity modes are not thermalized. The effective temperature exhibits a crossover between two regimes: a *classical* regime at low frequencies where the temperature is a weighted average of T_e and T_m, and a *quantum* regime at high frequencies, where the temperature approaches the largest between the two reservoirs' temperatures.

The effective temperature crucially depends on the ratio between the dissipation rates into the mirrors and into the environment – this is another difference with the single reservoir case. Measurements of the cavity quality factor yield the sum of the two dissipation rates, and are not sufficient to determine them separately. To address this, we analyze a microscopic model of the coupling between the cavity modes and the mirrors or the external environment, and derive an expression for the respective dissipation rates. One of the key results of this chapter is to quantitatively express these rates in terms of measurable macroscopic quantities, such as conductivity, reflectivity and other properties of the mirrors.

Additionally, we investigate what happens if the cavity modes are coupled to each other by non-linear interactions. The interaction induces a partial thermalization between modes at different temperatures, smoothing out the frequency dependence of the effective temperature. However, this effect is perturbative, and does not alter the qualitative physics we observed.

The remainder of this chapter is structured as follows. In Section 7.2 we introduce the cavity setup and the model, writing down the Lindblad equation. In Section 7.3 we derive the Lindblad dissipative rates from a microscopic coupling and relate them to macroscopic properties of the cavity; we carry out this analysis separately for the mirrors (Sec. 7.3.1) and the external environment (Sec. 7.3.2). In Section 7.4 we solve the Lindblad equation and analyze the properties of the photons populating the cavity. In Section 7.5 we address non linearities in the cavity which mix different modes and investigate their effects on the effective mode temperatures. Finally, in Section 7.6 we draw our conclusions.

7.2. The model

We consider a very general setup, sketched in Fig. 7.1: an electromagnetic cavity that supports multiple photon modes ν, each modeled as a quantum harmonic oscillator

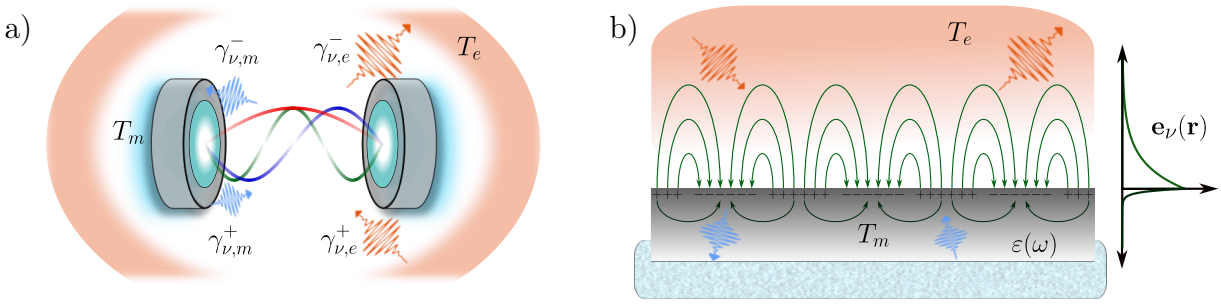


Figure 7.1.: Sketch of the prototypical system under consideration. (a) Fabry Perot cavity with the mirrors at temperature T_m and the surrounding environment at temperature T_e. Photons are exchanged by the cavity with the two reservoirs at the rates given in Eq. (7.6). (b) Approximate sketch of a nanoplasmonic cavity where the field is localized near a metal-vacuum interface. Photons are again lost due to interaction with the metal – at temperature T_m and with dielectric function $\varepsilon(\omega)$ – and with free space – at temperature T_e. The plot on the left sketches the decay of the field in the metal and in the vacuum.

with frequency ω_ν and volume volume V_ν.

We take into account two possible dissipation mechanisms corresponding to two distinct baths for each mode ν:

- emission into free space $\gamma_{\nu,e}$, i.e. the external electromagnetic environment, at temperature T_e ;
- absorption by the mirrors $\gamma_{\nu,m}$, at a colder temperature T_m .

The presence of two distinct thermal reservoirs places the cavity in a non-equilibrium setting, characterized by structured dissipative interactions where different photon modes interact differently with each reservoir. This captures the essential dissipative dynamics of different cavity settings (Fabry-Perot, nanoplasmonic structures, photonic crystal waveguides, etc.), whose different nature is encoded in the rates $\gamma_{\nu,e/m}$. For simplicity, we will often focus on the case of Fabry-Perot cavities with cryogenically cooled mirrors [40].

We describe the dynamics of the system using a Lindblad master equation formalism, which accounts for both unitary evolution and dissipative interactions with the reservoirs. We start from the total Hamiltonian of the system

$$H = H_c + H_{c-m} + H_m + H_{c-e} + H_e; \tag{7.1}$$

$$H_c = \sum_\nu H_\nu; \qquad H_\nu = \omega_\nu a_\nu^\dagger a_\nu, \tag{7.2}$$

where H_c is the cavity Hamiltonian, $H_{m/e}$ are the Hamiltonians of the mirrors and external free space respectively, H_{c-m} is the coupling between cavity and mirrors, and H_{c-e} is the coupling between the cavity and free space. The creation and annihilation operators for mode ν with frequency ω_ν are $a_\nu^\dagger$ and a_ν.

We can derive the Lindblad master equation for the density matrix ρ of the cavity field by tracing out the degrees of freedom of the mirrors and of free space. This is done explicitly in Section 7.3 under the assumption of weak coupling between cavity and the two reservoirs. Nonetheless, we can already write a phenomenological expression for the Lindblad equation based on some general assumptions:

$$\frac{d\rho}{dt} = -i[H_c, \rho] + \mathcal{L}_m(\rho) + \mathcal{L}_e(\rho), \tag{7.3}$$

where $\mathcal{L}_m(\rho)$ and $\mathcal{L}_e(\rho)$ are Lindblad superoperators representing the dissipative coupling of the cavity to the mirrors (at temperature T_m) and free space (at temperature T_e), respectively. Each mode is assumed to couple independently to the two reservoirs, with dissipation rates that are mode and reservoir-dependent, reflecting the distinct interactions with the mirrors and free space. Therefore, the Lindblad terms are written as

$$\mathcal{L}_\alpha(\rho) = \sum_\nu \gamma^-_{\nu,\alpha}\mathcal{D}[a_\nu](\rho) + \gamma^+_{\nu,\alpha}\mathcal{D}[a^\dagger_\nu](\rho); \tag{7.4}$$

$$\mathcal{D}[a](\rho) = a\rho a^\dagger - \frac{1}{2}\{a^\dagger a, \rho\}, \tag{7.5}$$

where $\alpha = m, e$ indicates the mirror or environment reservoir, while $\gamma^-_{\nu,\alpha}$ ($\gamma^+_{\nu,\alpha}$) is the dissipation rate for the destruction (creation) of a photon from mode ν due to the interaction with reservoir α.

The rates all satisfy the detailed balance relation given by $\gamma^+_{\nu,\alpha} = e^{-\omega_\nu/T_\alpha}\gamma^-_{\nu,\alpha}$. Since the exchange of photons with the reservoirs occurs via creation or destruction of bosonic excitations in the reservoirs, we can write the rates as

$$\begin{aligned} \gamma^-_{\nu,\alpha} &= \gamma_{\nu,\alpha}(1 + n_B(\omega_\nu, T_\alpha)); \\ \gamma^+_{\nu,\alpha} &= \gamma_{\nu,\alpha} n_B(\omega_\nu, T_\alpha), \end{aligned} \tag{7.6}$$

where $n_B(\omega_\nu, T_\alpha) = (e^{\omega_\nu/T_\alpha} - 1)^{-1}$ is the Bose-Einstein occupation number of the reservoir at temperature T_α and energy ω_ν. We have thus separated the contribution of thermal excitations in the reservoir – appearing in the n_B factor – from that of the spectral properties of the reservoirs, which are contained in $\gamma_{\nu,\alpha}$ [1]. Equations (7.4)-(7.6) combine to give $\mathcal{L}_\alpha = \sum_\nu \mathcal{L}_{\nu,\alpha}$ with

$$\mathcal{L}_{\nu,\alpha} = \gamma_{\nu,\alpha}\left((n_B + 1)\,\mathcal{D}[a_\nu](\rho) + n_B\mathcal{D}[a^\dagger_\nu](\rho)\right), \tag{7.7}$$

where, for simplicity of notation, we omitted the dependence on ω_ν and T_α.

The master equation (7.3)-(7.7) allows us to analyze the non-equilibrium steady state of the cavity, where the cavity modes can each acquire a distinct effective temperature depending on the relative strengths of $\gamma_{\nu,m}$ and $\gamma_{\nu,e}$.

[1] In principle, $\gamma_{\nu,\alpha}$ may have a slight dependence on the temperature, due to changes with temperature in the spectrum of the reservoir. This is more likely to occur for the mirrors rather than the external free space.

7.3. Derivation of the dissipation rates

In this section we derive the phenomenological Lindblad equation (7.3), starting from the microscopic Hamiltonian (7.1), for both the interaction with the mirrors and with free space.

The two derivations are treated separately in what follows. Before detailing out the calculations, we report the results, which allow to evaluate the dissipation rates in terms of macroscopic quantities.

The dissipation rate for the mirrors is given by

$$\boxed{\gamma_{\nu,m} = \frac{\sigma(\omega_\nu)}{2\epsilon_0}\frac{1}{V_\nu}\int_m d^3\mathbf{r}|\mathbf{e}_\nu(\mathbf{r})|^2.} \tag{7.8}$$

Here $\sigma(\omega_\nu)$ is the (real part of the) conductivity of the mirrors at frequency ω_ν, ϵ_0 is the vacuum dielectric constant. The volume of the mode ν is $V_\nu = \int d^3\mathbf{r}\varepsilon(\mathbf{r})|\mathbf{e}_\nu(\mathbf{r})|^2$, with $\varepsilon(\mathbf{r})$ the dielectric constant and $\mathbf{e}_\nu$ the mode function of the electric field. The integral $\int_m$ is calculated only over the volume of the mirrors. Equation (7.8) can be interpreted as the power dissipated by Joule heating in the mirrors, divided by the energy of the cavity electromagnetic field.

The dissipation rate into free space is given by

$$\boxed{\gamma_{\nu,e} = \sum_{\mathbf{k},\lambda}\frac{\pi\omega_\nu^2}{4VV_\nu}\left|\int d^3\mathbf{r}\,\varepsilon(\mathbf{r})\mathbf{f}_{\mathbf{k},\lambda}(\mathbf{r})\cdot\mathbf{e}_\nu^*(\mathbf{r})\right|^2\delta(\omega_\nu-\omega_{\mathbf{k}}).} \tag{7.9}$$

Here $\mathbf{f}_{\mathbf{k},\lambda}$ is the mode function of free space mode $\mathbf{k},\lambda$, and $V = \int d^3\mathbf{r}|\mathbf{f}_{\mathbf{k},\lambda}(\mathbf{r})|^2$ is its volume. Equation (7.9) can be effectively interpreted as the Fermi golden rule for the decay from the cavity modes into free space modes: it contains the relative overlap between the mode functions, summed over the modes with energy equal to ω_ν.

We reiterate that Eqs. (7.8) and (7.9) are very general, as they only require the knowledge of the conductivity and dielectric properties of the mirrors, which also determine the mode functions of both the cavity and free space.

Note that, when considering the dissipation due to one reservoir, we ignore the effect of the other reservoir. This assumption is justified if the mirrors and free space are uncorrelated and their ground state wavefunction factorizes. This is not true in general, as the mirrors and free space are coupled via an extra H_{m-e} term in the Hamiltonian (7.1). However, H_{m-e} is typically of the same order of magnitude as the coupling between mirrors and cavity. Within perturbation theory, the correlations between mirrors and environment in the ground state are of order $\sim H_{m-e}^2$, and produce a fourth order correction to the dissipation rates, while the leading order is quadratic in the couplings. Thus we can safely ignore the coupling between mirrors and external environment for the calculations that follow.

7.3.1. Mirror-cavity interaction

In this section we microscopically derive the dissipative dynamics due to the mirror-cavity interaction, i.e. $\mathcal{L}_m(\rho)$ in Eq. (7.3).

The interaction between cavity and mirrors is assumed to be a dipole interaction as

$$H_{c-m} = -\int_m d^3\mathbf{r}\, \mathbf{d}(\mathbf{r}) \cdot \mathbf{E}(\mathbf{r}), \tag{7.10}$$

where the integral is performed over the mirror volume. Here $\mathbf{d} = (d_x(\mathbf{r}), d_y(\mathbf{r}), d_z(\mathbf{r}))$ is the *dipole density* operator of the mirror, and

$$\mathbf{E}(\mathbf{r}) = i\sum_\nu \sqrt{\frac{\omega_\nu}{2\epsilon_0 V_\nu}}\big(\mathbf{e}_\nu(\mathbf{r})a_\nu - \mathbf{e}^*_\nu(\mathbf{r})a^\dagger_\nu\big) \tag{7.11}$$

the operator describing the electric field. The field polarization vector is given by $\mathbf{e}_\nu$, with ν labelling the photonic mode, and the mode volume is defined as $V_\nu = \int |\mathbf{e}_\nu(\mathbf{r})|^2 d\mathbf{r}$.

The Lindblad master equation describing the dissipation due to this interaction is derived from the microscopic model [279, 399]

$$\begin{aligned}\mathcal{L}_{\mathrm{m}}[\rho] = -\sum_\omega \int d^3\mathbf{r} d^3\mathbf{r}' \Gamma(\mathbf{r}-\mathbf{r}', \omega)\cdot \\ \cdot \Big[E_\omega(\mathbf{r})\rho E^\dagger_\omega(\mathbf{r}') - \frac{1}{2}\big\{E^\dagger_\omega(\mathbf{r}')E_\omega(\mathbf{r}), \rho\big\}\Big].\end{aligned} \tag{7.12}$$

Here

$$\Gamma(\mathbf{r}, \omega) \equiv \int_0^\infty d\tau e^{i\omega\tau} \langle \mathbf{d}(\mathbf{r}, \tau)\mathbf{d}(0,0)|\mathbf{d}(\mathbf{r}, \tau)\mathbf{d}(0,0)\rangle \tag{7.13}$$

is the one-side Fourier transform of the two-times dipole correlation function, and $\mathbf{E}_\omega(\mathbf{r}) = \mathbf{E}^{\mathrm{em}}_\omega(\mathbf{r}) + \mathbf{E}^{\mathrm{ab}}_\omega(\mathbf{r})$ is the electric field operator expressed in the energy eigenbasis (for the derivation see [7]), where

$$\begin{aligned}\mathbf{E}^{\mathrm{em}}_\omega(\mathbf{r}) &= i\sum_\nu \sqrt{\frac{\omega_\nu}{2\epsilon_0 V_\nu}}\delta(\omega_\nu - \omega)\mathbf{e}_\nu(\mathbf{r})\, a_\nu, \\ \mathbf{E}^{\mathrm{ab}}_\omega(\mathbf{r}) &= -i\sum_\nu \sqrt{\frac{\omega_\nu}{2\epsilon_0 V_\nu}}\delta(\omega_\nu + \omega)\mathbf{e}^*_\nu(\mathbf{r})\, a^\dagger_\nu,\end{aligned} \tag{7.14}$$

identify, for any frequency ω, two jump operators. We notice that $E^{\mathrm{ab}}_\omega E^{\mathrm{em}}_\omega = 0$, and thus we can write Eq. (7.12) as the sum of two contributions

$$\mathcal{L}_{\mathrm{m}}[\rho] = \mathcal{L}^{\mathrm{em}}_{\mathrm{m}}[\rho] + \mathcal{L}^{\mathrm{ab}}_{\mathrm{m}}[\rho], \tag{7.15}$$

with

$$\mathcal{L}^{\mathrm{em}}_{\mathrm{m}}[\rho] = \sum_\nu \gamma^-_{m,\nu}\Big[a_\nu \rho a^\dagger_\nu - \frac{1}{2}\big\{a^\dagger_\nu a_\nu, \rho\big\}\Big]; \tag{7.16}$$

$$\mathcal{L}^{\mathrm{ab}}_{\mathrm{m}}[\rho] = \sum_\nu \gamma^+_{m,\nu}\Big[a^\dagger_\nu \rho a_\nu - \frac{1}{2}\big\{a_\nu a^\dagger_\nu, \rho\big\}\Big], \tag{7.17}$$

$$\gamma^{\pm}_{m,\nu} = \frac{\omega_\nu}{2\epsilon_0 V_\nu} \int d^3\mathbf{r}\, d^3\mathbf{r}' \Gamma(\mathbf{r}-\mathbf{r}', \mp\omega_\nu)\mathbf{e}_\nu(\mathbf{r})\mathbf{e}^*_\nu(\mathbf{r}'). \tag{7.18}$$

The spatial integral can be rewritten as $\int d^3\mathbf{q}\tilde{\Gamma}(\mathbf{q},\omega_\nu)|\tilde{\mathbf{e}}_\nu(\mathbf{q})|^2$ by Fourier transforming to momentum space where $\tilde{\Gamma}(\mathbf{q},\omega) = \int d^3\mathbf{r} e^{-i\mathbf{q}\cdot\mathbf{r}}\Gamma(\mathbf{r},\omega)$. Since the electric field typically changes over distances much larger than the microscopic lengthscales of the mirrors, $\tilde{\Gamma}$ is approximately constant for small $\mathbf{q}$ and we can write

$$\gamma^{\pm}_{m,\nu} \approx \frac{\omega_\nu}{2\epsilon_0 V_\nu} \tilde{\Gamma}(0, \mp\omega_\nu) \int d^3\mathbf{r}|\mathbf{e}_\nu(\mathbf{r})|^2 \tag{7.19}$$

Using the Lehmann representation, see [7], it is possible to show that $\Gamma(-\mathbf{r},-\omega) = e^{-\beta_m\omega}\Gamma(\mathbf{r},\omega)$ – where $\beta_m = 1/T_m$ is the inverse temperature of the mirrors – so that $\tilde{\Gamma}(0,-\omega_\nu) = e^{-\beta_m\omega_\nu}\tilde{\Gamma}(0,\omega_\nu)$.

We can also relate Γ to the electric conductivity σ via the fluctuation-dissipation theorem. We use the Kubo formula [400]

$$\sigma(\mathbf{q},\,\omega) = \frac{1}{i}\int_0^\infty dt e^{i\omega t} \int d^3\mathbf{r} e^{-i\mathbf{q}\cdot\mathbf{r}} \left\langle [\mathbf{d}(\mathbf{r},t),\mathbf{J}]|[\mathbf{d}(\mathbf{r},t),\mathbf{J}]\right\rangle, \tag{7.20}$$

where the electric current density is $\mathbf{J}(\mathbf{r},t) = \partial_t\mathbf{d}(\mathbf{r},t)$. Deriving with respect to time inside the integral and integrating by parts, we find

$$\sigma(\mathbf{q},\,\omega) = \omega\int_0^\infty dt e^{i\omega t} \int d^3\mathbf{r} e^{-i\mathbf{q}\cdot\mathbf{r}} \left\langle [\mathbf{d}(\mathbf{r},t),\mathbf{d}]|[\mathbf{d}(\mathbf{r},t),\mathbf{d}]\right\rangle . \tag{7.21}$$

Explicitly writing out the expectation values in the Lehman representation (Ref. [7]) we obtain

$$\sigma(\mathbf{q},\omega) = \omega\,(1-e^{-\beta_m\omega})\,\tilde{\Gamma}(\mathbf{q},\omega). \tag{7.22}$$

This leads to the final expression for the jump rates

$$\begin{aligned}\gamma^{\pm}_{m,\nu} &= \pm\frac{1}{2\epsilon_0 V_\nu}\frac{\sigma(\omega_\nu)}{e^{\pm\beta_m\omega_\nu}-1}\int d^3\mathbf{r}|\mathbf{e}_\nu(\mathbf{r})|^2;\\ \gamma_{m,\nu} &= \frac{\sigma(\omega_\nu)}{2\epsilon_0 V_\nu}\int_m d^3\mathbf{r}|\mathbf{e}_\nu(\mathbf{r})|^2,\end{aligned} \tag{7.23}$$

where we have reintroduced the label m for the integral performed over the mirror space.

7.3.2. Environment dissipation rate

In this subsection we consider the coupling between the free space modes and the cavity modes and calculate the related dissipation rate. This coupling arises from the overlap between the cavity fields and the free space fields, which occurs inside the mirrors, see Fig. 7.2.

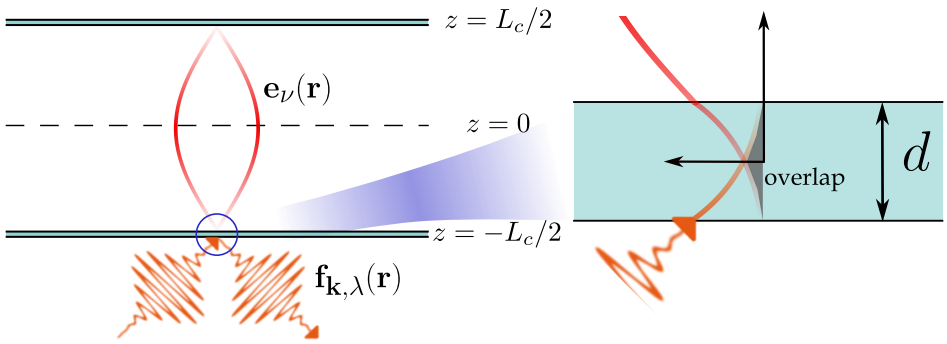


Figure 7.2.: Skectch of the electric field inside and outside of a Fabry-Perot cavity. The cavity is formed by two mirrors of thickness d located at $z = \pm L_c/2$. The fields modes inside the cavity are represented by $\mathbf{e}_\nu(\mathbf{r})$ while the free space modes are $\mathbf{f}_{\mathbf{k},\lambda}(\mathbf{r})$. The zoomed panel shows the overlap between the cavity modes and the free space modes, both of which decay exponentially inside the mirrors.

The electric field in space can be written as the sum of two terms $\mathbf{E}(\mathbf{r}) = \mathbf{E}_c(\mathbf{r}) + \mathbf{E}_e(\mathbf{r})$, where $\mathbf{E}_c(\mathbf{r})$ is the cavity field as in Eq. (7.11) and

$$\mathbf{E}_e(\mathbf{r}, t) = i \sum_{\mathbf{k},\lambda} \sqrt{\frac{\omega_k}{2\epsilon_0 V}} a_{\mathbf{k},\lambda}\, \mathbf{f}_{\mathbf{k},\lambda}(\mathbf{r}) e^{-i\omega_\mathbf{k} t} - \text{h.c.}, \tag{7.24}$$

is the free space field. The modes are labeled by the wavevector $\mathbf{k}$ and by λ, which accounts for polarization and for other quantum numbers that may arise from the geometry of the system. The frequency of the mode is $\omega_\mathbf{k}$ and $\mathbf{f}_{\mathbf{k},\lambda}$ is the respective mode function. In general, the environment modes $\mathbf{f}_{\mathbf{k},\lambda}$ vanish inside the cavity, while the cavity modes $\mathbf{e}_\nu$ vanish in the space outside the cavity, so that they overlap only inside the mirror, as discussed more in detail in the next subsection.

The total energy of the system is written as $\frac{\epsilon_0}{2}\int d\mathbf{r}\varepsilon(\mathbf{r})\mathbf{E}(\mathbf{r})^2$, where $\varepsilon(\mathbf{r})$ is the dielectric function at position $\mathbf{r}$. The magnetic field gives a contribution equal to that of the electric field, while the time average over the harmonic oscillations of the field contributes a factor 1/2. Taking the square of $\mathbf{E}$, we obtain *(i)* a term $\mathbf{E}_c^2$ that gives the Hamiltonian H_c of the cavity after quantization; *(ii)* a term $\mathbf{E}_e^2$ that gives the Hamiltonian $H_e = \sum_{\mathbf{k},\lambda} \omega_\mathbf{k} a^\dagger_{\mathbf{k},\lambda} a_{\mathbf{k},\lambda}$ of the free space modes; *(iii)* a cross term $2\mathbf{E}_e(\mathbf{r}) \cdot \mathbf{E}_c(\mathbf{r})$ which represents the coupling between cavity and free space.

Therefore, we can write the coupling Hamiltonian as

$$H_{c-e} = \epsilon_0 \int_m d^3\mathbf{r}\varepsilon(\mathbf{r})\mathbf{E}_e(\mathbf{r}) \cdot \mathbf{E}_c(\mathbf{r}), \tag{7.25}$$

where the subscript m indicates that the support of the integral is given by the mirrors, where the cavity and free space modes overlap.

In order to calculate the dissipation rate we proceed exactly as in Section 7.3.2 with

the substitution $-\mathbf{d} \to \epsilon_0 \mathbf{E}_e$. We obtain

$$\gamma^{\pm}_{\nu,e} = \frac{\epsilon_0}{2}\frac{\omega_\nu}{V_\nu}\int_m d^3\mathbf{r}\, d^3\mathbf{r}' \Gamma_e(\mathbf{r},\mathbf{r}',\mp\omega_\nu)\tilde{\mathbf{e}}^*_\nu(\mathbf{r})\tilde{\mathbf{e}}_\nu(\mathbf{r}') \tag{7.26}$$

where $\tilde{\mathbf{e}}_\nu(\mathbf{r}') = \varepsilon(\mathbf{r})\mathbf{e}_\nu(\mathbf{r}')$ and

$$\Gamma_e(\mathbf{r},\mathbf{r}',\omega) = \int_0^\infty dt e^{i\omega\tau}\langle \mathbf{E}_e(\mathbf{r},\tau)\mathbf{E}_e(\mathbf{r}',0)\rangle. \tag{7.27}$$

We use Eq. (7.24) to calculate the expectation value $\langle \mathbf{E}_e(\mathbf{r},\tau)\mathbf{E}_e(\mathbf{r}',0)\rangle$:

$$\langle \mathbf{E}_e(\mathbf{r},\tau)\mathbf{E}_e(\mathbf{r}',0)\rangle = \sum_{\mathbf{k},\lambda,\mathbf{k}',\lambda'} \frac{\sqrt{\omega_\mathbf{k}\omega_{\mathbf{k}'}}}{2\epsilon_0 V}\mathbf{f}_{\mathbf{k},\lambda}(\mathbf{r})\mathbf{f}^*_{\mathbf{k}',\lambda'}(\mathbf{r}')\cdot$$
$$\cdot\Big(\langle a_{\mathbf{k},\lambda}a^\dagger_{\mathbf{k}',\lambda'}\rangle e^{-i\omega_\mathbf{k}\tau} + \langle a^\dagger_{\mathbf{k},\lambda}a_{\mathbf{k}',\lambda'}\rangle e^{i\omega_\mathbf{k}\tau}\Big).$$

For a thermal state at temperature T_e, the expectation values are diagonal in $\mathbf{k}$ and λ, and involve the thermal distribution $n_\mathbf{k} = \frac{1}{e^{\omega_\mathbf{k}/T_e}-1}$:

$$\langle \mathbf{E}_e(\mathbf{r},\tau)\mathbf{E}_e(\mathbf{r}',0)\rangle = \sum_{\mathbf{k},\lambda} \frac{\omega_k}{2\epsilon_0 V}\mathbf{f}^*_{\mathbf{k},\lambda}(\mathbf{r})\mathbf{f}_{\mathbf{k},\lambda}(\mathbf{r}')\cdot$$
$$\cdot\Big((1+n_\mathbf{k})\, e^{-i\omega_k\tau} + n_\mathbf{k}\, e^{i\omega_k\tau}\Big).$$

Substituting into Eq. (7.27), we perform the Fourier transform $(\int_0^\infty dt e^{i\omega t}) = \pi\delta(\omega) - i\mathcal{P}\frac{1}{\omega}$ and retain the real part, obtaining

$$\Gamma_e(\mathbf{r},\mathbf{r}',\omega_\nu) = \sum_{\mathbf{k},\lambda}\frac{\pi\omega_\mathbf{k}}{2\epsilon_0 V}(1+n_\mathbf{k})\,\mathbf{f}_{\mathbf{k},\lambda}(\mathbf{r})\mathbf{f}^*_{\mathbf{k},\lambda}(\mathbf{r}')\delta(\omega_\nu-\omega_\mathbf{k}) \tag{7.28}$$

where we discarded the second term since it yields a $\delta(\omega_\nu+\omega_\mathbf{k})$ factor which is always zero given the positivity of both energies. Combining with Eq. (7.26) we find

$$\gamma_{\nu,e} = \sum_{\mathbf{k},\lambda}\frac{\pi\omega_\nu^2}{4VV_\nu}\left|\mathcal{A}_{\mathbf{k},\lambda,\nu}\right|^2\delta(\omega_\nu-\omega_\mathbf{k});$$
$$\mathcal{A}_{\mathbf{k},\lambda,\nu} \equiv \int_m d^3\mathbf{r}\,\varepsilon^*(\mathbf{r})\mathbf{f}_{\mathbf{k},\lambda}(\mathbf{r})\cdot\mathbf{e}^*_\nu(\mathbf{r}). \tag{7.29}$$

This expression contains $\mathcal{A}_{\mathbf{k},\lambda,\nu}$, the relative overlap between the cavity mode functions $\mathbf{e}_\nu(\mathbf{r})$ and the free-space mode functions $\mathbf{f}_{\mathbf{k},\lambda}(\mathbf{r})$ weighted by the dielectric function, summed over all free space modes at energy ω_ν.

7.3.3. Discussion and examples

The expressions for the dissipation rates Eqs. (7.8) and (7.9) are quite simple, intuitive and require the knowledge of a few ingredients.

The first two ingredients are the conductivity $\sigma(\omega)$ and the dielectric constant $\varepsilon(\omega)$ of the mirrors (or any other cavity medium). These are easily obtained experimentally via transport or spectroscopic measurements.

The other ingredients are the mode functions $\mathbf{e}_\nu$ and $\mathbf{f}_{\mathbf{k},\lambda}$. These are obtained by solving the Maxwell equations – which reduce to the Helmoltz equation for the electric field – for the geometry and the dielectric properties of the cavity. Such solution can be obtained analytically in some cases (e.g. a Fabry-Perot cavity) or numerically for more complicated cavity structures.

This point requires a more detailed discussion. In free space, the Helmoltz equation can be written as an eigenvalue problem of a self-adjoint differential operator. This way, the modes of the electromagnetic field are orthonormal, leading to a vanishing integral in Eq. (7.9). However, this argument is not entirely accurate when dielectric media (or boundary conditions) – which naturally divide the space into a cavity region and an external free space region [401] – are introduced. In such case, it is still possible to find orthonormal modes that separately satisfy the Helmoltz equation in each region (e.g. inside and outside the Fabry-Perot cavity, or the metallic substrate and the region above it for nanoplasmonic cavities) but at the price of some extra terms in the set of differential equations, which couple the modes in the two regions. These terms lead to an overlap between $\mathbf{e}_\nu$ and $\mathbf{f}_{\mathbf{k},\lambda}$, which typically occur at (or near) the boundary between the cavity region and the free space region. For a more formal discussion of these aspects, see for example Ref. [401].

In the following, we estimate the dissipation rates for two specific cavity setups: a Fabry-Perot cavity and a nanoplasmonic cavity.

Fabry Perot cavity – We consider a cavity delimited by two planar mirrors located at $z = \pm L_c/2$, so that fundamental frequency is $\omega_c = \pi c/L_c$. The mirrors have thickness $d \ll L_c$ and conductivity $\sigma(\omega)$, see Fig. 7.2. We assume the mirrors to be made of very good metals and to be highly reflective, so that the cavity has a high quality factor. Thus, in the range of frequencies of interest for our case, the negative dielectric constant is $\varepsilon(\omega) = 1 - \omega_p^2/\omega^2$, with the plasma frequency satisfying $\omega_p \gg \omega$. In such scenario, the electromagnetic field is exponentially suppressed inside the mirrors, with decay length $l_d \sim c/\omega_p$. The assumption of a high quality factor is equivalent to requiring that the mirrors are thick enough compared to the decay length, i.e. $\omega_p d/c \gg 1$.

As detailed in Ref. [7], in this regime the Fresnel equations dictate that the amplitude of the field inside the mirrors is reduced by a factor ω/ω_p compared to the field in the cavity volume. Therefore, we write the ratio $\frac{1}{V_\nu}\int_m d^3\mathbf{r}|\mathbf{e}_\nu(\mathbf{r})|^2$ in Eq. (7.8) as the square

of the amplitudes ratio times the ratio between the decay length and cavity length $\sim \left(\frac{\omega_\nu}{\omega_p}\right)^2 \times \frac{l_d}{L_c}$. Finally, we substitute the expression of ω_c and write the dissipation rates as

$$\gamma_{\nu,m} \sim \frac{\sigma(\omega_\nu)}{\epsilon_0}\left(\frac{\omega_\nu}{\omega_p}\right)^2 \frac{\omega_c}{\omega_p} \sim \omega_\nu \frac{1}{2}\frac{\sigma(\omega_\nu)}{\epsilon_0\omega_p}\frac{\omega_\nu\omega_c}{\omega_p^2} \tag{7.30}$$

A similar estimation can be performed to evaluate the overlap $\mathcal{A}$ of cavity modes and free space modes inside the mirrors in Eq. (7.29). Again from Fresnel equations, we find that both fields are suppressed by a factor ω/ω_p inside the mirror and exhibit an exponential decay $e^{-z\omega_p/c}$ ($e^{-(d-z)\omega_p/c}$) away from the surface that separates the mirror from free space (from the cavity). Therefore, their overlap integral $\mathcal{A}$ is simply given by $\sim (\omega/\omega_p)^2 d e^{-\omega_p d/c}\varepsilon(\omega) \sim d e^{-\omega_p d/c}$, where we have used $\varepsilon(\omega) \sim \omega_p^2/\omega^2$. Since the cavity mode volume is $\sim L_c \sim 1/\omega_c$, we estimate the dissipation rate as

$$\gamma_{\nu,e} \sim \omega_\nu^2\omega_c\frac{d^2}{c^2}e^{-2\omega_p d/c} \tag{7.31}$$

Combining Eqs. (7.30) and (7.31) we observe that the ratio of dissipation rates is given by:

$$\gamma_{\nu,m}/\gamma_{\nu,e} \sim \sigma(\omega_\nu)\ , \tag{7.32}$$

i.e. all the frequency dependence of the ratio of dissipation rates arise from the conductivity of the mirrors. Since most Fabry-Perot cavities operate in a frequency regime where the mirror conductivity is constant and equal to its dc value, they are well described by a frequency-independent γ_m/γ_e.

Nanoplasmonic cavity – We consider a very simple model of a nanoplasmonic cavity. A metallic substrate occupies the half space at $z < 0$, with vacuum at $z > 0$. The metal has dielectric constant $\varepsilon(\omega) = 1 - \omega_p^2/\omega^2$ and conductivity $\sigma(\omega)$, where $\omega_p \gg \omega$ is the plasma frequency. This configuration supports localized plasmonic modes that propagate along the x direction and decay exponentially away from the metallic surface in the z direction. The metallic substrate acts as the confining element of the cavity, similarly to the mirrors of a Fabry-Perot cavity.

The solution of the Maxwell equations, see Ref. [7], tells us that the electric field of a plasmon with frequency ω decays over a distance c/ω_p inside the metal and over a (much larger) distance $c\omega_p/\omega^2$ in the vacuum [398]. Moreover, the magnitude of the plasmonic field within the metal is smaller than the magnitude of the field in vacuum by a factor ω/ω_p. Thus, the main contribution to the volume of the mode $V_\nu \sim \int |\mathbf{e}_\nu|^2 \sim c\omega_p/\omega^2$ comes from the field in the vacuum.

The dissipation rate into the metal is then roughly equal to $\sim \frac{1}{V_\nu}\int_m |\mathbf{e}_\nu|^2 \sim 1/(c\omega_p/\omega^2)\times (\omega/\omega_p)^2 \times (c/\omega_p)$, where the first factor is the ratio of the square of the fields amplitude and the second factor is the ratio of the penetration lengths in the metal and in the vacuum. Precise calculations yield

$$\gamma_{\omega,m} = \frac{\sigma(\omega)}{2\epsilon_0}\left(\frac{\omega}{\omega_p}\right)^4 = \omega\frac{1}{2}\frac{\sigma(\omega)}{\epsilon_0\omega_p}\left(\frac{\omega}{\omega_p}\right)^3 . \tag{7.33}$$

The calculation of the dissipation rate into free space is more complicated, because the free space modes and the plasmonic modes overlap both in vacuum and inside the metal. The leading contribution arises from the overlap of the modes in the vacuum. We have to consider a finite propagation length of the plasmon along the metallic surface – which originates from losses in the metal – in order to break translational invariance, and thus momentum conservation, which would otherwise forbid any coupling between plasmons and free space modes [398]. Carrying out the calculations (details in Ref. [7]), we find

$$\gamma_{\omega,e} \sim \omega \left(\frac{\sigma(\omega)}{\epsilon_0 \omega}\right)^3 \left(\frac{\omega}{\omega_p}\right)^4 \sim \omega \frac{\omega}{\omega_p} \left(\frac{\sigma(\omega)}{\epsilon_0 \omega_p}\right)^3 . \tag{7.34}$$

In the case of nanoplasmonic cavities the ratio between the dissipation rates is then:

$$\gamma_{\omega,m}/\gamma_{\omega,e} \sim (\omega\epsilon_0/\sigma(\omega))^2 . \tag{7.35}$$

Assuming a typical Drude-Lorentz model, the conductivity is constant at low frequency and decays as $\sigma(\omega) \sim 1/\omega^2$ at high frequencies. Thus, $\gamma_{\omega,m}/\gamma_{\omega,e} \sim \omega^2$ and environment dissipation dominates at low frequencies, while $\gamma_{\omega,m}/\gamma_{\omega,e} \sim \omega^6$ and dissipation into the metal dominates at high frequencies.

7.4. Non-thermal cavity population

In this section we proceed to solve the Lindblad equation and find its steady state solution.

Under the assumptions of Section 7.2, each mode is independent, and the density matrix of the photon steady state factorizes into separate subspaces for each mode.[2] Thus $\rho = \bigotimes_\nu \rho_\nu$, where ρ_ν is the density matrix for mode ν, and the Lindblad equation for the entire system simplifies to a set of independent Lindblad equations for each mode according to:

$$\frac{d\rho_\nu}{dt} = -i[H_\nu, \rho_\nu] + \mathcal{L}_{\nu,m}(\rho_\nu) + \mathcal{L}_{\nu,e}(\rho_\nu), \tag{7.36}$$

where $\mathcal{L}_{\nu,m}$ and $\mathcal{L}_{\nu,e}$ are defined in Eq. (7.7).

We notice that Eq. (7.36) is equivalent to the Lindblad equation describing the coupling to a single thermal bath with total loss and gain rates:

$$\Gamma^+_\nu = \gamma^+_{\nu,e} + \gamma^-_{\nu,m} \qquad \Gamma^-_\nu = \gamma^-_{\nu,e} + \gamma^-_{\nu,m} . \tag{7.37}$$

[2] This is true even independently of the initial state, since inter-mode correlations decay exponentially over time.

These satisfy a detailed balance condition for an effective temperature T^*_ν:

$$\frac{\Gamma^+_\nu}{\Gamma^-_\nu} = e^{-\omega_\nu/T^*_\nu} \,. \tag{7.38}$$

Rearranging this detailed balance condition we find the effective temperature of the mode ν as:

$$\boxed{T^*_\nu = \frac{\omega_\nu}{-\log\left(r^-_{\nu,e} e^{-\omega_\nu/T_e} + r^-_{\nu,m} e^{-\omega_\nu/T_m}\right)}} \tag{7.39}$$

where we defined dimensionless relative rates:

$$r^-_{\nu,j} = \frac{\gamma^-_{\nu,j}}{\gamma^-_{\nu,m} + \gamma^-_{\nu,e}}, \qquad j = e/m. \tag{7.40}$$

We remark that T^*_ν in general depends on the mode ν thus giving an overall non-thermal steady state for the multimode cavity.

The result in Eq. (7.39) can also be found by calculating the Wigner function of the photon state and solving for the steady state, as detailed in Ref. [7].

The mode properties can also be characterized by the average occupation number $n_{\mathrm{ph},\nu} = \langle a^\dagger_\nu a_\nu \rangle$ and the probability $p_{n,\nu}$ to have n photons populating mode ν, defined as

$$n_{\mathrm{ph},\nu} = \langle a^\dagger_\nu a_\nu \rangle = \mathrm{Tr}(a^\dagger_\nu a_\nu \rho_\nu); \quad p_{n,\nu} = (\rho_\nu)_{nn}. \tag{7.41}$$

From Eqs. (7.36)-(7.39) it follows that each mode ν displays thermal properties with temperature T^*_ν, so that $\langle a^\dagger_\nu a_\nu \rangle = n_B(T^*_\nu)$ and $p_{n,\nu} = e^{-n\omega_\nu/T^*_\nu}$, .

We also comment on the relaxation of the cavity to its steady state. For simplicity, one can look at the relaxation rate of a coherence $\langle \hat{a}_\nu \rangle_{t=0} = \alpha_0$ for each mode ν. As discussed in Ref. [7], this relaxes with a combined rate $\gamma_{\nu,e} + \gamma_{\nu,m}$, independently of the effective temperature reached by the mode ν or the temperature of the individual baths. Moreover, for typical cavities, the total dissipation rate $\gamma_{\nu,e} + \gamma_{\nu,m}$ is in the range of MHz-GHz, meaning that relaxation to the steady state occurs on very fast timescales. This justifies studying directly the steady state properties and neglecting the transient dynamics.

We now more explicitly discuss some interesting scenarios for the mode dependent effective temperature T^*.

Fabry-Perot cavity. – The behavior of the effective temperature T^*_ν behavior as a function of the mode frequency ω_ν is plotted in Fig. 7.3 for different values of the ratio γ_e/γ_m, which we assume to be constant in frequency. As we have seen in Section 7.3.3, this is a good description of a Fabry-Perot cavity. The effective temperature exhibits two important regimes, namely a *classical* limit ($\omega_\nu \ll T_e, T_m$) and a *quantum* limit

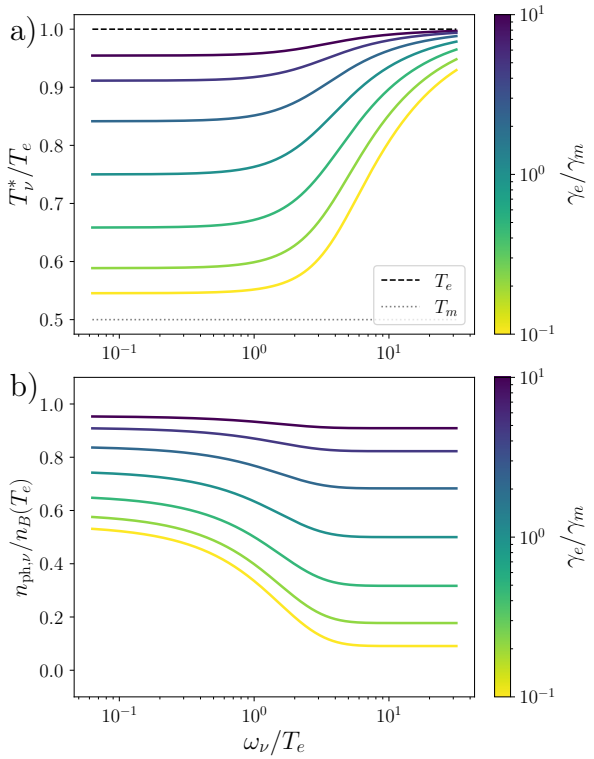


Figure 7.3.: Mode dependent effective temperature T^*_ν (a) and occupation $n_{\mathrm{ph},\nu}$ (b) for different constant bath coupling rates $\gamma_{\nu,e/m} = \gamma_{e/m}$ as a function of the mode frequency ω_ν. In particular lines go from electromagnetic enviroment dominated $\gamma_e/\gamma_m = 10$ (blue) to mirror dominated $\gamma_{\nu,e}/\gamma_{\nu,m} = 0.1$ (yellow). The mirror temperature is taken as half the electromagnetic enviroment temperature $T_m = 0.5T_e$. Note that the bosonic occupation is shown relative to the occupation at a fixed temperature T_e which becomes exponentially small when $\omega_\nu/T_e \gg 1$.

$(\omega_\nu \gg T_e, T_m)$. In these cases, assuming $T_e > T_m$ and expressing T^*_ν in terms of the temperature independent rates $\gamma_{\nu,e/m}$, we have:

$$\textit{classical}: \quad T^*_\nu \simeq \frac{\gamma_{\nu,e}T_e + \gamma_{\nu,m}T_m}{\gamma_{\nu,e} + \gamma_{\nu,m}}; \tag{7.42}$$

$$\textit{quantum}: \quad T^*_\nu \simeq T_e - \frac{T_e^2}{\omega_\nu}\log\left(\frac{\gamma_{\nu,e} + \gamma_{\nu,m}}{\gamma_{\nu,e}}\right). \tag{7.43}$$

The classical limit simply recovers a weighted average between the two thermal baths, while in the quantum regime the effective temperature is dominated by the largest temperature, which we assume to be T_e. The two regimes are connected by a crossover region, in which T^*_ν varies smoothly from the classical to the quantum value; this region occurs for frequencies of the order of T_e.

In Fig. 7.3b), we also plot the average photon occupation $\langle \hat{a}^\dagger_\nu \hat{a}_\nu \rangle$ of each mode ν, compared to the thermal occupation at the environment temperature $n_B(T_e)$. The

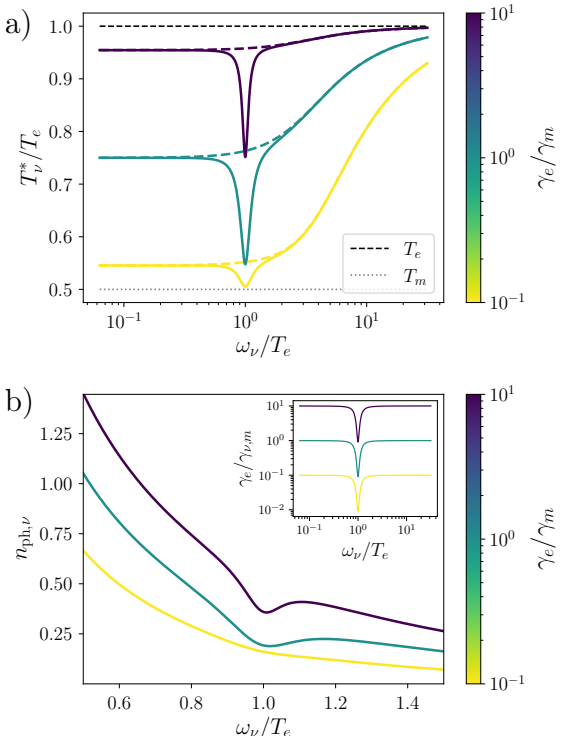


Figure 7.4.: (a) Cavity-mode dependent effective temperature for frequency-structured mirror dissipation rates as function of the frequency. The mirror dissipation is given by Eq. (7.46) with a resonance at $\omega_0/T_e = 1$, $1/\tau = 0.1T_e$ and $f_{\mathrm{res}} = 10$. The dashed lines indicate the behavior of T^*_ν if no resonance is present in $\gamma_{\nu,m}$ (i.e. if $f_{\mathrm{res}} = 0$). (b) Photon occupation number as function of the frequency ω_ν. A population inversion can be observed near the resonance frequency $\omega_\nu/T_e = 1$. The inset shows the behavior of $\gamma_e/\gamma_{\nu,m}$.

behavior in the two limiting regimes is:

$$\textit{classical}: \quad \langle \hat{a}^\dagger_\nu \hat{a}_\nu \rangle \simeq \frac{T^*_\nu}{T_e} n_B(T_e); \tag{7.44}$$

$$\textit{quantum}: \quad \langle \hat{a}^\dagger_\nu \hat{a}_\nu \rangle \simeq \frac{\gamma_{\nu,e}}{\gamma_{\nu,e} + \gamma_{\nu,m}} n_B(T_e). \tag{7.45}$$

In the classical limit we simply recover a thermal classical behaviour, i.e. occupation proportional to T^*_ν. In the quantum limit, despite the effective temperature being approximately the enviroment temperature $T^*_\nu \simeq T_e$, the occupation of the mode is always less than that of a thermal state at T_e. This holds in general also for intermediate frequency modes, the mode occupation is always smaller than the thermal value at the environment temperature. The reason is due to the logarithmic correction to T^*_ν in Eq. (7.43).

Structured dissipation rates. – It is in principle possible to shape the frequency dependence of T^*_ν by engineering structured dissipation rates beyond the simple flat ones ($\gamma_m/\gamma_e = const$) explored above. As an example, we consider the case of a mirror

dissipation rate strongly peaked near a specific frequency and show that this simple modification already generates interesting effects. This can occur when the mirrors (or an additional layer) have a strong resonance, leading to a large absorption and a large conductivity in Eq. (7.8). If the resonance is peaked and narrow enough, dissipation is dominated by the mirrors near the resonance; thus, the temperature of the photons is very close to that of the mirrors near the resonance, and behaves as in Fig. 7.3 away from the resonance.

For the sake of concreteness, we assume that the dissipation rate of the mirrors has a frequency independent term, plus an absorption term, which we model using the Lorentz oscillator model :

$$\gamma_{\nu,m} = \gamma_m \left(1 + f_{\text{res}} \frac{\omega_\nu^2/\tau^2}{(\omega_\nu^2 - \omega_0^2)^2 + \omega_\nu^2/\tau^2} \right), \tag{7.46}$$

where we employ $\omega_0/T_e = 1$ for the resonance frequency, $1/\tau = 0.1\omega_0$ for the width of the resonance and $f_{\text{res}} = 10$ for strength of the resonance. We also assume a frequency independent γ_e and study the behavior of the effective temperature for different values of γ_e/γ_m and for $T_m = 0.5T_e$.

In general, the Lindblad equation is not valid when the spectral density of the reservoir (and thus the rates) is frequency dependent [402–404]. Nonetheless, it is a good approximation when the dissipation rate is smaller than the typical scale on which the spectral density changes, i.e. when $\gamma_{m,\nu} \ll 1/\tau$, so that the cavity sees a flat spectral density. We assume that we are in this regime, which is a good approximation for many realistic setups.

Since $\gamma_{\nu,m}$ is peaked around ω_0, the ratio $\gamma_e/\gamma_{\nu,m}$ drops around ω_0, causing a drop of T_ν^* around ω_0, see Fig. 7.4a). This narrow dip in temperature leads to a dip in the energy behavior of the photon population and to a local population inversion, see Fig. 7.4b). The effects of the resonant increase in $\gamma_{\nu,m}$ are stronger when γ_e/γ_m is large, since for small values of γ_e/γ_m the temperature of the modes is already close to T_m and further modifications are small. In fact, there is no local population inversion in this case, as shown by the yellow curve in Fig. 7.4b).

These results showcase the possibility to engineer the properties of the photons inside the cavity by manipulating the frequency dependence of mirrors dissipation rate. Such effect can be easily achieved, for example, by adding specific absorptive layers to the mirrors, and allows to design cavities with highly non-thermal photon states. This effect could provide a novel route to better control quantum materials [222, 390, 405], atomic condensates [406] or other systems coupled to the cavity.

7.5. Non-linear mode mixing

In the previous sections, we have considered a purely quadratic Hamiltonian for the photons. However, realistic cavities may also exhibit coupling between different photon modes, originating from a nonlinear response of the cavity. These nonlinear interactions can arise from various mechanisms, including intrinsic material non-linearities (such as second-order susceptibility $\chi^{(2)}$ in dielectric cavities), effective non-linearities in plasmonic nanocavities, or parametric coupling induced by external driving fields. The presence of such nonlinearities may lead to modifications of the photon statistics and energy distribution, since now the modes are not independent of each other and one could expect a thermalization process between them.

To account for nonlinear effects in the cavity, we consider a cubic interaction term that couples two photon modes at a time. Specifically, we consider an interaction where two photons from a mode ν with frequency ω_ν can be destroyed to create a photon in mode 2ν with frequency $\omega_{2\nu} = 2\omega_\nu$, and vice versa. This process is characteristic of second harmonic generation or other non-linear mixing effects in electromagnetic systems.

The total Hamiltonian now consists of the free Hamiltonian of the cavity modes and the nonlinear interaction term $H = \sum_\nu \omega_\nu a_\nu^\dagger a_\nu + H_{\text{int}}$ with

$$H_{\text{int}} = \sum_\nu g_\nu \left(a_{2\nu}^\dagger a_\nu a_\nu + a_\nu^\dagger a_\nu^\dagger a_{2\nu} \right), \tag{7.47}$$

where g_ν is the non-linear coupling coefficient, which depends on the specific physical mechanism generating the interaction. The first term in H_{int} describes the annihilation of two photons in mode ν and the simultaneous creation of a photon in mode 2ν; the second term is its Hermitian conjugate, representing the reverse process in which a photon in mode 2ν decays into two photons in mode ν.

In order to investigate the effects of the nonlinear interaction on the photon distribution and on the thermal properties of the cavity modes, we restrict our analysis to three specific modes: $\nu_1 = \nu$, $\nu_2 = 2\nu$, and $\nu_3 = 4\nu$. In particular we choose ν such that $\omega_{\nu_1}/T_e = 1$ and $\gamma_m^- = \gamma_e^-$. Without any non-linear interaction, the temperatures of the three modes are $T_1(g = 0)/T_e = 0.76$, $T_2(g = 0)/T_e = 0.79$ and $T_3(g = 0)/T_e = 0.86$. The Hamiltonian of this reduced system, including the free evolution and the nonlinear coupling terms, is given by

$$H = \sum_i \omega_{\nu_i} a_{\nu_i}^\dagger a_{\nu_i} + g \left(a_{\nu_2}^\dagger a_{\nu_1}^2 + a_{\nu_3}^\dagger a_{\nu_2}^2 + \text{h.c.} \right), \tag{7.48}$$

where g is assumed to be constant for simplicity.

To fully capture the dynamics of the interacting modes, we solve for the steady-state density matrix ρ. The presence of nonlinear interactions introduces entanglement

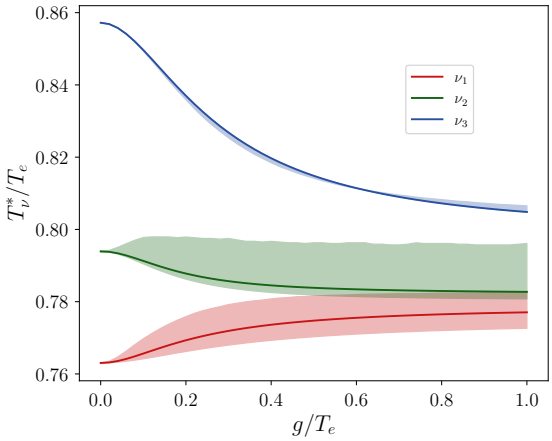


Figure 7.5.: Effective temperature T^*_ν for each of the three modes considered, as function of the non linear coupling g. The shaded regions indicate the interval of the effective temperature, due to deviations from thermal statistic for each mode.

between the modes, making a factorization of ρ impossible. Thus, we numerically solve for the full density matrix ρ by integrating the Lindblad master equation using the QuTiP package [407, 408]

$$\frac{d\rho}{dt} = -\frac{i}{\hbar}[H,\rho] + \sum_{\substack{i=1,2,3\\ c=e,m}} \mathcal{L}_{\nu_i,c}(\rho), \tag{7.49}$$

where $\mathcal{L}_{\nu_i,c}(\rho)$ is the dissipative term associated to photon mode ν_i and thermal reservoirs c.

We truncate the Hilbert space by imposing a maximum photon number m_i for each mode ν_i. The total Hilbert space is thus of dimension $(m_1+1)(m_2+1)(m_3+1)$, where the truncation parameters m_1, m_2, m_3 are chosen sufficiently large that the probability to have more than m_i photons in mode ν_i is negligible. Specifically, we choose $m_1 = 14$, $m_2 = 6$ and $m_3 = 3$. This truncation allows us to perform exact diagonalization of the dynamics of the system while keeping the numerical simulations feasibile.

From the steady-state solution of ρ, we extract the average photon occupation number of each mode $\langle n_{\nu_i}\rangle$ and the probability that mode ν_i is occupied by n photons, which are defined by generalizing Eq. (7.41)

$$\langle n_{\nu_i}\rangle = \mathrm{Tr}\left(a^\dagger_{\nu_i} a_{\nu_i}\rho\right); \quad p_{n,\nu_i} = [\mathrm{Tr}_{j\neq i}(\rho)]_{nn}. \tag{7.50}$$

We find that the population of each mode is not thermal, in contrast to the quadratic case of Sec. 7.4 where $p_{n,\nu} \sim e^{-n\omega_\nu/T^*_\nu}$. In order to study the properties of the photons we perform two analysis. *(i)* Calculate an average effective temperature T_{ν_i} by fitting the population of each mode with a Bose-Einstein distribution, $\langle n_{\nu_i}\rangle = n_B(\omega_{\nu_i}/T_{\nu_i})$. *(ii)* Perform a linear fit of $\ln p_{n,\nu_i}$ as function of n, in order to estimate how much p_{n,ν_i}

deviates from a thermal statistics and calculate the maximum and minimum effective temperatures that give the temperature range.

The results are plotted in Fig. 7.5 as a function of g, showing the effect of nonlinear interactions on the average effective temperature of each mode, and on the maximum and minimum temperature. We observe that for small g, the effective temperatures remain close to their $g = 0$ values dictated by the external reservoirs, and the range given by the minimum and maximum temperatures is small, so that the statistic of each mode remains quasi-thermal. However, as g increases, the nonlinear mode mixing terms increase thermalization between the different modes and their temperatures get closer to each other. The deviation of $p_{n,\nu}$ from a thermal statistic is larger for stronger g and for the two lower modes, an effect qualitatively similar to the Raman parametric amplification found in [409]. Nonetheless, the non-linear terms have an overall weak effect, which is negligible in realistic situations, where g is small compared to the typical energy scales of the cavity.

7.6. Conclusions

In this chapter, we investigated the dissipative dynamics and the (non) thermal properties of photons in a cryogenic electromagnetic cavity. We formulated a general description based on a Lindblad master equation, accounting for dissipation arising from the coupling to two thermal reservoirs at distinct temperatures (the cryogenically cooled mirrors and the warmer external environment). Our approach provides a clear method to calculate the properties of the cavity modes and estimate the relevance of thermal effects.

Our analysis reveals that each cavity mode displays a steady state characterized by a thermal statistics with a frequency-dependent effective temperature. The effective temperature exhibits a crossover from a low frequency classical regime, where it is a weighted average of the two reservoir regimes, to a high frequency quantum regime, where the cavity thermalizes to the warmer reservoir temperature.

We also showed that the frequency dependence of the dissipation rates can be exploited to tailor the properties of the cavity photons, for example modifying their energy distribution and creating a local population inversion. These results offer a new avenue for cavity engineering and for the control of materials embedded in the cavity. For example, it has been shown [405] that the electronic properties of a material can already be manipulated in a non invasive way by coupling it to a cryostat and to a cavity at different temperatures. Introducing a frequency structured photonic environment adds a new control parameter available for manipulating the material properties.

Our results highlight that extracting the total dissipation rate from measurements of the quality factor alone is insufficient, as the individual dissipation rates for mirrors

and environment are needed when they have different temperatures. Thus, we derived their explicit expressions from a microscopic model, and linked them to measurable macroscopic quantities such as conductivity and geometry of the mirrors. The expressions we derived hold for a generic cavity formed by a confining matter medium and by an external photonic environment, and only require the knowledge of a few experimental parameters. We performed explicit calculations for the case of a Fabry-Perot cavity and of a nanoplasmonic cavity.

Furthermore, we examined the effects of a nonlinear coupling between cavity modes. These interactions only cause weak modifications to the effective temperature, without inducing full thermalization, thus showing that our results are also valid for cavities with inter-mode interactions.

Our findings have important implications for experiments involving cryogenic cavities, particularly those investigating cavity-modified material properties. In particular, we provide simple expressions to calculate the dissipation rates from macroscopic properties of the cavity, which are all experimentally accessible, allowing researchers to determine when dissipation and thermal effects are significant. Our results also provide a theoretical foundation to optimize experimental cavity setups, mitigate thermal effects, or even engineer the properties of the cavity photons.

Chapter 8.

Concluding remarks

This thesis has explored the many-body physics of cavity-embedded quantum systems, emphasizing how the interplay between local matter degrees of freedom and delocalized photonic modes can reshape paradigms of condensed-matter theory. By combining analytical methods and numerically controlled matrix-product-state (MPS) simulations, we have analyzed phenomena ranging from photon condensation to excitation dynamics and topology, building a unified perspective on cavity-embedded quantum matter.

A first line of investigation focused on photon condensation in low-dimensional systems. Through minimal models, we have shown that photon condensation—often associated with Dicke superradiant transitions—can emerge in itinerant and correlated one-dimensional systems once magnetic or current-coupled cavity modes are introduced. A systematic comparison between photon mean-field theory and exact MPS calculations has clarified the regime of validity of semiclassical approaches and highlighted the potential role of quantum fluctuations in enhancing such instabilities. These results establish a controlled framework for studying collective light–matter phases in systems where locality and global coupling coexist.

The second major theme concerned the dynamics of excitations in hybrid cavity–matter systems. We demonstrated that the interplay between local interactions and global photon-mediated couplings produces excitations with mixed local and non-local character, whose dynamics are often governed by single-particle coupling energy scales. In particular, cavity-coupled Rydberg atom arrays constitute an ideal quantum-simulation platform to realize such regimes, where a crossover from local domain-wall dynamics to non-local meson–polariton motion in spin chains can be directly observed and tuned experimentally.

A third direction examined the relationship between topology and non-locality. Using fractional quantum Hall liquids and topological superconducting states as paradigmatic examples, we have shown that cavity-induced correlations do not necessarily destroy topological protection, provided that key symmetries are preserved. Furthermore we have shown how cavity QED can offer novel and more direct experimental probes to

the elusive graviton-modes of fractional quantum hall liquids.

Looking forward, several challenges and opportunities emerge. Much of the theoretical understanding so far relies on the single-mode approximation for the electromagnetic environment, which, while insightful, neglects the multimode structure in realistic cavities essential to faithfully capture vacuum contributions. Extending tensor-network methods to multimode scenarios represents a demanding but feasible next step. On the experimental side, realizing and understanding these effects in solid-state platforms will require careful modeling of various competing mechanisms, particularly when dealing with fragile correlated states. Addressing these challenges will be key in transforming cavity-embedding from a theoretical playground into a concrete tool with which to control quantum matter.

Appendices

Appendix A.

First-order photon condensation in magnetic cavities

A.1. Gaussian states and Wigner function

Given a bosonic degree of freedom $\hat{a}$, a Gaussian state can be identified by two complex parameters α, ξ, and one real positive parameter $N_{\rm th}$. For a single mode, the density matrix of a generic Gaussian state can be written as a displaced and squeezed thermal state:

$$\rho^G = \hat{D}(\alpha)\hat{S}(\xi)\frac{N_{\rm th}^{\hat{a}^\dagger\hat{a}}}{(1+N_{\rm th})^{\hat{a}^\dagger a}}\hat{S}^\dagger(\xi)\hat{D}^\dagger(\alpha)\ , \tag{A.1}$$

where $\hat{D}(\alpha)$ and $\hat{S}(\xi)$ are respectively the displacement and the squeezing operators:

$$\begin{aligned}\hat{D}(\alpha) &\equiv \exp\left[\alpha\hat{a}^\dagger - \alpha^*\hat{a}\right]\ ,\\ \hat{S}(\xi) &\equiv \exp\left[(\xi^*\hat{a}\hat{a} - \xi\hat{a}^\dagger\hat{a}^\dagger)/2\right]\ .\end{aligned} \tag{A.2}$$

The covariance matrix of the quadratures $\hat{X}$ and $\hat{P}$ for a generic state is defined as:

$$\boldsymbol{\sigma} \equiv \begin{pmatrix} \langle\hat{X}^2\rangle - \langle\hat{X}\rangle^2 & \langle\hat{X}\hat{P}+\hat{P}\hat{X}\rangle - \langle\hat{X}\rangle\langle\hat{P}\rangle \\ \langle\hat{X}\hat{P}+\hat{P}\hat{X}\rangle - \langle\hat{X}\rangle\langle\hat{P}\rangle & \langle\hat{P}^2\rangle - \langle\hat{P}\rangle^2 \end{pmatrix}\ . \tag{A.3}$$

For Gaussian states, every property can be expressed in terms of expectation values of the quadratures and their covariance matrix. In terms of the parameters α, $\xi = re^{i\theta}$ and $N_{\rm th}$, we have:

$$\langle\hat{X}\rangle = \sqrt{2}\,\mathrm{Re}[\alpha]\ ,\quad \langle\hat{P}\rangle = \sqrt{2}\,\mathrm{Im}[\alpha]\ , \tag{A.4}$$

$$\sigma_{11} = \left(\frac{1}{2}+N_{\rm th}\right)\Big(\cosh(2r)+\sinh(2r)\cos(\theta)\Big)\ , \tag{A.5}$$

$$\sigma_{22} = \left(\frac{1}{2}+N_{\rm th}\right)\Big(\cosh(2r)-\sinh(2r)\cos(\theta)\Big)\ , \tag{A.6}$$

$$\sigma_{12} = \sigma_{21} = \left(\frac{1}{2}+N_{\rm th}\right)\sinh(2r)\sin(\theta)\ . \tag{A.7}$$

The von Neumann entropy of the photon in a Gaussian state reads:

$$S(\rho^G) = (N_{\rm th}+1)\ln(N_{\rm th}+1) - N_{\rm th}\ln N_{\rm th}\ . \tag{A.8}$$

We remark here that the origin of a finite entropy, i.e., $N_{\rm th} > 0$, is not generically guaranteed to be the entanglement with some other quantum system, unlike the closed cavity system in the main text, since it can also have a classical contribution. For example, a harmonic oscillator with frequency $\omega_{\rm c}$ and at inverse temperature β is in a Gaussian state with $(\alpha, \xi, N_{\rm th}) = (0, 0, e^{-\beta\omega_{\rm c}})$.

Another definition for the Gaussian states is that their Wigner function:

$$W(x,p) = \frac{1}{\pi}\int dy e^{2ipy}\left\langle x+y\right|\hat{\rho}\left|x-y\right\rangle\ , \tag{A.9}$$

is a Gaussian:

$$W(x,p) = \frac{1}{\pi}\exp\left(-\frac{1}{2}(x-x_0, p-p_0)\boldsymbol{\sigma}^{-1}(x-x_0,p-p_0)^T\right)\ , \tag{A.10}$$

where $\boldsymbol{\sigma}$ it the covariance matrix, $x_0 = \langle\hat{X}\rangle$ and $p_0 = \langle\hat{P}\rangle$. We also recall that for a symmetrically ordered operator $\hat{O}(\hat{a},\hat{a}^\dagger)$ such as the Peierls phase the Wigner function can be used to compute expectation values as averages over the phase space:

$$\langle\hat{O}(\hat{a},\hat{a}^\dagger)\rangle = \int dxdpW(x,p)O\Big(\frac{x+ip}{\sqrt{2}}, \frac{x-ip}{\sqrt{2}}\Big)\ . \tag{A.11}$$

In the main text, therefore, we need to perform just Gaussian integrals to arrive at Eq. (1.16).

A.2. Photon mean-field in periodic boundary conditions

In this appendix, we expand on the case of periodic boundary condition without specifying the geometry. Using the same pseudo-spin representation defined in the text in momentum space we have that the light-matter Hamiltonian reads:

$$\hat{H} = \hat{H}_{\rm c} + \sum_{k,\alpha} H_k^\alpha(\hat{a},\hat{a}^\dagger)\hat{\sigma}_k^\alpha\ , \tag{A.12}$$

where at each momentum sector k we have:

$$\boldsymbol{H}_k(\hat{a},\hat{a}^\dagger) = -\Big(2t_0\cos(k)\cos\Big(\hat{\Phi}/2\Big), t_1 + t_2\cos(k), t_2\sin(k), 2t_0\sin(k)\sin\Big(\hat{\Phi}/2\Big)\Big)\ . \tag{A.13}$$

Note that this representation is possible because the cavity mode has zero momentum in the direction of the ladder. Focusing on the thermodynamic limit and the matter

state, we can work in the PMF approximation and restrict ourselves to coherent states for the cavity $|\alpha_0\rangle$ with the identification of the mean-field parameter defined in the main text: $\phi = 4g\alpha_0/\sqrt{N}$ and $R = 1$. In this way the mean-field electronic Hamiltonian with periodic boundary conditions is

$$\hat{H}_{\mathrm{m}}^{\mathrm{PMF}} = \sum_{k,\alpha} h_k^{\alpha} \hat{\sigma}_k^{\alpha} \ . \tag{A.14}$$

The two bands are:

$$\epsilon_{k,a} = 2t_0 \cos(k)\cos(\phi) + (-1)^a \sqrt{t_1^2 + t_2^2 + 2t_1 t_2 \cos(k) + 4t_0^2 \sin^2(k)\sin^2(\phi)} \ , \tag{A.15}$$

with $a = 1, 2$. For the square ladder case discussed extensively in the main text with $t_1 = t_0 = 1$, the chemical potential is $\mu = 0$ at every ϕ, and an indirect gap in the dispersion opens at $\phi = \frac{2}{3}\pi$. The minimization of the total energy as a function of ϕ then gives the PMF ground state.

A.3. Perturbation theory

The Hamiltonian at $g = 0$ has a factorized ground state that reads:

$$|\Psi_0\rangle = \prod_{\frac{\pi}{3}<|k|<\frac{2\pi}{3}} \hat{\tilde{c}}_{1,k}^{\dagger} \prod_{|k|<\frac{\pi}{3}} \hat{\tilde{c}}_{1,k}^{\dagger} \hat{\tilde{c}}_{2,k}^{\dagger} |0_{\mathrm{m}}, 0_{\mathrm{c}}\rangle \ , \tag{A.16}$$

where $|0_{\mathrm{m}}, 0_{\mathrm{c}}\rangle$ is the state with zero electrons and photons, and $\hat{\tilde{c}}_{a,k}^{\dagger}$ is the creation operator that diagonalize the bare electronic Hamiltonian and $a = 1, 2$ the band index. Different points in momentum space can have $N_k = 0, 1, 2$ number of electrons and this is a conserved quantity. Starting from $|\Psi_0\rangle$ and the expansion of the light-matter interaction in Eq. (1.23) we can compute perturbative corrections at small g. In particular we have $H \simeq H_0 + V_g$ with:

$$\hat{V}_g = \frac{g}{\sqrt{L}} \sum_{k,\alpha} \hat{\sigma}_k^{\alpha} d_{p,k}^{\alpha}(\phi = 0) \ . \tag{A.17}$$

The only non-zero matrix matrix element at first order are those with a single direct particle-hole excitation for the matter and one photon in the cavity:

$$f_k = \langle PH_k, 1_{\mathrm{c}}| \left(\delta\hat{a} + \delta\hat{a}^{\dagger}\right) \sum_{\alpha} \hat{\sigma}_k^{\alpha} d_{p,k}^{\alpha}(\phi = 0) \, |\Psi_0\rangle = 2\sin(k)\theta\left(|k| - \frac{\pi}{3}\right)\theta\left(\frac{2\pi}{3} - |k|\right) \ , \tag{A.18}$$

with $\theta(x)$ the Heaviside function. Summing over all momenta we arrive to the expression in the text for the ground state corrections:

$$\left|\Psi_{(1)}\right\rangle = |\Psi_0\rangle - \frac{g}{\sqrt{L}} \sum_{k} \frac{2f_k}{\omega_k + \omega_{\mathrm{c}}} |\mathrm{PH}_k, 1_{\mathrm{c}}\rangle \ . \tag{A.19}$$

The second-order expansion involves also the g^2 contribution and populate also the two-photon sector of the cavity, needed for the squeezing of the mode.

A.4. Details about DMRG simulations

For all the DMRG simulations performed here, the energy density difference between the final two DMRG sweeps has been kept below 10^{-8} to ensure convergence. In order to maintain computational feasibility, the dimension of the photon Hilbert space has been truncated to a maximum photon number of $N_{\max}^{\mathrm{PH}} = 63$. The photon Hilbert space must be large enough to describe coherent states found in the photon condesed regime but also the strong squeezing. We have verified that this truncation level is sufficient to obtain converged results for all values of g and system sizes up to $L = 76$.

In most of the presented figures, the bond dimension used for the MPS ansatz is $\chi = 600$, sufficient to achieve converged results for system sizes up to $L = 76$ with a tolerance of 10^{-8} on the energy density and a maximum truncation error of 10^{-6}. These are worse case values which are found in the normal phase where the fermions are gapless and entangled with the cavity. However, to better capture the thermodynamic limit, we have also analyzed larger system sizes up to $L = 136$. For these system sizes, we increased the bond dimension to $\chi = 1000$ to converge most observables, except for the non-Gaussianity of the photon state. This observable has been found to be particularly sensitive to a combination of numerical parameters including the number of DMRG sweeps and the bond dimension. This problem of convergence is particularly pronounced for values of g in the normal phase, where the entanglement in the system is higher. To account for this difficulty in the analysis, we have considered an empirical error of 10^{-5} in the data for Fig. 1.5.

We then also comment on the non-linear nature of the Peierls phase. This is represented in our code by using the exact matrix elements in the photon number basis $\{|n\rangle\}$ of the displacement operators $\hat{D}(ig/\sqrt{L})$ which reads [410]:

$$\langle n|\,\hat{D}(\alpha)\,|m\rangle = \sqrt{\frac{n!}{m!}}\alpha^{m-n}\exp\left(-\frac{|\alpha|^2}{2}\right)L_n^{(m-n)}(|\alpha|^2) \qquad \text{for} \qquad m \geq n\ , \tag{A.20}$$

with $L_n^{(m-n)}(x)$ a generalized Laguerre polynomial and for $m < n$ one can just take the complex conjugate since $\hat{D}$ is unitary. When one works at finite size or considers $g/\sqrt{L}$ fixed ("single-particle" strong coupling) the matrix elements of the displacement operator should be evaluated carefully in a truncated Hilbert space. For example the exponentiation of the matrix $ig\hat{X}/\sqrt{L}$ as $\langle n|\exp\left(ig\hat{X}/\sqrt{L}\right)|m\rangle$ in a truncated Hilbert space does not exactly corresponds to $\langle n|\,\hat{D}(ig/\sqrt{L})\,|m\rangle$. To be more quantitative in Fig. A.1 we plot the difference between the matrix elements obtained by exponentiating $ig\hat{X}/\sqrt{L}$ and the exact ones from Eq. (A.20) at a small photon Hilbert space cutoff $N_{\max}^{\mathrm{PH}} = 9$. This illustrates the necessity for a large photonic cut-off in the numerical simulations.

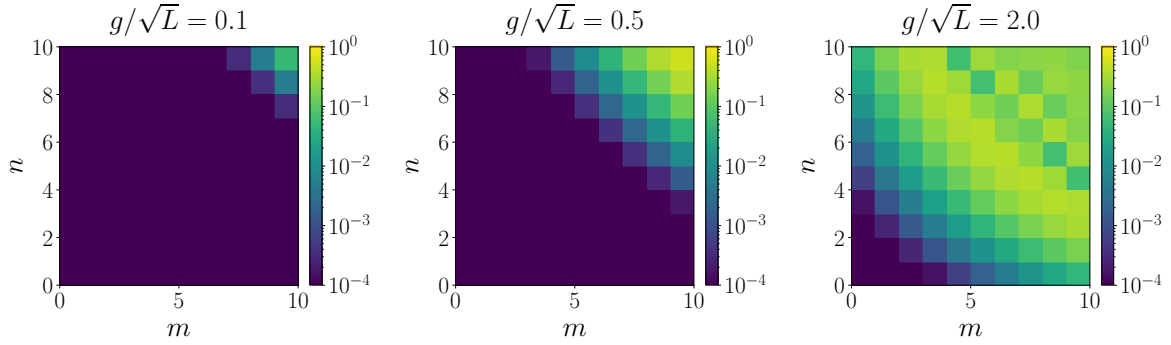


Figure A.1.: Absolute value of the difference $|D_{nm} - D^{\text{exp}}_{nm}|$ for three values of $g/\sqrt{L}$ where $D_{nm} = \langle n| \hat{D}(ig/\sqrt{L}) |m\rangle$ and D^{exp}_{nm} is obtained by exponentiating the finite matrix $X_{nm} = \langle n| \hat{X} |m\rangle$ in a truncated photon Hilbert space with $N^{\text{PH}}_{\text{max}} = 9$.

Appendix B.

Local vs non-local dynamics in cavity-coupled Rydberg atom arrays

B.1. Derivation of the rydberg-cavity Hamiltonian

In this section, we detail the derivation that motivates model Hamiltonian, Eq. (1), studied in the main text. The system under consideration involves an atomic array put inside a cavity, as shown in Fig. B.1, positioned in the maxima of the cavity field. Atoms are excited from the ground state $|g\rangle$, to a Rydberg state $|r\rangle$, via an intermediate state $|e\rangle$. The ground-to-intermediate state transition is driven by an off-resonant cavity mode, characterized by a coupling strength g_0, assumed equal for all atoms, and detuning Δ. The subsequent transition from the intermediate state to the Rydberg state is mediated by a classical laser field with a Rabi frequency Ω again assumed to be equal for all atoms. The combined two-photon transition $|g\rangle \leftrightarrow |r\rangle$ has detuning δ_0. In the rotating frame, the model Hamiltonian is expressed as $\hat{H}_{rf} = \hat{H}_0 + \hat{H}_1$, where

$$\begin{aligned}\hat{H}_0 &= \delta_0 \hat{a}^\dagger \hat{a} + (\Delta + \delta_0) \sum_j \hat{\sigma}_j^{ee} - \sum_j w_j \sigma_j^{gg} + V_{\mathrm{NN}} \sum_j \hat{\sigma}_j^{rr} \hat{\sigma}_{j+1}^{rr}, \\ \hat{H}_1 &= g_0 \sum_j (\hat{a}\hat{\sigma}_j^{eg} + \hat{a}^\dagger \hat{\sigma}_j^{ge}) + \Omega \sum_j (\hat{\sigma}_j^{re} + \hat{\sigma}_j^{er}).\end{aligned} \tag{B.1}$$

The Rydberg-Rydberg interaction is here truncated for simplicity.The canonical boson operator $\hat{a}$ annihilates cavity photons, and projectors $\hat{\sigma}^{\alpha\beta} = |\alpha\rangle\langle\beta|$ with $\alpha = g$, e, and r describe atomic operators. Additionally, we introduce a site-dependent detuning w_j induced by AC Stark shifts from the optical tweezers, along with the nearest-neighbor interaction V_{NN} for atoms in the Rydberg state.

In the far off-resonant limit $\Delta \gg 1$, the intermediate state is barely occupied. We adiabatically eliminate it by means of a Schrieffer-Wolff transformation defined as $\hat{H}' = e^{\hat{S}} \hat{H}_{rf} e^{-\hat{S}}$. We consider a generator $\hat{S} = \hat{S}_c + \hat{S}_l$, where $\hat{S}_c$ and $\hat{S}_l$ represent contributions from the cavity and the laser. The generators are chosen so that their commutator with

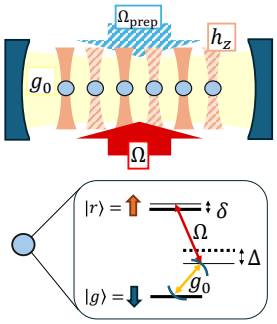


Figure B.1.: Light-atom setup. A linear Rydberg atom array is put inside a cavity. A two-photon transition is used to drive atoms from the ground state to the Rydberg state.

$\hat{H}_0$ produce $\left[\hat{S}, \hat{H}_0\right] = -\hat{H}_1$. Explicitly, they read:

$$\begin{aligned}\hat{S}_c &= g_0 \sum_j \left(\Delta + w_j\right)^{-1} (\hat{a}\hat{\sigma}_j^{eg} - \hat{a}^\dagger \hat{\sigma}_j^{ge}),\\ \hat{S}_l &= \Omega \sum_j \left(\Delta + \delta_0 - V_{\text{NN}}\hat{\sigma}_{j+1}^{rr} - V_{\text{NN}}\hat{\sigma}_{j-1}^{rr}\right)^{-1} (\hat{\sigma}_j^{er} - \hat{\sigma}_j^{re}).\end{aligned} \tag{B.2}$$

The laser term includes a site-dependent denominator operator $\hat{D}_j = \Delta + \delta_0 - V_{\text{NN}}\hat{\sigma}_{j+1}^{rr} - V_{\text{NN}}\hat{\sigma}_{j-1}^{rr}$. This operator is diagonal in the eigenbasis of $\hat{H}_0$, and accounts for the local atomic configuration. The commutators of the generators with $\hat{H}_0$ are given by:

$$\left[\hat{S}_c, \hat{H}_0\right] = -g_0 \sum_j (\hat{a}\hat{\sigma}_j^{eg} + \hat{a}^\dagger \hat{\sigma}_j^{ge}), \qquad \left[\hat{S}_l, \hat{H}_0\right] = -\Omega \sum_j (\hat{\sigma}_j^{er} + \hat{\sigma}_j^{re}). \tag{B.3}$$

With this choice the condition $\left[\hat{S}, \hat{H}_0\right] = -\hat{H}_1$ is met identically, and the effective Hamiltonian acquires the form:

$$\hat{H}_{eff} = \hat{P}\hat{H}_0\hat{P} + \frac{1}{2}\hat{P}\left[S, \hat{H}_1\right]\hat{P} + \cdots, \tag{B.4}$$

where $\hat{P} = \prod_j (1 - \hat{\sigma}_j^{ee})$ is the projector onto the subspace without atoms in the excited state. The second-order corrections to the Hamiltonian are obtained from the commutator $\left[S, \hat{H}_1\right]$. We find that the contribution coming from $\hat{S}_c$ reads

$$\hat{P}\left[\hat{S}_c, \hat{H}_1\right]\hat{P} = -\frac{2g_0^2}{\Delta}\hat{a}^\dagger\hat{a}\sum_j \hat{\sigma}_j^{gg} - \frac{g_0\Omega}{\Delta}\sum_j (\hat{a}\hat{\sigma}_j^{rg} + \hat{a}^\dagger\hat{\sigma}_j^{gr}) + \cdots, \tag{B.5}$$

where we project the result to the manifold of interest, and approximate $\frac{1}{\Delta + w_j} \approx \frac{1}{\Delta} + \cdots$, as we concentrate on the regime where Δ is the dominant energy scale, i.e., $\Delta \gg |w_j|$. Likewise, the contribution from $\hat{S}_l$ is obtained from the commutator:

$$\hat{P}\left[\hat{S}_l, \hat{H}_1\right]\hat{P} = -\frac{g_0\Omega}{\Delta}\sum_j (\hat{a}\hat{\sigma}_j^{rg} + \hat{a}^\dagger\hat{\sigma}_j^{gr}) - \frac{2\Omega^2}{\Delta}\sum_j \hat{\sigma}_j^{rr} + \cdots. \tag{B.6}$$

Note that terms arising from the commutation of $\hat{D}_j^{-1}$ vanish under projection, and the final expression follows from the large-Δ approximation $\hat{D}_j \approx \Delta$. Within this limit, the second-order effective Hamiltonian simplifies to

$$\hat{H}_{eff} = \delta \hat{a}^\dagger \hat{a} + \frac{1}{2}\sum_j h_j \hat{\sigma}_j^z + \frac{V_{\mathrm{NN}}}{4}\sum_j \hat{\sigma}_j^z \hat{\sigma}_{j+1}^z + g\sum_j (\hat{a}\hat{\sigma}_j^+ + \hat{a}^\dagger \hat{\sigma}_j^-) + \lambda \hat{a}^\dagger \hat{a}\sum_j \hat{\sigma}_j^z. \tag{B.7}$$

In passing to the spin notation we ignore additive constants and boundary terms. The mapping is achieved through the identification $\hat{\sigma}_j^+ = \hat{\sigma}_j^{rg}$, with $\hat{\sigma}_j^z = \hat{\sigma}_j^{rr} - \hat{\sigma}_j^{gg}$. The effective couplings are expressed as follows: $\delta = \delta_0 - N g_0^2/2\Delta$, $h_j = w_j + V_{\mathrm{NN}} - \Omega^2/\Delta$, $g = -g_0\Omega/\Delta$, and $\lambda = g_0^2/2\Delta$.

B.2. Cavity losses

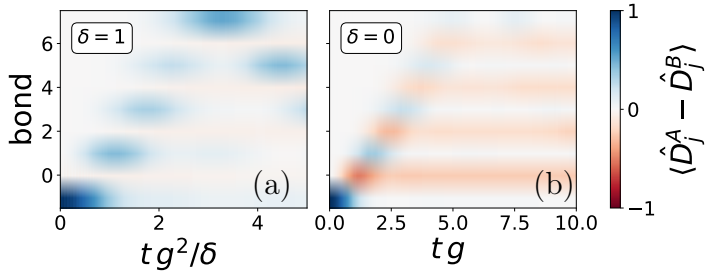


Figure B.2.: Effect of finite cavity photon losses $\kappa = g/2 = 0.05$ on domain wall dynamics for (a) off-resonant $\delta = 1$ and (b) resonant $\delta = 0$ cavity detunings. The initial state is prepared with a boundary domain wall of type A. $h_z = 0$ and $N = 8$.

The loss mechanism expected to be dominant in the set-up considered in this work is the loss of cavity photons, with a rate $\kappa \lesssim g$. We consider explicitly their effect on the single domain-wall dynamics via averaging quantum trajectories. In Fig. B.2 we show two scenarios for the cavity detuning $\delta = 0$ (a) and $\delta = 1$ (b) in a case of of weak-intermediate cavity losses $\kappa = g/2 = 0.05$. In particular we look at the dynamics of a type A domain wall initialized at the boundary of the atom array. This does not correspond to two actual initial rydberg atoms close to each other, but just the addition of a further boundary longitudinal field mimicking the presence of another rydberg atom. Note indeed that the bond at which the domain wall is $j = -1$, before the first atom.

The photon loss projects the system into states with a domain wall of type B instead of type A, giving the overall effect of freezing the dynamics as $J_B \ll J_A, g$. The actual timescale at which the domain wall of type A *decays* into a type B depend on the specific scenario. More in details we can see that the effect of photon losses is stronger on the $\delta = 0$ case where cavity photons are coherently generated during the dynamics

and the lifetime for the domain wall propagation is on the order of κ^{-1}. Instead in the $\delta = 1$ case the cavity is only virtually populated $\langle \hat{n}_{ph} \rangle \sim \frac{g^2}{\delta^2}$, thus inducing a longer lifetime for domain walls of type A of order $\kappa \frac{g^2}{\delta^2}$.

B.3. Atom decay and post-selection

We here investigate the role of atom decay. The Rydberg state considered in this work has an intrinsic lifetime of $\tau \sim 150\,\mu$s leading to a decay rate to the ground state of $\Gamma_r = 2\pi \times 1\,$kHz. Virtual population of the intermediate state leads to another decay channel for the rydberg state to the ground state of $\Gamma_{eff} = \Gamma_e(\Omega/\Delta)^2 \sim 2\pi \times 13\,$kHz leading to a total decay rate of the two-level atom ($|r\rangle$ and $|g\rangle$) of $\gamma_{at} = \Gamma_r + \Gamma_{eff} = 2\pi \times 14\,$kHz. This is explicitly shown in Fig. B.3(a) where decay of Rabi-oscillations $|r\rangle \to |g\rangle$ in the two level atom model is compared to the full three level atom without integrating out the intermediate state. In Fig. B.3(b) we further show the dependence of γ_{at}/g on Ω/Δ for different choice of Rydberg atom principal numbers n.

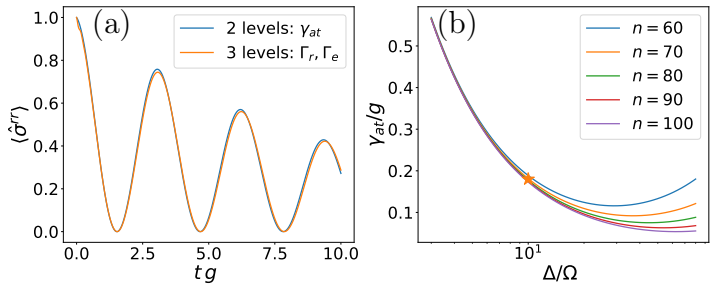


Figure B.3.: (a) Decay of cavity-induced Rabi oscillations between the rydberg state and ground state at $g_0 = 2\pi \times 0.8\,$MHz, $\Omega = 2\pi \times 50\,$MHz and $\Delta = 2\pi \times 500\,$MHz ($g = g_0\Omega/\Delta$) in the 3-level atom scheme (orange) and in the effective 2-level atom scheme (blu). In the three level atom both rydberg decay $\Gamma_r = 2\pi \times 1\,$kHz and intermediate state decay $\Gamma_e = 2\pi \times 1.35\,$MHz are included, well accounted for by an effective two-level atom decay of $\gamma_{at} = \Gamma_r + \Gamma_e(\Omega/\Delta)^2$. (b) Effective atom decay in the two-level atom γ_{at}/g as a function of intermediate state detuning Δ/Ω for different Rydberg principal quantum number n, assuming a rydberg decay $\Gamma_r^n = \Gamma_r^{70}\left(\frac{70}{n}\right)^3$ with $\Gamma_r^{70} = 2\pi \times 1\,$kHz

We now explore the effect that the atom decay has on the dynamics under consideration. In Fig. B.4 we show different scenario to exemplify of the dynamics of a single domain wall is affected[1]. In particular in (a) we show the unitary dynamics with no losses, in (b) the dynamics taking into account only photon loss, and in (c) the dynamics with both photon loss and atom decay. Each Rydberg decay from an the antiferromagnetic state correspond to the creation of a pair of type B domain walls, a process which at the level of unitary dynamics is strongly suppressed due to the high

[1]Here we use further longitudinal fields on the boundary atoms $h_z^0 = V$ and $h_z^{N-1} = V$ which mimick the presence of two further atoms fixed in the rydberg state at sites $j = -1$ and $j = N$, thus allowing a "bond" at $j = -1$ and $j = N - 1$

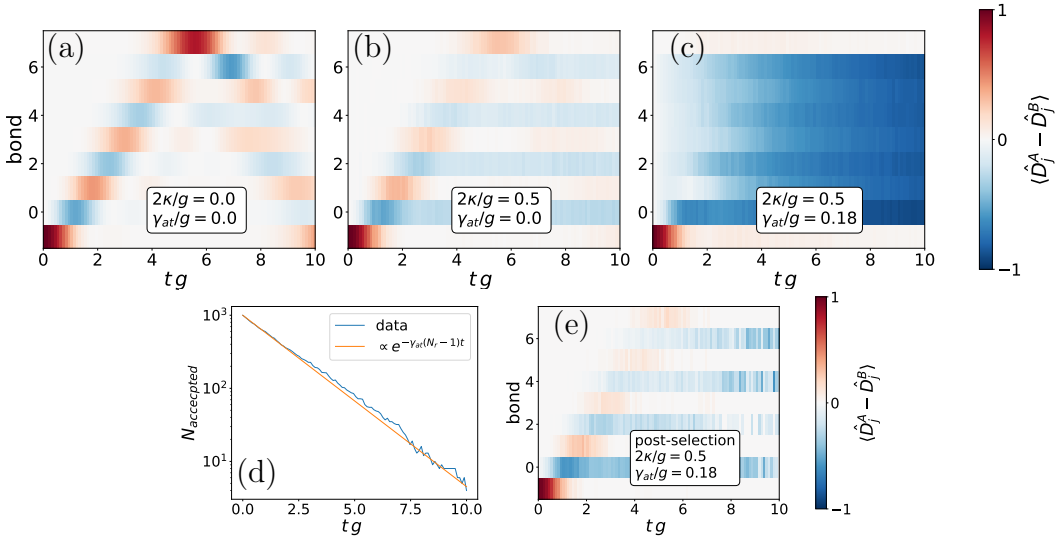


Figure B.4.: Effect of atom decay and cavity photon loss on the dynamics of a single domain wall of type A at $g = 0.1\,V$, $\delta = 0.$ and $V = 1$. Top row (a,b,c) shows the doain wall density obtained by averaging 1000 trajectories with respectively (a) no losses $2\kappa = 0.$,$\gamma_{at} = 0.$ (b) only photon loss $2\kappa/g = 0.5$,$\gamma_{at}/g = 0.$ (c) both photon and atom decay $2\kappa/g = 0.5$,$\gamma_{at}/g = 0.18$. Bottom row (d,e) shows post-selection results (as described in the text) with both photon loss and atom decay $2\kappa/g = 0.5$,$\gamma_{at}/g = 0.18$. In particular (d) shows the number of accepted atom array measurements ($N_{accepted}$) and (e) shows the domain wall density obtained from these snapshots.

energy cost of a domain wall $2V \gg g$. This allow for a simple post-selection strategy on the measured atom array configurations (snapshots in the σ^z basis) consisting in just discarding measurements which show more domain wall states than the initially prepeared state. The result of this procedure done by sampling 1000 quantum trajectories is shown in the bottom row of Fig. B.4. In particular panel (d) shows the number of accepted snapshots as a function of time and panel (e) the resulting expectation value averaged over the accepted snapshots. For comparison, panel (c) is produced with the same 1000 trajectories but no post-selection on the snapshots. The probability of accepting a trajectory is governed by $e^{-\gamma_{at}(N_r-1)t}$ with N_r the number of initial Rydberg and not $e^{-\gamma_{at}N_r t}$ because this procedure can only correct the Rydberg decay when the atom is not part of a domain wall. If the atom is part of a domain wall, its decay will not increase the total number of domain walls but just turn a domain wall of type A into type B. The number $N_r - 1$ is the actual average number of atoms in the Rydberg state during the coherent evolution.

Appendix C.

Topological protection of Majorana-polaritons in a cavity

C.1. Details on the light-matter coupling

In the following we detail the Peierls substitution for the tight-binding model under consideration. For general hopping terms the Peierls substitution reads:

$$\hat{c}^\dagger_{i,\sigma}\hat{c}_{j,\sigma'} \to \exp\left[i\int_{R_{i,\sigma}}^{R_{j,\sigma'}} d\boldsymbol{r}\cdot\hat{\boldsymbol{A}}(\boldsymbol{r})\right]\hat{c}^\dagger_{i,\sigma}\hat{c}_{j,\sigma'}\ , \tag{C.1}$$

with $e = c = \hbar = 1$. It is straightforward to show that the electric coupling $\boldsymbol{A}_E \propto \hat{y}$ only dresses the vertical hopping $t_\perp$ while the magnetic coupling $\boldsymbol{A}_B \propto y\hat{x}$ dresses only the horizontal hopping t_0. The superconducting coupling instead is more subtle. Regarding the electric coupling, it has been shown that [212], in order to preserve gauge invariance, one needs to dress the superconducting pairing terms as

$$\hat{c}_{i,\sigma}\hat{c}_{j,\sigma'} \to \exp\left[i\int_{\boldsymbol{R}_0}^{\boldsymbol{R}_{i,\sigma}} d\boldsymbol{r}\cdot\hat{\boldsymbol{A}}(\boldsymbol{r}) + i\int_{\boldsymbol{R}_0}^{\boldsymbol{R}_{j,\sigma'}} d\boldsymbol{r}\cdot\hat{\boldsymbol{A}}(\boldsymbol{r})\right]\hat{c}_{i,\sigma}\hat{c}_{j,\sigma'}\ , \tag{C.2}$$

where $\boldsymbol{R}_0$ is an arbitrary starting point and $\boldsymbol{R}_{j,\sigma}$ the position of the site in rung j and leg σ. It is easy to check that, with the choice of $\boldsymbol{R}_0$ in the center of the ladder, the dressing of the superconducting pairing in equation Eq. (4.1) in the main text vanishes for $\boldsymbol{A}_E \propto \hat{y}$. The orientation choice as well as the choice of the superconducting pairing is made to specifically avoid dressing the superconducting pairing. Equivalently for the magnetic field case with $\boldsymbol{A} \propto -y\hat{x}$ we also get a vanishing dressing on the chosen superconducting term.

We now comment on a problem that arises when coupling an electric field along x, which would be the natural choice on a Kitaev chain and that we did not include in Chapter 4. The dressing would be:

$$\boldsymbol{A}_x \propto \hat{x}\ :\qquad \hat{c}^\dagger_{j,+}\hat{c}^\dagger_{j,-} \to \hat{c}^\dagger_{j,+}\hat{c}^\dagger_{j,-}e^{2ig_x r_j(\hat{a}+\hat{a}^\dagger)}\ , \tag{C.3}$$

where we introduce a light-matter coupling constant g_x and the rung position r_j. This light-matter coupling give rise to some severe numerical issues regarding the truncation of photon Hilbert space as representing a displacement operator $\hat{D}(\alpha) = e^{\alpha\hat{a}-\alpha^*\hat{a}^\dagger}$ requires $N_{ph} \gg \alpha^2$, in the present case would be $N_{ph} \gg r_j^2 \propto L^2$. The ladder geometry reveals here to be crucial, along y we still have freedom to couple non-trivially a cavity mode and we don't get the thermodynamic limit problem of $r_j \propto L$ which instead we get along x.

C.2. Topology in absence of cavity

In the following we analyze the non-interacting Hamiltonian $\hat{H}_0$ in equation (4.1) of the main text and show the presence of a topological phase. In order to do so we introduce momentum space fermions $\hat{c}_{\sigma,k} = \frac{1}{\sqrt{L}}\sum_j e^{-ikj}\hat{c}_{\sigma,j}$ and the nambu operator $\hat{\psi}_k = (\hat{c}_{+,k}, \hat{c}_{+,k}, \hat{c}^\dagger_{-,-k}, -\hat{c}^\dagger_{+,-k})$. The hamiltonian can then be written as:

$$\hat{H}_0 = \frac{1}{2}\sum_k \hat{\psi}^\dagger_k \mathcal{H}_k \hat{\psi}_k \tag{C.4}$$

with $\mathcal{H}_k$ a 4×4 matrix:

$$\mathcal{H}_k = h^A_k \tau_z + h^B_k \sigma_z\tau_z - t_\perp \sigma_x + \Delta\tau_x \ , \tag{C.5}$$

$$h^A_k = -2t\cos(k)\cos(\phi_{ext}/2) \qquad h^B_k = 2t\sin(k)\sin(\phi_{ext}/2) \tag{C.6}$$

and σ_α (τ_α) acting on the leg degree of freedom (Nambu degree of freedom). The model has an intrinsic particle-hole symmetry $P = i\sigma_y\tau_y K$ with K complex conjugation. There is an emergent time-reversal symmetry $T' = i\sigma_y K$ at $t_\perp = 0$ which is broken at finite $t_\perp$. As stated in main text, the topological class is $\mathcal{D}$. The model is characterized by the $\mathbb{Z}_2$ topological index

$$(-1)^\nu = \mathrm{sgn}\left(t_\perp - \sqrt{\Delta^2 + (h^A_0)^2}\right)\mathrm{sgn}\left(t_\perp - \sqrt{\Delta^2 + (h^A_\pi)^2}\right) \tag{C.7}$$

given from the Pfaffian [193] at momenta $k = 0, \pi$. In the non-trivial phase, $\nu = 1$, the finite open ladder exhibits Majorana zero-modes at its boundaries.

More precisely, the model with open boundaries is diagonalized using the Bogoliubov transformation:

$$\hat{d}^\dagger_\mu = \sum_{n=(j,\sigma)} u_{n,\mu}\hat{c}^\dagger_n + v_{n,\mu}\hat{c}_n \qquad \hat{c}^\dagger_n = \sum_\mu u^*_{n,\mu}\hat{d}^\dagger_\mu + v_{n,\mu}\hat{d}_\mu \tag{C.8}$$

where $\sum_n |u_{n,\mu}|^2 + |v_{n,\mu}|^2 = 1$. This brings the Bogoliubov-de Genne onto:

$$H_0 = \sum_{\mu=1}^{L} \epsilon_\mu \hat{d}^\dagger_\mu \hat{d}_\mu \tag{C.9}$$

The Majorana zero-modes γ_L^0 and γ_R^0 will then form the complex fermion d_1 with $\epsilon_1 \simeq 0$:

$$\left|\overline{1}\right\rangle = \hat{d}_1^\dagger \left|\emptyset\right\rangle \quad d_1^\dagger = \frac{1}{2}(\gamma_L^0 + i\gamma_R^0) = \sum_{n=(\sigma,j)} u_{n,1}\hat{c}_n^\dagger + v_{n,1}\hat{c}_n \tag{C.10}$$

$$\hat{\gamma}_L^0 = \sum_n \psi_L^0(n)\hat{c}_n^\dagger + (\psi_L^0(n))^*\hat{c}_n \qquad \hat{\gamma}_R^0 = \sum_n \psi_R^0(n)\hat{c}_n^\dagger + (\psi_R^0(n))^*\hat{c}_n \tag{C.11}$$

$$\psi_L^0(n) = u_{n,1} + v_{n,1}^* \qquad \psi_R^0(n) = -i(u_{n,1} - v_{n,1}^*) \tag{C.12}$$

$$\sum_n |\psi_L^0(n)|^2 = \sum_n |\psi_R^0(n)|^2 = 1 \tag{C.13}$$

where $\left|\emptyset\right\rangle$ is the vacuum of quasi-particles and $\left|\overline{1}\right\rangle$ the other opposite parity ground state. Note that the fermion number parity of the vacuum $\left|\emptyset\right\rangle$ is not always the same and can be shown to be linked to the Pfaffian of the Bogoliubov transformation that diagonalize the single-particle hamiltonian [193, 213].

C.3. Theory of quasi-adiabatic continuation

C.3.1. General formalism

We give a more detailed discussion of the quasi-adiabatic dressing procedure. The concept here is to introduce an operator that continuously deforms the ground state manifold by progressively increasing the magnitude of cavity fluctuations. In a broader context, it can be applied to implement any perturbation, such as disorder for instance, in a continuous manner. This continuity is achieved by substituting the light-matter coupling constant g with sg, where s ranges from 0 to 1. This establishes a continuous interpolation denoted as H_s between the model with no cavity fluctuations at $s = 0$ and the model with complete fluctuations at $s = 1$. The unitary operator $\mathcal{V}_s$

$$\mathcal{V}_s = Te^{i\int_0^s \mathcal{D}_{s'}ds'} \qquad \mathcal{D}_s = -i\int_{-\infty}^{+\infty} dt\, F(\Delta_s t)\, e^{iH_s t}\partial_s H_s e^{-iH_s t}, \tag{C.14}$$

maps the ground state manifold at finite s to the one in the absence of cavity quantum fluctuations at $s = 0$. Δ_s is the spectral gap above the ground state subspace. The function $F(t)$ suppresses the long-time evolution to avoid a spatial spreading of operators spoiling locality as discussed below. The Fourier transform of $F(t)$ must satisfy

$$\tilde{F}(\omega) = \int_{-\infty}^{+\infty} dt e^{i\omega t}F(t) = -\frac{1}{\omega} \tag{C.15}$$

for $|\omega| \geq 1$. The choice of $\mathcal{V}_s$ is not unique (as the mapping of ground states does not fully determine $\mathcal{V}_s$) and, consequently, the form of $\tilde{F}(\omega)$ is not fixed for $|\omega| < 1$. It must however be such that $F(t)$ decays exponentially at long times to preserve locality. We now prove the need for Eq. (C.15) following Ref. [201]. We define the eigenstates of H_s

as $|j,s\rangle$ with $H_s|j,s\rangle = E_j^s|j,s\rangle$, and the spectrum E_j^s labeled by s. Using Eq. (C.15), the matrix elements of $\mathcal{D}_s$ are expressed as

$$i\langle j,s|\mathcal{D}_s|j',s\rangle = -\frac{\langle j,s|\partial_s H_s|j',s\rangle}{E_{j'}^s - E_j^s} = \langle j,s|\partial_s|j',s\rangle, \tag{C.16}$$

where either $j = 0,1$ (of the ground states) or $j' = 0$ so that $|E_{j'}^s - E_j^s| \geq \Delta_s$. We introduce the projector onto the ground state at finite s, $P_s = \sum_{j=0,1}|j,s\rangle\langle j,s|$. Then, we have

$$\langle j_1,s|\partial_s P_s|j_2,s\rangle = \sum_{j=0,1}\Big(\langle j_1,s|\partial_s|j,s\rangle\langle j,s|j_2,s\rangle - \langle j_1,s|j,s\rangle\langle j,s|\partial_s|j_2,s\rangle\Big) = i\langle j_1,s|[\mathcal{D}_s,P_s]|j_2,s\rangle, \tag{C.17}$$

regardless of j_1, j_2 and where we used Eq. (C.16). This proves that $\partial_s P_s = [\mathcal{D}_s, P_s]$ so that

$$P_s = \mathcal{V}_s P_0 \mathcal{V}_s^\dagger \tag{C.18}$$

where the solution for $\mathcal{V}_s$ is given in Eq. (C.14). Eq. (C.18) clearly identifies $\mathcal{V}_s$ as the unitary operator rotating the ground state manifold, and we have proven here that it requires the Fourier transform given in Eq. (C.15) (for $|\omega| \geq 1$).

One crucial point in the theory is the preservation of locality. This can be understood by examining the expression of $\mathcal{D}_s$ in Eq. (C.18). One first considers $\partial_s H_s$ which is local (in fact a sum of local terms) for fermionic variables since H_s is. Then $\partial_s H_s(t) = e^{iH_s t}\partial_s H_s e^{-iH_s t}$ evolves this operator in time and the exponential suppression of $F(t)$ ensures that the final result for $\mathcal{D}_s$ is local.

C.3.2. Perturbation theory

The results of adiabatic continuity are very powerful and general and they only require the perturbation to maintain the parity symmetry and the gap to remain finite. However, they only give a closed form for the rotated Majorana and an analytical solution is possible only in perturbation theory in g. Performing such a perturbation from Eq. (C.18) for the magnetic cavity, we find:

$$\hat{\gamma}_L \simeq \hat{\gamma}_L^0 + ig_B\left[\mathcal{D}_0, \hat{\gamma}_L^0\right] + \mathcal{O}(g_B^2) \tag{C.19}$$

The Hamiltonian expands as $\hat{H} = \hat{H}_0 + V_1\left(\hat{a} + \hat{a}^\dagger\right)$ with

$$\hat{V}_1 = \sum_{\alpha=L,R} C_\alpha \hat{\gamma}_\alpha^0 + \ldots \qquad C_\alpha = -\sum_{\mu\neq 1}\left(\lambda_\mu^\alpha \hat{d}_\mu^\dagger - (\lambda_\mu^\alpha)^* \hat{d}_\mu\right) \tag{C.20}$$

where $\ldots$ contains fermionic bilinears that do not involve the zero energy mode or are exponentially suppressed interactions between Majorana fermions of the form $\hat{\gamma}_L^0\hat{\gamma}_R^0$. The coefficients λ_μ^α are given by:

$$\lambda_\mu^\alpha = \frac{itg_B}{2}\sum_n \sigma e^{i\sigma\phi_{ext}/2}(u_n^*\psi_\alpha^0(n+1) - v_{n+1,\mu}^*(\psi_\alpha^0(n))^*) + \sigma e^{-i\sigma\phi_{ext}/2}(v_{n,\mu}^*(\psi_\alpha^0(n+1))^* - u_{n+1,\mu}^*\psi_\alpha^0(n) \tag{C.21}$$

We emphasize that the operators C_α have a fermionic spatial support which is exponentially localized on each end of the ladder. Using the fact that $[\hat{\gamma}^0_\alpha, H_0] = 0$, we can write the commutator in Eq. (C.19) as:

$$ig_B[\mathcal{D}_0, \hat{\gamma}^0_L] = \int_{-\infty}^{+\infty} dt\, F(\Delta_0 t) 2C_L(t)(\hat{a}(t) + \hat{a}^\dagger(t)) \qquad 2C_L(t) = e^{iH_0 t}[V_1, \hat{\gamma}^0_L]e^{-iH_0 t} \tag{C.22}$$

with $\hat{a}(t) = \hat{a}e^{-i\omega_c t}$. The commutator $[V_1, \hat{\gamma}^0_L] = 2C_L$ is exponentially localized on the left end of the ladder. $C_L(t)$ diffuses spatially as time evolves but the time integral in Eq. (C.22) is cut off by $F(\Delta_0 t)$ and the result is again left-localized with exponential precision. Using the expression in Eq. (C.20) for C_α, we find:

$$ig_B[\mathcal{D}_0, \hat{\gamma}^0_L] = -\frac{2}{\Delta_0}\sum_{\mu\neq 1} \lambda^L_\mu \hat{d}^\dagger_\mu \left[\hat{a}^\dagger \tilde{F}\left(\frac{\epsilon_\mu + \omega_c}{\Delta_0}\right) + \hat{a}\tilde{F}\left(\frac{\epsilon_\mu - \omega_c}{\Delta_0}\right)\right] - h.c. \tag{C.23}$$

To make further progress, we need to determine the explicit form of $\tilde{F}(\omega)$, and there are two possibilities that can be distinguished:

1. the single-photon energy $\hbar\omega_c$ does not cross the electronic spectrum. In that case, we introduce a minimal energy $\delta = \min_\mu|\omega_c - \varepsilon_\mu|$ and define $\tilde{F}(\omega) = -1/\omega$ down to $|\omega| \geq \delta/\Delta_0$. Since $\delta > 0$, this choice is compatible with the desired exponential suppression of $F(\Delta_0 t)$ for large $t \simeq 1/\delta$. The smaller δ, the larger the Majorana end states however expand spatially. The resulting Majorana polaritons are expressed as

$$\hat{\gamma}_\alpha \simeq \hat{\gamma}^0_\alpha + 2\sum_{\mu\neq 1}\left(\frac{\lambda^\alpha_\mu \hat{d}^\dagger_\mu \hat{a}^\dagger + h.c.}{\epsilon_\mu + \omega_c} + \frac{\lambda^\alpha_\mu \hat{d}^\dagger_\mu \hat{a} + h.c.}{\epsilon_\mu - \omega_c}\right). \tag{C.24}$$

   Reverting to the original fermionic operators, they adopt the form written in Eq. (4.9) in the main text with the wavefunctions:

$$\Psi^{1+}_L(n) = \psi^{1+}_L(n) + \phi^{1+}_L(n)\,, \qquad \Psi^{1-}_L(n) = \psi^{1-}_L(n) + \phi^{1-}_L(n)\,, \tag{C.25}$$

$$\psi^{1+}_L(n) = 2\sum_{\mu\neq 1}\frac{\lambda^L_\mu u_{n,\mu}}{\epsilon_\mu + \omega_c}, \qquad \psi^{1-}_L(n) = 2\sum_{\mu\neq 1}\frac{\lambda^L_\mu v_{n,\mu}}{\epsilon_\mu + \omega_c}, \tag{C.26}$$

$$\phi^{1+}_L(n) = 2\sum_{\mu\neq 1}\frac{\lambda^L_\mu v^*_{n,\mu}}{\epsilon_\mu - \omega_c}, \qquad \phi^{1-}_L(n) = 2\sum_{\mu\neq 1}\frac{\lambda^L_\mu u^*_{n,\mu}}{\epsilon_\mu - \omega_c}. \tag{C.27}$$

   It can be checked numerically, as illustrated in Fig. 4.5 of the main text, that these wavefunctions are exponentially localized on the left end of the ladder as expected from the quasi-adiabatic construction. A key feature of the hybrid Majorana operators in Eq. (C.24) is also that they commute with the full Hamiltonian,

$$[\hat{H}, \hat{\gamma}_L] = [\hat{H}, \hat{\gamma}_R] = 0 \tag{C.28}$$

   up to exponentially small corrections. It implies a twofold degenerate spectrum where the even and odd parity sectors have the same energies. The Majorana operators are called **strong edge modes** [201, 202, 205, 206].

2. the single-photon energy crosses the energy of an electronic state, $\hbar\omega_c = \varepsilon_{\mu_0}$. In this case, the choice $\tilde{F}(\omega) = -1/\omega$ cannot be made for all ω without violating locality. We thus keep choosing $\tilde{F}(\omega) = -1/\omega$ except for energies ϵ_μ close to ϵ_{μ_0} where $\tilde{F}(\omega)$ has to be suppressed to ensure the exponential drop in real time. For simplicity, we use $\tilde{F}(\omega) = 0$ only for $\omega = 0$, and obtain

$$\hat{\gamma}_r \simeq \hat{\gamma}_r^0 + 2 \sum_{\mu\neq 1,\mu_0} \left(\frac{\lambda_\mu^r \hat{d}_\mu^\dagger \hat{a}^\dagger + h.c.}{\epsilon_\mu + \omega_c} + \frac{\lambda_\mu^r \hat{d}_\mu \hat{a}^\dagger + h.c.}{\epsilon_\mu - \hbar\omega_c} \right). \tag{C.29}$$

where, in comparison with Eq. (C.24), only the μ_0 term has been excluded. In general, the commutation of the edge Majorana zero-modes with the Hamiltonian can be traced back to the choice $\tilde{F}(\omega) = -1/\omega$ made down to the smallest energies. Here, since there is one term missing, the Majorana polaritons no longer commute with the Hamiltonian which makes them **weak edge modes**. The terms that are missing for commutation involve $\hat{d}_\mu a^\dagger$ and $\hat{d}_\mu^\dagger a$. Nevertheless, since these two operators have a vanishing expectation within the ground state manifold, it implies that $\hat{\gamma}_L$ and $\hat{\gamma}_R$ still commute with the Hamiltonian when restricted to the ground state manifold, as demonstrated in the main text in the broader non-perturbative context. Consequently, the spectrum remains twofold degenerate in the ground state but not for excited states.

Finally, it is important to note that the presence of weak edge modes directly arises from a resonance condition $\hbar\omega_c = \varepsilon_{\mu_0}$ between a single photon and an electronic excitation. For higher orders in g in perturbation theory, we anticipate the possibility of multi-photon and multi-electron resonances. This will lift the degeneracy for most of the states in the many-body spectrum transforming the majorana modes into weak-edge modes. Indeed notice that in Fig. 4.2 of the main text there is no resonance between the first excited state $\Delta E = \epsilon_2 \simeq 0.33$ and the cavity frequency $\omega_c = 1$.

C.4. Details about the DMRG numerics

In order to perform our DMRG calculations for parity resolved ground and excited states we use the ITensor library [107]. The MPS ansatz is mapped onto the physical degrees of freedom as in Ref [1] and we implement the fermionic parity quantum number. The photon Hilbert space truncated dimension is $N_{max} = 64$, well above convergence. All of the results are obtained with a MPS bond dimension $\chi = 400$, enough to obtain a discarded weight below 10^{-9} for the ground states and 10^{-7} for the excited states. The ground state degeneracy shown in the main text is also converged up to 10^{-8}, even though the energy of each ground state itself do not reach this level of accuracy (Fig C.1). This cancellation is rooted in the fact that the finite bond dimension affects in the same way both parity sector ground states.

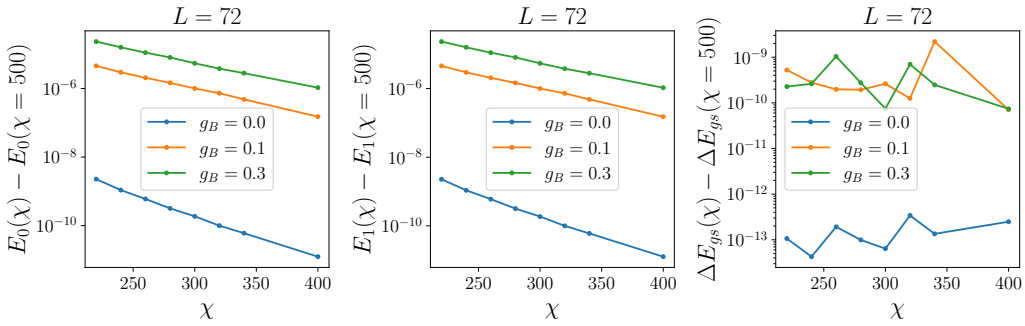


Figure C.1.: (a,b) Convergence of ground state energy for parity sector $p = 0$ and $p = 1$ for three values of the light-matter interaction strenght at $L = 72$

Appendix D.

Theory of Fractional Quantum Hall liquids coupled to quantum light and emergent graviton-polaritons

D.1. Test of the LLL truncation

In this Appendix we study more in detail the LLL truncation by directly including a finite number of Landau Levels $n_{LL} > 1$. We are going to compare results obtained with the two Hamiltonians used in the main text for a single LL $n_{LL} = 1$, namely $\hat{H}_\chi$ (Eq. (5.45)) and $\hat{H}_{\chi,\mu}$ (Eq. (5.47)), with the difference between the two being the single-particle cavity-induced vacuum Stark shift. For the sake of simplicity we are going to consider a mode function of the form $f_c(x) = C_1 x$ without an homogenues part. Whenever we indicate a number of $n_{LL} > 1$ we imply an Hamiltonian of the form:

$$\begin{aligned}\hat{H}^{n_{LL}} =& \hat{H}_{int}^{n_{LL}} + \hat{H}_0^{n_{LL}} + \omega_c \hat{a}^\dagger \hat{a} + \\ &+ i\omega_c(\hat{a}^\dagger - \hat{a})\hat{P}^{n_{LL}} + \omega_c \left(\hat{P}^{n_{LL}}\right)^2\end{aligned} \tag{D.1}$$

where the supscript n_{LL} implies a projection over the Hilbert space of n_{LL} LLs. Note that this form already for $n_{LL} = 2$ incorporate all relevant light-matter matrix elements of the LLL in the $n_{LL} \to \infty$ limit, but not all interaction matrix elements.

In Fig. D.1 we show the energy gap to the first excited state as a function of the coupling g (linear gradient) for two cyclotron frequencies $\omega_B = 100$ (a) and $\omega_B = 5000$ (b). Already at $g = 0.$ we have that higher LL create a discrepancy between different n_{LL}. It is indeed known that truncating electron-electron interaction inter-LL matrix elements has a slow convergence with n_{LL}, sometimes even giving physically different results by passing from $n_{LL} = 2$ to $n_{LL} = 3$ [256]. This discrepancy at $g = 0.$ is in any case well controlled by $1/\omega_B$ and indeed is heavily reduced in panel (b) where $\omega_B = 5000$. At finite $g > 0$ we instead clearly see that the model without vacuum-

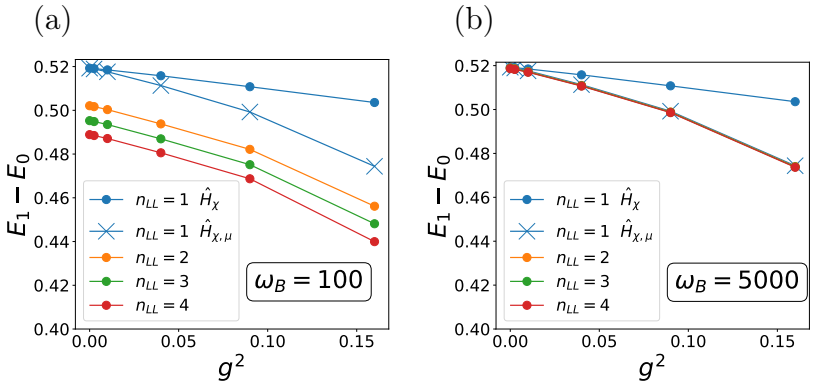


Figure D.1.: Energy gap from ED as a function of g^2 for different Landau Level truncations n_{LL}. The case of $n_{LL} = 1$ shows both scenarios with (cross) and without (dots) cavity-induced vacuum Stark shifts. The cyclotron frequency is $\omega_B = 100$ and $\omega_B = 5000$ in panel (a) and (b). Note that the Landau Level truncation affect the energy gap also at $g = 0$, with corrections of order $1/\omega_B$. At $g > 0$ instead the discrepancy between different $N_{LL} = 1$ and N_{LL} remains finite (order g^2 at small g) if the cavity-induced vacuum Stark shifts (μ_k) are ignored. Other parameters $N_e = 4$, $L_y = 10$ and $\omega_c = 1$.

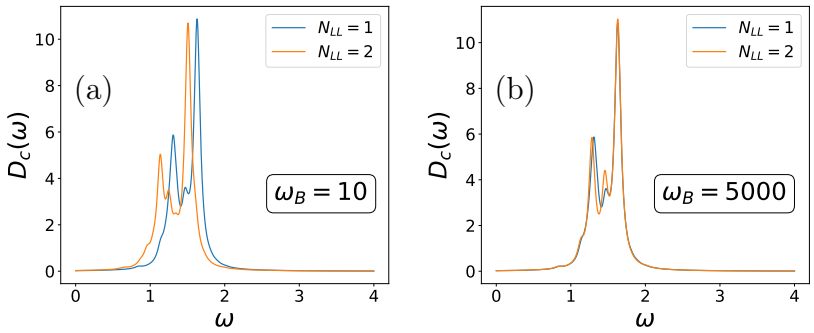


Figure D.2.: Cavity density of states $D_c(\omega)$ obtained with ED for different number of Landau Levels $N_{LL} = 1, 2$ both showing the graviton-polariton splitting with a resonant cavity $\omega_c = 1.5$. The cyclotron frequency is $\omega_B = 10$ and $\omega_B = 5000$ in panel (a) and (b). Other parameters $g = 0.1$, $N_e = 6$, $L_y = 10$ and $\eta = 0.05$.

induced Stark shifts $\hat{H}_\chi$ does not recover higher n_{LL} models, while $\hat{H}_{\chi,\mu}$ falls on top. Note that the discrepancy between $\hat{H}_\chi$ and $\hat{H}_{\chi,\mu}$ is of order g^2 as expected.

We now also check that the prediction of graviton-polaritons persist. To this end we show in Fig. D.2 the cavity density of states for two cyclotron frequencies, now $\omega_B = 10$ (a) and $\omega_B = 5000$ (b). In blue we show the result obtained with the LLL model $\hat{H}_\chi$ while in orange the model at $n_{LL} = 2$. Even at realistic values of the cyclotron frequency in terms of interaction energy scales $\omega_B = 10$, the polariton doublet is quite clear, featuring a shift in the graviton energy due to higher Landau Level mixing ($\sim 1/\omega_B$). This is confirmed by the fact that the shift of the doublet vanishes when ω_B is much larger (panel (b)).

As a last check we show how the LLL model $\hat{H}_{\chi,\mu}$ correctly captures also the

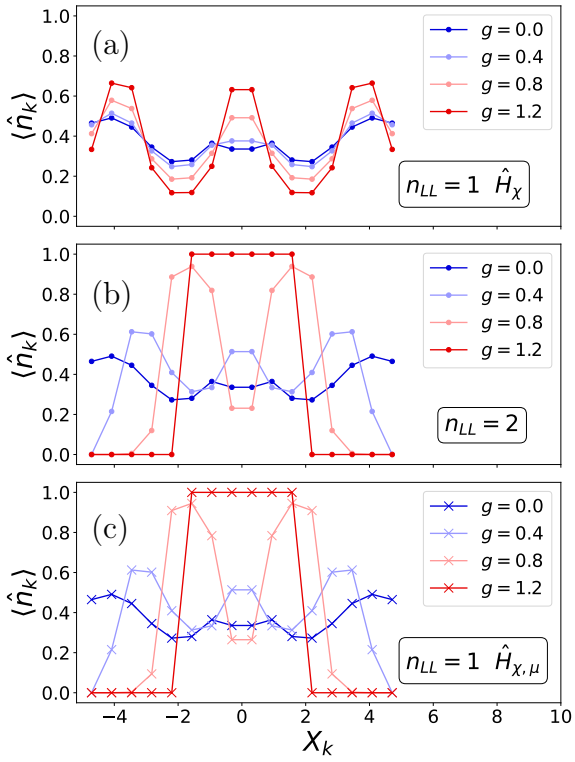


Figure D.3.: Electronic orbital occupation $\hat{n}_k = \sum_n \hat{c}^\dagger_{k,n}\hat{c}_{k,n}$ for different values of g as a function of orbitals position $X_k = kl_B^2$. Large cyclotron frequency $\omega_B = 5000$ but different Landau Level truncation to $N_{LL} = 1$ and $N_{LL} = 2$ respectively in panel (a) and (b). Other parameters $\omega_c = 1.$, $N_e = 6$, $L_y = 10$ and $\omega_B = 5000$.

ultrastrong-coupling behaviour when $\omega_B \to \infty$. This is done in Fig. D.3 where we compare orbital densities for both LLL models and the $n_{LL} = 2$ model up to high values of $g \simeq 1$. While in the LLL model $\hat{H}_\chi$ we see formation of stripes with $n = 2$ electrons, in both cases of $n_{LL} = 2$ and $\hat{H}_{\chi,\mu}$ we see how the cavity-induced vacuum Stark shift attracts electrons in the center forming phase separation between a fully filled LLL in the middle and nothing away from it. This is the ultimate fate of the system in the strong coupling limit of what has been explored in Sec. 5.5.3. Intermediate values of the coupling are difficult to analyze for such small system and might also show intermediate phases. We also remark that actually reaching phase separation will strongly depend on the presence of a neutralizing charge background absent in our case.

D.2. Cavity losses

We consider the effect of losses by introducing a weakly coupled photonic bath with Hamiltonian $\hat{H}_B$ and temperature T_B. In the weak system-bath coupling regime it is possible to derive a Lindblad master equation for the evolution of the system density

matrix [279], where by system here we mean both cavity and electrons together. Under standard approximations in this derivation (Born, Markov and secular) it is possible to show that the steady state of the system is going to be a thermal state [279]:

$$\hat{\Theta} = \frac{1}{\mathrm{Tr}\left[\exp\left(-\frac{1}{T_B}\hat{H}\right)\right]} \exp\left(-\frac{1}{T_B}\hat{H}\right) \tag{D.2}$$

where $\hat{\Theta}$ is the steady state density matrix of the electron-cavity system and $\hat{H}$ its Hamiltonian. The relevant information of equation D.2 is that for a weakly coupled bath, i.e. weak cavity losses, it is sufficient to look at the cavity plus electron system, independently on the strength of the cavity coupling. Moreover we remark that there is no conceptual difference with the coupling to an external electronic bath, the steady state for weakly coupled thermal environment is indeed a thermal state. In the $T_B \to 0$ limit we then have that the state of the system is up to exponential corrections the ground state of the electron-cavity Hamiltonian $\hat{H}$.

The deep consequence then is that the topological properties of the system will not be affected by cavity losses when the temperature of the photon bath is low. For example we can adapt the adiabatic flux insertion procedure of Section 5.3.1 to the case of an environment, assuming adiabaticity can still be reached in the open system scenario. The reason behind this robustness it is that the quantized resistivity is a ground state property and no photon losses can occur from the ground state when $T_B = 0$. At finite photon bath temperature $T_B > 0$ corrections to the quantization of transport are expected by the fact that we are giving a finite weight to excited states. Non-trivial effects may arise when the bath temperature for the electrons T_B^{el} is different from the bath temperature of the cavity T_B^c [40, 411], giving rise to a competition whose study is beyond the scope of this work.

D.3. Photon mean-field argument

In this Appendix we provide a more in depth discussion of the photon mean-field theory used in Sec. 5.5.2.

Due to the linear nature of the coupling term, the mean-field state generally reads:

$$|\Psi\rangle = |\alpha\rangle\,|\psi\rangle\,, \tag{D.3}$$

with $|\psi\rangle$ being an electronic wavefunction defined on the LLL, and $|\alpha\rangle$ being a coherent state. Minimizing the mean-field state energy over the coherent state value gives:

$$\alpha = i\sum_k \chi_k \langle\psi|\,\hat{n}_k\,|\psi\rangle\,. \tag{D.4}$$

In order to find the best mean-field ansatz, one should then take the photon mean-field

Hamiltonian for the electrons:

$$\hat{H}_{\mathrm{PMF}} = \hat{H}_{\mathrm{int}} + \omega_c \left[\sum_k \chi_k \big(\hat{n}_k - \langle \psi | \, \hat{n}_k \, | \psi \rangle \big) \right]^2 , \tag{D.5}$$

and find the ground state $|\psi\rangle$ with a self-consistent procedure [1].

This minimization still requires the solution of a complicated many-body Hamiltonian. However we can now clearly see two different terms competing, the first is the electron-electron interaction and the second is due to effective cavity mediated interactions. The latter has a very specific form, e.g., when calculated on the ground state $|\psi\rangle$, it is the variance of the polarization operator $\hat{P}$. This has two important consequences. First it is a positive number and second it is, in general, an extensive quantity, being proportional to N_e. These are not specific to the FQH set-up, but a more general property of Dipole gauge Hamiltonians where the so-called self polarization term is present [49]. For other models where only the linear coupling is present, e.g., the Dicke model, the all-to-all nature of the mode leads to collective enhanced cavity-mediated interactions which contribute superextensively, and grow as $g^2 N_e^2$. For this reason one can usually work with a collective coupling $g\sqrt{N_e}$. Here instead we clearly see that the cavity mediated interactions are controlled by the so-called single particle coupling constant g.

We can now discuss two limiting cases: $g = 0$ and $g \to \infty$. In the first case, we recover a pure Laughlin state, eigenstate of the first part of the Hamiltonian. In the second case instead, there will be a massive degeneracy of states with no fluctuations of the polarization operator $\hat{P}$ lifted only by the interactions $\hat{H}_{\mathrm{int}}$. All product states in the orbital basis will, for example, have no orbital density fluctuations and hence give identically zero contributions to the second term. Among these states we can write down stripe states with index n:

$$|S_n\rangle = |\{0_n 1_n 0_n\}\rangle \, , \tag{D.6}$$

where 0_n (1_n) indicates the repetition of zero (one) electron in n consecutive orbitals and the curly bracket indicate the repetition of such unit cell. Note that these states satisfy the bulk filling factor 1/3 by construction. The electron-electron interaction energy contribution of these states is also relatively simple to calculate. The mean-field energy of the stripe state $|S_n\rangle$ is:

$$E_{S_n} = \langle S_n | \, \hat{H}_{\mathrm{int}} \, | S_n \rangle = \sum_{k_1, k_2 \in K_{\mathrm{occ}}} 2 V_{k_1, k_2, k_2, k_1} , \tag{D.7}$$

where K_{occ} is the set of orbitals which are occupied in $|S_n\rangle$, and V_{k_1,k_2,k_2,k_1} are matrix elements given by Eq. (5.6). By changing the circumference of the cylinder L_y the energy per particle will also change, as shown in Fig. 5.9(f) of the main text. For each number of particles per stripe n, there is an L_y that minimizes the mean-field energy, which increases with n.

This behavior can be well understood by working in the thermodynamic limit $L_y \to \infty$. In this setting, the stripe state can be essentially viewed as an array of filled Fermi seas, each with Fermi momentum $k_{\rm F} = \pi n/L_y$, and whose centers are separated in momentum by $\Delta k = 6k_{\rm F}$. The circumference L_y controls the range of the electron-electron interactions V_{k_1,k_2,k_2,k_1} on the momentum basis via an exponential $\propto e^{-(k_1-k_2)^2/2}$. Thus, if we start from small L_y, i.e., large $k_{\rm F}$ for some n fixed, the most prominent contribution to E_{S_n} must come from interactions between electrons living on the same stripe. Then, by increasing L_y, interactions among electrons on different stripes are expected to become stronger. We thus expand the energy E_{S_n} as the sum

$$E_{S_n} = E_{S_n}^{(0)} + E_{S_n}^{(1)} + \cdots , \tag{D.8}$$

where $E_{S_n}^{(0)}$ and $E_{S_n}^{(1)}$ respectively represent the energy contributions of electrons on the same and nearest neighbor stripes. Taking the continuum limit $\sum_k \to \frac{L_y}{2\pi}\int \mathrm{d}k$, we estimate these two energy contributions (details on Appendix D.4) to be

$$E_{S_n}^{(0)} = 2N_e\Big[\,\mathrm{erf}(\sqrt{2}k_{\rm F}) + \frac{2e^{-2k_{\rm F}^2}-2}{\sqrt{2\pi}k_{\rm F}}\Big], \tag{D.9}$$

and

$$\begin{aligned} E_{S_n}^{(1)} = 4N_e\Big[&\,\mathrm{erf}(\sqrt{8}k_{\rm F}) - 3\,\mathrm{erf}(\sqrt{18}k_{\rm F}) + 2\,\mathrm{erf}(\sqrt{32}k_{\rm F}) \\ &+ \frac{e^{-8k_{\rm F}^2} - 2e^{-18k_{\rm F}^2} + e^{-32k_{\rm F}^2}}{\sqrt{2\pi}k_{\rm F}}\Big], \end{aligned} \tag{D.10}$$

where $\mathrm{erf}(x)$ is the Gauss error function. In Fig. 5.9(f) we plot the approximate form of E_{S_n} as a function of $1/k_{\rm F}$. Within this approximation, we find the minimum lies at $k_{\rm F,min} \simeq 0.62$, with a corresponding energy gap $E_{S_n}/N_e \simeq 0.25$. This means the number of electrons per stripe $n_S \approx L_y/5$ is only dictated by L_y in the thermodynamic limit as discussed above, see Eq. (5.78).

On the other hand we have that the Laughlin state $|\Psi_L\rangle$ is an eigenstate of $\hat{H}_{\rm int}$ with zero energy. This means the variational energy of the Laughlin state depends only on the light-induced interaction:

$$E_L = \omega_c \sum_{kk'} \chi_k \chi_{k'} \langle \Psi_L |\, \delta\hat{n}_k \delta\hat{n}_{k'} \,| \Psi_L \rangle \,, \tag{D.11}$$

where we have defined $\delta\hat{n}_k = \hat{n}_k - \langle\Psi_L|\,\hat{n}_k\,|\Psi_L\rangle$. Given that $\chi_k \propto k^2$, it is possible to compute this energy contribution via the long-wavelength behaviour of the static structure factor $S(\boldsymbol{q})$. From Eq. (5.77), we observe that E_L is directly tied to the S_4^{xx} component, so when we send $N_e \to \infty$, the mean-field energy scales as

$$E_L/N_e \approx S_4^{xx}\omega_c g^2/\nu, \tag{D.12}$$

where $\nu = 1/3$.

The outcome is that a transition to the stripe phase must take place once the energy of the Laughlin state E_L becomes equal or larger than the energy E_{S_n}. Replacing the value for the unperturbed Laughlin state, $S_4^{xx} = (1-\nu)/24\nu$, we find the magnitude of the critical point $g = g_\star$ goes as $\omega_c g_\star^2 \approx 1$. This is far below the observed values in the numerics, which happen close to $g \simeq 3$. One key reason behind this difference is the renormalization of S_4^{xx} as a function of the light-matter interaction as shown in Fig. 5.8. Given S_4^{xx} becomes smaller, the energy of the real ground state scales slower than g^2, and the transition is pushed towards a higher value of g. In particular, by using the numerical data for S_4^{xx} as a function of g, we have checked the true ground state energy agrees well with the formula in Eq. (D.12). The strong resilience of the FQH liquid to cavity fluctuations is then to be attributed to the change in its geometry, interpreted as a hidden variational parameter [229].

D.4. Stripe energy estimation

In this appendix we explicit our derivation for the approximate form of the mean-field energy E_{S_n} associated to the stripe state $|S_n\rangle = |\{0_n 1_n 0_n\}\rangle$. From the photon mean-field argument, the energy E_{S_n} is given by the expectation value $E_{S_n} = \langle S_n | \hat{H}_{\text{int}} | S_n \rangle$ as shown in Eq. (D.7). Writing out explicitly the matrix elements of $\hat{H}_{\text{int}}$, we have

$$E_{S_n} = \frac{\sqrt{8\pi}}{L_y} \sum_{k_1,k_2 \in K_{\text{occ}}} (k_1 - k_2)^2 e^{-(k_1-k_2)^2/2}, \tag{D.13}$$

where we recall K_{occ} denotes the set of orbitals that are occupied in the stripe state. Note the sums over k_1 and k_2 run independently. Let us then proceed to the thermodynamic limit by sending $L_y, n \to \infty$, while keeping their ratio n/L_y fixed. From the ratio n/L_y we define the Fermi momentum $k_{\text{F}} = \pi n/L_y$ of the stripes. With this, we may replace the original restricted sum over K_{occ} by $\sum_{k\in K_{\text{occ}}} \to \sum_\sigma \frac{L_y}{2\pi} \int_{-k_{\text{F}}}^{k_{\text{F}}} \mathrm{d}q$, where we sum over stripes labeled by the integer index σ, and integrate over occupied states within each stripe $|q| < k_{\text{F}}$. The electronic filling $\nu = 1/m$, with $m = 3$, fixes the relative distance among neighboring stripes, so we further replace the original momenta k in the summand by $k \to q + 2mk_{\text{F}}\sigma$ within the integral, where q is the momenta measured from the stripe center. We are then led to

$$\begin{aligned} E_{S_n} = \frac{L_y/\pi}{\sqrt{2\pi}} \sum_{\sigma_1\sigma_2} \int_{-k_{\text{F}}}^{k_{\text{F}}} \mathrm{d}q_1 \mathrm{d}q_2 (q_{12} + 6k_{\text{F}}\sigma_{12})^2 \\ \times e^{-\frac{1}{2}(q_{12}+6k_{\text{F}}\sigma_{12})^2}, \end{aligned} \tag{D.14}$$

where the integrand only depends on the relative variables $q_{12} = q_1 - q_2$ and $\sigma_{12} = \sigma_1 - \sigma_2$.

To extract a series, which only depends on the relative stripe coordinate $|\sigma_{12}|$, we assume translation invariance along x, so that we may simplify the formula in Eq.

(D.14) to

$$E_{S_n} = \frac{N_e}{\sqrt{2\pi}k_{\mathrm{F}}} \sum_{\sigma_{12}} \int_{-k_{\mathrm{F}}}^{k_{\mathrm{F}}} \mathrm{d}q_1 \mathrm{d}q_2 (q_{12} + 6k_{\mathrm{F}}\sigma_{12})^2 \times e^{-\frac{1}{2}(q_{12}+6k_{\mathrm{F}}\sigma_{12})^2}, \tag{D.15}$$

where we use that the total number of stripes must be fixed so that $N_{\mathrm{stripes}} = N_e/n$. In this form we see the energy can be naturally expanded as $E_{S_n} = \sum_r E_{S_n}^{(r)}$ for $r = |\sigma_{12}|$, where thanks to the exponential factor, these contributions decrease quite quickly as a function of r.

Let us then evaluate the first two contributions, corresponding to $\sigma_{12} = 0$ and $\sigma_{12} = \pm 1$. When $\sigma_{12} = 0$, both q_1 and q_2 belong to the same stripe. The integral is elementary and gives the energy contribution

$$E_{S_n}^{(0)} = 2N_e \big[\mathrm{erf}(\sqrt{2}k_{\mathrm{F}}) + \frac{2e^{-2k_{\mathrm{F}}^2} - 2}{\sqrt{2\pi}k_{\mathrm{F}}} \big], \tag{D.16}$$

where $\mathrm{erf}(x)$ is the error function, defined as $\mathrm{erf}(x) = \frac{2}{\sqrt{\pi}} \int_0^x \mathrm{d}t\, e^{-t^2}$. Likewise, we evaluate the contribution for $\sigma_{12} = \pm 1$, which comes from the interaction of neighboring stripes. The integral yields the same result for both $\sigma_{12} = +1$ and $\sigma_{12} = -1$, of course, and the energy contribution $E_{S_n}^{(1)}$ is found to be

$$E_{S_n}^{(1)} = 4N_e \Big[\mathrm{erf}(\sqrt{8}k_{\mathrm{F}}) - 3\,\mathrm{erf}(\sqrt{18}k_{\mathrm{F}}) + 2\,\mathrm{erf}(\sqrt{32}k_{\mathrm{F}}) + \frac{e^{-8k_{\mathrm{F}}^2} - 2e^{-8k_{\mathrm{F}}^2} + e^{-32k_{\mathrm{F}}^2}}{\sqrt{2\pi}k_{\mathrm{F}}} \Big]. \tag{D.17}$$

These two functions are plotted in the inset of Fig. 5.9(f). When added together they provide an estimate for the minimum of E_{S_n}, which sets the minimum energy gap to the stripe state as $E_{S_n}/N_e \simeq 0.25$ and fixes the Fermi momentum of that stripe state to $1/k_{\mathrm{F,min}} \simeq 1.62$.

D.5. Stripes as an array of Tomonaga-Luttinger liquids

In this appendix we discuss the potential low-energy theory for the light-induced stripe phase found numerically. We start from the photon mean-field ansatz $|S_n\rangle$, incorporating fluctuations phenomenologically. First, we consider the (infinitely) large light-matter coupling limit, where we assume the energy penalty to introduce δn_k fluctuations is so large we can only spare to build excitation with definite density occupation $n_k = 0, 1$. This is a great simplification that essentially allow us to treat the problem as an array of 1D free electron systems. This state is naturally gapped

along x, but remain gapless along the y direction, and can be viewed as an archetype of a smectic metal state [412–414], a state with zero shear modulus [415]. The gapless modes take the form of particle-hole excitations near the Fermi points of each stripe $k_\sigma = \pm k_\mathrm{F} + 6k_\mathrm{F}\sigma$, where $\sigma = 0, \pm 1, \pm 2, \ldots$ denotes the stripe index. To verify this, we first consider a particle excitation with momentum $k = k_\mathrm{F} + q$, assuming $q \ll k_\mathrm{F}$ so the excitation lies close to the right Fermi point of the stripe $\sigma = 0$. In this limit, similar to the analysis carried out in Appendix D.4, we approximate the energy cost of adding one electron by the integral:

$$\varepsilon(k_\mathrm{F} + q) \simeq \sqrt{\frac{2}{\pi}} \int_{-k_\mathrm{F}}^{k_\mathrm{F}} \mathrm{d}k (k_\mathrm{F} - k + q)^2 e^{-\frac{1}{2}(k_\mathrm{F} - k + q)^2}, \tag{D.18}$$

where we integrate over the nearest stripe only, throwing out energy contributions from distant stripes that are suppressed by the exponential factor. Evaluating the integral in the limit $q \to 0$, we find the linear dispersion relation $\varepsilon(k_\mathrm{F} + q) \approx \varepsilon(k_\mathrm{F}) + v_\mathrm{F} q + \cdots$, where $v_\mathrm{F} = \sqrt{\frac{2}{\pi}} 4k_\mathrm{F}^2 e^{-2k_\mathrm{F}^2}$ plays the role of the Fermi velocity. It thus follows that the particle-hole excitation $c_{k+q}^\dagger c_k \, |S_n\rangle$ in the vicinity of the Fermi level has a dispersion relation of the form $\omega(q) \approx v_\mathrm{F}|q| + \cdots$. Taking into account the pertubative addition of interactions, the free fermion behavior is then compatible with a sliding Tomonaga-Luttinger liquid (sTLL) model description of the stripe phase.

In this setting, the reintroduction of the light-matter coupling with a linear gradient profile couples to the number of excitations in each stripe separately, penalizing certain processes that change this number. In this way the gradient of the electric field fights against correlated hopping operators, such as the one used in coupled wire constructions to drive a transition to the FQH state [416]. If the gradient is strong enough even processes leading to stripe crystallization [414] (i.e., phase locking with $2k_\mathrm{F}$ density modulations along the stripes) are disfavored. Note that these couplings are controlled by the field variations across the intra- and inter-stripe distances $\Delta x \sim k_\mathrm{F} l_B^2$. The detailed interplay among these competing operators lies beyond our current mean-field ansatz, and we leave these refinements for future work.

D.6. Excited state targeting

In this section we present additional numerical result on the DMRG excited state targetting used in the main text (Fig. 5.6). As discussed in Ref. [272], excited states of local effective Hamiltonians constructed during DMRG sweeps are good approximations to excited states of the full Hamiltonian. By construction they are variational estimates, orthogonal to lower energy states at a fixed position during the sweep. The persistence of a certain excited state during the sweep was found to be a good indication of a converged excited state [272]. In Fig. D.4 we show the excited state spectrum obtained during a sweep as a function of the updating sites for different values of the

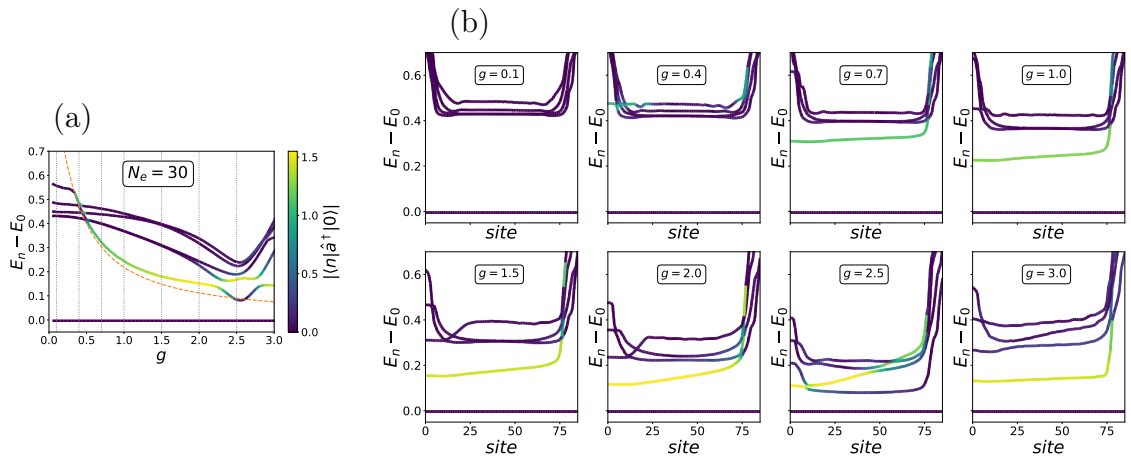


Figure D.4.: Excited state targettig with DMRG local effective Hamiltonians. Panel (a) shows the middle-chain value of the excited state as a function of coupling g for a system size $N_e = 30$ and $L_y = 16$. Orange dashed line indicate the lower polariton of the effective model. Panel (b) shows the site dependency of the excited states for different values of g, marked by vertical gray dotted lines in panel (a). The colorbar indicate the one photon matrix element with the ground state.

coupling g. A three site update is used here. In the FQH phase $g \lesssim 2.5$ we observe a good convergence of the lowest magnetoroton state (blu line) while the polariton state (lighter line) is flat only away from the transition. The asymmetric nature of our MPS ansatz (Sec. 5.2.7) with the photon on the left side clearly shows up here. Indeed the best variational estimate for the polariton state is not found in the bulk but closer to the cavity site. On the other hand magnetoroton excitations shows a phenomenology similar to Ref. [272] and have a lower variational energy in the bulk.

D.7. Large cavity frequency limit

In this appendix we briefly discuss the large cavity frequency limit $\omega_c \gg V_0$. This regime is subtle within the truncated model, as higher Landau level corrections become significant when ω_c approaches the cyclotron gap ω_B. Setting these refinements aside, the large ω_c regime can be understood intuitively: as $\omega_c \to \infty$, cavity photons become increasingly energetic, effectively decoupling from the low-energy electronic degrees of freedom. This behavior is consistent across dipole-gauge models and corresponds to the static limit in the path integral formulation presented in Ref. [72]. Note however that in order to take the large cavity frequency limit one need to assume the linear interaction term $ig\omega_c(\hat{a} - \hat{a}^\dagger)\hat{P}$ to be smaller than the cost of a photon, otherwise no elimination of the cavity mode is possible. The physically motivated choice of keeping $g\sqrt{\omega_c}$ fixed, or equivalently the Rabi frequency $\Omega = 2\tilde{\gamma}_0 g\sqrt{\omega_c V_0}$ fixed, acually does automatically the job in the $\omega_c \to \infty$ limit. Perturbation theory provides a straightforward way to verify this decoupling. To outline the derivation, we divide the Hamiltonian in diagonal and

off-diagonal terms:

$$\hat{H}_\chi = \hat{H}' + \hat{H}'' \tag{D.19}$$
$$\hat{H}' = \omega_c \hat{a}^\dagger \hat{a} + \hat{H}_{\text{int}} + g^2 \omega_c \hat{P}^2 \tag{D.20}$$
$$\hat{H}'' = ig\omega_c(\hat{a} - \hat{a}^\dagger)\hat{P}\ ; \tag{D.21}$$

Using a Schrieffer-Wolff transformation with a generator:

$$\hat{S} = -ig(\hat{a} + \hat{a}^\dagger)\hat{P} \tag{D.22}$$

one can successfully decouple the photon dynamics and get an effective Hamiltonian up to second order in perturbation theory:

$$\hat{H}_{\text{eff}} = e^{\hat{S}} \hat{H}_\chi e^{-\hat{S}} \simeq \hat{H}' - g^2 \omega_c \hat{P}^2 + O\left(g^3 \omega_c\right) = \tag{D.23}$$
$$= \hat{H}_{\text{int}} + \omega_c \hat{a}^\dagger \hat{a} + O\left(g^3 \omega_c\right)\ . \tag{D.24}$$

We thus find the $\hat{P}^2$ terms cancel out, leaving us with just the decoupled theory $\hat{H}_{\text{eff}} \simeq \hat{H}_0 = \hat{H}_{\text{int}} + \omega_c \hat{a}^\dagger \hat{a}$ up to second-order in g. Note that the corrections identified in [45], with the caveat of being obtained in a different LLL truncation scheme, scale with the gradient to the fourth power.

Bibliography

[1] Z. Bacciconi, G. M. Andolina, T. Chanda, G. Chiriacò, M. Schirò, and M. Dalmonte, *First-order photon condensation in magnetic cavities: A two-leg ladder model,* SciPost Phys. **15**, 113 (2023) .

[2] Z. Bacciconi, H. Xavier, M. Capone, and M. Dalmonte, *Cavity-modified quasi-long range order in one dimensional quantum systems,* In preparation, .

[3] Z. Bacciconi, H. B. Xavier, M. Marinelli, D. S. Bhakuni, and M. Dalmonte, *Local vs Nonlocal Dynamics in Cavity-Coupled Rydberg Atom Arrays,* Phys. Rev. Lett. **134**, 213604 (2025) .

[4] Z. Bacciconi, G. M. Andolina, and C. Mora, *Topological protection of Majorana polaritons in a cavity,* Phys. Rev. B **109**, 165434 (2024) .

[5] Z. Bacciconi, H. B. Xavier, I. Carusotto, T. Chanda, and M. Dalmonte, *Theory of Fractional Quantum Hall Liquids Coupled to Quantum Light and Emergent Graviton-Polaritons,* Phys. Rev. X **15**, 021027 (2025) .

[6] H. B. Xavier, Z. Bacciconi, T. Chanda, D. T. Son, and M. Dalmonte, *Chiral Gravitons on the Lattice,* arXiv:2505.02905 [cond-mat.str-el] (2025).

[7] Z. Bacciconi, G. Piccitto, A. M. Verga, G. Falci, E. Paladino, and G. Chiriacò, *Dissipation and non-thermal states in cryogenic cavities,* arXiv:2504.00591 [quant-ph] (2025).

[8] G. M. Andolina, Z. Bacciconi, A. Nardin, P. Rabl, M. Schirò, and D. D. Bernardis, *Electrostatics-induced breakdown of the integer quantum Hall effect in cavity QED,* To appear soon, .

[9] F. Schlawin, D. M. Kennes, and M. A. Sentef, *Cavity quantum materials,* Applied Physics Reviews **9**, 011312 (2022) .

[10] F. J. Garcia-Vidal, C. Ciuti, and T. W. Ebbesen, *Manipulating matter by strong coupling to vacuum fields,* Science **373**, eabd0336 (2021) .

[11] J. Bloch, A. Cavalleri, V. Galitski, M. Hafezi, and A. Rubio, *Strongly correlated electron–photon systems,* Nature **606**, 41 (2022) .

[12] F. Mivehvar, F. Piazza, T. Donner, and H. Ritsch, *Cavity QED with quantum gases: new paradigms in many-body physics,* Advances in Physics **70**, 1 (2021) .

[13] H. Walther, B. T. H. Varcoe, B.-G. Englert, and T. Becker, *Cavity quantum electrodynamics,* Reports on Progress in Physics **69**, 1325 (2006) .

[14] S. Haroche and D. Kleppner, *Cavity Quantum Electrodynamics,* in *Confined Electrons and Photons: New Physics and Applications*, edited by E. Burstein and C. Weisbuch (Springer US, Boston, MA, 1995) pp. 849–855.

[15] E. M. Purcell, H. C. Torrey, and R. V. Pound, *Resonance Absorption by Nuclear Magnetic Moments in a Solid,* Phys. Rev. **69**, 37 (1946) .

[16] P. Forn-Díaz, L. Lamata, E. Rico, J. Kono, and E. Solano, *Ultrastrong coupling regimes of light-matter interaction,* Rev. Mod. Phys. **91**, 025005 (2019) .

[17] D. N. Basov, A. Asenjo-Garcia, P. J. Schuck, X. Zhu, and A. Rubio, *Polariton panorama,* Nanophotonics **10**, 549 (2020) .

[18] H. A. Bethe, *The Electromagnetic Shift of Energy Levels,* Phys. Rev. **72**, 339 (1947) .

[19] G. Scalari, C. Maissen, D. Turčinková, D. Hagenmüller, S. D. Liberato, C. Ciuti, C. Reichl, D. Schuh, W. Wegscheider, M. Beck, and J. Faist, *Ultrastrong Coupling of the Cyclotron Transition of a 2D Electron Gas to a THz Metamaterial,* Science **335**, 1323 (2012) .

[20] I. Epstein, D. Alcaraz, Z. Huang, V.-V. Pusapati, J.-P. Hugonin, A. Kumar, X. M. Deputy, T. Khodkov, T. G. Rappoport, J.-Y. Hong, N. M. R. Peres, J. Kong, D. R. Smith, and F. H. L. Koppens, *Far-field excitation of single graphene plasmon cavities with ultracompressed mode volumes,* Science **368**, 1219 (2020) .

[21] S. Dai, Z. Fei, Q. Ma, A. S. Rodin, M. Wagner, A. S. McLeod, M. K. Liu, W. Gannett, W. Regan, K. Watanabe, T. Taniguchi, M. Thiemens, G. Dominguez, A. H. C. Neto, A. Zettl, F. Keilmann, P. Jarillo-Herrero, M. M. Fogler, and D. N. Basov, *Tunable Phonon Polaritons in Atomically Thin van der Waals Crystals of Boron Nitride,* Science **343**, 1125 (2014) .

[22] H. Ritsch, P. Domokos, F. Brennecke, and T. Esslinger, *Cold atoms in cavity-generated dynamical optical potentials,* Rev. Mod. Phys. **85**, 553 (2013) .

[23] K. Baumann, C. Guerlin, F. Brennecke, and T. Esslinger, *Dicke quantum phase transition with a superfluid gas in an optical cavity,* Nature **464**, 1301–1306 (2010) .

[24] J. Léonard, A. Morales, P. Zupancic, T. Esslinger, and T. Donner, *Supersolid formation in a quantum gas breaking a continuous translational symmetry,* Nature **543**, 87–90 (2017) .

[25] D. Hagenmüller, J. Schachenmayer, S. Schütz, C. Genes, and G. Pupillo, *Cavity-Enhanced Transport of Charge,* Phys. Rev. Lett. **119**, 223601 (2017) .

[26] G. Arwas and C. Ciuti, *Quantum electron transport controlled by cavity vacuum fields,* Phys. Rev. B **107**, 045425 (2023) .

[27] M. A. Sentef, M. Ruggenthaler, and A. Rubio, *Cavity quantum-electrodynamical polaritonically enhanced electron-phonon coupling and its influence on superconductivity,* Science Advances **4**, eaau6969 (2018) .

[28] F. Schlawin, A. Cavalleri, and D. Jaksch, *Cavity-Mediated Electron-Photon Superconductivity,* Phys. Rev. Lett. **122**, 133602 (2019) .

[29] O. Dmytruk and M. Schirò, *Controlling topological phases of matter with quantum light,* Communications Physics **5**, 271 (2022) .

[30] F. P. M. Méndez-Córdoba, J. J. Mendoza-Arenas, F. J. Gómez-Ruiz, F. J. Rodríguez, C. Tejedor, and L. Quiroga, *Rényi entropy singularities as signatures of topological criticality in coupled photon-fermion systems,* Phys. Rev. Res. **2**, 043264 (2020) .

[31] D.-P. Nguyen, G. Arwas, Z. Lin, W. Yao, and C. Ciuti, *Electron-Photon Chern Number in Cavity-Embedded 2D Moiré Materials,* Phys. Rev. Lett. **131**, 176602 (2023) .

[32] D.-P. Nguyen, G. Arwas, and C. Ciuti, *Electron conductance and many-body marker of a cavity-embedded topological one-dimensional chain,* Phys. Rev. B **110**, 195416 (2024) .

[33] A. Chiocchetta, D. Kiese, C. P. Zelle, F. Piazza, and S. Diehl, *Cavity-induced quantum spin liquids,* Nature Communications **12**, 5901 (2021) .

[34] P. Fadler, K. P. Schmidt, J. Li, and M. Eckstein, *Engineering photon-mediated long-range spin interactions in Mott insulators,* Phys. Rev. B **109**, 085149 (2024) .

[35] L. Weber, E. Viñas Boström, M. Claassen, A. Rubio, and D. M. Kennes, *Cavity-renormalized quantum criticality in a honeycomb bilayer antiferromagnet,* Communications Physics **6** (2023), 10.1038/s42005-023-01359-x .

[36] G. Chiriacò, M. Dalmonte, and T. Chanda, *Critical Light-Matter Entanglement at Cavity Mediated Phase Transitions,* Physical Review B **106**, 155113 (2022) .

[37] Y. Ashida, A. İmamoğlu, J. Faist, D. Jaksch, A. Cavalleri, and E. Demler, *Quantum Electrodynamic Control of Matter: Cavity-Enhanced Ferroelectric Phase Transition,* Phys. Rev. X **10**, 041027 (2020) .

[38] K. Lenk, J. Li, P. Werner, and M. Eckstein, *Dynamical mean-field study of a photon-mediated ferroelectric phase transition,* Phys. Rev. B **106**, 245124 (2022) .

[39] R. Riolo, A. Tomadin, G. Mazza, R. Asgari, A. H. MacDonald, and M. Polini, *Tuning Fermi liquids with polaritonic cavities,* Proceedings of the National Academy of Sciences **122**, e2407995122 (2025) .

[40] G. Jarc, S. Y. Mathengattil, A. Montanaro, F. Giusti, E. M. Rigoni, R. Sergo, F. Fassioli, S. Winnerl, S. Dal Zilio, D. Mihailovic, P. Prelovšek, M. Eckstein, and D. Fausti, *Cavity-Mediated Thermal Control of Metal-to-Insulator Transition in 1T-TaS2,* Nature **622**, 487 (2023) .

[41] G. L. Paravicini-Bagliani, F. Appugliese, E. Richter, F. Valmorra, J. Keller, M. Beck, N. Bartolo, C. Rössler, T. Ihn, K. Ensslin, C. Ciuti, G. Scalari, and J. Faist, *Magneto-transport controlled by Landau polariton states,* Nature Physics **15**, 186 (2018) .

[42] E. Orgiu, J. George, J. A. Hutchison, E. Devaux, J. F. Dayen, B. Doudin, F. Stellacci, C. Genet, J. Schachenmayer, C. Genes, G. Pupillo, P. Samorì, and T. W. Ebbesen, *Conductivity in organic semiconductors hybridized with the vacuum field,* Nature Materials **14**, 1123 (2015) .

[43] F. Appugliese, J. Enkner, G. L. Paravicini-Bagliani, M. Beck, C. Reichl, W. Wegscheider, G. Scalari, C. Ciuti, and J. Faist, *Breakdown of topological protection by cavity vacuum fields in the integer quantum Hall effect,* Science **375**, 1030 (2022) .

[44] J. Enkner, L. Graziotto, F. Appugliese, V. Rokaj, J. Wang, M. Ruggenthaler, C. Reichl, W. Wegscheider, A. Rubio, and J. Faist, *Testing the Renormalization of the von Klitzing Constant by Cavity Vacuum Fields,* Phys. Rev. X **14**, 021038 (2024) .

[45] J. Enkner, L. Graziotto, D. Boriçi, F. Appugliese, C. Reichl, G. Scalari, N. Regnault, W. Wegscheider, C. Ciuti, and J. Faist, *Tunable vacuum-field control of fractional and integer quantum Hall phases,* Nature **641**, 884–889 (2025) .

[46] L. Graziotto, J. Enkner, S. Chattopadhyay, J. B. Curtis, E. Koskas, C. Reichl, W. Wegscheider, G. Scalari, E. Demler, and J. Faist, *Cavity QED Control of Quantum Hall Stripes,* arXiv:2502.15490 [cond-mat.mes-hall] (2025).

[47] I. Keren, T. A. Webb, S. Zhang, J. Xu, D. Sun, B. S. Y. Kim, D. Shin, S. S. Zhang, J. Zhang, G. Pereira, J. Yao, T. Okugawa, M. H. Michael, E. V. Boström, J. H. Edgar, S. Wolf, M. Julian, R. P. Prasankumar, K. Miyagawa, K. Kanoda, G. Gu, M. Cothrine, D. Mandrus, M. Buzzi, A. Cavalleri, C. R. Dean, D. M. Kennes, A. J. Millis, Q. Li, M. A. Sentef, A. Rubio, A. N. Pasupathy, and D. N. Basov, *Cavity-altered superconductivity,* arXiv:2505.17378 [cond-mat.supr-con] (2025).

[48] M. Kiffner, J. Coulthard, F. Schlawin, A. Ardavan, and D. Jaksch, *Mott Polaritons in Cavity-Coupled Quantum Materials,* New Journal of Physics **21**, 073066 (2019) .

[49] M. Schuler, D. D. Bernardis, A. M. Läuchli, and P. Rabl, *The vacua of dipolar cavity quantum electrodynamics,* SciPost Phys. **9**, 066 (2020) .

[50] G. Passetti, C. J. Eckhardt, M. A. Sentef, and D. M. Kennes, *Cavity Light-Matter Entanglement through Quantum Fluctuations,* Phys. Rev. Lett. **131**, 023601 (2023) .

[51] C.-M. Halati, A. Sheikhan, and C. Kollath, *Theoretical methods to treat a single dissipative bosonic mode coupled globally to an interacting many-body system,* Phys. Rev. Research **2**, 043255 (2020) .

[52] J. B. Curtis, Z. M. Raines, A. A. Allocca, M. Hafezi, and V. M. Galitski, *Cavity Quantum Eliashberg Enhancement of Superconductivity,* Physical Review Letters **122**, 167002 (2019) .

[53] S. Latini, D. Shin, S. A. Sato, C. Schäfer, U. D. Giovannini, H. Hübener, and A. Rubio, *The ferroelectric photo ground state of $SrTiO_3$: Cavity materials engineering,* Proceedings of the National Academy of Sciences **118**, e2105618118 (2021) .

[54] K. Rzażewski, K. Wódkiewicz, and W. Żakowicz, *Phase Transitions, Two-Level Atoms, and the A^2 Term,* Phys. Rev. Lett. **35**, 432 (1975) .

[55] I. Bialynicki-Birula and K. Rzążewski, *No-go theorem concerning the superradiant phase transition in atomic systems,* Phys. Rev. A **19**, 301 (1979) .

[56] K. Gawędzki and K. Rzążewski, *No-go theorem for the superradiant phase transition without dipole approximation,* Phys. Rev. A **23**, 2134 (1981) .

[57] D. Hagenmüller and C. Ciuti, *Cavity QED of the Graphene Cyclotron Transition,* Phys. Rev. Lett. **109**, 267403 (2012) .

[58] C. Ciuti and P. Nataf, *Comment on "Superradiant Phase Transitions and the Standard Description of Circuit QED",* Phys. Rev. Lett. **109**, 179301 (2012) .

[59] T. Jaako, Z.-L. Xiang, J. J. Garcia-Ripoll, and P. Rabl, *Ultrastrong-coupling phenomena beyond the Dicke model,* Phys. Rev. A **94**, 033850 (2016) .

[60] M. Bamba, K. Inomata, and Y. Nakamura, *Superradiant Phase Transition in a Superconducting Circuit in Thermal Equilibrium,* Phys. Rev. Lett. **117**, 173601 (2016) .

[61] G. Mazza and A. Georges, *Superradiant Quantum Materials,* Phys. Rev. Lett. **122**, 017401 (2019) .

[62] V. Bužek, M. Orszag, and M. Roško, *Instability and Entanglement of the Ground State of the Dicke Model,* Phys. Rev. Lett. **94**, 163601 (2005) .

[63] K. Rzażewski and K. Wódkiewicz, *Comment on "Instability and Entanglement of the Ground State of the Dicke Model",* Phys. Rev. Lett. **96**, 089301 (2006) .

[64] A. F. Kockum, A. Miranowicz, S. D. Liberato, S. Savasta, and F. Nori, *Ultrastrong coupling between light and matter,* Nature Reviews Physics **1**, 19 (2019) .

[65] D. De Bernardis, P. Pilar, T. Jaako, S. De Liberato, and P. Rabl, *Breakdown of gauge invariance in ultrastrong-coupling cavity QED,* Phys. Rev. A **98**, 053819 (2018) .

[66] O. Di Stefano, A. Settineri, V. Macrì, L. Garziano, R. Stassi, S. Savasta, and F. Nori, *Resolution of gauge ambiguities in ultrastrong-coupling cavity quantum electrodynamics,* Nature Physics **15**, 803–808 (2019) .

[67] S. Savasta, O. Di Stefano, A. Settineri, D. Zueco, S. Hughes, and F. Nori, *Gauge principle and gauge invariance in two-level systems,* Phys. Rev. A **103**, 053703 (2021) .

[68] G. M. Andolina, F. M. D. Pellegrino, V. Giovannetti, A. H. MacDonald, and M. Polini, *Cavity quantum electrodynamics of strongly correlated electron systems: A no-go theorem for photon condensation,* Phys. Rev. B **100**, 121109 (2019) .

[69] G. M. Andolina, F. M. D. Pellegrino, A. Mercurio, O. Di Stefano, M. Polini, and S. Savasta, *A non-perturbative no-go theorem for photon condensation in approximate models,* The European Physical Journal Plus **137**, 1348 (2022) .

[70] J. Li, D. Golez, G. Mazza, A. J. Millis, A. Georges, and M. Eckstein, *Electromagnetic coupling in tight-binding models for strongly correlated light and matter,* Phys. Rev. B **101**, 205140 (2020) .

[71] K. Lenk and M. Eckstein, *Collective excitations of the U(1)-symmetric exciton insulator in a cavity,* Phys. Rev. B **102**, 205129 (2020) .

[72] O. Dmytruk and M. Schiró, *Gauge fixing for strongly correlated electrons coupled to quantum light,* Phys. Rev. B **103**, 075131 (2021) .

[73] P. Nataf, T. Champel, G. Blatter, and D. M. Basko, *Rashba Cavity QED: A Route Towards the Superradiant Quantum Phase Transition,* Phys. Rev. Lett. **123**, 207402 (2019) .

[74] G. M. Andolina, F. M. D. Pellegrino, V. Giovannetti, A. H. MacDonald, and M. Polini, *Theory of Photon Condensation in a Spatially Varying Electromagnetic Field,* Physical Review B **102**, 125137 (2020) .

[75] D. Guerci, P. Simon, and C. Mora, *Superradiant Phase Transition in Electronic Systems and Emergent Topological Phases,* Phys. Rev. Lett. **125**, 257604 (2020) .

[76] D. Guerci, P. Simon, and C. Mora, *Moiré lattice effects on the orbital magnetic response of twisted bilayer graphene and Condon instability,* Phys. Rev. B **103**, 224436 (2021) .

[77] J. Román-Roche, F. Luis, and D. Zueco, *Photon Condensation and Enhanced Magnetism in Cavity QED,* Phys. Rev. Lett. **127**, 167201 (2021) .

[78] G. Manzanares, T. Champel, D. M. Basko, and P. Nataf, *Superradiant quantum phase transition for Landau polaritons with Rashba and Zeeman couplings,* Phys. Rev. B **105**, 245304 (2022) .

[79] J. H. Condon, *Nonlinear de Haas-van Alphen Effect and Magnetic Domains in Beryllium,* Phys. Rev. **145**, 526 (1966) .

[80] C. J. Eckhardt, G. Passetti, M. Othman, C. Karrasch, F. Cavaliere, M. A. Sentef, and D. M. Kennes, *Quantum Floquet engineering with an exactly solvable tight-binding chain in a cavity,* Communications Physics **5** (2022), 10.1038/s42005-022-00880-9 .

[81] E. Orignac and T. Giamarchi, *Meissner effect in a bosonic ladder,* Phys. Rev. B **64**, 144515 (2001) .

[82] S. T. Carr, B. N. Narozhny, and A. A. Nersesyan, *Spinless fermionic ladders in a magnetic field: Phase diagram,* Phys. Rev. B **73**, 195114 (2006) .

[83] S. Greschner, M. Piraud, F. Heidrich-Meisner, I. P. McCulloch, U. Schollwöck, and T. Vekua, *Spontaneous Increase of Magnetic Flux and Chiral-Current Reversal in Bosonic Ladders: Swimming against the Tide,* Phys. Rev. Lett. **115**, 190402 (2015) .

[84] M. Calvanese Strinati, E. Cornfeld, D. Rossini, S. Barbarino, M. Dalmonte, R. Fazio, E. Sela, and L. Mazza, *Laughlin-like States in Bosonic and Fermionic Atomic Synthetic Ladders,* Phys. Rev. X **7**, 021033 (2017) .

[85] B. Beradze and A. Nersesyan, *Spectrum, Lifshitz transitions and orbital current in frustrated fermionic ladders with a uniform flux,* The European Physical Journal B **96** (2023), 10.1140/epjb/s10051-022-00472-0 .

[86] I. V. Tokatly, D. R. Gulevich, and I. Iorsh, *Vacuum anomalous Hall effect in gyrotropic cavity,* Phys. Rev. B **104**, L081408 (2021) .

[87] D. D. Sedov, V. Shirobokov, I. V. Iorsh, and I. V. Tokatly, *Cavity-induced chiral edge currents and spontaneous magnetization in two-dimensional electron systems,* Phys. Rev. B **106**, 205114 (2022) .

[88] A. Ghirri, C. Bonizzoni, M. Maksutoglu, A. Mercurio, O. Di Stefano, S. Savasta, and M. Affronte, *Ultrastrong Magnon-Photon Coupling Achieved by Magnetic Films in Contact with Superconducting Resonators,* Physical Review Applied **20** (2023), 10.1103/physrevapplied.20.024039 .

[89] S. R. White, *Density matrix formulation for quantum renormalization groups,* Phys. Rev. Lett. **69**, 2863 (1992) .

[90] S. R. White, *Density-matrix algorithms for quantum renormalization groups,* Phys. Rev. B **48**, 10345 (1993) .

[91] U. Schollwöck, *The density-matrix renormalization group in the age of matrix product states,* Annals of Physics **326**, 96 (2011) .

[92] R. Orús, *A practical introduction to tensor networks: Matrix product states and projected entangled pair states,* Annals of Physics **349**, 117 (2014) .

[93] C.-M. Halati, A. Sheikhan, H. Ritsch, and C. Kollath, *Numerically Exact Treatment of Many-Body Self-Organization in a Cavity,* Phys. Rev. Lett. **125**, 093604 (2020) .

[94] C.-M. Halati, A. Sheikhan, and C. Kollath, *Breaking strong symmetries in dissipative quantum systems: Bosonic atoms coupled to a cavity,* Phys. Rev. Research **4**, L012015 (2022) .

[95] S. Gammelmark and K. Mølmer, *Interacting spins in a cavity: Finite-size effects and symmetry-breaking dynamics,* Phys. Rev. A **85**, 042114 (2012) .

[96] J. Klaers, J. Schmitt, F. Vewinger, and M. Weitz, *Bose–Einstein condensation of photons in an optical microcavity,* Nature **468**, 545 (2010) .

[97] J. M. Luttinger, *The Effect of a Magnetic Field on Electrons in a Periodic Potential,* Phys. Rev. **84**, 814 (1951) .

[98] C. Cohen-Tannoudji, J. Dupont-Roc, and G. Grynberg, eds., *Photons and Atoms: Introduction to Quantum Electrodynamics* (Wiley, 1997).

[99] A. Stokes and A. Nazir, *Implications of gauge freedom for nonrelativistic quantum electrodynamics,* Rev. Mod. Phys. **94**, 045003 (2022) .

[100] A. Stokes and A. Nazir, *Uniqueness of the Phase Transition in Many-Dipole Cavity Quantum Electrodynamical Systems,* Phys. Rev. Lett. **125**, 143603 (2020) .

[101] C. Kollath, A. Sheikhan, S. Wolff, and F. Brennecke, *Ultracold Fermions in a Cavity-Induced Artificial Magnetic Field,* Phys. Rev. Lett. **116**, 060401 (2016) .

[102] W. Zheng and N. R. Cooper, *Superradiance Induced Particle Flow via Dynamical Gauge Coupling,* Phys. Rev. Lett. **117**, 175302 (2016) .

[103] S. Singh, R. N. C. Pfeifer, and G. Vidal, *Tensor network decompositions in the presence of a global symmetry,* Phys. Rev. A **82**, 050301 (2010) .

[104] S. Singh, R. N. C. Pfeifer, and G. Vidal, *Tensor network states and algorithms in the presence of a global U(1) symmetry,* Phys. Rev. B **83**, 115125 (2011) .

[105] G. M. Crosswhite, A. C. Doherty, and G. Vidal, *Applying matrix product operators to model systems with long-range interactions,* Phys. Rev. B **78**, 035116 (2008) .

[106] B. Pirvu, V. Murg, J. I. Cirac, and F. Verstraete, *Matrix product operator representations,* New Journal of Physics **12**, 025012 (2010) .

[107] M. Fishman, S. R. White, and E. M. Stoudenmire, *The ITensor Software Library for Tensor Network Calculations,* SciPost Phys. Codebases , 4 (2022) .

[108] G. Mazza and M. Polini, *Hidden excitonic quantum states with broken time-reversal symmetry,* Phys. Rev. B **108**, L241107 (2023) .

[109] P. Pilar, D. De Bernardis, and P. Rabl, *Thermodynamics of ultrastrongly coupled light-matter systems,* Quantum **4**, 335 (2020) .

[110] K. Lenk, J. Li, P. Werner, and M. Eckstein, *Collective theory for an interacting solid in a single-mode cavity,* arXiv:2205.05559 [cond-mat.str-el] (2022).

[111] M. G. Genoni and M. G. A. Paris, *Quantifying non-Gaussianity for quantum information,* Phys. Rev. A **82**, 052341 (2010) .

[112] D. Walls and G. J. Milburn, eds., *Quantum Optics* (Springer Berlin Heidelberg, 2008).

[113] I. Amelio, L. Korosec, I. Carusotto, and G. Mazza, *Optical dressing of the electronic response of two-dimensional semiconductors in quantum and classical descriptions of cavity electrodynamics,* Phys. Rev. B **104**, 235120 (2021) .

[114] J. J. Hopfield, *Theory of the Contribution of Excitons to the Complex Dielectric Constant of Crystals,* Phys. Rev. **112**, 1555 (1958) .

[115] C. Ciuti, G. Bastard, and I. Carusotto, *Quantum vacuum properties of the intersubband cavity polariton field,* Phys. Rev. B **72**, 115303 (2005) .

[116] A. Mercurio, G. M. Andolina, F. M. D. Pellegrino, O. Di Stefano, P. Jarillo-Herrero, C. Felser, F. H. L. Koppens, S. Savasta, and M. Polini, *Photon Condensation, Van Vleck Paramagnetism, and Chiral Cavities,* Physical Review Research **6**, 013303 (2024) .

[117] M. Hayn, C. Emary, and T. Brandes, *Phase transitions and dark-state physics in two-color superradiance,* Phys. Rev. A **84**, 053856 (2011) .

[118] A. Baksic, P. Nataf, and C. Ciuti, *Superradiant phase transitions with three-level systems,* Phys. Rev. A **87**, 023813 (2013) .

[119] M. Ferraretto, A. Richaud, L. D. Re, L. Fallani, and M. Capone, *Enhancement of chiral edge currents in (d+1)-dimensional atomic Mott-band hybrid insulators,* SciPost Phys. **14**, 048 (2023) .

[120] J. Bloch, A. Cavalleri, V. Galitski, M. Hafezi, and A. Rubio, *Strongly Correlated Electron–Photon Systems,* Nature **606**, 41 (2022) .

[121] F. Schlawin, D. M. Kennes, and M. A. Sentef, *Cavity Quantum Materials,* Applied Physics Reviews **9**, 011312 (2022) .

[122] F. Mivehvar, F. Piazza, T. Donner, and H. Ritsch, *Cavity QED with Quantum Gases: New Paradigms in Many-Body Physics,* Advances in Physics **70**, 1 (2021) .

[123] Z. Yan, J. Ho, Y.-H. Lu, S. J. Masson, A. Asenjo-Garcia, and D. M. Stamper-Kurn, *Superradiant and Subradiant Cavity Scattering by Atom Arrays,* Phys. Rev. Lett. **131**, 253603 (2023) .

[124] X. Zhang, Y. Chen, Z. Wu, J. Wang, J. Fan, S. Deng, and H. Wu, *Observation of a superradiant quantum phase transition in an intracavity degenerate Fermi gas,* Science **373**, 1359 (2021) .

[125] H. Hosseinabadi, R. J. Valencia-Tortora, A. N. Mikheev, D. E. Chang, J. Zeiher, R. Moessner, and J. Marino, *The $(PXP)^2$ model: long-range quantum scars in optical cavities,* arXiv:2510.02246 [quant-ph] (2025).

[126] A. N. Mikheev, H. Hosseinabadi, and J. Marino, *Prethermalization of light and matter in cavity-coupled Rydberg arrays,* arXiv:2504.06267 [cond-mat.stat-mech] (2025).

[127] S. Latini, E. Ronca, U. D. Giovannini, H. Hübener, and A. Rubio, *Cavity Control of Excitons in Two-Dimensional Materials,* Nano Letters **19**, 3473 (2019) .

[128] V. Rokaj, J. Wang, J. Sous, M. Penz, M. Ruggenthaler, and A. Rubio, *Weakened Topological Protection of the Quantum Hall Effect in a Cavity,* Phys. Rev. Lett. **131**, 196602 (2023) .

[129] C. Ciuti, *Cavity-mediated electron hopping in disordered quantum Hall systems,* Phys. Rev. B **104**, 155307 (2021) .

[130] N. Bartolo and C. Ciuti, *Vacuum-dressed cavity magnetotransport of a two-dimensional electron gas,* Phys. Rev. B **98**, 205301 (2018) .

[131] F. Mattiotti, J. Dubail, D. Hagenmüller, J. Schachenmayer, J.-P. Brantut, and G. Pupillo, *Multifractality in the interacting disordered Tavis-Cummings model,* Phys. Rev. B **109**, 064202 (2024) .

[132] J. Rohn, M. Hörmann, C. Genes, and K. P. Schmidt, *Ising model in a light-induced quantized transverse field,* Phys. Rev. Res. **2**, 023131 (2020) .

[133] S. Coleman, *There are no Goldstone bosons in two dimensions,* Communications in Mathematical Physics **31**, 259–264 (1973) .

[134] N. D. Mermin and H. Wagner, *Absence of Ferromagnetism or Antiferromagnetism in One- or Two-Dimensional Isotropic Heisenberg Models,* Phys. Rev. Lett. **17**, 1133 (1966) .

[135] A. J. Beekman, L. Rademaker, and J. van Wezel, *An introduction to spontaneous symmetry breaking,* SciPost Phys. Lect. Notes , 11 (2019) .

[136] T. Giamarchi, *Quantum Physics in One Dimension* (Oxford University Press, 2003).

[137] P. Calabrese and J. Cardy, *Entanglement entropy and conformal field theory,* Journal of Physics A: Mathematical and Theoretical **42**, 504005 (2009) .

[138] Z. Li, S. Choudhury, and W. V. Liu, *Long-range-ordered phase in a quantum Heisenberg chain with interactions beyond nearest neighbors,* Phys. Rev. A **104**, 013303 (2021) .

[139] O. Carlsson, S. Chattopadhyay, J. B. Curtis, F. Lindel, L. Graziotto, J. Faist, and E. Demler, *Casimir Stabilization of Fluctuating Electronic Nematic Order,* arXiv:2510.05088 [cond-mat.str-el] (2025).

[140] C. J. Eckhardt, A. Grankin, D. M. Kennes, M. Ruggenthaler, A. Rubio, M. A. Sentef, M. Hafezi, and M. H. Michael, *Surface-Mediated Ultrastrong Cavity Coupling of Two-Dimensional Itinerant Electrons,* Phys. Rev. Lett. **135**, 156902 (2025) .

[141] I. Buluta and F. Nori, *Quantum Simulators,* Science **326**, 108–111 (2009) .

[142] J. I. Cirac and P. Zoller, *Goals and opportunities in quantum simulation,* Nature Physics **8**, 264–266 (2012) .

[143] E. Zohar, J. I. Cirac, and B. Reznik, *Quantum simulations of lattice gauge theories using ultracold atoms in optical lattices,* Reports on Progress in Physics **79**, 014401 (2015) .

[144] M. Dalmonte and S. Montangero, *Lattice gauge theory simulations in the quantum information era,* Contemporary Physics **57**, 388–412 (2016) .

[145] M. C. Bañuls, R. Blatt, J. Catani, A. Celi, J. I. Cirac, M. Dalmonte, L. Fallani, K. Jansen, M. Lewenstein, S. Montangero, C. A. Muschik, B. Reznik, E. Rico, L. Tagliacozzo, K. Van Acoleyen, F. Verstraete, U.-J. Wiese, M. Wingate, J. Zakrzewski, and P. Zoller, *Simulating lattice gauge theories within quantum*

technologies, The European Physical Journal D **74** (2020), 10.1140/epjd/e2020-100571-8 .

[146] C. W. Bauer, Z. Davoudi, A. B. Balantekin, T. Bhattacharya, M. Carena, W. A. de Jong, P. Draper, A. El-Khadra, N. Gemelke, M. Hanada, D. Kharzeev, H. Lamm, Y.-Y. Li, J. Liu, M. Lukin, Y. Meurice, C. Monroe, B. Nachman, G. Pagano, J. Preskill, E. Rinaldi, A. Roggero, D. I. Santiago, M. J. Savage, I. Siddiqi, G. Siopsis, D. Van Zanten, N. Wiebe, Y. Yamauchi, K. Yeter-Aydeniz, and S. Zorzetti, *Quantum Simulation for High-Energy Physics,* PRX Quantum **4**, 027001 (2023) .

[147] M. Kormos, M. Collura, G. Takács, and P. Calabrese, *Real-time confinement following a quantum quench to a non-integrable model,* Nature Physics **13**, 246–249 (2016) .

[148] Z.-Y. Ge and F. Nori, *Confinement-induced enhancement of superconductivity in a spin-$\frac{1}{2}$ fermion chain coupled to a $\mathbb{Z}_2$ lattice gauge field,* Phys. Rev. B **107**, 125141 (2023) .

[149] Z.-Y. Ge, Y.-R. Zhang, and F. Nori, *Nonmesonic Quantum Many-Body Scars in a 1D Lattice Gauge Theory,* Phys. Rev. Lett. **132**, 230403 (2024) .

[150] E. A. Martinez, C. A. Muschik, P. Schindler, D. Nigg, A. Erhard, M. Heyl, P. Hauke, M. Dalmonte, T. Monz, P. Zoller, and R. Blatt, *Real-time dynamics of lattice gauge theories with a few-qubit quantum computer,* Nature **534**, 516–519 (2016) .

[151] H. Bernien, S. Schwartz, A. Keesling, H. Levine, A. Omran, H. Pichler, S. Choi, A. S. Zibrov, M. Endres, M. Greiner, V. Vuletić, and M. D. Lukin, *Probing many-body dynamics on a 51-atom quantum simulator,* Nature **551**, 579–584 (2017) .

[152] D. González-Cuadra, M. Hamdan, T. V. Zache, B. Braverman, M. Kornjača, A. Lukin, S. H. Cantú, F. Liu, S.-T. Wang, A. Keesling, M. D. Lukin, P. Zoller, and A. Bylinskii, *Observation of string breaking on a (2 + 1)D Rydberg quantum simulator,* Nature **642**, 321–326 (2025) .

[153] Y. Liu, W.-Y. Zhang, Z.-H. Zhu, M.-G. He, Z.-S. Yuan, and J.-W. Pan, *String-Breaking Mechanism in a Lattice Schwinger Model Simulator,* Phys. Rev. Lett. **135**, 101902 (2025) .

[154] A. De, A. Lerose, D. Luo, F. M. Surace, A. Schuckert, E. R. Bennewitz, B. Ware, W. Morong, K. S. Collins, Z. Davoudi, *et al.*, *Observation of string-breaking dynamics in a quantum simulator,* arXiv preprint arXiv:2410.13815 (2024) .

[155] T. A. Cochran, B. Jobst, E. Rosenberg, Y. D. Lensky, G. Gyawali, N. Eassa, M. Will, A. Szasz, D. Abanin, R. Acharya, L. Aghababaie Beni, T. I. Andersen, M. Ansmann, F. Arute, K. Arya, A. Asfaw, J. Atalaya, R. Babbush, B. Ballard, J. C. Bardin, A. Bengtsson, A. Bilmes, A. Bourassa, J. Bovaird, M. Broughton, D. A. Browne, B. Buchea, B. B. Buckley, T. Burger, B. Burkett, N. Bushnell, A. Cabrera, J. Campero, H.-S. Chang, Z. Chen, B. Chiaro, J. Claes, A. Y. Cleland, J. Cogan, R. Collins, P. Conner, W. Courtney, A. L. Crook, B. Curtin, S. Das, S. Demura, L. De Lorenzo, A. Di Paolo, P. Donohoe, I. Drozdov, A. Dunsworth, A. Eickbusch, A. M. Elbag, M. Elzouka, C. Erickson, V. S. Ferreira, L. F. Burgos, E. Forati, A. G. Fowler, B. Foxen, S. Ganjam, R. Gasca, E. Genois, W. Giang, D. Gilboa, R. Gosula, A. Grajales Dau, D. Graumann, A. Greene, J. A. Gross, S. Habegger, M. Hansen, M. P. Harrigan, S. D. Harrington, P. Heu, O. Higgott, J. Hilton, H.-Y. Huang, A. Huff, W. Huggins, E. Jeffrey, Z. Jiang, C. Jones, C. Joshi, P. Juhas, D. Kafri, H. Kang, A. H. Karamlou, K. Kechedzhi, T. Khaire, T. Khattar, M. Khezri, S. Kim, P. Klimov, B. Kobrin, A. Korotkov, F. Kostritsa, J. Kreikebaum, V. Kurilovich, D. Landhuis, T. Lange-Dei, B. Langley, K.-M. Lau, J. Ledford, K. Lee, B. Lester, L. Le Guevel, W. Li, A. T. Lill, W. Livingston, A. Locharla, D. Lundahl, A. Lunt, S. Madhuk, A. Maloney, S. Mandrà, L. Martin, O. Martin, C. Maxfield, J. McClean, M. McEwen, S. Meeks, A. Megrant, K. Miao, R. Molavi, S. Molina, S. Montazeri, R. Movassagh, C. Neill, M. Newman, A. Nguyen, M. Nguyen, C.-H. Ni, K. Ottosson, A. Pizzuto, R. Potter, O. Pritchard, C. Quintana, G. Ramachandran, M. Reagor, D. Rhodes, G. Roberts, K. Sankaragomathi, K. Satzinger, H. Schurkus, M. Shearn, A. Shorter, N. Shutty, V. Shvarts, V. Sivak, S. Small, W. C. Smith, S. Springer, G. Sterling, J. Suchard, A. Sztein, D. Thor, M. Torunbalci, A. Vaishnav, J. Vargas, S. Vdovichev, G. Vidal, C. Vollgraff Heidweiller, S. Waltman, S. X. Wang, B. Ware, T. White, K. Wong, B. W. K. Woo, C. Xing, Z. J. Yao, P. Yeh, B. Ying, J. Yoo, N. Yosri, G. Young, A. Zalcman, Y. Zhang, N. Zhu, N. Zobrist, S. Boixo, J. Kelly, E. Lucero, Y. Chen, V. Smelyanskiy, H. Neven, A. Gammon-Smith, F. Pollmann, M. Knap, and P. Roushan, *Visualizing dynamics of charges and strings in (2 + 1)D lattice gauge theories,* Nature **642**, 315–320 (2025) .

[156] X. Liang, Z. Yue, Y.-X. Chao, Z.-X. Hua, Y. Lin, M. K. Tey, and L. You, *Observation of Anomalous Information Scrambling in a Rydberg Atom Array,* Phys. Rev. Lett. **135**, 050201 (2025) .

[157] R. C. Farrell, M. Illa, A. N. Ciavarella, and M. J. Savage, *Quantum simulations of hadron dynamics in the Schwinger model using 112 qubits,* Phys. Rev. D **109**, 114510 (2024) .

[158] G. Lagnese, F. M. Surace, M. Kormos, and P. Calabrese, *False vacuum decay in quantum spin chains,* Phys. Rev. B **104**, L201106 (2021) .

[159] Z.-H. Zhu, Y. Liu, G. Lagnese, F. M. Surace, W.-Y. Zhang, M.-G. He, J. C. Halimeh, M. Dalmonte, S. C. Morampudi, F. Wilczek, *et al.*, *Probing false vacuum decay on a cold-atom gauge-theory quantum simulator,* arXiv preprint arXiv:2411.12565 (2024) .

[160] J. Bloch, A. Cavalleri, V. Galitski, M. Hafezi, and A. Rubio, *Strongly correlated electron–photon systems,* Nature **606**, 41 (2022) .

[161] W. Nie, M. Antezza, Y.-x. Liu, and F. Nori, *Dissipative Topological Phase Transition with Strong System-Environment Coupling,* Phys. Rev. Lett. **127**, 250402 (2021) .

[162] T. Chanda, R. Kraus, G. Morigi, and J. Zakrzewski, *Self-organized topological insulator due to cavity-mediated correlated tunneling,* Quantum **5**, 501 (2021) .

[163] R. J. Valencia-Tortora, S. P. Kelly, T. Donner, G. Morigi, R. Fazio, and J. Marino, *Crafting the dynamical structure of synchronization by harnessing bosonic multilevel cavity QED,* Phys. Rev. Res. **5**, 023112 (2023) .

[164] G.-L. Zhu, C.-S. Hu, H. Wang, W. Qin, X.-Y. Lü, and F. Nori, *Nonreciprocal Superradiant Phase Transitions and Multicriticality in a Cavity QED System,* Phys. Rev. Lett. **132**, 193602 (2024) .

[165] H. Hosseinabadi, D. E. Chang, and J. Marino, *Quantum-to-classical crossover in the spin glass dynamics of cavity QED simulators,* Phys. Rev. Res. **6**, 043313 (2024) .

[166] H. Hosseinabadi, D. E. Chang, and J. Marino, *Far from equilibrium field theory for strongly coupled light and matter: Dynamics of frustrated multimode cavity QED,* Phys. Rev. Res. **6**, 043314 (2024) .

[167] M. Schiró, M. Bordyuh, B. Öztop, and H. E. Türeci, *Phase Transition of Light in Cavity QED Lattices,* Phys. Rev. Lett. **109**, 053601 (2012) .

[168] O. Viehmann, J. von Delft, and F. Marquardt, *Observing the Nonequilibrium Dynamics of the Quantum Transverse-Field Ising Chain in Circuit QED,* Phys. Rev. Lett. **110**, 030601 (2013) .

[169] M. Dalmonte, S. I. Mirzaei, P. R. Muppalla, D. Marcos, P. Zoller, and G. Kirchmair, *Realizing dipolar spin models with arrays of superconducting qubits,* Phys. Rev. B **92**, 174507 (2015) .

[170] J. Gelhausen, M. Buchhold, A. Rosch, and P. Strack, *Quantum-optical magnets with competing short- and long-range interactions: Rydberg-dressed spin lattice in an optical cavity,* SciPost Phys. **1**, 004 (2016) .

[171] Z. Li, S. Choudhury, and W. V. Liu, *Fast scrambling without appealing to holographic duality,* Phys. Rev. Res. **2**, 043399 (2020) .

[172] T. O. Puel and T. Macrì, *Confined Meson Excitations in Rydberg-Atom Arrays Coupled to a Cavity Field,* Phys. Rev. Lett. **133**, 106901 (2024) .

[173] A. Mallick, M. Lewenstein, J. Zakrzewski, and M. Plodzien, *String-breaking dynamics in an Ising chain with local vibrations,* Phys. Rev. B **112**, 024311 (2025) .

[174] J. Ho, Y.-H. Lu, T. Xiang, C. C. Rusconi, S. J. Masson, A. Asenjo-Garcia, Z. Yan, and D. M. Stamper-Kurn, *Optomechanical self-organization in a mesoscopic atom array,* arXiv:2410.12754 [quant-ph] (2024).

[175] A. Browaeys and T. Lahaye, *Many-body physics with individually controlled Rydberg atoms,* Nature Physics **16**, 132–142 (2020) .

[176] D. Bluvstein, S. J. Evered, A. A. Geim, S. H. Li, H. Zhou, T. Manovitz, S. Ebadi, M. Cain, M. Kalinowski, D. Hangleiter, J. P. Bonilla Ataides, N. Maskara, I. Cong, X. Gao, P. Sales Rodriguez, T. Karolyshyn, G. Semeghini, M. J. Gullans, M. Greiner, V. Vuletić, and M. D. Lukin, *Logical quantum processor based on reconfigurable atom arrays,* Nature **626**, 58–65 (2023) .

[177] M. Yang and S. R. White, *Time-dependent variational principle with ancillary Krylov subspace,* Phys. Rev. B **102**, 094315 (2020) .

[178] Z.-Y. Ge, H. Fan, and F. Nori, *Effective field theories and finite-temperature properties of zero-dimensional superradiant quantum phase transitions,* Phys. Rev. Res. **6**, 023123 (2024) .

[179] F. Minganti, I. I. Arkhipov, A. Miranowicz, and F. Nori, *Continuous dissipative phase transitions with or without symmetry breaking,* New Journal of Physics **23**, 122001 (2021) .

[180] F. Minganti, I. I. Arkhipov, A. Miranowicz, and F. Nori, *Liouvillian spectral collapse in the Scully-Lamb laser model,* Phys. Rev. Res. **3**, 043197 (2021) .

[181] M. Saffman, *Quantum computing with atomic qubits and Rydberg interactions: progress and challenges,* Journal of Physics B: Atomic, Molecular and Optical Physics **49**, 202001 (2016) .

[182] S. Ma, A. P. Burgers, G. Liu, J. Wilson, B. Zhang, and J. D. Thompson, *Universal Gate Operations on Nuclear Spin Qubits in an Optical Tweezer Array of* ^{171}Yb *Atoms,* Phys. Rev. X **12**, 021028 (2022) .

[183] T. Thiele, J. Deiglmayr, M. Stammeier, J.-A. Agner, H. Schmutz, F. Merkt, and A. Wallraff, *Imaging electric fields in the vicinity of cryogenic surfaces using Rydberg atoms,* Phys. Rev. A **92**, 063425 (2015) .

[184] Y.-T. Chen, M. Szurek, B. Hu, J. de Hond, B. Braverman, and V. Vuletic, *High finesse bow-tie cavity for strong atom-photon coupling in Rydberg arrays,* Optics Express **30**, 37426 (2022) .

[185] R. C. Das, S. Khan, T. Ravi, and K. Pandey, *Direct spectroscopy of Rubidium using a narrow-line transition at 420 nm,* The European Physical Journal D **78** (2024), 10.1140/epjd/s10053-024-00831-9 .

[186] L. Winter and O. Zilberberg, *Fractional quantum Hall edge polaritons,* arXiv:2308.12146 [cond-mat.mes-hall] (2024).

[187] M. C. Dartiailh, T. Kontos, B. Douçot, and A. Cottet, *Direct Cavity Detection of Majorana Pairs,* Phys. Rev. Lett. **118**, 126803 (2017) .

[188] M. Trif and Y. Tserkovnyak, *Resonantly Tunable Majorana Polariton in a Microwave Cavity,* Phys. Rev. Lett. **109**, 257002 (2012) .

[189] T. L. Schmidt, A. Nunnenkamp, and C. Bruder, *Microwave-controlled coupling of Majorana bound states,* New Journal of Physics **15**, 025043 (2013) .

[190] O. Dmytruk, M. Trif, and P. Simon, *Cavity quantum electrodynamics with mesoscopic topological superconductors,* Phys. Rev. B **92**, 245432 (2015) .

[191] L. C. Contamin, M. R. Delbecq, B. Douçot, A. Cottet, and T. Kontos, *Hybrid light-matter networks of Majorana zero modes,* npj Quantum Information **7**, 171 (2021) .

[192] O. Dmytruk and M. Trif, *Microwave detection of gliding Majorana zero modes in nanowires,* Phys. Rev. B **107**, 115418 (2023) .

[193] A. Kitaev, *Unpaired Majorana fermions in quantum wires,* Physics Uspekhi **44**, 131 (2001) .

[194] C.-K. Chiu, J. C. Y. Teo, A. P. Schnyder, and S. Ryu, *Classification of topological quantum matter with symmetries,* Rev. Mod. Phys. **88**, 035005 (2016) .

[195] H. Yao and S. Ryu, *Interaction effect on topological classification of superconductors in two dimensions,* Phys. Rev. B **88**, 064507 (2013) .

[196] T. Morimoto, A. Furusaki, and C. Mudry, *Breakdown of the topological classification $\mathbb{Z}$ for gapped phases of noninteracting fermions by quartic interactions,* Phys. Rev. B **92**, 125104 (2015) .

[197] L. Fidkowski and A. Kitaev, *Effects of interactions on the topological classification of free fermion systems,* Phys. Rev. B **81**, 134509 (2010) .

[198] L. Fidkowski and A. Kitaev, *Topological phases of fermions in one dimension,* Phys. Rev. B **83**, 075103 (2011) .

[199] J. Andberger, L. Graziotto, L. Sacchi, M. Beck, G. Scalari, and J. Faist, *Terahertz chiral subwavelength cavities breaking time-reversal symmetry via ultrastrong light-matter interaction,* Phys. Rev. B **109**, L161302 (2024) .

[200] F. Tay, A. Mojibpour, S. Sanders, S. Liang, H. Xu, G. C. Gardner, A. Baydin, M. J. Manfra, A. Alabastri, D. Hagenmüller, and J. Kono, *Ultrastrong photon-photon coupling,* arXiv:2308.12427 [quant-ph] (2023).

[201] A. Alexandradinata, N. Regnault, C. Fang, M. J. Gilbert, and B. A. Bernevig, *Parafermionic phases with symmetry breaking and topological order,* Phys. Rev. B **94**, 125103 (2016) .

[202] F. Iemini, C. Mora, and L. Mazza, *Topological Phases of Parafermions: A Model with Exactly Solvable Ground States,* Phys. Rev. Lett. **118**, 170402 (2017) .

[203] A. M. Turner, F. Pollmann, and E. Berg, *Topological phases of one-dimensional fermions: An entanglement point of view,* Phys. Rev. B **83**, 075102 (2011) .

[204] L. Fidkowski, *Entanglement Spectrum of Topological Insulators and Superconductors,* Phys. Rev. Lett. **104**, 130502 (2010) .

[205] P. Fendley, *Parafermionic edge zero modes in Zn-invariant spin chains,* Journal of Statistical Mechanics: Theory and Experiment **2012**, P11020 (2012) .

[206] A. S. Jermyn, R. S. K. Mong, J. Alicea, and P. Fendley, *Stability of zero modes in parafermion chains,* Phys. Rev. B **90**, 165106 (2014) .

[207] J. Alicea and P. Fendley, *Topological Phases with Parafermions: Theory and Blueprints,* Annual Review of Condensed Matter Physics **7**, 119 (2016) .

[208] Y. Oreg, G. Refael, and F. von Oppen, *Helical Liquids and Majorana Bound States in Quantum Wires,* Phys. Rev. Lett. **105**, 177002 (2010) .

[209] R. M. Lutchyn, J. D. Sau, and S. Das Sarma, *Majorana Fermions and a Topological Phase Transition in Semiconductor-Superconductor Heterostructures,* Phys. Rev. Lett. **105**, 077001 (2010) .

[210] K. Flensberg, F. von Oppen, and A. Stern, *Engineered platforms for topological superconductivity and Majorana zero modes,* Nature Reviews Materials **6**, 944 (2021) .

[211] S. Ryu, A. P. Schnyder, A. Furusaki, and A. W. W. Ludwig, *Topological insulators and superconductors: tenfold way and dimensional hierarchy,* New Journal of Physics **12**, 065010 (2010) .

[212] A. Cottet, T. Kontos, and B. Douçot, *Electron-photon coupling in mesoscopic quantum electrodynamics,* Phys. Rev. B **91**, 205417 (2015) .

[213] S. S. Hegde and S. Vishveshwara, *Majorana wave-function oscillations, fermion parity switches, and disorder in Kitaev chains,* Phys. Rev. B **94**, 115166 (2016) .

[214] D. Shaffer, M. Claassen, A. Srivastava, and L. H. Santos, *Entanglement and topology in Su-Schrieffer-Heeger cavity quantum electrodynamics,* Phys. Rev. B **109**, 155160 (2024) .

[215] Q. Niu, D. J. Thouless, and Y.-S. Wu, *Quantized Hall conductance as a topological invariant,* Phys. Rev. B **31**, 3372 (1985) .

[216] J. B. Curtis, Z. M. Raines, A. A. Allocca, M. Hafezi, and V. M. Galitski, *Cavity Quantum Eliashberg Enhancement of Superconductivity,* Phys. Rev. Lett. **122**, 167002 (2019) .

[217] G. M. Andolina, A. De Pasquale, F. M. D. Pellegrino, I. Torre, F. H. L. Koppens, and M. Polini, *Amperean superconductivity cannot be induced by deep subwavelength cavities in a two-dimensional material,* Phys. Rev. B **109**, 104513 (2024) .

[218] J. Li and M. Eckstein, *Manipulating Intertwined Orders in Solids with Quantum Light,* Phys. Rev. Lett. **125**, 217402 (2020) .

[219] V. Rokaj, M. Penz, M. A. Sentef, M. Ruggenthaler, and A. Rubio, *Polaritonic Hofstadter butterfly and cavity control of the quantized Hall conductance,* Phys. Rev. B **105**, 205424 (2022) .

[220] D. De Bernardis, M. Jeannin, J.-M. Manceau, R. Colombelli, A. Tredicucci, and I. Carusotto, *Magnetic-field-induced cavity protection for intersubband polaritons,* Phys. Rev. B **106**, 224206 (2022) .

[221] G. M. Andolina, P. A. Erdman, F. Noé, J. Pekola, and M. Schirò, *Dicke superradiant heat current enhancement in circuit quantum electrodynamics,* Phys. Rev. Res. **6**, 043128 (2024) .

[222] G. Chiriacò, *Thermal Purcell Effect and Cavity-Induced Renormalization of Dissipations,* Physical Review B **110**, L161107 (2024) .

[223] D. C. Tsui, H. L. Stormer, and A. C. Gossard, *Two-Dimensional Magnetotransport in the Extreme Quantum Limit,* Phys. Rev. Lett. **48**, 1559 (1982) .

[224] R. B. Laughlin, *Anomalous Quantum Hall Effect: An Incompressible Quantum Fluid with Fractionally Charged Excitations,* Phys. Rev. Lett. **50**, 1395 (1983) .

[225] J. Nakamura, S. Liang, G. C. Gardner, and M. J. Manfra, *Direct observation of anyonic braiding statistics,* Nature Physics **16**, 931 (2020) .

[226] S. M. Girvin, A. H. MacDonald, and P. M. Platzman, *Magneto-roton theory of collective excitations in the fractional quantum Hall effect,* Phys. Rev. B **33**, 2481 (1986) .

[227] A. Pinczuk, B. S. Dennis, L. N. Pfeiffer, and K. West, *Observation of collective excitations in the fractional quantum Hall effect,* Phys. Rev. Lett. **70**, 3983 (1993) .

[228] J. Liang, Z. Liu, Z. Yang, Y. Huang, U. Wurstbauer, C. R. Dean, K. W. West, L. N. Pfeiffer, L. Du, and A. Pinczuk, *Evidence for chiral graviton modes in fractional quantum Hall liquids,* Nature **628**, 78 (2024) .

[229] F. D. M. Haldane, *Geometrical Description of the Fractional Quantum Hall Effect,* Phys. Rev. Lett. **107**, 116801 (2011) .

[230] D. T. Son, *Newton-Cartan Geometry and the Quantum Hall Effect,* arXiv:1306.0638 [cond-mat.mes-hall] (2013).

[231] S. Golkar, D. X. Nguyen, and D. T. Son, *Spectral sum rules and magneto-roton as emergent graviton in fractional quantum Hall effect,* Journal of High Energy Physics **2016**, 16 (2016) .

[232] S.-F. Liou, F. D. M. Haldane, K. Yang, and E. H. Rezayi, *Chiral Gravitons in Fractional Quantum Hall Liquids,* Phys. Rev. Lett. **123**, 146801 (2019) .

[233] Z. Liu, A. Gromov, and Z. Papic, *Geometric quench and nonequilibrium dynamics of fractional quantum Hall states,* Phys. Rev. B **98**, 155140 (2018) .

[234] M. Ippoliti, R. N. Bhatt, and F. D. M. Haldane, *Geometry of flux attachment in anisotropic fractional quantum Hall states,* Phys. Rev. B **98**, 085101 (2018) .

[235] D. X. Nguyen, F. D. M. Haldane, E. H. Rezayi, D. T. Son, and K. Yang, *Multiple Magnetorotons and Spectral Sum Rules in Fractional Quantum Hall Systems,* Phys. Rev. Lett. **128**, 246402 (2022) .

[236] A. C. Balram, Z. Liu, A. Gromov, and Z. Papić, *Very-High-Energy Collective States of Partons in Fractional Quantum Hall Liquids,* Phys. Rev. X **12**, 021008 (2022) .

[237] S. Pu, A. C. Balram, J. Taylor, E. Fradkin, and Z. Papić, *Microscopic Model for Fractional Quantum Hall Nematics,* Phys. Rev. Lett. **132**, 236503 (2024) .

[238] H. Li and F. D. M. Haldane, *Entanglement Spectrum as a Generalization of Entanglement Entropy: Identification of Topological Order in Non-Abelian Fractional Quantum Hall Effect States,* Phys. Rev. Lett. **101**, 010504 (2008) .

[239] N. Regnault, *Entanglement spectroscopy and its application to the quantum Hall effects,* in *Topological Aspects of Condensed Matter Physics* (Oxford University PressOxford, 2017) p. 165–216.

[240] W. Kohn, *Cyclotron Resonance and de Haas-van Alphen Oscillations of an Interacting Electron Gas,* Phys. Rev. **123**, 1242 (1961) .

[241] *We note that the electric quadrupole moment of quantum Hall liquids [242], visible only by field gradients, has been proposed as fundamental in their understanding.* ().

[242] F. D. M. Haldane, *Incompressible Quantum Hall fluids as Electric Quadrupole fluids,* arXiv:2302.12472 [cond-mat.str-el] (2023).

[243] M. P. Zaletel, R. S. K. Mong, and F. Pollmann, *Topological Characterization of Fractional Quantum Hall Ground States from Microscopic Hamiltonians,* Phys. Rev. Lett. **110**, 236801 (2013) .

[244] M. P. Zaletel and R. S. K. Mong, *Exact matrix product states for quantum Hall wave functions,* Phys. Rev. B **86**, 245305 (2012) .

[245] S. Paeckel, T. Köhler, A. Swoboda, S. R. Manmana, U. Schollwöck, and C. Hubig, *Time-evolution methods for matrix-product states,* Annals of Physics **411**, 167998 (2019) .

[246] J. Haegeman, J. I. Cirac, T. J. Osborne, I. Pižorn, H. Verschelde, and F. Verstraete, *Time-Dependent Variational Principle for Quantum Lattices,* Phys. Rev. Lett. **107**, 070601 (2011) .

[247] J. Haegeman, C. Lubich, I. Oseledets, B. Vandereycken, and F. Verstraete, *Unifying time evolution and optimization with matrix product states,* Phys. Rev. B **94**, 165116 (2016) .

[248] D. J. Thouless, *Topological interpretations of quantum Hall conductance,* Journal of Mathematical Physics **35**, 5362–5372 (1994) .

[249] P. Kumar and R. N. Bhatt, *Possible continuous transition from fractional quantum Hall to stripe phase at* $\nu_e = 7/3$*,* Phys. Rev. B **106**, 115101 (2022) .

[250] D. Tong, *Lectures on the Quantum Hall Effect,* arXiv:1606.06687 [hep-th] (2016).

[251] E. H. Rezayi and F. D. M. Haldane, *Laughlin state on stretched and squeezed cylinders and edge excitations in the quantum Hall effect,* Phys. Rev. B **50**, 17199 (1994) .

[252] D. De Bernardis, T. Jaako, and P. Rabl, *Cavity quantum electrodynamics in the nonperturbative regime,* Phys. Rev. A **97**, 043820 (2018) .

[253] R. Sáez-Blázquez, D. de Bernardis, J. Feist, and P. Rabl, *Can We Observe Nonperturbative Vacuum Shifts in Cavity QED?* Phys. Rev. Lett. **131**, 013602 (2023) .

[254] J. Keller, G. Scalari, S. Cibella, C. Maissen, F. Appugliese, E. Giovine, R. Leoni, M. Beck, and J. Faist, *Few-Electron Ultrastrong Light-Matter Coupling at 300 GHz with Nanogap Hybrid LC Microcavities,* Nano Letters **17**, 7410–7415 (2017) .

[255] I. Sodemann and A. H. MacDonald, *Landau level mixing and the fractional quantum Hall effect,* Phys. Rev. B **87**, 245425 (2013) .

[256] M. P. Zaletel, R. S. K. Mong, F. Pollmann, and E. H. Rezayi, *Infinite density matrix renormalization group for multicomponent quantum Hall systems,* Phys. Rev. B **91**, 045115 (2015) .

[257] E. H. Rezayi, *Landau Level Mixing and the Ground State of the $\nu = 5/2$ Quantum Hall Effect,* Phys. Rev. Lett. **119**, 026801 (2017) .

[258] Y. Todorov and C. Sirtori, *Intersubband polaritons in the electrical dipole gauge,* Phys. Rev. B **85**, 045304 (2012) .

[259] A. Nardin and I. Carusotto, *Linear and nonlinear edge dynamics of trapped fractional quantum Hall droplets,* Phys. Rev. A **107**, 033320 (2023) .

[260] *More in details, the origin of the coupling is an effective shift of the single-particle orbitals $X_k \simeq k\, l_B^2 + \frac{l_B^2}{\omega_B}\partial_x W(x)$ that makes Eq. (5.42) non-trivial even for a constant electric field. In the case of bulk disordered systems, the single-particle potential depends on both coordinates, $W(x, y)$, and the coupling arises directly from the dressing of $\hat{H}_0$ since momentum along y is no longer conserved [129].* ().

[261] M. Greiner, O. Mandel, T. Esslinger, T. W. Hänsch, and I. Bloch, *Quantum phase transition from a superfluid to a Mott insulator in a gas of ultracold atoms,* nature **415**, 39 (2002) .

[262] P. M. Preiss, R. Ma, M. E. Tai, J. Simon, and M. Greiner, *Quantum gas microscopy with spin, atom-number, and multilayer readout,* Physical Review A **91**, 041602 (2015) .

[263] N. R. Cooper, *Rapidly rotating atomic gases,* Advances in Physics **57**, 539 (2008) .

[264] M. Roncaglia, M. Rizzi, and J. Dalibard, *From rotating atomic rings to quantum Hall states,* Scientific reports **1**, 43 (2011) .

[265] J. Dalibard, F. Gerbier, G. Juzeliūnas, and P. Öhberg, *Colloquium: Artificial gauge potentials for neutral atoms,* Reviews of Modern Physics **83**, 1523 (2011) .

[266] P. Kumar and F. D. M. Haldane, *Neutral excitations of quantum Hall states: A density matrix renormalization group study,* Phys. Rev. B **106**, 075116 (2022) .

[267] J. A. Ćwik, P. Kirton, S. De Liberato, and J. Keeling, *Excitonic spectral features in strongly coupled organic polaritons,* Phys. Rev. A **93**, 033840 (2016) .

[268] C. Ciuti and I. Carusotto, *Input-output theory of cavities in the ultrastrong coupling regime: The case of time-independent cavity parameters,* Phys. Rev. A **74**, 033811 (2006) .

[269] A. Settineri, O. Di Stefano, D. Zueco, S. Hughes, S. Savasta, and F. Nori, *Gauge freedom, quantum measurements, and time-dependent interactions in cavity QED,* Phys. Rev. Res. **3**, 023079 (2021) .

[270] G. Misguich and T. Jolicoeur, *DMRG study of FQHE systems in the open cylinder geometry,* Journal of Physics: Conference Series **1740**, 012043 (2021) .

[271] Y. He, K. Yang, M. O. Goerbig, and R. S. K. Mong, *Charge density waves and their transitions in anisotropic quantum Hall systems,* Communications Physics **4**, 116 (2021) .

[272] N. Chepiga and F. Mila, *Excitation spectrum and density matrix renormalization group iterations,* Phys. Rev. B **96**, 054425 (2017) .

[273] *Many-Body Methods for Real Materials : Autumn School organized by the Institute for Advanced Simulation at Forschungszentrum Jülich, 16 - 20 September 2019 : Lecture Notes of the Autumn School on Correlated Electrons 2019*, Vol. Jülich (RWTH Aachen University, 2019).

[274] C. B. Dag and V. Rokaj, *Engineering topology in graphene with chiral cavities,* Phys. Rev. B **110**, L121101 (2024) .

[275] F. Mivehvar, H. Ritsch, and F. Piazza, *Superradiant Topological Peierls Insulator inside an Optical Cavity,* Phys. Rev. Lett. **118**, 073602 (2017) .

[276] T. Chanda, R. Kraus, J. Zakrzewski, and G. Morigi, *Bond order via cavity-mediated interactions,* Phys. Rev. B **106**, 075137 (2022) .

[277] J. Fraxanet, A. Dauphin, M. Lewenstein, L. Barbiero, and D. González-Cuadra, *Higher-Order Topological Peierls Insulator in a Two-Dimensional Atom-Cavity System,* Phys. Rev. Lett. **131**, 263001 (2023) .

[278] M. P. Zaletel, R. S. K. Mong, and F. Pollmann, *Flux insertion, entanglement, and quantized responses,* Journal of Statistical Mechanics: Theory and Experiment **2014**, P10007 (2014) .

[279] H.-P. Breuer and F. Petruccione, *The Theory of Open Quantum Systems* (Oxford University PressOxford, 2007).

[280] A. Sterdyniak, B. A. Bernevig, N. Regnault, and F. D. M. Haldane, *The hierarchical structure in the orbital entanglement spectrum of fractional quantum Hall systems,* New Journal of Physics **13**, 105001 (2011) .

[281] T. V. Zache, C. Kokail, B. Sundar, and P. Zoller, *Entanglement Spectroscopy and probing the Li-Haldane Conjecture in Topological Quantum Matter,* Quantum **6**, 702 (2022) .

[282] J. J. Bisognano and E. H. Wichmann, *On the duality condition for quantum fields,* Journal of Mathematical Physics **17**, 303 (1976) .

[283] M. Dalmonte, V. Eisler, M. Falconi, and B. Vermersch, *Entanglement Hamiltonians: From Field Theory to Lattice Models and Experiments,* Annalen der Physik **534**, 202200064 (2022) .

[284] B. Swingle and T. Senthil, *Geometric proof of the equality between entanglement and edge spectra,* Phys. Rev. B **86**, 045117 (2012) .

[285] X. G. Wen, *Chiral Luttinger liquid and the edge excitations in the fractional quantum Hall states,* Phys. Rev. B **41**, 12838 (1990) .

[286] X. G. Wen, *Theory of the edge states in fractional quantum Hall effects,* International Journal of Modern Physics B **06**, 1711 (1992) .

[287] R. Laughlin, *Excitons in the fractional quantum Hall effect,* Physica B+C **126**, 254 (1984) .

[288] R. K. Kamilla, X. G. Wu, and J. K. Jain, *Excitons of composite fermions,* Phys. Rev. B **54**, 4873 (1996) .

[289] F. D. M. Haldane, *"Hall viscosity" and intrinsic metric of incompressible fractional Hall fluids,* arXiv:0906.1854 [cond-mat.str-el] (2009).

[290] P. Kumar and F. D. M. Haldane, *A numerical study of bounds in the correlations of fractional quantum Hall states,* SciPost Phys. **16**, 117 (2024) .

[291] R.-Z. Qiu, F. D. M. Haldane, X. Wan, K. Yang, and S. Yi, *Model anisotropic quantum Hall states,* Phys. Rev. B **85**, 115308 (2012) .

[292] K. A. Villegas Rosales, P. T. Madathil, Y. J. Chung, L. N. Pfeiffer, K. W. West, K. W. Baldwin, and M. Shayegan, *Fractional Quantum Hall Effect Energy Gaps: Role of Electron Layer Thickness,* Phys. Rev. Lett. **127**, 056801 (2021) .

[293] B. Paulillo, J. Manceau, A. Degiron, N. Zerounian, G. Beaudoin, I. Sagnes, and R. Colombelli, *Circuit-tunable sub-wavelength THz resonators: hybridizing optical cavities and loop antennas,* Optics Express **22**, 21302 (2014) .

[294] K. I. Bolotin, F. Ghahari, M. D. Shulman, H. L. Stormer, and P. Kim, *Observation of the fractional quantum Hall effect in graphene,* Nature **462**, 196 (2009) .

[295] D. Hagenmüller, S. De Liberato, and C. Ciuti, *Ultrastrong coupling between a cavity resonator and the cyclotron transition of a two-dimensional electron gas in the case of an integer filling factor,* Phys. Rev. B **81**, 235303 (2010) .

[296] S. Messelot, C. Symonds, J. Bellessa, J. Tignon, S. Dhillon, J.-B. Brubach, P. Roy, and J. Mangeney, *Tamm cavity in the terahertz spectral range,* ACS photonics **7**, 2906 (2020) .

[297] D. Session, M. Jalali Mehrabad, N. Paithankar, T. Grass, C. J. Eckhardt, B. Cao, D. Gustavo Suarez Forero, K. Li, M. S. Alam, K. Watanabe, T. Taniguchi, G. S. Solomon, N. Schine, J. Sau, R. Sordan, and M. Hafezi, *Optical pumping of electronic quantum Hall states with vortex light,* Nature Photonics (2024), 10.1038/s41566-024-01565-1 .

[298] I. V. Kukushkin, K. v. Klitzing, and K. Eberl, *Spin Polarization of Composite Fermions: Measurements of the Fermi Energy,* Phys. Rev. Lett. **82**, 3665 (1999) .

[299] N. R. Cooper, J. Dalibard, and I. B. Spielman, *Topological bands for ultracold atoms,* Rev. Mod. Phys. **91**, 015005 (2019) .

[300] T. Ozawa, H. M. Price, A. Amo, N. Goldman, M. Hafezi, L. Lu, M. C. Rechtsman, D. Schuster, J. Simon, O. Zilberberg, and I. Carusotto, *Topological photonics,* Rev. Mod. Phys. **91**, 015006 (2019) .

[301] D.-W. Zhang, Y.-Q. Zhu, Y. X. Zhao, H. Yan, and S.-L. Zhu, *Topological quantum matter with cold atoms,* Adv. Phys. **67**, 253 (2018) .

[302] F. D. M. Haldane, *Nobel Lecture: Topological quantum matter,* Rev. Mod. Phys. **89**, 040502 (2017) .

[303] E. Fradkin, *Field Theories of Condensed Matter Physics* (Cambridge University Press, Cambridge, England, 2013).

[304] R. Moessner and J. E. Moore, *Topological Phases of Matter* (Cambridge University Press, Cambridge, England, 2021).

[305] B. Zeng, X. Chen, D.-L. Zhou, and X.-G. Wen, *Quantum Information Meets Quantum Matter* (Springer, New York, 2019).

[306] D. R. Hofstadter, *Energy levels and wave functions of Bloch electrons in rational and irrational magnetic fields,* Phys. Rev. B **14**, 2239 (1976) .

[307] D. Jaksch and P. Zoller, *Creation of effective magnetic fields in optical lattices: the Hofstadter butterfly forcold neutral atoms,* New J. Phys. **5**, 56 (2003) .

[308] M. Gerster, M. Rizzi, P. Silvi, M. Dalmonte, and S. Montangero, *Fractional quantum Hall effect in the interacting Hofstadter model via tensor networks,* Phys. Rev. B **96**, 195123 (2017) .

[309] J. Motruk and F. Pollmann, *Phase transitions and adiabatic preparation of a fractional Chern insulator in a boson cold-atom model,* Phys. Rev. B **96**, 165107 (2017) .

[310] P. Rosson, M. Lubasch, M. Kiffner, and D. Jaksch, *Bosonic fractional quantum Hall states on a finite cylinder,* Phys. Rev. A **99**, 033603 (2019) .

[311] L. Schoonderwoerd, F. Pollmann, and G. Möller, *Interaction-driven plateau transition between integer and fractional Chern Insulators,* arXiv (2019), 10.48550/arXiv.1908.00988 .

[312] F. A. Palm, M. Buser, J. Léonard, M. Aidelsburger, U. Schollwöck, and F. Grusdt, *Bosonic Pfaffian state in the Hofstadter-Bose-Hubbard model,* Phys. Rev. B **103**, L161101 (2021) .

[313] J. Boesl, R. Dilip, F. Pollmann, and M. Knap, *Characterizing fractional topological phases of lattice bosons near the first Mott lobe,* Phys. Rev. B **105**, 075135 (2022) .

[314] C. Zerba, A. Seidel, F. Pollmann, and M. Knap, *Emergent Fracton Hydrodynamics in the Fractional Quantum Hall Regime of Ultracold Atoms,* arXiv (2024), 10.48550/arXiv.2410.07326 .

[315] A. Nardin, D. De Bernardis, R. O. Umucalılar, L. Mazza, M. Rizzi, and I. Carusotto, *Quantum Nonlinear Optics on the Edge of a Few-Particle Fractional Quantum Hall Fluid in a Small Lattice,* Phys. Rev. Lett. **133**, 183401 (2024) .

[316] P. Lunt, P. Hill, J. Reiter, P. M. Preiss, M. Galka, and S. Jochim, *Realization of a Laughlin State of Two Rapidly Rotating Fermions,* Phys. Rev. Lett. **133**, 253401 (2024) .

[317] M. Aidelsburger, M. Atala, M. Lohse, J. T. Barreiro, B. Paredes, and I. Bloch, *Realization of the Hofstadter Hamiltonian with Ultracold Atoms in Optical Lattices,* Phys. Rev. Lett. **111**, 185301 (2013) .

[318] H. Miyake, G. A. Siviloglou, C. J. Kennedy, W. C. Burton, and W. Ketterle, *Realizing the Harper Hamiltonian with Laser-Assisted Tunneling in Optical Lattices,* Phys. Rev. Lett. **111**, 185302 (2013) .

[319] T. Neupert, L. Santos, C. Chamon, and C. Mudry, *Fractional Quantum Hall States at Zero Magnetic Field,* Phys. Rev. Lett. **106**, 236804 (2011) .

[320] T. Scaffidi and S. H. Simon, *Exact solutions of fractional Chern insulators: Interacting particles in the Hofstadter model at finite size,* Phys. Rev. B **90**, 115132 (2014) .

[321] M. Aidelsburger, M. Lohse, C. Schweizer, M. Atala, J. T. Barreiro, S. Nascimbène, N. R. Cooper, I. Bloch, and N. Goldman, *Measuring the Chern number of Hofstadter bands with ultracold bosonic atoms,* Nat. Phys. **11**, 162 (2015) .

[322] M. Mancini, G. Pagano, G. Cappellini, L. Livi, M. Rider, J. Catani, C. Sias, P. Zoller, M. Inguscio, M. Dalmonte, and L. Fallani, *Observation of chiral edge states with neutral fermions in synthetic Hall ribbons,* Science **349**, 1510 (2015) .

[323] B. K. Stuhl, H.-I. Lu, L. M. Aycock, D. Genkina, and I. B. Spielman, *Visualizing edge states with an atomic Bose gas in the quantum Hall regime,* Science **349**, 1514 (2015) .

[324] V. Lienhard, P. Scholl, S. Weber, D. Barredo, S. de Léséleuc, R. Bai, N. Lang, M. Fleischhauer, H. P. Büchler, T. Lahaye, *et al.*, *Realization of a density-dependent Peierls phase in a synthetic, spin-orbit coupled Rydberg system,* Phys. Rev. X **10**, 021031 (2020) .

[325] A. Impertro, S. Huh, S. Karch, J. F. Wienand, I. Bloch, and M. Aidelsburger, *Realization of strongly-interacting Meissner phases in large bosonic flux ladders,* arXiv (2024), 10.48550/arXiv.2412.09481 .

[326] D. T. Son, *Chiral Metric Hydrodynamics, Kelvin Circulation Theorem, and the Fractional Quantum Hall Effect,* arXiv (2019), 10.48550/arXiv.1907.07187 .

[327] K. Yang, *Acoustic wave absorption as a probe of dynamical geometrical response of fractional quantum Hall liquids,* Phys. Rev. B **93**, 161302 (2016) .

[328] A. Gromov and D. T. Son, *Bimetric Theory of Fractional Quantum Hall States,* Phys. Rev. X **7**, 041032 (2017) .

[329] X. G. Wen and A. Zee, *Shift and spin vector: New topological quantum numbers for the Hall fluids,* Phys. Rev. Lett. **69**, 953 (1992) .

[330] Y.-H. Du, U. Mehta, D. X. Nguyen, and D. T. Son, *Volume-preserving diffeomorphism as nonabelian higher-rank gauge symmetry,* SciPost Phys. **12**, 050 (2022) .

[331] Y. Wang, J. Huxford, D. X. Nguyen, G. Ji, Y. B. Kim, and B. Yang, *Dynamics and lifetime of geometric excitations in moir\'e systems,* arXiv (2025), 10.48550/arXiv.2502.02640 .

[332] D. X. Nguyen, D. T. Son, and C. Wu, *Lowest Landau Level Stress Tensor and Structure Factor of Trial Quantum Hall Wave Functions,* arXiv (2014), 10.48550/arXiv.1411.3316 .

[333] D. X. Nguyen and D. T. Son, *Probing the spin structure of the fractional quantum Hall magnetoroton with polarized Raman scattering,* Phys. Rev. Res. **3**, 023040 (2021) .

[334] M. Collura, G. Lami, N. Ranabhat, and A. Santini, *Tensor Network Techniques for Quantum Computation* (SISSA Medialab S.r.l., Italy, 2024).

[335] Z. Liu, A. C. Balram, Z. Papic, and A. Gromov, *Quench Dynamics of Collective Modes in Fractional Quantum Hall Bilayers,* Phys. Rev. Lett. **126**, 076604 (2021) .

[336] A. Kirmani, K. Bull, C.-Y. Hou, V. Saravanan, S. M. Saeed, Z. Papić, A. Rahmani, and P. Ghaemi, *Probing Geometric Excitations of Fractional Quantum Hall States on Quantum Computers,* Phys. Rev. Lett. **129**, 056801 (2022) .

[337] M. Long, H. Lu, H.-Q. Wu, and Z. Y. Meng, *Spectra of Magnetoroton and Chiral Graviton Modes of Fractional Chern Insulator,* arXiv (2024), 10.48550/arXiv.2501.00247 .

[338] See Supplemental Material for extra ED and MPS results, including results for fluxes $n_\phi = 1/7$ and $1/5$, weights for smaller droplets, and a brief phase diagram characterization on cylinders., .

[339] J. Léonard, S. Kim, J. Kwan, P. Segura, F. Grusdt, C. Repellin, N. Goldman, and M. Greiner, *Realization of a fractional quantum Hall state with ultracold atoms,* Nature **619**, 495 (2023) .

[340] P. Roushan, C. Neill, A. Megrant, Y. Chen, R. Babbush, R. Barends, B. Campbell, Z. Chen, B. Chiaro, A. Dunsworth, A. Fowler, E. Jeffrey, J. Kelly, E. Lucero, J. Mutus, P. J. J. O'Malley, M. Neeley, C. Quintana, D. Sank, A. Vainsencher, J. Wenner, T. White, E. Kapit, H. Neven, and J. Martinis, *Chiral ground-state currents of interacting photons in a synthetic magnetic field,* Nat. Phys. **13**, 146 (2017) .

[341] I. T. Rosen, S. Muschinske, C. N. Barrett, A. Chatterjee, M. Hays, M. A. DeMarco, A. H. Karamlou, D. A. Rower, R. Das, D. K. Kim, B. M. Niedzielski, M. Schuldt, K. Serniak, M. E. Schwartz, J. L. Yoder, J. A. Grover, and W. D. Oliver, *A synthetic magnetic vector potential in a 2D superconducting qubit array,* Nat. Phys. **20**, 1881 (2024) .

[342] B. Yang, Z.-X. Hu, C. H. Lee, and Z. Papić, *Generalized Pseudopotentials for the Anisotropic Fractional Quantum Hall Effect,* Phys. Rev. Lett. **118**, 146403 (2017) .

[343] Y. Liu, T. Zhao, and T. Xiang, *Resolving Geometric Excitations of Fractional Quantum Hall States,* arXiv (2024), 10.48550/arXiv.2406.11195 .

[344] X. Shen, C. Wang, X. Hu, R. Guo, H. Yao, C. Wang, W. Duan, and Y. Xu, *Magnetorotons in Moir\'e Fractional Chern Insulators,* arXiv (2024), 10.48550/arXiv.2412.01211 .

[345] A. S. Sørensen, E. Demler, and M. D. Lukin, *Fractional Quantum Hall States of Atoms in Optical Lattices,* Phys. Rev. Lett. **94**, 086803 (2005) .

[346] M. Hafezi, A. S. Sørensen, E. Demler, and M. D. Lukin, *Fractional quantum Hall effect in optical lattices,* Phys. Rev. A **76**, 023613 (2007) .

[347] M. Hafezi, A. S. Sørensen, M. D. Lukin, and E. Demler, *Characterization of topological states on a lattice with Chern number,* Europhys. Lett. **81**, 10005 (2007) .

[348] G. Moore and N. Read, *Nonabelions in the fractional quantum Hall effect,* Nucl. Phys. B **360**, 362 (1991) .

[349] T. Oka and H. Aoki, *Photovoltaic Hall Effect in Graphene,* Physical Review B **79**, 081406 (2009) .

[350] N. Goldman and J. Dalibard, *Periodically Driven Quantum Systems: Effective Hamiltonians and Engineered Gauge Fields,* Physical Review X **4**, 031027 (2014) .

[351] D. V. Else, B. Bauer, and C. Nayak, *Floquet Time Crystals,* Physical Review Letters **117**, 090402 (2016) .

[352] A. Eckardt, *Colloquium: Atomic Quantum Gases in Periodically Driven Optical Lattices,* Reviews of Modern Physics **89**, 011004 (2017) .

[353] T. Oka and S. Kitamura, *Floquet Engineering of Quantum Materials,* Annual Review of Condensed Matter Physics **10**, 387 (2019) .

[354] N. Tsuji, T. Oka, and H. Aoki, *Nonequilibrium Steady State of Photoexcited Correlated Electrons in the Presence of Dissipation,* Physical Review Letters **103**, 047403 (2009) .

[355] J. W. McIver, B. Schulte, F.-U. Stein, T. Matsuyama, G. Jotzu, G. Meier, and A. Cavalleri, *Light-Induced Anomalous Hall Effect in Graphene,* Nature Physics **16**, 38 (2020) .

[356] M. Lucchini, F. Medeghini, Y. Wu, F. Vismarra, R. Borrego-Varillas, A. Crego, F. Frassetto, L. Poletto, S. A. Sato, H. Hübener, U. De Giovannini, Á. Rubio, and M. Nisoli, *Controlling Floquet States on Ultrashort Time Scales,* Nature Communications **13**, 7103 (2022) .

[357] S. Kitamura and H. Aoki, *Floquet Topological Superconductivity Induced by Chiral Many-Body Interaction,* Communications Physics **5**, 1 (2022) .

[358] V. Macrì, A. Ridolfo, O. Di Stefano, A. F. Kockum, F. Nori, and S. Savasta, *Nonperturbative Dynamical Casimir Effect in Optomechanical Systems: Vacuum Casimir-Rabi Splittings,* Phys. Rev. X **8**, 011031 (2018) .

[359] D. A. R. Dalvit, P. A. M. Neto, and F. D. Mazzitelli, *Fluctuations, Dissipation and the Dynamical Casimir Effect,* in *Casimir Physics*, edited by D. Dalvit, P. Milonni, D. Roberts, and F. da Rosa (Springer Berlin Heidelberg, Berlin, Heidelberg, 2011) pp. 419–457.

[360] D. Fausti, R. I. Tobey, N. Dean, S. Kaiser, A. Dienst, M. C. Hoffmann, S. Pyon, T. Takayama, H. Takagi, and A. Cavalleri, *Light-Induced Superconductivity in a Stripe-Ordered Cuprate,* Science **331**, 189 (2011) .

[361] M. Mitrano, A. Cantaluppi, D. Nicoletti, S. Kaiser, A. Perucchi, S. Lupi, P. Di Pietro, D. Pontiroli, M. Riccò, S. R. Clark, D. Jaksch, and A. Cavalleri, *Possible Light-Induced Superconductivity in K_3C_{60} at High Temperature,* Nature **530**, 461 (2016) .

[362] V. R. Morrison, Robert. P. Chatelain, K. L. Tiwari, A. Hendaoui, A. Bruhács, M. Chaker, and B. J. Siwick, *A Photoinduced Metal-like Phase of Monoclinic VO2 Revealed by Ultrafast Electron Diffraction,* Science **346**, 445 (2014) .

[363] G. Chiriacò, A. J. Millis, and I. L. Aleiner, *Transient Superconductivity without Superconductivity,* Physical Review B **98**, 220510(R) (2018) .

[364] L. Hruby, N. Dogra, M. Landini, T. Donner, and T. Esslinger, *Metastability and Avalanche Dynamics in Strongly Correlated Gases with Long-Range Interactions,* Proceedings of the National Academy of Sciences **115**, 3279 (2018) .

[365] G. Chiriacò and A. J. Millis, *Voltage-Induced Metal-Insulator Transition in a One-Dimensional Charge Density Wave,* Physical Review B **98**, 205152 (2018) .

[366] A. Zong, A. Kogar, Y.-Q. Bie, T. Rohwer, C. Lee, E. Baldini, E. Ergeçen, M. B. Yilmaz, B. Freelon, E. J. Sie, H. Zhou, J. Straquadine, P. Walmsley, P. E. Dolgirev, A. V. Rozhkov, I. R. Fisher, P. Jarillo-Herrero, B. V. Fine, and N. Gedik, *Evidence for Topological Defects in a Photoinduced Phase Transition,* Nature Physics **15**, 27 (2019) .

[367] A. Kogar, A. Zong, P. E. Dolgirev, X. Shen, J. Straquadine, Y.-Q. Bie, X. Wang, T. Rohwer, I.-C. Tung, Y. Yang, R. Li, J. Yang, S. Weathersby, S. Park, M. E. Kozina, E. J. Sie, H. Wen, P. Jarillo-Herrero, I. R. Fisher, X. Wang, and N. Gedik, *Light-Induced Charge Density Wave in LaTe3,* Nature Physics **16**, 159 (2020) .

[368] G. Chiriacò, A. J. Millis, and I. L. Aleiner, *Negative Absolute Conductivity in Photoexcited Metals,* Physical Review B **101**, 041105 (2020) .

[369] Z. Sun and A. J. Millis, *Transient Trapping into Metastable States in Systems with Competing Orders,* Physical Review X **10**, 021028 (2020) .

[370] G. Chiriacò and A. J. Millis, *Polarity Dependent Heating at the Phase Interface in Metal-Insulator Transitions,* Physical Review B **102**, 085116 (2020) .

[371] G. Kurizki, P. Bertet, Y. Kubo, K. Mølmer, D. Petrosyan, P. Rabl, and J. Schmiedmayer, *Quantum Technologies with Hybrid Systems,* Proceedings of the National Academy of Sciences **112**, 3866 (2015) .

[372] D. N. Basov, R. D. Averitt, D. van der Marel, M. Dressel, and K. Haule, *Electrodynamics of Correlated Electron Materials,* Reviews of Modern Physics **83**, 471 (2011) .

[373] J. Schachenmayer, C. Genes, E. Tignone, and G. Pupillo, *Cavity-Enhanced Transport of Excitons,* Physical Review Letters **114**, 196403 (2015) .

[374] M. Kiffner, J. R. Coulthard, F. Schlawin, A. Ardavan, and D. Jaksch, *Manipulating Quantum Materials with Quantum Light,* Physical Review B **99**, 085116 (2019) .

[375] M. Kiffner, J. R. Coulthard, F. Schlawin, A. Ardavan, and D. Jaksch, *Erratum: Manipulating Quantum Materials with Quantum Light [Phys. Rev. B 99, 085116 (2019)],* Physical Review B **99**, 099907 (2019) .

[376] D. Hagenmüller, S. Schütz, J. Schachenmayer, C. Genes, and G. Pupillo, *Cavity-Assisted Mesoscopic Transport of Fermions: Coherent and Dissipative Dynamics,* Physical Review B **97**, 205303 (2018) .

[377] J. Flick, N. Rivera, and P. Narang, *Strong Light-Matter Coupling in Quantum Chemistry and Quantum Photonics,* Nanophotonics **7**, 1479 (2018) .

[378] P. Nataf and C. Ciuti, *No-Go Theorem for Superradiant Quantum Phase Transitions in Cavity QED and Counter-Example in Circuit QED,* Nature Communications **1**, 72 (2010) .

[379] F. Schlawin, A. Cavalleri, and D. Jaksch, *Cavity-Mediated Electron-Photon Superconductivity,* Physical Review Letters **122**, 133602 (2019) .

[380] S. Kéna-Cohen and J. Yuen-Zhou, *Polariton Chemistry: Action in the Dark,* ACS Central Science **5**, 386 (2019) .

[381] A. Chakraborty and F. Piazza, *Long-Range Photon Fluctuations Enhance Photon-Mediated Electron Pairing and Superconductivity,* Physical Review Letters **127**, 177002 (2021) .

[382] Y. Ashida, A. İmamoğlu, and E. Demler, *Cavity Quantum Electrodynamics at Arbitrary Light-Matter Coupling Strengths,* Physical Review Letters **126**, 153603 (2021) .

[383] L. Giannelli, E. Paladino, M. Grajcar, G. S. Paraoanu, and G. Falci, *Detecting Virtual Photons in Ultrastrongly Coupled Superconducting Quantum Circuits,* Physical Review Research **6**, 013008 (2024) .

[384] J. Feist and F. J. Garcia-Vidal, *Extraordinary Exciton Conductance Induced by Strong Coupling,* Physical Review Letters **114**, 196402 (2015) .

[385] X. Zhong, T. Chervy, L. Zhang, A. Thomas, J. George, C. Genet, J. A. Hutchison, and T. W. Ebbesen, *Energy Transfer between Spatially Separated Entangled Molecules,* Angewandte Chemie (International ed. in English) **56**, 9034 (2017) .

[386] J. Feist, J. Galego, and F. J. Garcia-Vidal, *Polaritonic Chemistry with Organic Molecules,* ACS Photonics **5**, 205 (2017) .

[387] A. Thomas, L. Lethuillier-Karl, K. Nagarajan, R. M. Vergauwe, J. George, T. Chervy, A. Shalabney, E. Devaux, C. Genet, J. Moran, and T. W. Ebbesen, *Tilting a Ground-State Reactivity Landscape by Vibrational Strong Coupling,* Science **363**, 615 (2019) .

[388] G. G. Rozenman, K. Akulov, A. Golombek, and T. Schwartz, *Long-Range Transport of Organic Exciton-Polaritons Revealed by Ultrafast Microscopy,* ACS Photonics **5**, 105 (2017) .

[389] J. Lather, P. Bhatt, A. Thomas, T. W. Ebbesen, and J. George, *Cavity Catalysis by Cooperative Vibrational Strong Coupling of Reactant and Solvent Molecules,* Angewandte Chemie International Edition **58**, 10635 (2019) .

[390] F. Fassioli, J. Faist, M. Eckstein, and D. Fausti, *Controlling radiative heat flow through cavity electrodynamics,* arXiv:2403.00851 [physics.optics] (2024).

[391] C. Gardiner and P. Zoller, *Quantum Noise: A Handbook of Markovian and Non-Markovian Quantum Stochastic Methods with Applications to Quantum Optics* (Springer Berlin Heidelberg, 2004).

[392] E. Paladino, Y. M. Galperin, G. Falci, and B. L. Altshuler, $1/f$ *Noise: Implications for Solid-State Quantum Information,* Reviews of Modern Physics **86**, 361 (2014) .

[393] G. Jarc, S. Y. Mathengattil, F. Giusti, M. Barnaba, A. Singh, A. Montanaro, F. Glerean, E. M. Rigoni, S. D. Zilio, S. Winnerl, and D. Fausti, *Tunable Cryogenic Terahertz Cavity for Strong Light–Matter Coupling in Complex Materials,* Review of Scientific Instruments **93**, 033102 (2022) .

[394] S. Pannir-Sivajothi and J. Yuen-Zhou, *Blackbody Radiation and Thermal Effects on Chemical Reactions and Phase Transitions in Cavities,* ACS Nano **19**, 9896 (2025) .

[395] F. Rüting and C. Weiss, *Cavity Resonances Dominating the Photon Statistics in the Non-Equilibrium Steady State,* Journal of Physics: Conference Series **826**, 012022 (2017) .

[396] P. Portugal, F. Brange, K. S. U. Kansanen, P. Samuelsson, and C. Flindt, *Photon Emission Statistics of a Driven Microwave Cavity,* Physical Review Research **5**, 033091 (2023) .

[397] S. A. Maier, *Plasmonics: Fundamentals and Applications* (Springer US, New York, NY, 2007).

[398] L. Novotny and B. Hecht, *Principles of Nano-Optics*, 2nd ed. (Cambridge University Press, Cambridge, 2012).

[399] A. D'Abbruzzo and D. Rossini, *Self-Consistent Microscopic Derivation of Markovian Master Equations for Open Quadratic Quantum Systems,* Physical Review A **103**, 052209 (2021) .

[400] R. Kubo, *Statistical-Mechanical Theory of Irreversible Processes. I. General Theory and Simple Applications to Magnetic and Conduction Problems,* Journal of the Physical Society of Japan **12**, 570 (1957) .

[401] C. Viviescas and G. Hackenbroich, *Field Quantization for Open Optical Cavities,* Physical Review A **67**, 013805 (2003) .

[402] M. Thorwart, E. Paladino, and M. Grifoni, *Dynamics of the spin-boson model with a structured environment,* Chemical Physics **296**, 333 (2004) The Spin-Boson Problem: From Electron Transfer to Quantum Computing ... to the 60th Birthday of Professor Ulrich Weiss.

[403] S. Weiss, J. Eckel, M. Thorwart, and R. Egger, *Iterative real-time path integral approach to nonequilibrium quantum transport,* Phys. Rev. B **77**, 195316 (2008) .

[404] D. Tamascelli, A. Smirne, S. F. Huelga, and M. B. Plenio, *Nonperturbative Treatment of non-Markovian Dynamics of Open Quantum Systems,* Phys. Rev. Lett. **120**, 030402 (2018) .

[405] R. Flores-Calderón, M. M. Islam, M. Pini, and F. Piazza, *Nonthermal Electron-Photon Steady States in Open Cavity Quantum Materials,* Physical Review Research **7**, 013073 (2025) .

[406] L. Mixa, H. Keßler, A. Hemmerich, and M. Thorwart, *Enhancing Exotic Quantum Fluctuations in a Strongly Entangled Cavity BEC System,* Physical Review Research **6**, L012024 (2024) .

[407] J. R. Johansson, P. D. Nation, and F. Nori, *QuTiP: An Open-Source Python Framework for the Dynamics of Open Quantum Systems,* Computer Physics Communications **183**, 1760 (2012) .

[408] J. R. Johansson, P. D. Nation, and F. Nori, *QuTiP 2: A Python Framework for the Dynamics of Open Quantum Systems,* Computer Physics Communications **184**, 1234 (2013) .

[409] H. P. Ojeda Collado, M. H. Michael, J. Skulte, A. Rubio, and L. Mathey, *Equilibrium Parametric Amplification in Raman-Cavity Hybrids,* Physical Review Letters **133**, 116901 (2024) .

[410] K. E. Cahill and R. J. Glauber, *Ordered Expansions in Boson Amplitude Operators,* Phys. Rev. **177**, 1857 (1969) .

[411] G. Chiriacò, *Thermal Purcell effect and cavity-induced renormalization of dissipations,* arXiv:2310.15184 [physics.optics] (2023).

[412] V. J. Emery, E. Fradkin, S. A. Kivelson, and T. C. Lubensky, *Quantum Theory of the Smectic Metal State in Stripe Phases,* Phys. Rev. Lett. **85**, 2160 (2000) .

[413] A. Vishwanath and D. Carpentier, *Two-Dimensional Anisotropic Non-Fermi-Liquid Phase of Coupled Luttinger Liquids,* Phys. Rev. Lett. **86**, 676 (2001) .

[414] R. Mukhopadhyay, C. L. Kane, and T. C. Lubensky, *Sliding Luttinger liquid phases,* Phys. Rev. B **64**, 045120 (2001) .

[415] M. J. Lawler and E. Fradkin, *Quantum Hall smectics, sliding symmetry, and the renormalization group,* Phys. Rev. B **70**, 165310 (2004) .

[416] C. L. Kane, R. Mukhopadhyay, and T. C. Lubensky, *Fractional Quantum Hall Effect in an Array of Quantum Wires,* Phys. Rev. Lett. **88**, 036401 (2002) .